2023

Light transport by topological confinement

BOSTON UNIVERSITY

COLLEGE OF ENGINEERING

Dissertation

LIGHT TRANSPORT BY TOPOLOGICAL CONFINEMENT

by

ZELIN MA

B.A., Sun Yat-sen University, 2015

Submitted in partial fulfillment of the

requirements for the degree of

Doctor of Philosophy

2023

Approved by

First Reader

Siddharth Ramachandran, Ph.D.
Distinguished Professor of Engineering
Professor of Electrical and Computer Engineering
Professor of Physics
Professor of Materials Science and Engineering

Second Reader

David Bishop, Ph.D.
Professor of Electrical and Computer Engineering
Professor of Physics
Professor and Division Head of Materials Science and Engineering
Professor of Mechanical Engineering
Professor of Biomedical Engineering

Third Reader

Miloš Popović, Ph.D.
Associate Professor of Electrical and Computer Engineering

Fourth Reader

Poul Kristensen, Ph.D.
OFS-Fitel, Broenby, Denmark

莫若以明 ——《莊子》

ACKNOWLEDGMENTS

This thesis owes its existence to the support from the Office of Naval Research (ONR), the Air Force Office of Scientific Research (AOFSR), the Department of Defense (DoD), Brookhaven National Labs, and the Department of Electrical and Computer Engineering at Boston University.

I would like to express my deepest gratitude to Professor Siddharth Ramachandran for providing me with the opportunity to work on this project. I am grateful for his expertise, enthusiasm, and mentorship in guiding me through the challenges of my research. I have learned a great deal from him both within and outside of the lab. Without his guidance and motivation, I would not have achieved what I have accomplished so far.

I would like to thank my committee members, Professor David Bishop, Professor Miloš Popović, and Dr. Poul Kristensen, whose generous dedication of time and expertise has been invaluable in supporting this work.

The exceptional efforts of Dr. Kristensen, who meticulously fabricated all the fibers used in this thesis, have been paramount to the existence of this document. I have gained an extensive understanding of fiber manufacturing from him, and his insights and intelligence have been essential to the research presented. I am deeply appreciative of his journey from Denmark to Boston to attend my prospectus and dissertation defense.

My gratitude extends to all my collaborators. Many thanks to Dr. Andrea Rubano and Prof. Lorenzo Marrucci for providing the q-plate. Professor Miles Padgett and Dr. Steven Johnson's insights on the single pixel camera measurement have been enlightening. Collaborating with Professor Jian Wang on various applications of OAM modes in fibers

has been a pleasure. My appreciation also goes to other collaborators, including but not limited to Professor Federico Capasso, Dr. Noah A. Rubin, Dr. Ahmed H. Dorrah, Professor Fufei Pang, and Professor Dong-Il Yeom.

I would like to extend my gratitude to all my lab mates, both present and past: Dr. Lars Rishøj, Dr. Patrick Gregg, Dr. Jeff. Demas, Dr. Boyin Tai, Dr. Lu Yan, Dr. Tao He, Dr. Du-Ri Song, Dr. Xinglin Zeng, Dr. Aku Antikainen, Dr. Geo Philip Muppathiyil, Dr. Xiao Liu, Dr. Havva Begüm Kabagöz, Aaron Greenberg, Daniel Shahar, Vineetha Ashok, Purva Bhumkar, Aidan McCall, Jianyu Yang, Andrew Chang, and Isabelle Boegholm. Their insightful discussions, delightful company, and lab assistance have been invaluable. Special thanks to Dr. Rishøj for his helpful guidance when I first joined the lab, to Dr. Muppathiyil for his instruction on time-of-flight measurement, and to Dr. Prabhakar for his guidance on utilizing the q-plate. I am particularly grateful to Dr. Gregg, who taught me about the excitation of OAM modes in optical fibers and laid much of the foundation for the OAM fibers, without which this thesis would not have been possible.

I would like to thank my undergraduate advisors, Prof. Siyuan Yu and Dr. Hui Chen, for introducing me to the world of OAM light and patiently guiding me from ignorance into the realm of scientific research. I would like to thank all my friends who have shared in both the joyful moments and hard times along this journey. My apologies for not being able to enumerate all your names, as the list would always be incomplete. Special thanks to Liang Wendao, Yang Zhao, Duan Zhiqiang and Xu Zhiyuan, whose presence illuminated my life during some gloomy days. Lastly, my deepest thanks go to my family for their unwavering love and support, a debt I can never fully repay.

LIGHT TRANSPORT BY TOPOLOGICAL CONFINEMENT

ZELIN MA

Boston University, College of Engineering, 2023

Major Professor: Siddharth Ramachandran, Ph.D., Distinguished Professor of Engineering, Professor of Electrical and Computer Engineering, Professor of Physics, Professor of Materials Science and Engineering

ABSTRACT

The growth of data capacity in optical communications links, which form the critical backbone of the modern internet, is facing a slowdown due to fundamental nonlinear limitations, leading to an impending "capacity crunch" on the horizon. Current technology has already exhausted degrees of freedom such as wavelength, amplitude, phase and polarization, leaving spatial multiplexing as the last available dimension to be efficiently exploited. To minimize the significant energy requirements associated with digital signal processing, it is critical to explore the upper limit of unmixed spatial channels in an optical fiber, which necessitates ideally packing spatial channels either in real space or in momentum space. The former strategy is realized by uncoupled multi-core fibers whose channel count has already saturated due to reliability constraint limiting fiber sizes. The later strategy is realized by the unmixed multimode fiber whose high spatial efficiency suggest the possibility of high channel-count scalability but the right subset of mode ought to be selected in order to mitigate mode coupling that is ever-present due to the plethora of perturbations a fiber normally experiences. The azimuthal modes in ring-core fibers turn out to be one of the most spatially efficient in this regard, by exploiting light's orbital angular momentum (OAM). Unmixed mode counts have reached 12 in a ~1km fiber and

24 in a ~10m fiber. However, there is a fundamental bottleneck for scalability of conventionally bound modes and their relatively high crosstalks restricts their utility to device length applications.

In this thesis, we provide a fundamental solution to further fuel the unmixed-channel count in an MMF. We utilize the phenomenon of topological confinement, which is a regime of light guidance beyond conventional cutoff that has, to the best of our knowledge, never been demonstrated till publications based on the subject matter of this thesis. In this regime, light is guided by the centrifugal barrier created by light's OAM itself rather than conventional total internal reflection arising from the index inhomogeneity of the fiber. The loss of these topologically confined modes (TCMs) decreases down to negligible levels by increasing the OAM of fiber modes, because the centrifugal barrier that keeps photons confined to a fiber core increases with the OAM value of the mode. This leads to low-loss transmission in a km-scale fiber of these cutoff modes. Crucially, the mode-dependent confinement loss of TCMs further lifts the degeneracy of wavevectors in the complex space, leading to frustration of phase-matched coupling. This thus allows further scaling the mode count that was previously hindered by degenerate mode coupling in conventionally bound fiber modes. The frustrated coupling of TCMs thus enables a record amount of unmixed OAM modes in any type of fiber that features a high index contrast, whether specially structured as a ring-core, or simply constructed as a step-index fiber. Using all these favorable attributes, we achieve up to 50 low-loss modes with record low crosstalk (approaching -45 dB/km) over a 130-nm bandwidth in a ~1km-long ring-core fiber. The TCM effect promises to be inherently

scalable, suggesting that even higher modes counts can be obtained in the future using this design methodology. Hence, the use of TCMs promises breaking the record spectral efficiency, potentially making it the choice for transmission links in future Space-Division-Multiplexing systems.

Apart from their chief attribute of significantly increasing the information content per photon for quantum or classical networks, we expect that this new light guidance may find other applications such as in nonlinear signal processing and light-matter interactions.

TABLE OF CONTENTS

LIST OF TABLES

LIST OF FIGURES

LIST OF ABBREVIATIONS

A_{eff}	Effective area
BER	Bit Error Rate
CW	Continuous-wave
DCF	Dispersion Compensating Fiber
ECL	External Cavity Laser
EDFA	Erbium Doped Fiber Amplifier
FMF	Few-Mode Fiber
FT	Fourier transform
GRIN	Graded Index
HOM	Higher Order Mode
HWP	Half-Wave Plate
LCP	Left Circular Polarization
LP	Linearly Polarized
MCVD	Modified Chemical Vapor Deposition
MDM	Mode Division Multiplexing
MIMO	Multiplexing Multi-Input Multiple-Output
MMF	Multimode Fiber
MUBs	Mutually Unbiased Bases
MUX	Multimode Fiber
n_{eff}	Effective Refractive index
OAM	Orbital Angular Momentum
OD	Outer Diameter
OSA	Optical Spectrum Analyzer
PBD	Polarization Beam Displacer
PBS	Polarization Beam Splitter
PM	Polarization Maintaining
polcon	Polarization Controller
QAM	Quadrature Amplitude Modulation
QPSK	Quadrature Phase Shift Keying
QWP	Quarter-Wave Plate
RCP	Right Circular Polarization
SAM	Spin Angular Momentum
SDM	Space Division Multiplexing
SLM	Spatial Light Modulator
SMF	Single Mode Fiber
SNR	Signal-to-Noise Ratio

SOa	Spin-Orbit aligned
SOaa	Spin-Orbit anti-aligned
SOC	Spin-Orbit Coupled
SPM	Self-Phase Modulation
TCM	Topologically Confined Mode
TE	Transverse Electric
TM	Transverse Magnetic
WDM	Wavelength Division Multiplexing
WGA	Weak Guidance Approximation

Chapter 1

1. Introduction

1.1. Optical Communication and Capacity Crunch

The interconnectivity of our world owes much to the revolutionary impact of optical communication, which has radical transformed our societies during the last four decades. While optical communication has been enabled by advancements in technologies like lasers, fast detectors, and transmitters, the backbone of the communication infrastructure relies heavily on optical fibers. Following its invention in the 1970s, optical fiber cables rapidly replaced copper wire communication links, due to their larger bandwidth, cheaper price, and greater stability.

Driven by the technologies shown in Fig. 1.1, the information capacity of a single optical fiber has increased by several orders of magnitude since the 1980s. Despite an exponential increase in demand for data services, the growth of data capacity is nevertheless experiencing a slowdown due to the fundamental limits of current technology. Optical fiber capacity and interface rates scale at ~20% per year, while global traffic continues to grow ~45% per year (Winzer et al. 2017). As a result, we are headed towards a so-called capacity crunch.

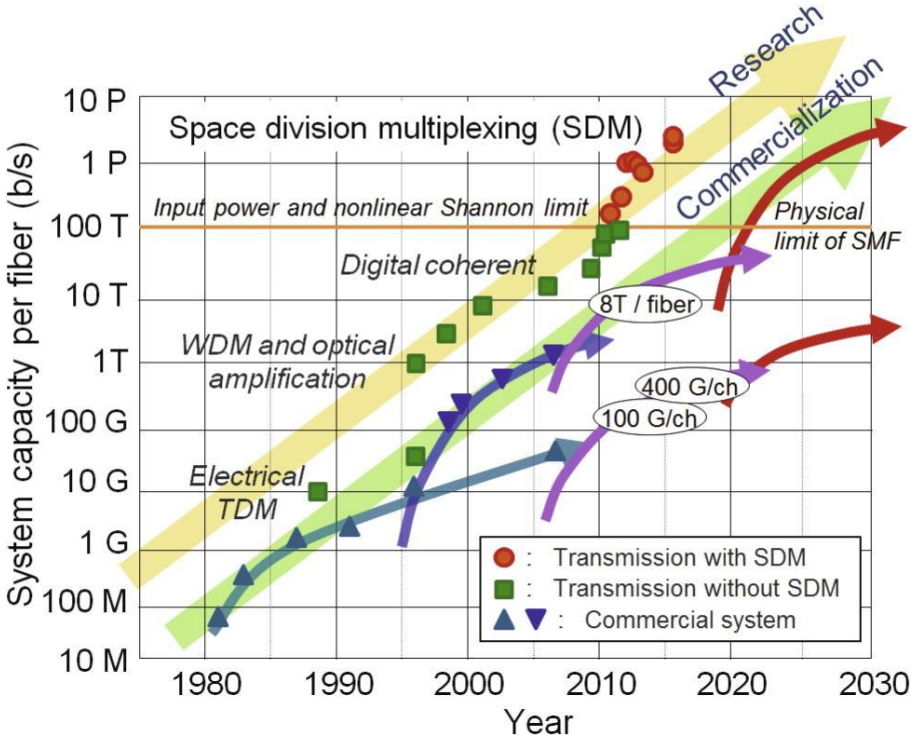

Figure 1.1: The evolution of system capacity per fiber in optical communication systems (Mizuno et al., 2017). While fiber capacity has increased dramatically since 1980, it is now facing a capacity crunch around 100Tb/s due to the fundamental nonlinear Shannon limit. System capacity beyond this limit was demonstrated using space-division multiplexing (SDM), which could expand capacity.

The theoretical information capacity is given by the Shannon formula (Shannon, 1948)

$$C = B \cdot \log_2(1 + SNR) \tag{1.1}$$

where B is the bandwidth and SNR represents the signal-to-noise ratio.

The primary limit of the current system derives from the fiber nonlinearity manifested under high optical power, which fundamentally restrains the maximum SNR allowed in the communication system. This nonlinear, Shannon capacity limit suggests that maximum spectral efficiency (i.e., the ratio of capacity to bandwidth) is around 10 bit/s/Hz, meaning the maximum capacity of a standard, single-mode fiber (SMF) is about 100Tbit/s in the conventional telecom band (Mitra et al. 2001). To mitigate fiber nonlinearity, various

types of special fibers have been developed, such as micro-structured fibers with hollow cores (Roberts et al, 2005) and fibers with lower nonlinear indices based on new materials (Dragic et al, 2012), but none of them have been competitive with silica fiber in terms of cost, material loss, and fabrication complexity.

Wavelength-division multiplexing (WDM) fueled the capacity evolution during the 1990s, with a growth rate of about 78% per year over 10 years (R.-J. Essiambre et al., 2010). Conventional bandwidth is limited to C-band (1530nm to 1565nm) due to the gain window of Erbium-Doped Fiber Amplifier (EDFA). Although various optical amplification technologies that could broaden the WDM window are currently being studied, it is estimated that this strategy would yield less than a fivefold increase in system capacity because of the limited low-loss window of silica fiber and paucity of gain media outside conventional bands (Winzer et al., 2014).

For a given bandwidth and SNR, the Shannon formula provides a theoretical capacity that can only be achieved with optimum constellation and coding. Modulation techniques have also significantly advanced such that the practical capacity has nearly approached the theoretical Shannon limit (Winzer et al., 2012).

Current technologies have already exhausted the dimensions of wavelength, polarization, time, and phase, leaving spatial diversity as the remaining dimension to efficiently exploit (Winzer et al., 2014). Similar to WDM, partial division multiplexing (SDM) could offer multiple orders of magnitude of capacity enhancement, and thus a potential solution to address the tremendous growth in demand for data services.

1.2. Space-Division Multiplexing

Unlike wavelength channels, spatial channels can more easily mix in one fiber, inevitably resulting in crosstalk that fundamentally impairs the SNR. One approach to reducing crosstalk involves isolating independent spatial channels. In this approach, crosstalk is one of the significant metrics for evaluating the capacity of the unmixed SDM system. In such a system with *M* multiple channels, the Shannon formula becomes (Luis et al., 2017)

$$\mathrm{C} = \mathrm{B}\sum_{i=1}^{M}\log_2(1+(\mathrm{SNR}_i^{-1}+\mathrm{XT}_i)^{-1}) \tag{1.2}$$

where XT_i is the sum of the crosstalk (XT) from all other channels to the *i*-th channel. Although the channel count is critical in multiplying the capacity, there is a trade-off between M and XT.

One direct approach to accommodate multiple channels within a fiber is the utilization of uncoupled multicore fibers (MCFs), where additional independent cores are added to a SMF. Although complete elimination of inter-core coupling is not possible regardless of the core separation distance, the term "uncoupled" signifies that the mode coupling (or crosstalk) is sufficiently low for the desired modulation format and transmission distance (detailed in Chapter 8). By employing large core spacing and core trenches to suppress inter-core coupling, crosstalk levels of approximately -40 dB/km can be achieved for up to 22 homogeneous cores in a fiber with a cladding diameter of 260 μm. This has led to successful transmission demonstrations of 2.15 Pb/s when combined with WDM techniques (Puttnam et al., 2015).

However, limitations in reliability necessitate that the fiber diameter remains below approximately 250 μm (Sakamoto et al., 2017), thereby fundamentally restricting the number of cores that can be accommodated within a single fiber. By incorporating heterogeneous cores that suppress inter-core coupling, the core count can be maximized to 37 (Sasaki et al., 2017). Nevertheless, this introduces sensitivity to macro-bending due to bend-induced effective index variation (Saitoh et al., 2013), resulting in significant degradation of crosstalk (e.g., up to -20 dB/km) around and below the threshold bending radius (approximately 30 mm, dependent on the inter-core index difference). Despite notable advancements, both the capacity and core count have reached a saturation point, suggesting an inherent scalability limit for MCF technology.

Perhaps a simpler way to increase capacity would be adding more SMFs as “fiber bundles”. Indeed, this is the current approach to relieving the capacity crunch without drastically altering current optical fiber cable infrastructure. To justify the replacement of the fiber bundle, any SDM technology must present an obvious cost or energy advantage. In this context, the limitation on capacity is more fundamentally related to the cost and energy expended per bit (Winzer et al., 2011). Although optical fiber has a higher capacity than copper wire, it was not until the 1970s, when the cost of optical fiber was reduced to that of copper wire, that optical fiber was widely adopted. Subsequent mass production further drove down the price, firmly establishing optical fiber as the dominant links for long-haul communications systems.

Replacing the entire infrastructure of the telecom system, especially for sub-ocean fiber cables spanning over 1000 km, will be an expensive endeavor. Instead, a more

feasible approach would involve integrating SDM technology gradually, starting with certain fiber components through an incremental strategy. This approach allows the current SMF-based system to benefit from SDM capabilities, even if long-haul transmission remains the ultimate objective. In particular, an SDM amplifier with shared pump amplification could be helpful in reducing energy consumption even in the current SMF-based telecom system. Notably, this approach has already been successfully implemented in submarine optical communication, marking the first commercial adoption of SDM technology (Google, 2019).

Given the challenges associated with mitigating the mixing of spatial channels, an alternative approach is to intentionally mix and then disentangle them using MIMO Multiple-Input Multiple-Output (MIMO) digital signal processing (DSP). This technique is already well-established in wireless radio-wave antennae. Since spatial channels arguably mix after a long distance (i.e., in fiber with a reasonably high channel count), the question is not whether, but when to use MIMO DSP. In this approach, one must thoroughly mix the spatial channels, which can be done using conventional multimode fibers (MMFs). Data transmission using up to 15 spatial modes with 30 by 30 MIMO was demonstrated in a ~23km graded index MMF and had spatial efficiency much higher than that of the MCF (Fontaine et al., 2015).

However, MIMO DSP requires scaling the number of finite impulse response (FIR) filters as the square of the number of modes. This computation is very power consuming and such complexity limits the potential scalability. As such, it doesn't fully address the power and cost concerns pertaining to the current fiber bundle. Given that the MIMO

algorithm is designed for a specific system with a given number of channels, it is incompatible with a system that adds, drops, and re-routes individual SDM tributaries. Furthermore, this solution cannot be applied to single photons in quantum networks.

On the other hand, MIMO DSP is not incompatible with unmixed SDM. Coupled-core MCF with "partial MIMO" reaches the maximum capacity ever demonstrated by a single fiber (Soma et al., 2017). In this regard, the number of unmixed channels is still the backbone. By introducing brute-force MIMO DSP on spatial channels that can be potentially disentangled physically, one unnecessarily wastes the system's energy consumption and computation power. Therefore, it is critical to figure out the scalability of unmixed spatial channels, based on which there should be a suitable combination with partial MIMO to reach minimal cost and energy per bit. Nonetheless, the balance with MIMO is not the primary concern in this dissertation. We still focus on the former question – what is the scalability of unmixed spatial channels in a fiber?

On the other hand, MIMO DSP and unmixed SDM are not mutually exclusive. Coupled-core MCFs implementing "partial MIMO" have achieved the highest demonstrated capacity by a single fiber (Soma et al., 2017). In this context, the number of unmixed channels remains the backbone. Implementing brute-force MIMO DSP on spatial channels that can potentially be physically disentangled would result in unnecessary energy consumption and computational demands on the system. Therefore, it becomes imperative to determine the scalability of unmixed spatial channels, as this knowledge will guide the appropriate combination of partial MIMO for achieving minimal cost and energy per bit. However, it should be noted that achieving a balance with MIMO is not the primary focus

of this dissertation. Instead, the central focus remains on investigating the scalability of unmixed spatial channels within a fiber.

Similar to isolating spatial cores in real space, separating spatial modes of an MMF in momentum space can also mitigate mode coupling. However, due to their higher state density and external perturbations, spatial modes in an MMF are prone to easy coupling, making it a fiber typically considered one in which all the modes mix. This mode mixing is also compounded by a lack of pure mode excitation, which distinguishes it from the inherent mode coupling that occurs within the fiber. Nevertheless, with advancements in mode excitation and characterization techniques, there has been a recent re-examination of the modal properties within an MMF. By carefully selecting a suitable subset of modes and reducing the number of undesired modes, it becomes possible to achieve a substantial number of unmixed modes within a highly multimode fiber. As depicted in Figure 1.2, significant advancements have been made in the development of unmixed-mode count within 10-100m-long MMF (Ramachandran et al., 2009, Ramachandran et al., 2010, Bozinovic et al., 2012, Gregg et al., 2019, Tugchin et al., 2015, Jung et al., 2017, Sit et al., 2018, Yan et al., 2019, Zhu et al, 2020, Liu et al., 2020, Rottwitt et al., 2019, Zhu et al., 2017, Ramachandran et al., 2008, Demas et al., 2015, Rishoj et al., 2019) and with >1km-long MMF (Bozinovic et al., 2011, Bozinovic et al., 2013, Ung et al., 2014, Gregg et al., 2015, Nejad et al., 2016, Gregg et al., 2016, Wang et al., 2016, Ingerslev et al., 2018, Cozzolino et al., 2019, Liu et al., 2016, Wang et al., 2022, Lu et al., 2022).

The available modes within multimode fibers (MMFs) can be classified into two categories: radial modes and azimuthal modes. Among these, the azimuthal modes in ring-

core fibers have proven to be the most spatially efficient, leveraging the concept of light's orbital angular momentum (OAM). Remarkable progress has been achieved in the realm of unmixed mode count, with a ~1 km fiber demonstrating up to 12 unmixed modes (Gregg et al., 2016), and a ~10 m fiber showcasing 24 unmixed modes (Gregg et al., 2019), as illustrated in Fig. 1.2. Since a fiber core occupies a much smaller area, the spatial efficiency is much higher than that of MCFs. However, the further scalability of this approach still faces challenges in terms of mode coupling, and the relatively high crosstalk associated with it limits its practical application to device lengths.

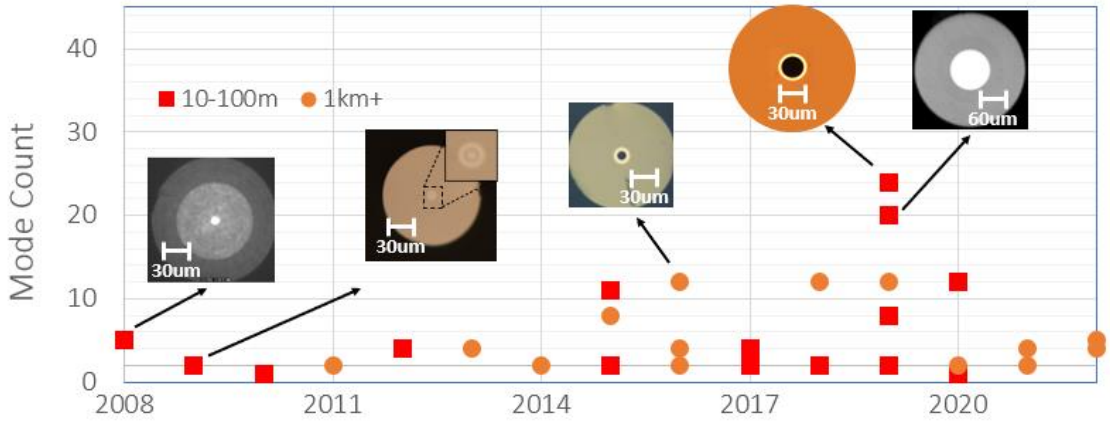

Figure 1.2: Development of unmixed-mode count in an MMF with 10-100m long and with >1km long. The fibers illustrated here include simple step-index fibers utilizing high-order radial modes and ring-core fibers utilizing high-order azimuthal modes. The mode-count record is 24 over 10s-m length and 12 over 1-km length, both in ring-core fibers.

Overall, the field of SDM research has progressed beyond merely pursuing capacity-focused hero experiments. The current focus lies in optimizing existing technologies and exploring various SDM devices for related applications. It is important to note that the availability of unmixed spatial modes also provide a large tool box for intriguing applications involving linear and nonlinear inter-modal interactions.

1.3. Beyond Cutoff

Conventionally, the cutoff of fiber modes is believed to be determined by the fiber's index contrast, as it dictates the condition for total internal reflection (TIR). The previous section highlighted the significance of selecting the appropriate subset of modes, which primarily exists at the high-order end and accordingly gets limited by this forbiddance region. However, despite the extensive research conducted on MMFs and OAM modes in recent years, there remains a lack of comprehensive understanding regarding the fundamental concept of cutoff.

The high-order radial and azimuthal modes mentioned earlier exhibit fundamentally distinct behavior in close proximity to, and even beyond, the conventional cutoff. Surprisingly, light with high OAM can be guided beyond this cutoff limit. This unique regime of guidance – topological confinement –holds the potential to further enhance the scalability of uncoupled MMFs, and is the central topic of this thesis.

1.4. Thesis Content and Organization

This thesis presents topological confinement as a unique regime of light guidance able to surpass the conventional TIR-based cutoff. Our findings demonstrate how topological confinement can address mode mixing issues in MMFs and achieve a record number of low-loss and low-crosstalk modes. These outcomes have direct applications in classic and quantum communication, as well as in various inter-modal interactions in nonlinear as well as quantum regimes.

The thesis is organized as follows:

Chapter 2 and 4 provide an overview of the theoretical framework of this thesis. These chapters cover the properties of modes, and form a basis from which to understand the issue of mode coupling in MMF. Based on the theories reviewed, we conclude that OAM modes are the preferable eigenmodes for unmixed spatial channels. Chapter 3 provides the techniques for mode characterization and excitation used in this thesis.

Chapter 5 describes our efforts to scale the number of unmixed OAM bound modes. Based on our experiments, we conclude that mode count is fundamentally restricted by the challenges associated with shaping the refractive index profile and the fabrication process of the fiber.

Chapter 6 then describes the principle of topologically confined modes (TCMs) and its potential to further scale mode count. Chapter 7 details the frustrated coupling phenomenon in TCMs. This effect fundamentally suppresses coupling between modes, leading to a record mode count in ring-core and step-index fibers. Chapter 8 demonstrates the inherently low crosstalk of TCMs, around two orders of magnitude lower than that of the bound modes. Chapter 9 demonstrates ~1km transmission of TCMs with record low crosstalk in the telecom S, C and L bands. The spectral efficiency is estimated to be on par with that of the uncoupled MCF.

The final chapter, Chapter 9, summarizes the overall findings of our topologically confined mode research and discusses possible directions for future research.

Appendix A details our method of making end caps for the ring-core fiber to avoid Fresnel reflections at the fiber end-facets. Appendix B summarizes the theoretical

framework underlying the phase matched layer (PML) scalar mode solver used throughout the thesis.

Chapter 2

2. High-Order Modes in Fibers

An eigenmode (or simply “mode”) of a fiber is a stable state of the electric field that maintains its transverse distribution along the propagation in a fiber. To understand the light propagation in optical fibers, one must identify a fiber's eigenmodes and their associated properties. This chapter will show that some modes are valid in certain circumstances or approximations, but do not emerge as true eigenmodes in a more general and rigorous case. That said, this thesis still uses the common nomenclature (e.g., LP modes) to refer these modes. Additionally, the term “true” or “real” is used to designate which eigenmodes actually satisfy the initial definition.

Since its invention in the 1970s, single-mode fibers (SMFs) have captured the interest of researchers, overshadowing the utilization of multimode fibers (MMFs). SMFs have become the backbone of modern communications infrastructure, while MMFs are rarely employed for long-haul transmission. The abundance of HOMs in an MMF creates a significant challenge to exciting and propagating specific modes. The modal dispersion of MMFs thus becomes detrimental to the signals. Although the demand for fibers with large effective areas and low nonlinearity (primarily for fiber laser applications) has sparked attention towards multimode fibers (Ramachandran et al., 2006; Abedin et al., 2019), the focus has predominantly revolved around eliminating HOMs to achieve effective single-mode guidance. This has been accomplished through the use of specialized fibers such as photonic-bandgap fibers (Cregan et al., 1999), anti-resonant fibers (Benebid,

2002), or leakage channel fibers (Dong et al., 2007).

For a considerable period, it was commonly believed that all modes within a highly multimode fiber inevitably mix, which proved advantageous for applications in MIMO DSP (Fontaine, 2018), spectrometry (Redding et al., 2013), and imaging (Cizmar et al., 2012). Notably, this mode mixing could be attributed to impure mode excitation or in-fiber mode coupling. With the advancement of mode excitation and characterization techniques, the independent utilization of HOMs and their interactions has become possible, rekindling interest in multimode fibers in recent years. This powerful toolbox provides many more degrees of freedom to manipulate, with each HOM having a characteristic phase and group velocity, group-velocity dispersion, and modal area. Consequently, a range of applications has emerged, including dispersion engineering (Ramachandran et al., 2001; Gnauck et al., 2000), tailored Raman/Brillouin scattering (Rishoj et al., 2019; Russell et al., 1990), third-harmonic generation (Omenetto et al., 2001), expanded supercontinuum generation (Efimov et al., 2003), power-scalable source engineering (Demas et al., 2017), and novel forms of quantum sources (Cruz-Delgado et al., 2016). Moreover, the ability to control specific HOMs offers a plethora of additional spatial channels (Bozinovic et al., 2013; Ingerslev et al., 2018), holding promise for alleviating the impending capacity limitations.

Therefore, the objective of this chapter is to obtain the eigenmodes within the fiber and elucidate their fundamental properties. Starting from the classic wave equation, we derived the conventional scalar modes. The degeneracy of scalar modes is lifted due to spin-orbit interactions, leading to exact eigenmode solutions that can be mathematically expressed in the OAM and vectorial bases. Through a thorough review of the essential

properties of these modes within a generate context, this chapter establishes the theoretical framework that serves as the foundation for the subsequent chapters of this thesis.

2.1. Total Internal Reflection and Waveguiding

Since its demonstration by Colladon, Babinet and Tyndall more than 150 years ago, total internal reflection (TIR) has been the primary means for waveguiding. As shown in the in Fig. 2.1, a light ray is totally internally reflected only if

$$0 \leq \theta_z \leq \theta_c \tag{2.1}$$

where θ_c is the complement of the critical angle given by

$$\theta_c = \cos^{-1}\left(\frac{n_{\mathrm{cl}}}{n_{\mathrm{co}}}\right) \tag{2.2}$$

where n_{co} and n_{cl} are the refractive index of the core and cladding, respectively.

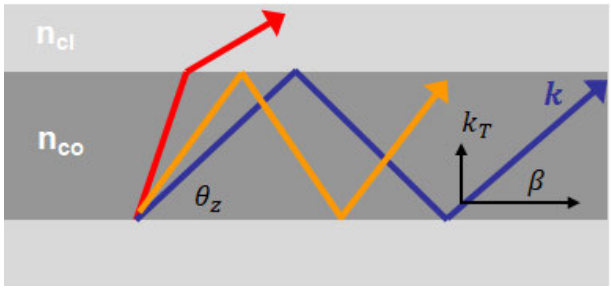

Figure 2.1: Schematic of light guidance in a step-index planar waveguide. The refractive index of the core (n_{co}) is higher than that of the cladding (n_{cl}). θ_z is the angle between the wavevector $\boldsymbol{k}$ and the z axis. The blue and yellow rays are totally internally reflected in the waveguide, whereas the red ray is unbound because its θ_z is too large. $\underline{k}_{\mathrm{T}}$ and β are the transverse and longitudinal component of the wavevector $\boldsymbol{k}$.

The ray picture is valid only if the wavelength of light is much smaller than the size of the waveguide. Otherwise, only discrete values of θ_z are permitted for a given wavelength of light. The transverse component of the wavevector $\boldsymbol{k}$, k_T, must meet the the

transverse resonance requirement. Each discretized θ_z represents to a mode. The longitudinal (z) component of the wavevector $\boldsymbol{k}$ is given by

$$\beta = n_{\mathrm{co}} k_0 \cos\theta_z \tag{2.3}$$

where $k_0 = 2\pi/\lambda$ is the free-space wavevector of light with wavelength λ. β is also known as the propagation constant of a mode. The phase shift of each mode is thus given by βz. The β of bound modes is given by the TIR condition (Eq. 2.1 & 2.2) as

$$n_{\mathrm{cl}} k_0 \leq \beta \leq n_{\mathrm{co}} k_0 \tag{2.4}$$

Usually, β of a mode is represented by its effective refractive index as

$$n_{eff} = \frac{\beta}{k_0} = \frac{\lambda}{2\pi}\beta \tag{2.5}$$

Under this representation, the phase shift of each distinct zig-zag light path in a waveguide with core index n_{co} is equivalently considered as the phase shift of a longitudinal light path in a waveguide with core index n_{eff}. The TIR condition represented by β (Eq. 2.3) thus can be rewritten as

$$n_{\mathrm{cl}} < n_{eff} < n_{\mathrm{co}} \tag{2.6}$$

In contrast, a mode is cut off when $\beta < k_0 n_{cl}$, which translates to

$$n_{eff} < n_{cl} \tag{2.7}$$

2.2. Scalar Modes

The electromagnetic method can provide more general and rigorous analysis of modes in optical fibers. The wave equation of the electrical field $\boldsymbol{\mathcal{E}}$ in inhomogeneous media can be directly derived from Maxwell equation as (Ghatak and Thyagarajan, 1998)

$$\nabla^2 \boldsymbol{\mathcal{E}} + \nabla\left(\frac{1}{n^2}\nabla n^2 \cdot \boldsymbol{\mathcal{E}}\right) - \epsilon_0 \mu_0 n^2 \frac{\partial^2 \boldsymbol{\mathcal{E}}}{\partial n^2} = 0 \tag{2.8}$$

where ϵ_0 is the permittivity of free space, μ_0 is the free space magnetic permeability, n is the refractive index. The electrical field $\boldsymbol{\mathcal{E}}$ have components in three orthogonal polarization that they are coupled with each other.

In a circularly symmetric fiber, the refractive index depends only on the radial coordinate r:

$$n^2 = n^2(r) \tag{2.9}$$

By substituting it into Eq. (2.8) in cylindrical coordinates, one can see that the time, the longitudinal coordinate z, and the azimuthal coordinate φ parts can be separated. Therefore, the solution of the first equation can be written in the form of

$$\boldsymbol{\mathcal{E}} = \boldsymbol{\mathcal{E}}_r(r) e^{iL\varphi} e^{i(\omega t - \beta z)} \tag{2.10}$$

where ω is the angular frequency, L is the azimuthal quantum number as $L = 0, \pm 1, \pm 2, \pm 3, etc$, β is the propagation constant of a mode.

In a simple and common step-index fiber

$$n(r) = \begin{cases} n_{\text{co}}; & r < a \quad core \\ n_{\text{cl}}; & r > a \quad cladding \end{cases} \tag{2.11}$$

where $n_{co} \approx n_{cl}$, which allows the well-known weakly guiding approximation or the scalar wave approximation. It is valid for common practical fibers with extremely low index contrasts. The light propagating in such a fiber is approximated to a free-space beam with transverse electric and magnetic field so it can have an arbitrary state of polarization. In other words, the polarization and field distribution are decoupled. The scalar field distribution can be written as

$$\Psi = F(r)e^{iL\varphi}e^{i(\omega t-\beta z)} \tag{2.12}$$

where $F(r)$ is the field distribution in the radial direction.

Substituting Eq. (2.12) into Eq. (2.8) and using cylindrical coordinates, we obtain

$$\frac{d^2F(r)}{dr^2}+\frac{1}{r}\frac{dF(r)}{dr}+\left(k_0^2n^2-\beta^2-\frac{L^2}{r^2}\right)F(r)=0 \tag{2.13}$$

which is the classic Bessel's equation. Given the convergence requirement at $r = 0$ and $r \to \infty$, we obtain the solution as

$$F(r)=\begin{cases}\dfrac{A}{J_L(U)}J_L\left(\dfrac{Ur}{a}\right); & r<a\\ \dfrac{A}{K_L(W)}K_L\left(\dfrac{Wr}{a}\right); & r>a\end{cases} \tag{2.14}$$

where

$$U = a(k_0^2n_1^2-\beta^2)^{\frac{1}{2}} \tag{2.15}$$

$$W = a(\beta^2-k_0^2n_2^2)^{\frac{1}{2}} \tag{2.16}$$

Both *U* and *W* take real values for all the bound modes with $n_{cl} < n_{eff} < n_{co}$. $J_L(x)$ is the Bessel function of the first kind, which oscillates like sine function but with a reducing amplitude. $K_L(x)$ is the modified Bessel function of the second kind, which has an asymptotic form as

$$K_L(\tilde{x}) \underset{\tilde{x}\to\infty}{\longrightarrow} \left(\frac{\pi}{2\tilde{x}}\right)^{\frac{1}{2}}e^{-\tilde{x}} \tag{2.17}$$

where $\tilde{x} = \frac{Wr}{a}$. Hence, the field decays with increase radius at an exponential rate in the cladding. For a given L, there will multiple solutions yielding discrete $\beta_{L,m}$, where m is the radial quantum number (m=1,2,3…). The solutions can be obtained by considering continuous derivative of the field at $r = a$. Effectively, the fields are stationary waves in the radial direction, with ($m - 1$) signifying the number of intensity nulls. For cutoff mode with $n_{eff} < n_{cl}$, W becomes imaginary, so that the field in the cladding shows oscillating distribution according to Eq. (2.17).

Other than the complex representation $e^{iL\varphi}$, a more conventional solution of the azimuthal dependence is in the sinusoidal form as $\sin L\varphi$ or $\cos L\varphi$, where L usually take positive integer (equivalent to the negative ones). These two representations are mathematically equivalent from Euler's theorem. One set of solution can be decomposed into the combination of the another. Note that this equivalency also applies to the wave function depended on time and z, while the exponential representation $e^{i(\omega t - \beta z)}$ is more convenient to handle. In the form of sinusoidal representation, the transverse dependence of the modal field can be written as

$$\psi(r, \varphi) = F_{|L|,m}(r) \begin{bmatrix} \cos(L\varphi) \\ \sin(L\varphi) \end{bmatrix} \tag{2.18}$$

which is well known as the linearly polarized (LP) mode. The even ($\cos(L\varphi)$) and odd ($\sin(L\varphi)$ modes are degenerate in β. Accounting for two orthogonal polarizations, there can be four degenerate modes for a given combination of L (non-zero) and m.

$$\begin{bmatrix} \mathrm{LP}_{L,m,x}^{even} \\ \mathrm{LP}_{L,m,x}^{odd} \\ \mathrm{LP}_{L,m,y}^{odd} \\ \mathrm{LP}_{L,m,y}^{even} \end{bmatrix} = F_{L,m}(r) \begin{bmatrix} \hat{x}\cos(L\varphi) \\ \hat{x}\sin(L\varphi) \\ \hat{y}\sin(L\varphi) \\ \hat{y}\cos(L\varphi) \end{bmatrix} \tag{2.19}$$

For $L = 0$, it possesses a two-fold degeneracy as

$$\begin{bmatrix} \mathrm{LP}_{0,m}^{x} \\ \mathrm{LP}_{0,m}^{y} \end{bmatrix} = F_{0,m}(r) \begin{bmatrix} \hat{x} \\ \hat{y} \end{bmatrix} \tag{2.20}$$

These degenerate modes continue to be orthogonal in transverse fields (i.e. their overlap integrals between either two modes are zero). Orthogonality is defined in terms of field distribution, whereas degeneracy is defined in terms of β (or n_{eff}). Notice that the fourfold degeneracy is only true under the scalar wave approximation and is no longer valid for high-|L modes in a fiber with a relatively large index contrast (as shown in Sec 2.3).

Figure 2.2 depicts the intensity distribution of several even LP modes with different L and m combinations. The field with L=0 and m=1 is the well-known fundamental mode of a single-mode fiber (SMF).

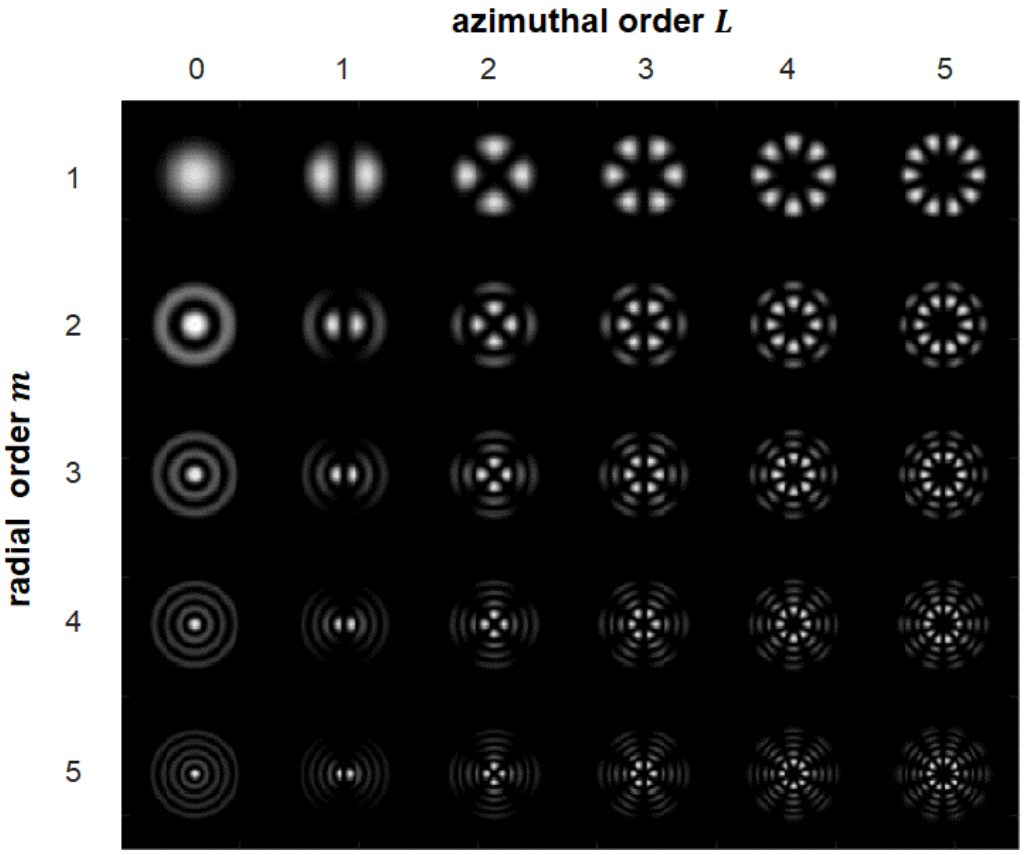

Figure 2.2: Intensity patterns of representative LP even modes with various combination of radial order *m* (1-5) and azimuthal order *L* (0-5).

The spatial distribution of the electric field determines the effective area (A_{eff}) of a certain mode, given by (Agrawal, 2019)

$$A_{eff} = \frac{(\int |\psi|^2 dA)^2}{\int |\psi|^4 dA} \tag{2.21}$$

where dA is the spatial element. The effective area is a critical metric in fiber nonlinearity. Large A_{eff} is particularly advantageous for improving the nonlinear resistance of a fiber.

The aforementioned modal characteristics assume a fixed wavelength. Yet, a mode is naturally dispersive – n_{eff} decreases monotonically with increasing wavelength. The chromatic dispersion of a certain n_{eff} follows the same trend as the silica dispersion but

the slope is more steep. Thus, each mode has a cutoff wavelength (λ_c) beyond which the n_{eff} become lower than the cladding (silica) index, such that the mode is cut off (Eq. 2.7). Figure 2.3 illustrates the n_{eff} distribution of modes in a step-index fiber with index contrast ($\Delta n = n_{co} - n_{cl}$) equal to 0.035 and core diameter equal to 10 μm. Various modes have varied cutoff wavelengths due to their distinct n_{eff} curves (i.e. modal dispersion). Note that two modes with distinct L and m value can be "accidentally degenerate" at a wavelength where the two n_{eff} curves intersect (e.g., LP_{02} & LP_{31} at ~1000nm). This can result in strong mode coupling, as covered in Chapter 4.

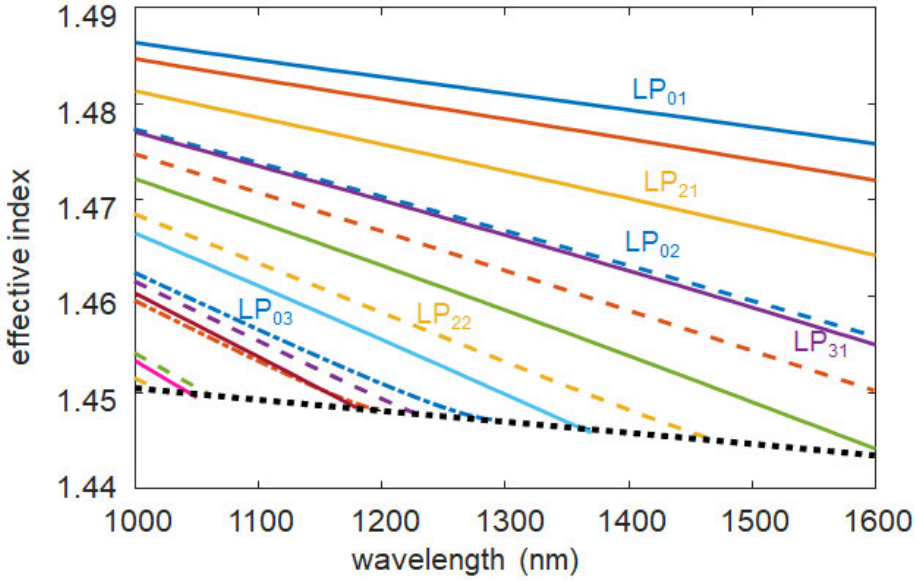

Figure 2.3: n_{eff} distribution of all the modes in a step-index fiber with index contrast equal to 0.035 and core diameter equal to 10 μm. Solid, dash, dash-dot color lines represent modes with m=1, m=2, m=3. The black dashed line is the refractive index of silica.

Due to chromatic dispersion, the group velocity of a light pulse traveling through a fiber is different from its phase velocity. Similar to the relationship between phase velocity and effective index, group velocity is dictated by the group index, given by

$$n_g = n_{eff} - \lambda \frac{dn_{eff}}{d\lambda} \tag{2.22}$$

The pulse broadening is characterized by the group-velocity dispersion (GVD)

$$D = -\frac{\lambda}{c}\frac{d^2 n_{eff}}{d\lambda^2} \tag{2.23}$$

In addition to linear polarization, a scalar mode can exhibit an arbitrary state of uniform polarization due to the degeneracy of two orthogonally polarized LP modes. Similarly, it is also possible to have circularly polarized (CP) modes, which represent spatially uniform circular polarization distributions:

$$\begin{bmatrix} \mathrm{CP}_{L,m,+}^{even} \\ \mathrm{CP}_{L,m,+}^{odd} \\ \mathrm{CP}_{L,m,-}^{odd} \\ \mathrm{CP}_{L,m,-}^{even} \end{bmatrix} = F_{L,m}(r) \begin{bmatrix} \hat{\sigma}^+ \cos(L\varphi) \\ \hat{\sigma}^+ \sin(L\varphi) \\ \hat{\sigma}^- \sin(L\varphi) \\ \hat{\sigma}^- \cos(L\varphi) \end{bmatrix} \tag{2.24}$$

where $\hat{\sigma}^{\pm} = \hat{x} \pm i\hat{y}$, representing left- or right-handed circular polarization, respectively. Again, it becomes two-fold degenerate for L=0:

$$\begin{bmatrix} \mathrm{CP}_{0,m}^{+} \\ \mathrm{CP}_{0,m}^{-} \end{bmatrix} = F_{0,m}(r) \begin{bmatrix} \hat{\sigma}^+ \\ \hat{\sigma}^- \end{bmatrix} \tag{2.25}$$

Figure 2.4 shows the intensity profiles of two representative modes, with $L = 0$, and m = 1 and 3, respectively. Both m = 1 and 3 modes can exhibit either linear or circular polarization. Note that m = 1 modes have a flat phase front, as contrasted with high-m modes where each adjacent intensity ring of the mode accumulates a π phase shift and hence their fields are flipped. Linear combinations of the modes in any polarization bases yield modes in another bases. Circular polarization modes can be represented as linear combinations of the two orthogonal linear polarization modes, as illustrated by the lines

along with the $+i$ and $-i$ signs connecting modes of the different bases. Conversely, linear polarization modes can be decomposed into two orthogonal circular polarization modes as well. The linear and circular polarizations are thus equivalent, forming the typical mutually unbiased bases (MUB), which are commonly used to transmit quantum information (Durt et al., 2010). Generally, the fundamental mode of SMFs and the entire class of $L = 0$ modes are two-fold degenerate (in polarization) and any arbitrary polarization state of these modes propagates similarly in a fiber.

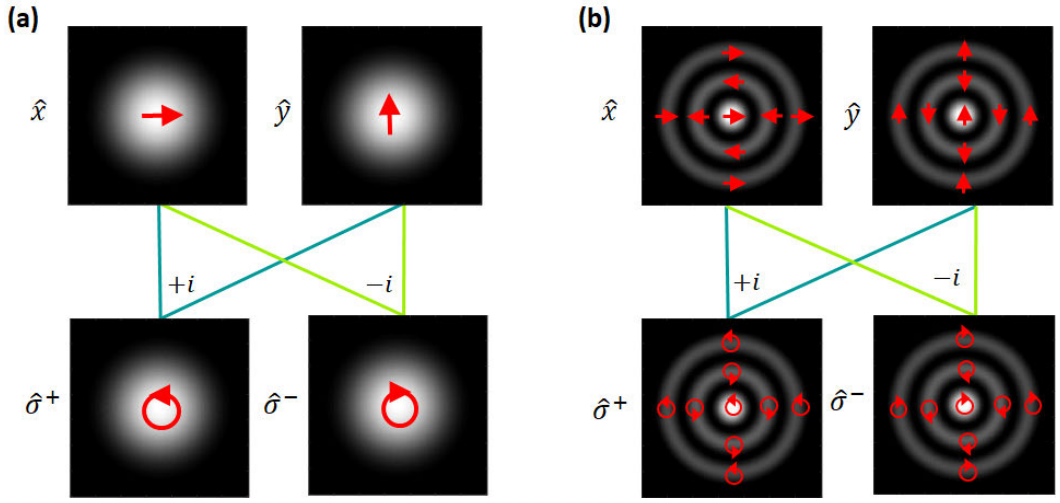

Figure 2.4: Intensity distributions for $L = 0$ modes with either linear (straight arrows in top row) or circular (circular arrows in bottom row). The relationship between linear and circular polarizations are shown for the (a) $m = 1$ and (b) $m = 3$ modes. The colored lines indicate linear combination and the $+i$ or $-i$ terms represent a $\pi/2$ or $-\pi/2$ phase shift. Circular polarization representations where the arrowhead is on the top portion of respective circles is π phase-shifted from those in which they are on the bottom of the circle.

2.3. OAM and Spin-Orbit Interaction

As mentioned above, the sine and exponential representations of the azimuthal function are mathematically equivalent. In other words, they are mutually unbiased bases and one can be represented as a combination of the other. In either base, there are four degenerate modes

for a given $|L|$ including two independent polarizations. However, it is under the assumption of weakly guided approximation which is only valid for modes with low $|L|$. For high-L modes, only one of them is the set of eigenmode bases and the four-fold degeneracy is lifted.

It was demonstrated by Allen in 1992 (Allen et al., 1992) that a beam with helical phase $e^{iL\varphi}$ carries orbital angular momentum (OAM), different from conventional spin angular momentum (SAM) carried by circularly polarized light. The OAM of light is a new degree of freedom and has gained a lot of attention since then given that it theoretically allows unlimited scalability for both classical and quantum communications.

Figure 2.5 shows the intensity distribution of a few representative OAM modes with various combination of the L and m.

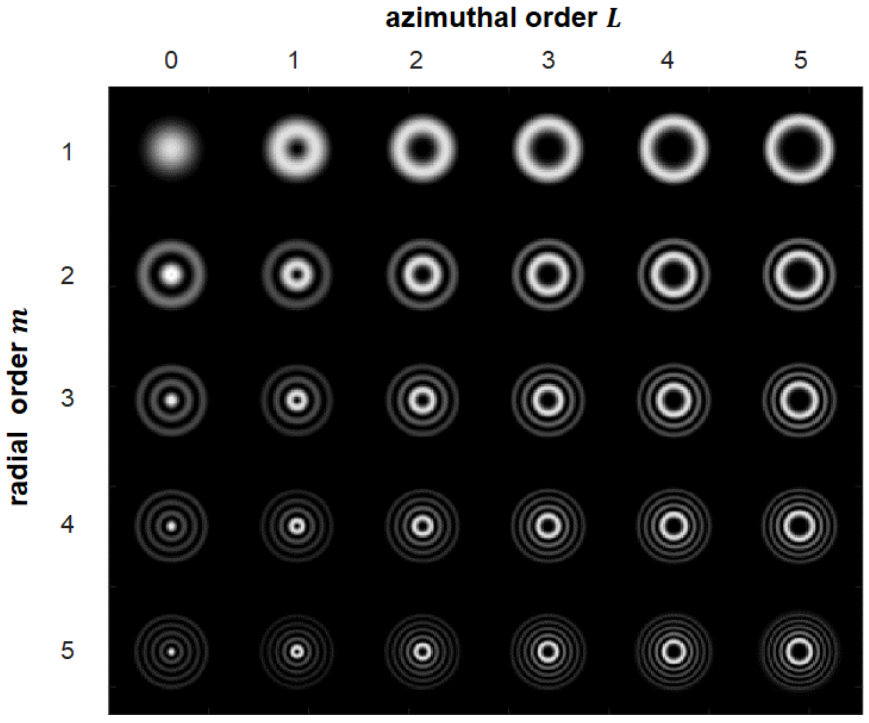

Figure 2.5: Intensity patterns of representative OAM modes with various combination of radial order m (1-5) and azimuthal order L (0-5).

Depending on the signs of OAM and SAM, there are four combinations, thus four near-degenerate modes for a given $|L|$. They can be classified into two categories: Spin-Orbit aligned (SOa) modes whose signs of $\hat{\sigma}$, and L are the same and Spin-Orbit anti-aligned (SOaa) modes whose signs of $\hat{\sigma}$, and L are the opposite. Under weakly guiding approximation, all these four modes for a given $|L|$ are degenerate in the propagation constant β and hence the n_{eff}. This degeneracy is lifted due to spin-orbital interaction (SOI), which arises from the anisotropy of the fiber's refractive index distribution (Leary et al., 2009, Vitullo et al., 2017). It is analogous to the atomic spin-orbit interaction that splits the degeneracy of electronic energy level. The degree of SOI depends on the alignment of spin and orbital angular momentum. In other word, the SOa and SOaa have different propagation constant. Therefore, the electrical field (of $|L| > 1$) now become

$$\boldsymbol{E}_{L,m} = \begin{bmatrix} \mathrm{OAM}_{+L}^{+} e^{i\beta'_{L,m}z} \\ \mathrm{OAM}_{-L}^{-} e^{i\beta'_{L,m}z} \\ \mathrm{OAM}_{+L}^{-} e^{i\beta''_{L,m}z} \\ \mathrm{OAM}_{-L}^{+} e^{i\beta''_{L,m}z} \end{bmatrix} \tag{2.26}$$

where

$$\begin{bmatrix} \mathrm{OAM}_{+L}^{+} \\ \mathrm{OAM}_{-L}^{-} \\ \mathrm{OAM}_{+L}^{-} \\ \mathrm{OAM}_{-L}^{+} \end{bmatrix} = F_{L,m}(r) \begin{bmatrix} \hat{\sigma}^{+} \exp(iL\varphi) \\ \hat{\sigma}^{-} \exp(-iL\varphi) \\ \hat{\sigma}^{-} \exp(iL\varphi) \\ \hat{\sigma}^{+} \exp(-iL\varphi) \end{bmatrix} \tag{2.27}$$

Note that we leave aside the case of $|L| = 1$, which contains TE and TM mode and has its own peculiar behavior (Ramachandran et al., 2013).

The splitting of effective index between the SOa and SOaa modes Δn_{eff} can be written as (Snyder and Love, 1983, Ramachandran et al., 2005).

$$\Delta n_{eff} = \frac{L}{k^2 a^2 n_{co}^2} \int_0^{\infty} |E(r)|^2 \frac{\partial \Delta n(r)}{\partial r} dr \qquad (2.28)$$

where r is the radial coordinate, $E(r)$ is the normalized electric field for the unperturbed mode, a is the size of the fiber core, k is the free-space wave vector defined as $k = \omega/c$, where ω is the angular frequency, $\Delta n(r)$ is the refractive index profile relative to the index of the infinite cladding, and n_{co} is the maximum refractive index.

Immediately apparent is that the Δn_{eff} increases with L. Also, the δn_{eff} is larger for higher modal intensity at the core/cladding interface and steeper index slope which can be enhanced by using step-index fiber with high Δn. As it is not clear whether the integral on the interaction of the field with fiber index gradients has an analytical solution, we numerically calculate this (using a standard scalar mode solver with details shown in the Appendix B) in various step-index fiber with Δn=0.035 and core diameter ranging from 15um to 40um.

The Δn_{eff} is plotted with respect to L^2 and L^3, and shown in Fig. 2.6a and 2.6b, respectively. We found $\Delta n_{eff} \propto L^2$ only for small-size step-index with core diameter around 15μm while it becomes $\Delta n_{eff} \propto L^3$ for core diameter $\geq 20\mu m$ and the coefficient of determination R^2 become higher for larger fibers.

Also shown in Fig. 2.6 is that the Δn_{eff} for the bound mode with highest-$|L|$ become smaller for larger fibers. This is due to lower intensity at the interface in a fiber with weaker confinement.

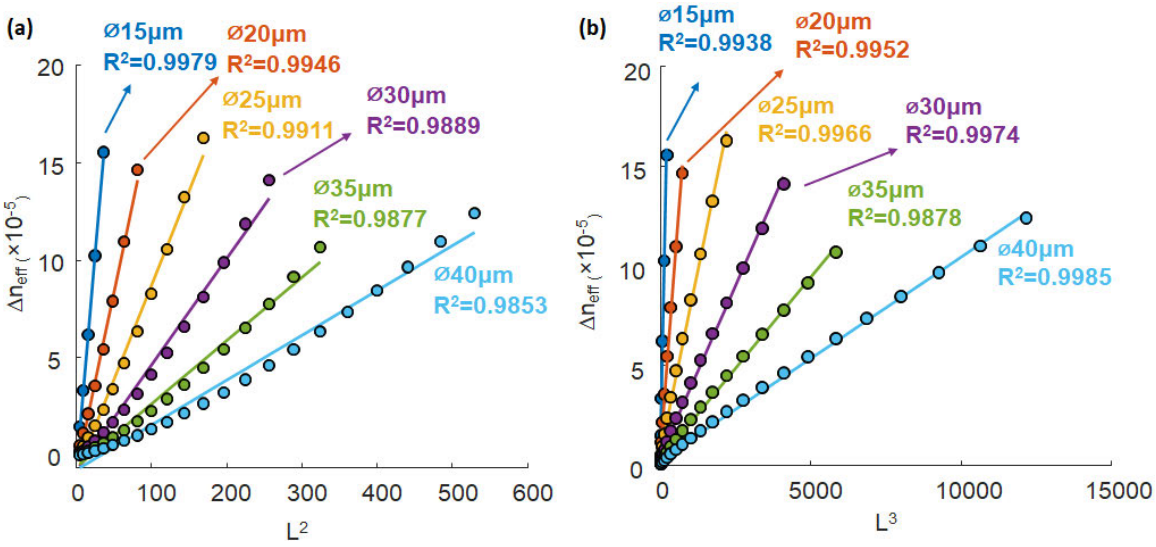

Figure 2.6: Δn_{eff} versus (a) L^2 and (b) L^3, calculated in step-index fibers with size from 15um to 40um. The R^2 is used to evaluate the fitting.

The corresponding group index difference can be derived from Δn_{eff} and also follows the similar trend of similar dependence as Δn_{eff} that the Δn_g scales as L^2 for small-size fiber (core diameter ~15μm) and scales as L^3 for fiber with core diameter $\geq 20\mu m$, as shown in Fig. 2.7.

$$\Delta n_g = c\frac{d\left(k\Delta n_{eff}\right)}{d\omega}$$

$$= -\frac{c^2 L}{\omega^2 a^2 n_{co}^2}\left(\int_0^\infty |E(r)|^2 \frac{\partial \Delta n(r)}{\partial r} dr - \omega \frac{d}{d\omega}\int_0^\infty |E(r)|^2 \frac{\partial \Delta n(r)}{\partial r} dr\right) \qquad (2.29)$$

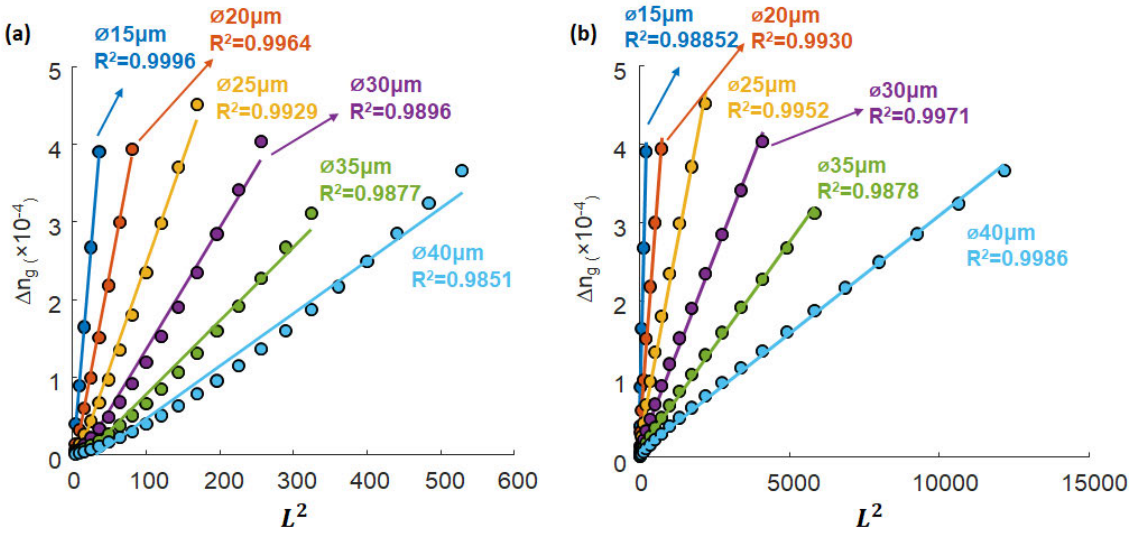

Figure 2.7: Δn_g versus (a) L^2 and (b) L^3, calculated in step-index fibers with size from 15um to 40um. The R^2 is used to evaluate the fitting.

Such dependence of the group index on the OAM order L is demonstrated by directly measuring the arrival time of different L's in a ring-core fiber with 16-μm core diameter using a single-pixel camera. Note the modal fields primarily locate at the outer core/cladding interface, especially for high-L modes with sufficiently higher Δn_{eff} (details in Chapter 4) to separate the two near-degenerate modes. Therefore, both Δn_{eff} and Δn_g of high-$|L|$ modes have the similar dependence on L in a ring-core fiber.

Figure 2.8 is a plot of the difference in arrival times over a 200-m ring-core fiber, versus square of mode order L^2, for the modes whose temporal separation was measurable in the experiment (Johnson et al., 2019). The excellent match with a straight line fit (linear regression R^2 coefficient 0.999) of the data clearly indicates that the modes in this fiber follow the splitting as dictated by the spin-orbit interaction of light and the associated polarization correction.

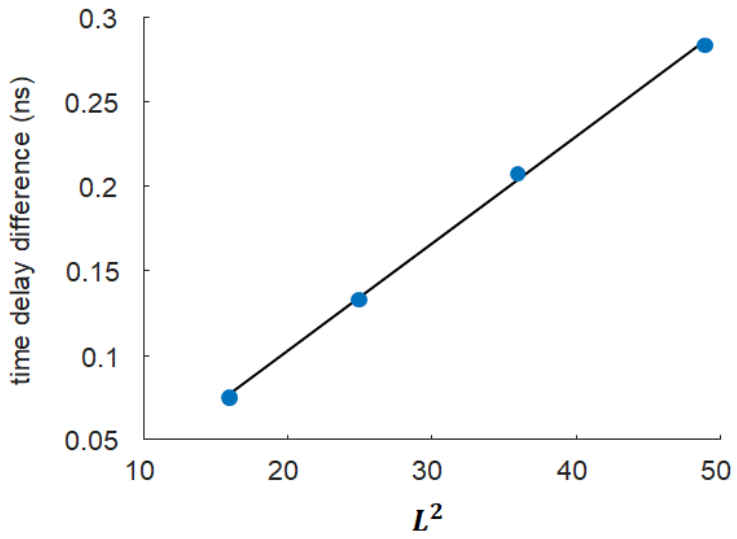

Figure 2.8: Time delay difference of OAM modes in a 200-m-long ring-core fiber with 16-um ring diameter.

2.4. Vector, OAM and Scalar Modes

Actually, a more conventional bases of representing these degeneracy-lifted (not scalar) modes are the vector modes (HE/EH modes) (Snyder and Love, 1983). Their field distribution (for $L > 1$) can be shown as follows

$$\boldsymbol{E}_{L,m} = \begin{bmatrix} \mathrm{HE}_{L+1,m}^{even} e^{i\beta'_{L,m}z} \\ \mathrm{HE}_{L+1,m}^{odd} e^{i\beta'_{L,m}z} \\ \mathrm{EH}_{L-1,m}^{even} e^{i\beta''_{L,m}z} \\ \mathrm{EH}_{L-1,1}^{odd} e^{i\beta''_{L,m}z} \end{bmatrix} \tag{2.30}$$

where

$$\begin{bmatrix} \mathrm{HE}_{L+1,m}^{even} \\ \mathrm{HE}_{L+1,m}^{odd} \\ \mathrm{EH}_{L-1,m}^{even} \\ \mathrm{EH}_{L-1,m}^{odd} \end{bmatrix} \cong F_{L,m}(r) \begin{bmatrix} \hat{x}\ \cos(L\varphi) - \hat{y}\ \sin(L\varphi) \\ \hat{x}\ \sin(L\varphi) + \hat{y}\ \cos(L\varphi) \\ \hat{x}\ \cos(L\varphi) + \hat{y}\ \sin(L\varphi) \\ \hat{x}\ \sin(L\varphi) - \hat{y}\ \cos(L\varphi) \end{bmatrix} \tag{2.31}$$

For $L = 0$ modes in most weakly guided fibers, the vector modes $\mathrm{HE}_{1,m}$ are almost identical to the scalar modes (with higher index contrast, this approximation breaks down, but, to first order, the field distributions remain the same, with only a small modification to β). In contrast, vector modes with $L > 0$ have spatially non-uniform polarization distributions, distinct from their scalar counterpart. We leave aside the case of $|L| = 1$ associated with TE and TM modes (Ramachandran et al., 2013), which have peculiar behaviors compared with HE/EH modes.

The relationship between vector and OAM modes is given by

$$\begin{bmatrix} \mathrm{OAM}_{+L}^{+} \\ \mathrm{OAM}_{-L}^{-} \\ \mathrm{OAM}_{+L}^{-} \\ \mathrm{OAM}_{-L}^{+} \end{bmatrix} = \begin{bmatrix} \mathrm{HE}_{L+1,m}^{even} + i\mathrm{HE}_{L+1,m}^{odd} \\ \mathrm{HE}_{L+1,m}^{even} - i\mathrm{HE}_{L+1,m}^{odd} \\ \mathrm{EH}_{L-1,m}^{even} - i\mathrm{EH}_{L-1,m}^{odd} \\ \mathrm{EH}_{L-1,m}^{even} + i\mathrm{EH}_{L-1,m}^{odd} \end{bmatrix} \tag{2.32}$$

These vector and OAM modes are illustrated in Fig. 2.9, where the lines along with the +*i* and -*i* signs show the linear combinations that rotate modes from one basis to another. The aforementioned SOI leads to the degeneracy lifting of the β for SOa and SOaa modes. Correspondingly, in the vector basis, the β of the HE and EH modes differ. As in the case of the $L = 0$ modes shown in Fig. 2.4, the SOa OAM modes and HE vector modes are linear combinations of one another, thus forming a pair of mutually unbiased bases (MUBs). Similarly, the SOaa OAM modes and EH vector modes form a *separate* pair of MUBs.

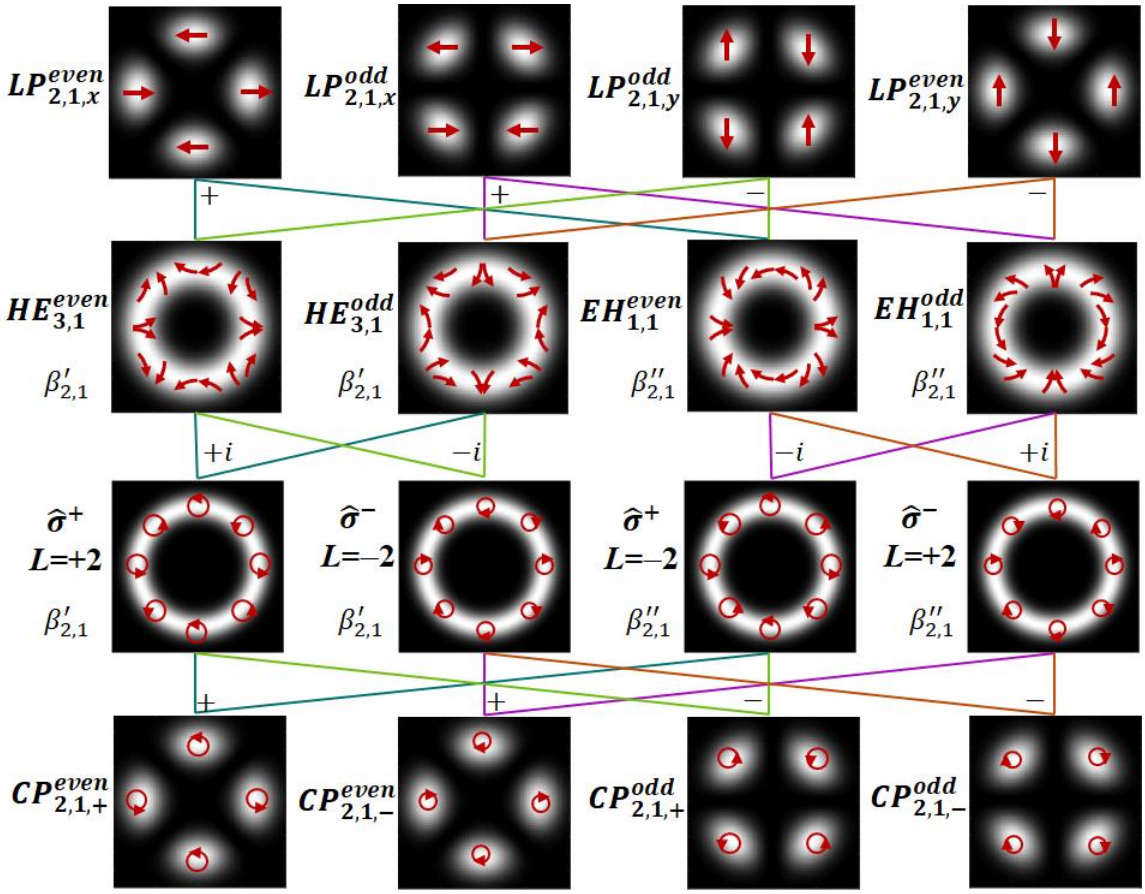

Figure 2.9: Intensity and polarization patterns of LP (first row), vector (second row), OAM modes (third row) and CP (fourth row) with azimuthal index $|L| = 2$ and radial index $m = 1$. Colored lines show linear combinations between groups. The $+i$ or $-i$ terms represent a $\pi/2$ or $-\pi/2$ phase shift in the linear combinations. Azimuthal shifts of the arrows on the OAM modes indicate an azimuthal phase shift. The propagation constant is $\beta'_{2,1}$ for SOa modes (and the corresponding HE modes), and $\beta''_{2,1}$ for SOaa modes (and the corresponding EH modes).

These intensity and polarization pattern of the scalar mode with LP and CP designations are also illustrated in the Fig. 2.9. Again, lines along with the + and - signs show how a LP or CP mode can also be represented as a linear combination of two vector or OAM modes. In terms of the transverse field distribution, the scalar modes are mathematically equivalent to vector/OAM modes. However, SOI lifts the degeneracy of the real eigenbasis – OAM/vector modes. Thus, a scalar mode for $|L| > 1$ becomes a

mixture of two OAM or vector modes of different βs, leading to the accumulation of different phases along propagation. This phase difference directly results in power oscillation between two odd and even scalar modes, suggesting that scalar modes are no longer the real eigenmodes even in a strictly straight, perturbation-free fiber. In this regard, the scalar wave approximation is only valid when SOI is weak enough that $\beta'_{2,1}$ and $\beta''_{2,1}$ become nearly identical – in a fiber with low index contrast or for modes with low $|L|$ (according to Eq. 2.28).

The SOI-induced degeneracy-lifting start to manifest in high-$|L|$ modes of fibers with relatively high index contrast. Consider the LP_{61} mode in the previously mentioned 15-um step index fiber with 0.035 index contrast. Given that the Δn_{eff} is up to 10^{-4}, the length required for the phase difference between modes with β' and β'' to accumulate π is $10^4\lambda$=7.25 mm (at 1550nm), which is the length over which the power oscillates between odd and even LP mode. It is analogous to the oscillation between two polarization modes in a polarization-maintaining fiber. In such a case, it would be highly imprecise to use scalar modes as the eigenmodes of a circularly symmetric fiber. Due to this inherent instability, their employment necessitates pre- or post-processing, optically or electronically, for information recovery.

2.5. Summary and Discussion

This chapter derives the scalar modes in a weakly guided step-index fiber and describe some critical properties, including cutoff, intensity distribution, degeneracy, dispersion, and polarization. The four-fold degeneracy is lifted due to spin-orbit interaction, which intensities for high-$|L|$ modes. As a result, the OAM and vector modes turn out to be the

true eigenmodes rather than the conventional scalar modes whose power oscillates between odd and even modes along propagation. Finding the subset of modes that propagate with high linear stability is of paramount importance. The OAM and vector modes are mathematically equivalent bases but with subtle difference which will be elucidated in the following chapter.

Chapter 3

3. Mode Excitation and Characterization

In the previous chapter, it was demonstrated that OAM and vector modes are the true eigenmodes, superseding the conventional scalar modes. Notably, these modes are mathematically equivalent, implying that any OAM mode can be decomposed into a combination of vector modes, and vice versa. In Chapter 4, we will delve into the stability of these modes; however, before that, let's focus on the mode excitation and characterization, with particular attention to OAM modes. There are two key reasons for this focus: (a) vector modes can be regarded as a linear combination of OAM modes, and (b) we will subsequently show in the next chapter that OAM modes are fundamentally more stable than vector modes.

3.1. Mode Excitation of OAM modes in fibers

To excite specific OAM modes in a fiber, we first generate the corresponding OAM mode in free space and then couple it into the fiber. The free-space OAM mode possesses the same topological charge as the desired OAM mode in the fiber. The coupling efficiency and modal purity of the excited OAM mode depend on the alignment between the free-space OAM beam and the desired OAM eigenmode of the fiber. Due to slight differences in their radial intensity distributions, there is inevitably some coupling loss during this process.

Among various methods to generate OAM modes in free space, the experiments in this thesis primarily rely on a spatial light modulator (SLM) for OAM generation, except

for specific sections (Sec. 4.2 & 4.3). SLMs offer exceptional controllability by spatially modulating a liquid crystal film, allowing near-arbitrary phase patterns to be imprinted on an incident optical field. This high level of control provides distinct advantages over other OAM generation techniques, such as q-plate or spiral phase plate. Additionally, our SLM-based OAM generation involves not only imparting the helical phase front for OAM but also introducing (a) a grating to separate the OAM beam and unconverted Gaussian beam; (b) a combination of spherical and conical phase fronts to control the size and thickness of the ring-shaped beam; (c) amplitude sculpting to regulate the ringing effect of the radial intensity profile (Gregg, 2017). The specific SLMs used in these experiments are the Hamamatsu LCOS-SLM X10468-08 and the Santec SLM-200. The Hamamatsu SLM is used for mode excitation in Gen4 and Gen5 fibers, while the Santec SLM is employed for mode excitation in all other fibers, such as Gen6 fiber, HOM3, and GenX fiber.

The experimental setup for mode excitation and characterization of OAM modes in fibers is shown in Figure 3.1. The input Gaussian beam is converted into an OAM beam using the SLM. A combination of a linear polarizer (LP) and quarter-wave plate (QWP) transforms the linear polarization into circular polarization, which is the polarization state carried by the OAM eigenmode. The circularly polarized OAM beam is then coupled into the fiber under test. The fiber end on the input side is positioned on a 6-axis stage (Thorlabs MAX601D), which not only enables us to adjust the transverse position of the fiber end but also its angle (specifically, yaw and pitch dimensions). Precise alignment is essential to effectively excite the desired fiber mode using the free-space OAM beam, necessitating adjustments in both lateral displacement and angle.

The output is characterized by the spatial interferometry (Sec. 3.2), time of flight (ToF, Sec. 3.3) and polarization binning (Sec. 3.4). The spatial interferometry utilizes a ~1550-nm CW external cavity laser (ECL, HP 8168F), an InGaAs Allied Vision Technologies "Goldeye" camera, and polarization binning. The ToF measurement utilizes a ~1550-nm, 5-ps pulse laser (PriTel FFL), a fast detector (Thorlabs 30 DET08C), and an oscilloscope (Agilent Infiniium DCA with module 86109A). The polarization binning utilizes the ps laser, the polarization displacer and the InGaAs camera using image stitching.

The power of all parasitic modes (m=1 modes with different L's, high-m modes) is minimized to <−20dB by (a) optimizing the phase pattern on the SLM; (b) walking the input beam using mirrors M1 and M2; (c) adjusting the displacement and angle of the fiber input end.

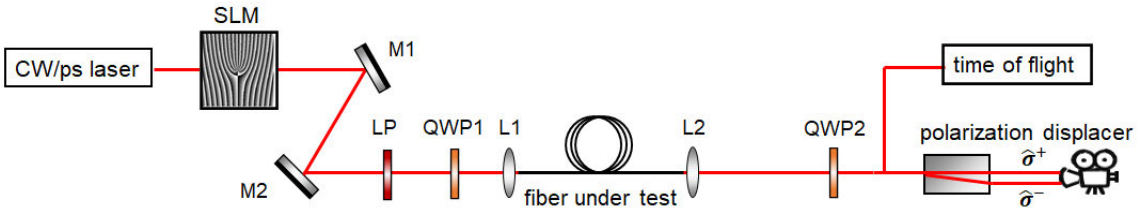

Figure 3.1: Experimental setup of mode excitation and characterization.

3.2. Spatial Interferometry

Each OAM mode has a distinct azimuthal phase distribution in the form of $e^{iL\varphi}$. For a given OAM mode, its interference with different OAM modes shows different azimuthal fringes depending on the ΔL between the two interfering modes. Therefore, the power ratio of each parasitic mode can be obtained by analyzing the spatial frequency of the

interference pattern in the azimuthal dimension on the ring. This method, referred to as the "Ring Method", relies on spatial interferometry and requires a coherent source as well as the assumption of a dominant mode. It is the primary means of measuring modal purity throughout the thesis.

3.2.1 Principle of Ring Method

Assuming interference between two OAM modes with $L = L_0$ and $L = L_i$, we may write the total field as

$$E(r,\varphi) = \gamma_0 F_0(r) e^{iL_0\varphi} + \gamma_i F_i(r) e^{iL_i\varphi} = F_0(r) e^{iL_0\varphi}\left(|\gamma_0| e^{i\varphi_0} + |\gamma_i| e^{i\varphi_i} e^{i\Delta L\varphi}\right) \quad (3.1)$$

Where γ_0 and γ_i are the complex weights the modes, $F_0(r)$ and $F_0(r)$ are the radial distribution of the modal amplitudes, $\Delta L = L_i - L_0$, and we assume $F_i \approx F_0$.

The azimuthal intensity distribution can be obtained by taking the complex square as

$$|E|^2/|F_0|^2 = |\gamma_0|^2 + |\gamma_i|^2 + |\gamma_0||\gamma_i|\left(e^{i\varphi_0} e^{-i\varphi_i} e^{-i\Delta L\varphi} + e^{-i\varphi_0} e^{i\varphi_i} e^{i\Delta L\varphi}\right)$$

$$= |\gamma_0|^2 + |\gamma_i|^2 + 2|\gamma_0||\gamma_i| \cos\left(\Delta L\varphi - \Delta\varphi_{i,0}\right) \quad (3.2)$$

where $\Delta\varphi_{i,0} = \varphi_i - \varphi_0$. We can expand the cosine term as

$$|E\,|^2/|F_0|^2 = |\gamma_0|^2 + |\gamma_i|^2 + 2|\gamma_0||\gamma_i|\left(\cos\Delta L\varphi \cos\Delta\varphi_{i,0} + \sin\Delta L\varphi \sin\Delta\varphi_{i,0}\right) \quad (3.3)$$

such that it is in the form of the Fourier series

$$|E\,|^2/F_0^2 = \frac{1}{2}a_0 + \sum_{j=1}^{n}\left[a_j \cos(j\varphi) + b_j \sin(j\varphi)\right] \quad (3.4)$$

The Fourier coefficients are depended on the phase difference $\Delta\varphi_{i,0}$, which can be eliminated by defining a new coefficient

$$g_j^2 = a_j^2 + b_j^2 \tag{3.5}$$

So, we have

$$g_{\Delta L}^2 = a_{\Delta L}^2 + b_{\Delta L}^2 = 4|\gamma_0|^2|\gamma_i|^2\left(\cos\Delta\varphi_{i,0}{}^2 + \sin\Delta\varphi_{i,0}{}^2\right) = 4|\gamma_0|^2|\gamma_i|^2 \tag{3.6}$$

We assume $E_0 = \gamma_0 F_0(r)e^{iL_0\varphi}$ is the dominant mode, therefore

$$g_0 = \frac{1}{2}a_0 = |\gamma_0|^2 + |\gamma_i|^2 \approx |\gamma_0|^2 \tag{3.7}$$

So, the power ratio

$$\eta_{\Delta L} = \frac{|\gamma_i|^2}{|\gamma_0|^2} = \frac{g_{\Delta L}^2}{4{g_0}^2} \tag{3.8}$$

We have only examined a parasitic mode so far. In the following, we will take account all the parasitic modes with ΔL spanning from $-i$ to $+i$. Then Eq. 3.2 becomes

$$|E\,|^2/F_0^2 = |\gamma_0|^2 +$$

$$\sum_{i=1}^{n}\left[|\gamma_{-i}|^2 + |\gamma_{+i}|^2 + 2|\gamma_0||\gamma_{+i}|\cos\left(i\varphi - \Delta\varphi_{i,0}\right) + 2|\gamma_0||\gamma_{-i}|\cos\left(i\varphi + \Delta\varphi_{-i,0}\right)\right] \tag{3.9}$$

As most of the power is in the dominant mode E_0, the coupling terms between parasitic modes have been neglected. Similarly, we have

$$g_0 \approx |\gamma_0|^2 \tag{3.10}$$

$$|g_i|^2 = a_i^2 + b_i^2 = 4|\gamma_0|^2\left[|\gamma_{+i}|^2 + |\gamma_{-i}|^2 + 2|\gamma_{+i}^{+}||\gamma_{-i}^{+}|\cos\left(\Delta\varphi_{0,i} + \Delta\varphi_{0,-i}\right)\right] \tag{3.11}$$

Therefore, the two parasitic modes with $\Delta L = \pm i$ need to be considered together. Suppose the phase term can neglected, we have power ratio of the two as

$$\eta_{-i,+i} = \frac{|\gamma_{-i}|^2 + |\gamma_{+i}|^2}{|\gamma_0|^2} = \frac{g_i^2}{4{g_0}^2} \tag{3.12}$$

The above spatial interferometry analysis is applicable only for scalar fields. Assuming that power exists in both orthogonal polarizations, the power ratio of parasitic modes with $\Delta L = \pm i$ in both polarizations is

$$\eta_{-i,+i}^{\pm} = \left(\frac{{g_{+i}^{+}}^2}{4{g_0^{+}}^2} + \frac{{g_{+i}^{-}}^2}{4{g_0^{-}}^2} \right) \Big/ (g_0^{+} + g_0^{-}) \tag{3.13}$$

where the superscript $+$ and $-$ represent two orthogonal polarizations (e.g., left/right-handed circular polarization). However, the phase difference in Eq. 3.11 can make a big difference to the calculated parasitic power. It can be averaged out by sweeping the wavelength to cover the whole 2π phase wrap. The phase term can be rewritten as

$$\Delta\varphi_{0,i} + \Delta\varphi_{0,-i} = \left[\Delta\beta_{i,0}(\lambda) + \Delta\beta_{-i,0}(\lambda)\right] z \tag{3.14}$$

We may define a beating wavelength $\Delta\lambda$ after which the phase term passes for 2π. Thus, we have

$$\left[\Delta\beta_{i,0}(\lambda + \Delta\lambda) + \Delta\beta_{-i,0}(\lambda + \Delta\lambda)\right] z - \left[\Delta\beta_{i,0}(\lambda) + \Delta\beta_{-i,0}(\lambda)\right] z = 2\pi \tag{3.14}$$

It can be calculated as

$$\Delta\lambda = \frac{\lambda^2}{z(\Delta n_{g,i,0} + \Delta n_{g,-i,0})} \tag{3.15}$$

Figure 3.2 is an exemplary Ring Method analysis for an *L*=37 SOa mode out of a 25-m Gen6A3 ring-core fiber. A ~1550-nm CW external cavity laser (ECL, HP 8168F) is used to obtain mode images within a 3-nm range, recorded with an InGaAs Allied Vision Technologies "Goldeye" camera. The azimuthal intensity on the ring is taken for Ring Method analysis. The $\Delta L = 1\ \&2$ contents exhibit periodic dependence on the wavelength, and their beating wavelengths correspond to their group indices. According to Eq. 3.15,

longer fiber results in more frequent beating, necessitating a smaller wavelength range for sweeping.

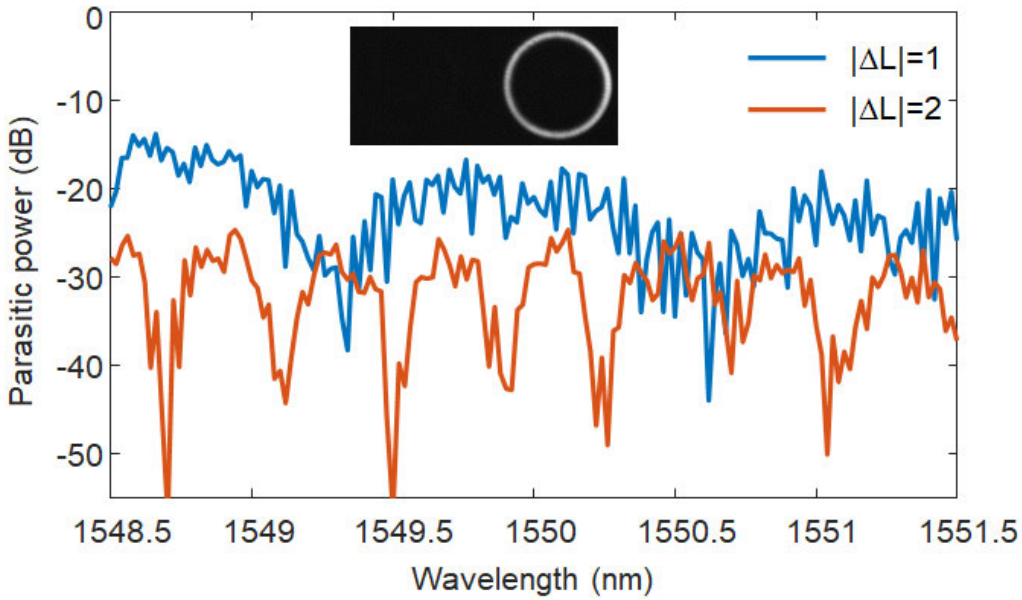

Figure 3.2: Δ*L*=1 and Δ*L*=2 content within 3-nm range at 1550 nm for *L*=37 SOa in 25-m Gen6A3 fiber. The inset is the output image of the mode at 1550 nm using a CW laser.

After averaging the power of the parasitic modes in the 3-nm wavelength range, we obtain the overall parasitic power for *L*=37 SOa mode as shown in Fig. 3.3. The dominant Δ*L*=1 content (resulted from *L*=36 or 38) is <−20dB, indicating the mode purity of *L*=37 SOa mode is >20dB. The ~−55dB noise floor is due to numerical artifact of the Ring Method, which is detailed below.

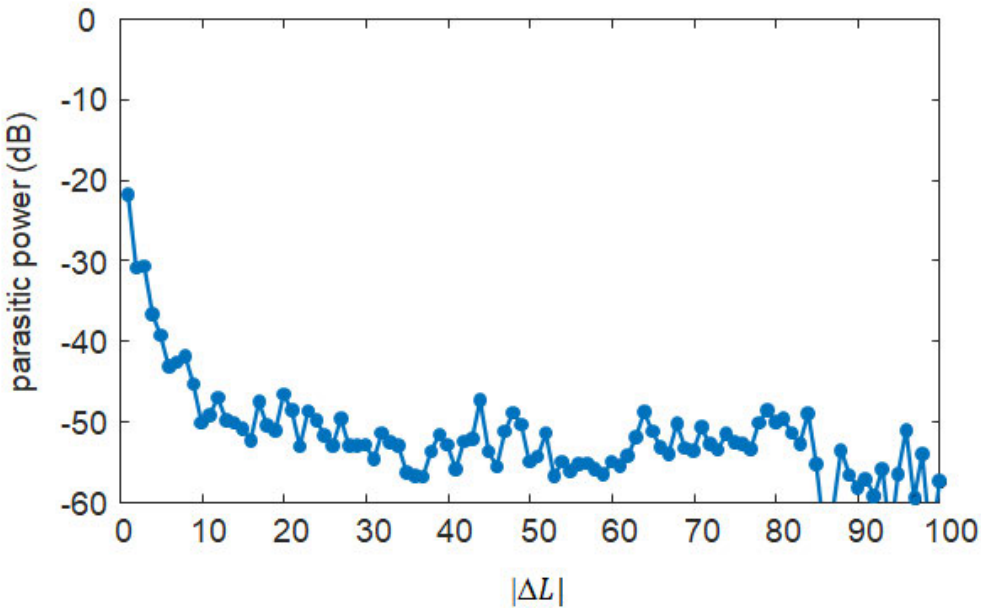

Figure 3.3: Wavelength-averaged power of parasitic modes for L=37 SOa input in 25-m Gen6A3 fiber.

3.1.2 Numerical Artifact

The dynamic range of the camera may limit the minimum paratactic power that may be measured using the Ring Method. Given that the parasitic modal power may drop below −40 dB/km (Chapter 8), it is essential to determine the measuring range of the Ring Method within the dynamic range of the camera.

Specifically, the intra-$|L|$ mode coupling occurs between near-degenerate modes with the same $|L|$ but opposite signs ($L_i = -L_0$), or $\Delta L = 2L_0$. As each pixel value is an integer and the cosine term ranges from −1 to 1, there is azimuthal variation in Eq. 3.2 only if

$$2|\gamma_0||\gamma_i| \geq 0.5 \tag{3.16}$$

Therefore, the lowest parasitic power that can be detected theoretically is

$$\eta_i = \frac{|\gamma_i|^2}{|\gamma_0|^2} = \frac{1}{16|\gamma_0|^4} \tag{3.17}$$

The InGaAs camera has 12-bit dynamic range, indicating the max of pixel value can go up 4095, so we can just assume $|\gamma_0|^2 = 4000$. Therefore, the lowest parasitic power that can be detected theoretically is

$$10\log_{10}\left(\frac{1}{16|\gamma_0|^4}\right) = -84dB \tag{3.18}$$

In other words, the lowest power the parasitic can go down is in the order of the square of the dynamic range of the camera.

Using L=40 as the dominant mode ($L_0 = 40$)) whose intensity ($|\gamma_0|^2$) is supposed to be 4000, we numerically confirm this noise floor limitation. If we take the unit pixel value (i.e., 1) as a reference, the pixel value 4000 corresponds to 36dB. The intensity of the parasitic mode L=−40 ($|\gamma_i|^2$) varies from 26dB to 136dB lower than the dominant mode (equivalently 10dB to −100dB higher the unit pixel value). Before calculating the power weight using the Fourier coefficient, the intensity is rounded to an integer. Figure 3.4 shows the comparison between the actual ΔL=2L (L=−40) content and the one calculated from the Ring Method. As shown in Fig. 3.4, the $\Delta L = 2L$ content matches well with the actual one down to −82.6dB, close to the theoretical value −84dB. Note that the numerical parasitic power becomes infinitely small below this limit, therefore it not the cause of noise floor in Fig. 3.3. In any case, it is much lower than the noise floor of Ring Method using experimental images, which is ∼−55dB (Fig. 3.3).

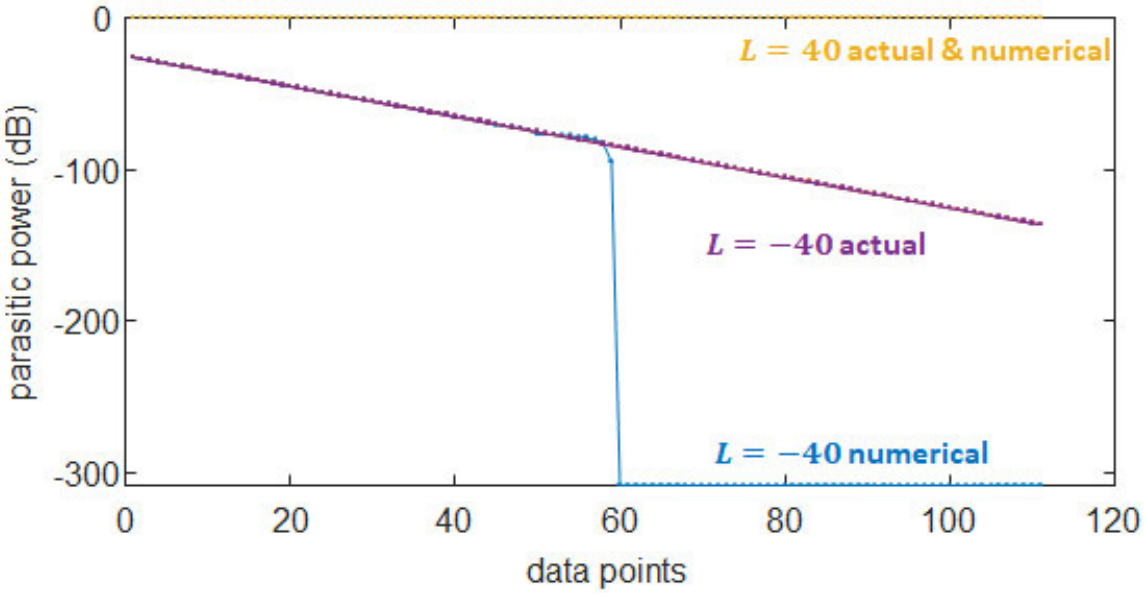

Figure 3.4: Comparison between the actual L=–40 (ΔL=2L) content and the one calculated from the Ring Method.

To fully replicate the Ring Method process and investigate the noise floor, it is necessary to begin with a 2-D mode image. The radial distribution of the intensity can be constructed using

$$F_0(r) = e^{-(r-r_0)^2/\omega_0^2} \tag{3.19}$$

where r_0 and ω_0 determine the radius and thickness of the ring, respectively. Again, the dominant mode is $L_0 = 40$ with intensity $|\gamma_0|^2 = 4000$. The parasitic mode $-L_0$ has intensity $|\gamma_i|^2$ varying from 26dB (Fig. 3.5a) to 136dB (Fig. 3.5b) lower than the dominant mode. The ring diameter $(2r_0)$ is fixed at 114 (pixels), which is also the size of the experimental images, constrained by the camera window.

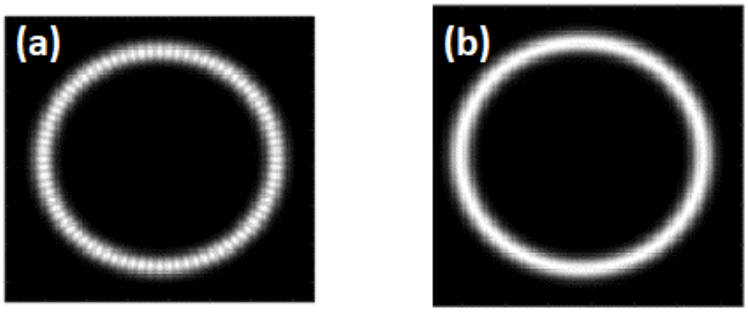

Figure 3.5: The overall intensity pattern as a combination of a dominant L=40 and a parasitic L=−40 with power ratio (a) 26dB and (b) 136dB lower than the dominant.

As shown in Fig. 3.6, the numerical L=−40 content of the 114-pixel-diameter ring remains at ~−60 dB regardless the actual L=−40 content. In addition, such noise floor is higher for smaller ring diameters (~−53dB for 56-pixel-diameter ring) and lower for larger ring diameters (~−73dB for 228-pixel-diameter ring). Prior to hitting the noise floor, each of the three numerical parasitic powers closely matches the real one.

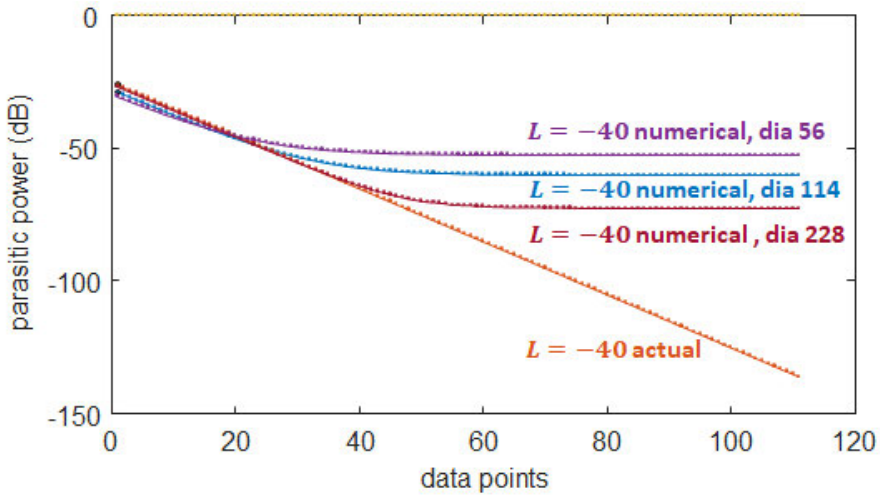

Figure 3.6: The numerical L=−40 content calculated from Ring Method in an aggregate ring pattern with various actual −40 content. The variation of the ring diameter leads to the variation of the noise floor.

The variation in noise floor with ring diameter arises from imperfect azimuthal sampling during the transition from Cartesian to polar coordinates. As shown in Fig. 3.7a,

the azimuthal sampling exhibits a smoother pattern for larger ring diameters. This results in a decrease in the noise floor from ~−60dB to ~−75dB, as depicted in Fig. 3.7b.

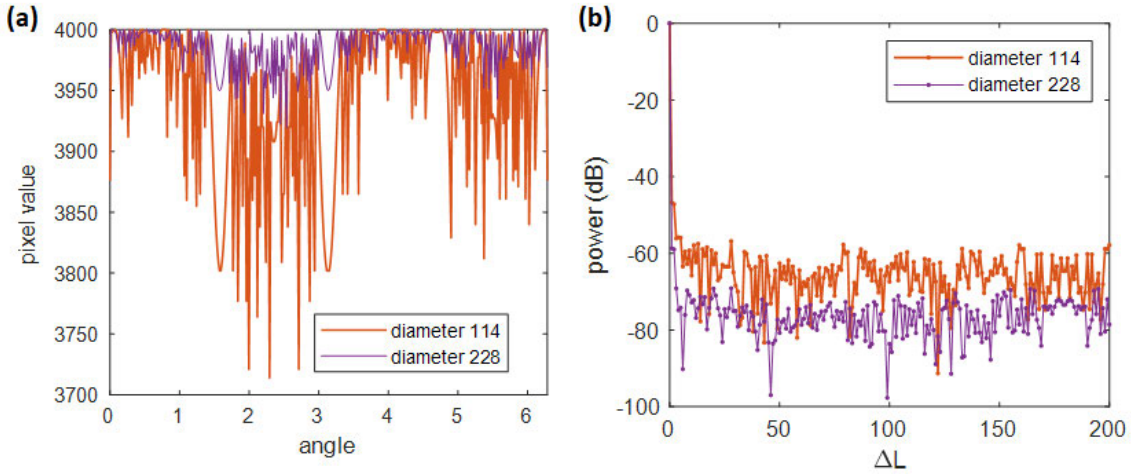

Figure 3.7: (a) pixel value versus azimuthal angle on the ring with two different diameters; (b) parasitic power versus ΔL for two rings with different diameters

The imperfect azimuthal sampling from Cartesian to polar coordinate also results in a broadening of the $\Delta L=2L$ content, in contrast to a single peak calculated from the ideal 1-D case (Fig. 3.8).

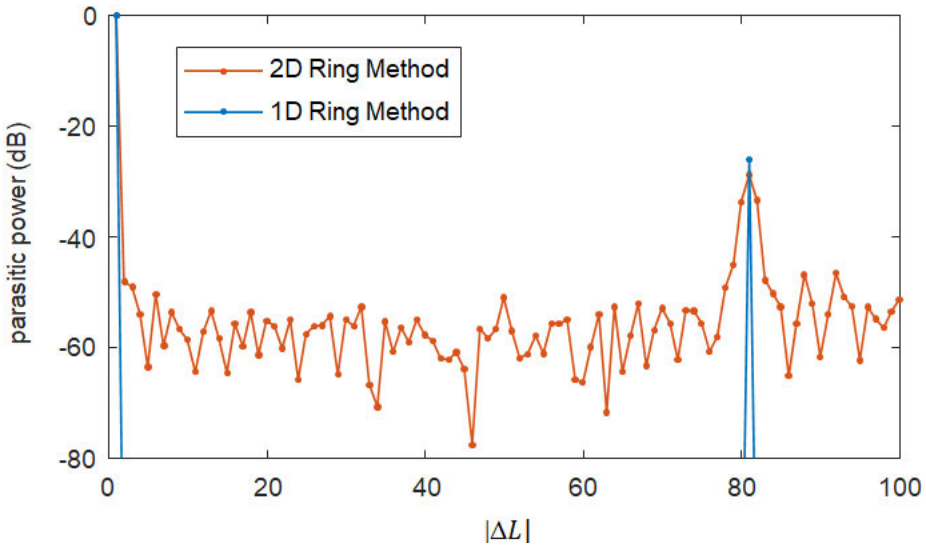

Figure 3.8: Parasitic power versus ΔL with different parasitic power calculated from 1D and 2D Ring Method.

3.1.3 Identification of high-*m* modes

The Ring Method described above is only applicable for m=1 modes with similar radial intensity profile. As demonstrated in Fig. 3.9, the interference between modes with L and m differences causes intensity variations in both the azimuthal and radial directions.

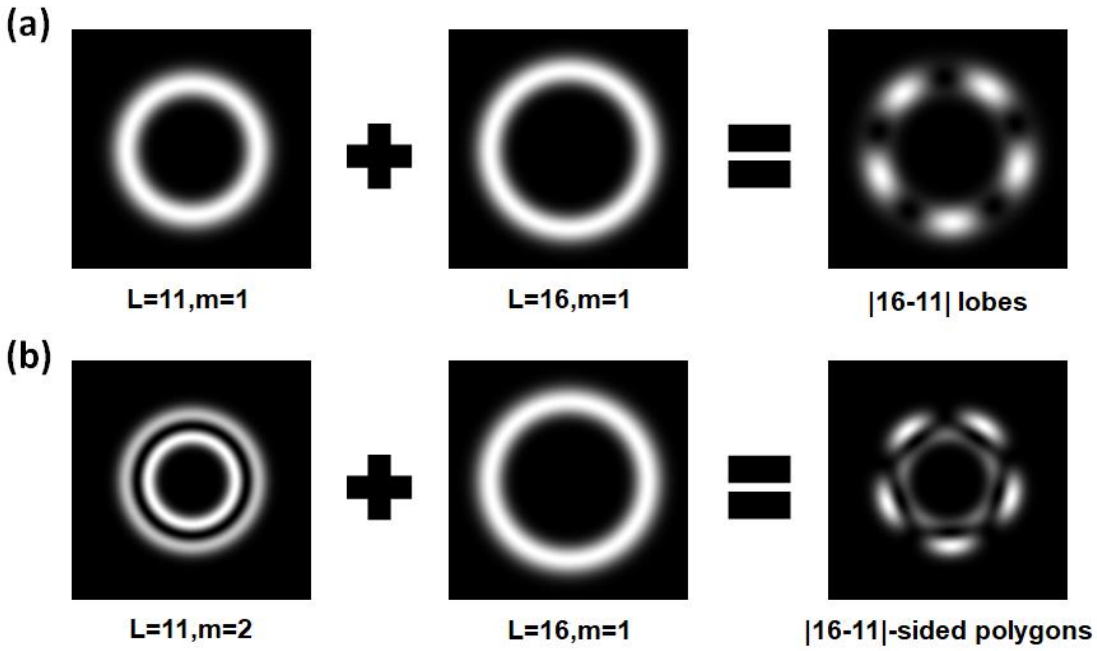

Figure 3.9: Schematic of different interference patterns with m=1 and m=2 modes using simulated modal fields. (a) interference between L=11, m=1 and L=16, m=1 modes result in |16-11| lobes; (b) interference between L=11, m=2 and L=16, m=1 modes result in |16-11|-sided polygons. The double rings in the interference pattern indicates inference with an m=2 mode.

Even though the Ring Method is inapplicable to calculate the parasitic power in this scenario, it is very beneficial to identify the parasitic high-m modes based on the azimuthal symmetry and the number of rings in the radial direction, as illustrated in Fig. 3.10.

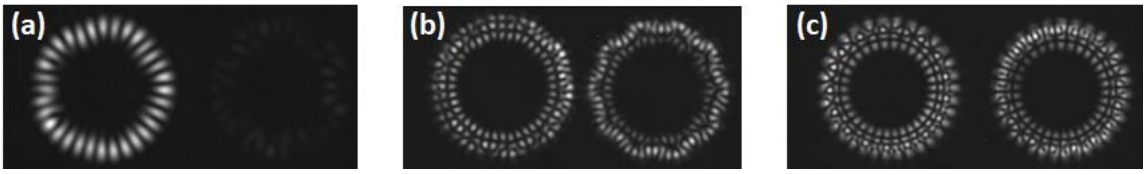

Figure 3.10: Exemplary inference patterns with high-*m* modes. (a) *L*=16, *m*=1 × *L*=10, *m*=2 in 1.1km Gen5A3 fiber; (b) *L*=30, *m*=1 × *L*=20, *m*=3 in 500-m Gen6A3 fiber; (c) *L*=33, *m*=1 × *L*=16, *m*=4 in 500-m Gen6A3 fiber.

3.3. Time Domain Analysis

In a fiber, the pulse of each mode travels at a different group velocity and arrives at different times after propagating through a sufficient length of fiber. Given their time separation, their power ratio can be directly measured. This time-of-flight (ToF) measurement can be achieved by converting the optical pulse to an electrical signal to be measured on an oscilloscope.

Figure 3.11 shows an exemplary ToF measurement for an *L*=32 SOa mode transmitted through a ~500m Gen6A3 ring-core fiber. We use a ~1550-nm, 5-ps pulse laser (PriTel FFL), a fast detector (Thorlabs 30 DET08C), and an oscilloscope (Agilent Infiniium DCA with module 86109A). The setup is detailed in Fig. 3.1. The pulse width of the ToF signal is determined by the detector's bandwidth, and the ringing observed after each peak is due to the detector's limited bandwidth (5 GHz). The ToF trace is an average of 256 signals to lower the noise floor, which can be further lowered by increasing the average time (Chapter 8). As shown in Fig. 3.9, most of the power is coupled to *L*=32 SOa, while the parasitic modes accidentally excited at the input are separated in time. Their delay difference corresponds to their group index difference. In this case, the parasitic powers are all below −20dB, indicating >20dB purity for *L*=32 SOa mode. ToF measurement is

especially valuable when dealing with the unintentional excitation of high-*m* modes featuring multiple rings. The Ring Method mentioned earlier, which assumes an identical radial distribution for all modes, cannot effectively measure the content of these high-*m* mode. Therefore, ToF measurements is a useful tool for real-time alignment during mode excitation processes.

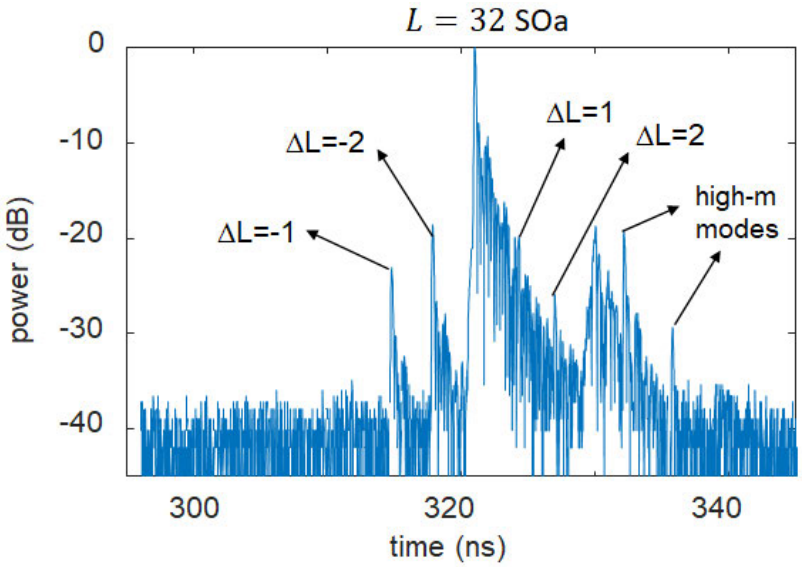

Figure 3.11: TOF signal for an *L*=32 SOa mode transmitting through a ~500m Gen6A3 ring-core fiber at 1550nm.

This undesirable excitation of parasitic modes is practically inevitable. When coupling a free-space OAM beam to an μm-scale ring-core, a slight transverse misalignment or angle offset might result in the excitation of neighboring-|*L*| modes (Δ*L*=1). However, this issue is technical and has nothing to do with the fiber's inherent qualities. Free-space mode coupling necessitates precise control, which may be enhanced using an integration strategy in which the OAM generator is attached to the ring-core fiber.

The aforementioned discrete peaks in ToF are caused by mode excitation rather than in-fiber mode coupling. If there is mode coupling between two modes within the fiber,

parasitic modes can be continuously generated, starting from the input side of the fiber. As a result, power is distributed in time between the two coupled modes, leading to a shoulder of the launched mode in the ToF measurement. The range of distributed coupling is again determined by the group difference between the two modes. The power coupled to the parasitic mode is calculated as the ratio of the integration of the shoulder (on a linear scale) to the integration of the peak. Figure 3.12 is the ToF measurement for an L=30 SOa, m=1 mode transmitted through a ~500m Gen6A3 ring-core fiber at 1550nm. The L=30, m=1 mode has accidental degeneracy with L=20, m=3 at 1550nm. Thus, the mode coupling between them is manifested as distributed coupling in ToF. In this case, the mode coupling is ~−20 dB. For the output image using ECL, this mode coupling is evident as as interference pattern between the two modes.

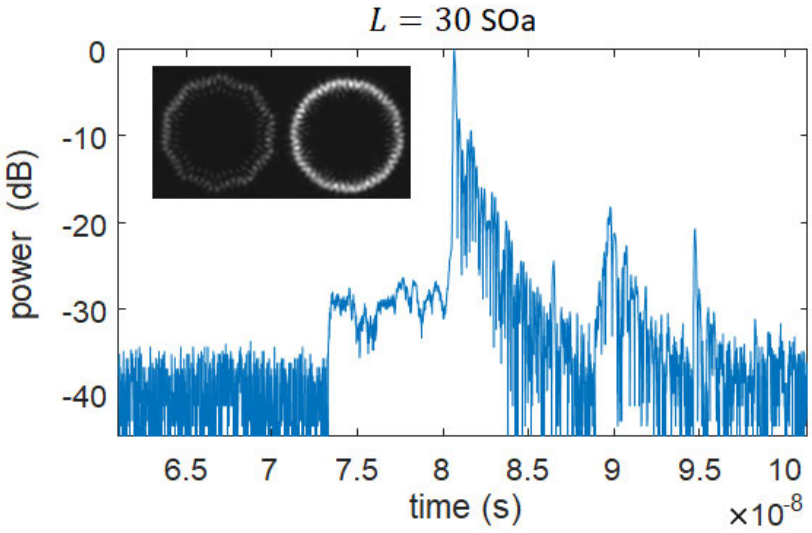

Figure 3.12: TOF signal for an L=30 SOa mode transmitting through a ~500m Gen6A3 ring-core fiber at 1550nm. Inset: output image using a 1550-nm ECL.

3.4. Polarization Binning

The aforementioned spatial interferometry method is valid only for scalar field. However, OAM modes in fibers can have either left and right circular polarization (LCP/RCP). One must thus separate sperate the two circular polarizations prior to using the Ring Method analysis. Using a combination of a quarter-wave plate (QWP) and polarization beam displacer (PBD), which separates the horizontal and vertical polarizations, such separation between LCP and RCP can be equivalently achieved. The QWP is rotated at a 45-degree angle with regard to the PBD. On the input side, the QWP and linear polarizer (LP) are likewise calibrated with the PBD.

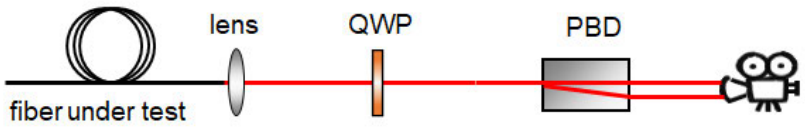

Figure 3.13: Experimental setup for polarization binning.

Due to the principle of OAM conservation, however, the two degenerate SOa or SOaa modes with opposing circular polarizations do not couple for high-$|L|$ modes (Gregg et al., 2015). Given the maturity of the 2×2 MIMO technology, the separation of these two degenerate modes with orthogonal polarizations may not be crucial in telecommunication, but it may allow additional degrees of freedom for nonlinear intermodal interaction (Liu et al., 2021). It's important to note that this PER is determined by comparing the power ratio of two circular polarization bases, which are derived from two orthogonal linear polarizations in two specific directions (horizontal and vertical). This definition slightly

differs from the conventional PER calculation, which typically involves comparing two orthogonal linear polarizations with maximum and minimum power.

The PER measurement of the fiber modes is limited by the PER of the PBD. It is can be directly measured using the laser beam and a power meter (Fig. 3.14). After passing through the PBD, the PER of the laser Gaussian beam reduces from 50dB to 35dB, indicating that the PER of the PBD is 35dB.

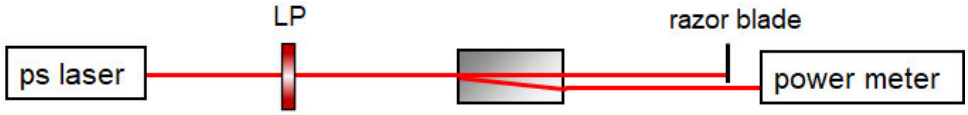

Figure 3.14: Experimental setup for measuring the PER using power meter.

While it is possible to calculate the PER by measuring the power of the two bins using a power meter, it is considerably more convenient and practical to directly measure it using the camera. This approach helps avoid any unnecessary system disruption and minimizes external perturbations, which is particularly crucial when characterizing a large number of modes. It is sufficient to just integrate the pixel values within the region containing the mode image for each bin and use this information to represent the power in each polarization. These mode images can be easily obtained during the Ring Method measurement.

However, the maximum PER that can be determined using the picture is restricted by the dynamic range (12 bits) and camera noise Using the camera, the PER of the aforementioned Gaussian beam is reduced to 23dB, while the power meter measures 35dB. The dynamic range of the camera can be equivalently increased by imaging stitching. Intensity profiles at the output of the fiber are recorded as images with different exposure

times of the camera. As shown in the Fig. 3.15, the parasitic bin is buried under the noise floor for low exposure times as short as 100 μs. By increasing the exposure time up to 95559 μs, the power of the parasitic bin finally surpasses the noise floor. After removing the saturated and near-saturated pixels, these two images (normalized for exposure time) are stitched together to obtain a final image with effectively much higher dynamic range. Consequently, the PER is enhanced to 35dB, which is close to the actual PER measured by the power meter. This approach is slightly different from the conventional image stitching technique (Demas et al., 2015), in which the final image is created by stitching together a sequence of images with continuous exposure times.

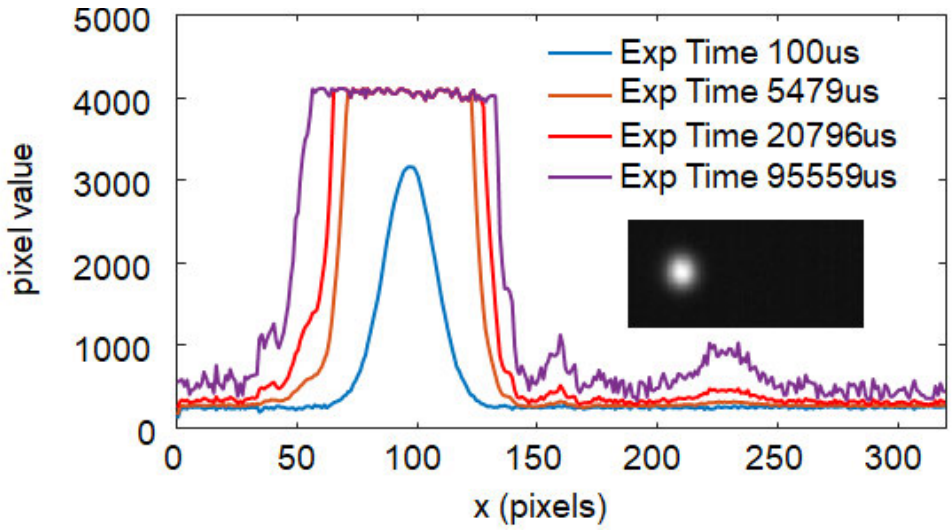

Figure 3.15: Transverse distribution of the pixel value for Gaussian beams under different exposure time.

Rotating a QWP placed between the LP and PBD alters the measured PER in order to compare the PER measured by image stitching and directly by the power meter (Fig. 3.16). It turns out that the difference between the two is only 1dB, validating the accuracy of this approach for measuring the PER.

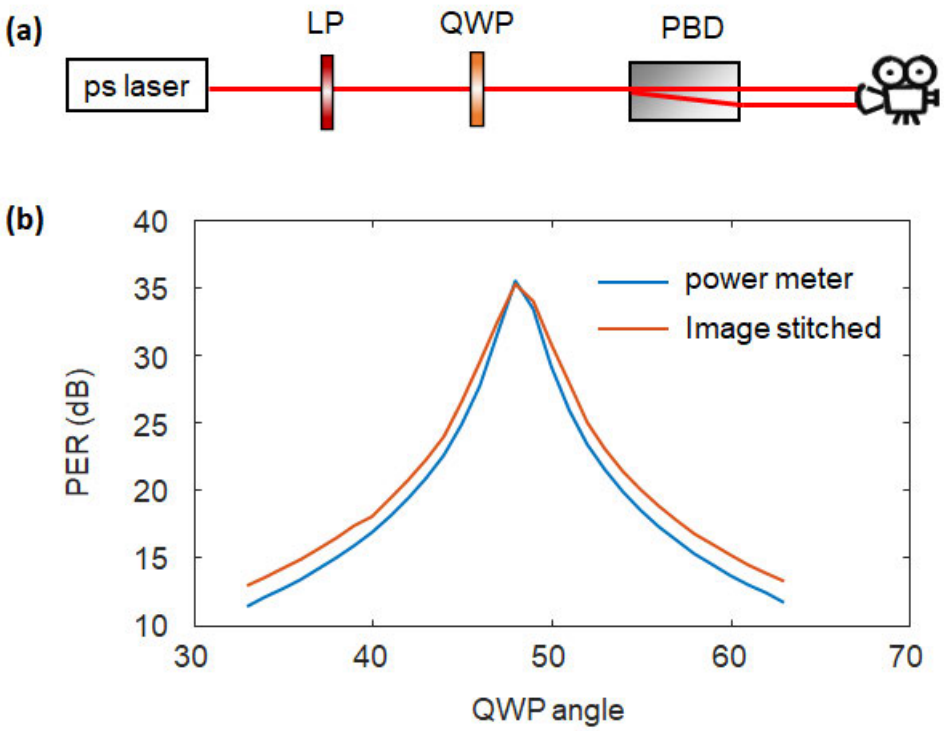

Figure 3.16: (a) Experimental setup for measuring the PER of the beam out of the ps laser; (b) PER versus QWP angle using power meter and imaging stitching

3.5. Backward Mode Excitation

By directing the output beam of each mode back into the same fiber, it is possible to excite the same mode in the reverse direction. This effectively extends the travel distance of the mode within the fiber. This technique is particularly beneficial when doubling the length of a 0.5-km fiber to 1 km, as demonstrated in Chapter 9.

A straightforward approach to direct the output light back to the fiber is by adding a mirror at the output end. However, the sign of both L and $\hat{\sigma}$ flip after mirror reflections. Although it still remains as SOa or SOaa mode, the two degenerate modes are supposed to be independent channels. The utilization of all four modes of a certain $|L|$ is critical for reaching high mode counts. No matter how many mirrors are added, there are always an

odd number of reflections which inevitably flip the sign of both L and $\hat{\sigma}$. Note that the sign of $\hat{\sigma}$ can be corrected by adding a QWP at the output but the mode is converted between SOa and SOaa as the sign of L also flips.

The solution to achieve an even number of reflections is by using a Sagnac reflector, as shown in the grey box of Fig. 3.17. A beam splitter (BS2) splits the output light into two paths, each of which travels in a clockwise or counterclockwise direction, before merging them back into a single route that returns to the fiber. Both the clockwise and counter-clockwise path undergo four reflections, and thus the sign of L remains unchanged. We note that this is identical, in nature, to the interferometers used in Gyroscopes (Post, 1967), and hence ignoring effects due to earth's rotation, the clockwise and counter-clockwise paths are equivalent. Note that, in such a situation, the idle port of the BS2 experiences destructive interference while the returning port (back to the fiber) experiences constructive interference. Hence, the Sagnac reflector is theoretically lossless (similar to a mirror in this regard). A half wave plate (HWP) is used to correct the polarization rotation inside the Sagnac reflector. This polarization is due to the inevitable non-planar light path along which the Pancharatnam-Berry geometric phase accumulated (Ma et al., 2020). The QWP2 ensures linear polarization when light is reflected on the mirrors or BS in the Sagnac reflector to avoid polarization scrambling due to a phase shift between horizontal and vertical polarizations that is known to occur on mirrors.

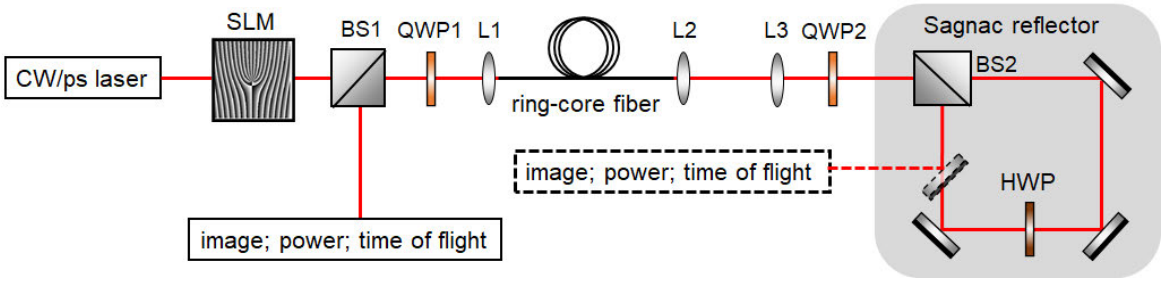

Figure 3.17: Experimental setup with Sagnac reflector. The transparent mirror with dashed border inside the Sagnac reflector represents a flip mirror, used for diagnosis and alignment. CW laser is a 1550-nm external cavity laser with continuous wave output and ps laser is a 1550-nm picosecond pulse laser. SLM: spatial light modulator; BS: beam splitter; QWP: quarter wave plate; HWP: half wave plate; L1, L2, L3 are lenses with focal lengths of 8 mm, 8 mm and 40 mm, respectively.

An additional lens, L3 (f=400mm), is added to construct an equivalent 8-f imaging system together with L2 (f=8 mm). The incorporation of this system is crucial in preserving the size of each modal beam as it exits the fiber facet and re-enters, effectively preventing the excitation of the m=2 mode during backward propagation. Subsequently, after travelling through the ~0.5-km fiber once more (resulting in a total fiber length of ~1 km equivalently), the light within each mode is detected on the opposite side following routing by the beam splitter, BS1. Note that other reflections in the system can inevitably mix with the desired light reflected by Sagnac reflector. The primary source of this undesired reflection is the Fresnel reflection at the fiber facet. To mitigate this issue, endcaps, commonly employed in fiber lasers (Limpert et al., 2006), are spliced to each end of the ~0.5km fiber (Appendix B). This prevents the reflection from the fiber facet from interfering with the backward-excited modes, ensuring clean modal detection.

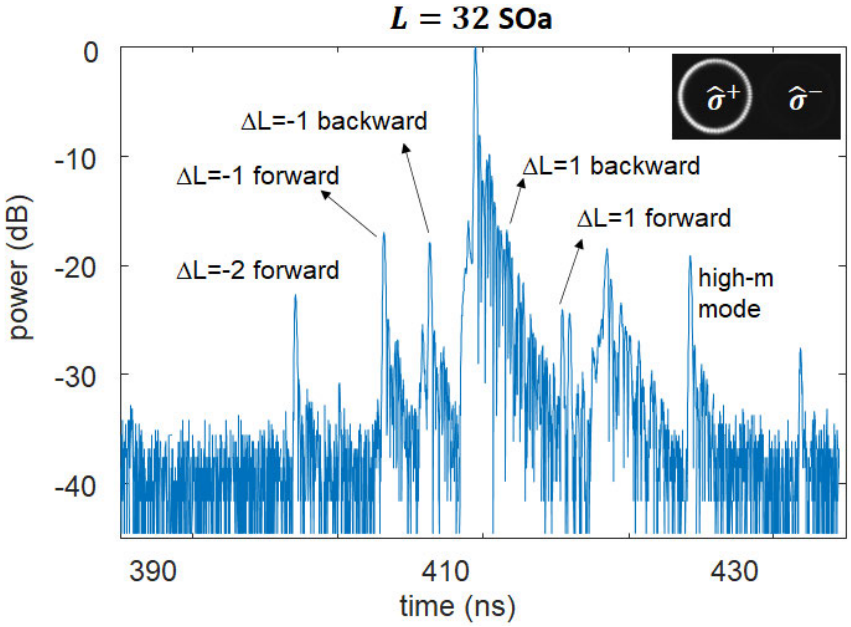

Figure 3.18: Exemplary ToF of *L*=32 SOa mode after transmitting through an equivalent 1-km Gen6A3 fiber. The inset image is the corresponding output image using a ECL source.

Figure 3.18 is an exemplary backward ToF signal for an *L*=32 SOa input, and the inset is the corresponding backward modal image obtained using an ECL. It clearly distinguishes between parasitic modes resulting from forward and backward excitation. For example, due to the doubled travel distance, the delay of parasitic Δ*L*=-1 mode generated at the forward input is double that of the mode generated at the backward input. The forward and backward mode excitations are sequentially optimized until all parasitic power are below -20dB (with a few outliers up to -15dB). It suggests that the mode excitation is the same for both sides. The spatial interferometry reveals purity >20dB for the modal image from both the forward and backward side. Even though the spatial interferometry accounts for all the sources of impurity (e.g. mode excitation from both sides, in-fiber mode coupling), we know that this 20-dB purity is determined by mode excitation based on the ToF measurement.

Chapter 4

4. Propagation Stability of Fiber Modes

The propagation stability of fiber modes is crucial regardless of whether they function as independent spatial channels or are involved in inter-modal interactions. By definition, the transverse electric field of an eigenmode should remain unchanged along a cylindrically symmetric fiber. However, such an ideal fiber does not exist in the real world. A slight modification to the fiber structure changes the eigenmodes such that the original modes are no longer true eigenmodes and their power is decomposed into these new eigenmodes along propagation. Equivalently, these pseudo-modes mix with each other throughout propagation. An immediate example is the scaler modes discussed in the previous chapter. Due to strong SOI, the weakly guidance approximation is no longer valid for high-$|L|$ modes in a high-index-contrast fiber. The phase difference between two near-degenerate OAM/vector modes manifests as oscillating power between odd and even scalar modes.

Strictly speaking, one must re-solve the wave equation for the waveguide's new eigenmodes. Under common fiber perturbations (bends, twist, pressures, etc.) that slightly alter the fiber structure, one can still assume that the ideal eigenmodes are valid but should investigate how perturbations lead to the mixing of theoretically orthogonal modes. This mode mixing may result in a loss of signal purity or information. In fact, even SMF is two-moded since it has two orthogonal polarization eigenmodes. Bend- or geometry-induced fiber birefringence can result in polarization-mode dispersion in classical communications links and entanglement-preservation loss in quantum links. Therefore, it is essential to

comprehend and evaluate mode coupling under common perturbations and to deduce the conditions under which modes remain stable so that each mode can be utilized independently.

The fiber perturbations may be quite complicated and stochastic when accounting for the fiber imperfection (defect, interface roughness, etc.) that is highly dependent on the state of the art in manufacturing. Typically, these perturbations are benign, but they may readily accumulate across hundreds to thousands of kilometers of fiber and have a major impact. For some first-principles insight, this chapter concentrates on shorter fiber lengths ranging from a few meters to kilometers (lengths representing scales of fiber usage in the majority of applications, such as fiber lasers and amplifiers, data-center links, nonlinear devices, and sensors) and more tractable perturbations as the fiber bends. Prior to analyzing the mode coupling, it was assumed that each mode could be excited with sufficient purity.

This chapter will also show that the 3D redirection of light, which is a typical perturbation encountered by an optical fiber, can lead somewhat counter-intuitively to the failure of using one set of modes (namely, the vector modes) as the real eigenmodes while the other mathematically equivalent one (the OAM modes) remains valid. This directly contributes to the instability of vector modes, similar to the oscillation of power between odd and even scalar modes discussed in the previous chapter. In contrast, the circularly polarized OAM eigenbasis represents the most stable set of modes for light transmission. Therefore, the question raised in the preceding chapter, which is about the real eigenmodes in a fiber, can be fully answered.

4.1. Mode Coupling and Fiber Perturbation

Instead of resolving the eigenmode equations, it is common practice to assume that the eigenmodes stay unchanged and to examine how the eigenmodes interact with one another under these perturbations. The mode coupling can be well explained and characterized by the coupled mode theory (Marcuse, 1991).

Consider the mode coupling between two modes $\boldsymbol{E_1}(r,\varphi)$ and $\boldsymbol{E_2}(r,\varphi)$. The total field at any value of z can be written as a linear combination of the two:

$$\boldsymbol{E}(r,\varphi,z) = A_1(z)\boldsymbol{E_1}(r,\varphi)e^{-i\beta_1 z} + A_2(z)\boldsymbol{E_2}(r,\varphi)e^{-i\beta_2 z} \tag{4.1}$$

where $A_1(z)$ and $A_2(z)$ are the amplitudes of the two modes. Ideally, two eigenmodes are orthogonal with each other. However, under a variety of ever-present perturbations (manufacture imperfection, bending, twisting), they exhibit a non-zero coupling coefficient κ given by the combined overlap integral that accounts for the transverse deformation term $\overline{\overline{\boldsymbol{P_{pert}}(r,\varphi)}}$:

$$\kappa = \frac{\omega\epsilon_0}{4i}\iint \boldsymbol{E_1}(r,\varphi)\overline{\overline{\boldsymbol{P_{pert}}(r,\varphi)}}\boldsymbol{E_2^*}(r,\varphi)dA \tag{4.2}$$

where the perturbation term $\overline{\overline{\boldsymbol{P_{pert}}(r,\varphi)}}$ is a matrix, accounting for the fact that the fields here are vector instead of scalar quantities. In other words, perturbation may also be accompanied by birefringence in the form of an off-diagonal matrix element that combines orthogonal polarizations. Here, it is assumed that the transverse perturbation is decoupled from the longitudinal one, which will be considered later.

Under such perturbation, the electric field of one certain eigenmode is projected onto that of the other one. A simple example is the projection between two orthogonal

linear polarizations due to bend-induced birefringence. Even if this birefringence is minimal, the effect will accumulate throughout propagation since the two degenerate polarization modes are inherently in phase along the fiber. In other words, this mode coupling is the highest for modes that are degenerate in β. Even under mild transverse deformation, the coherent accumulation may therefore make a considerable difference. This explains why bend easily causes polarization mixing between the two degenerate SMF with identical field distribution but orthogonal polarizations.

However, non-degenerate modes with distinct β exhibit a continually varying phase difference during propagation. Consequently, the coupled electric field is mostly canceled out. In order for these coupled field to add up coherently, a phase-matching wavevector *K* is required. The *z*-dependent amplitudes of the two modes are given by the coupled mode equations:

$$\frac{dA_1}{dz} = \kappa A_2 e^{i\Gamma z} \tag{4.3}$$

$$\frac{dA_2}{dz} = -\kappa A_1 e^{-i\Gamma z} \tag{4.4}$$

where $\Gamma = \beta_1 - \beta_2 - K$. One can thus solve the amplitude and the power in each mode along the fiber. Suppose all the power is only in mode $\boldsymbol{E_1}$, the z-dependent power in each mode is given by

$$\frac{P_1(z)}{P_1(0)} = 1 - \frac{\kappa^2}{\gamma^2}\, sin^2\, \gamma z \tag{4.5}$$

$$\frac{P_2(z)}{P_1(0)} = \frac{\kappa^2}{\gamma^2}\, sin^2\, \gamma z \tag{4.6}$$

where $\gamma^2 = \kappa^2 + \Gamma^2/4$, $P_1(0)$ is the power launched into mode $\boldsymbol{E_1}$. Part of the power oscillates between two modes along the z direction. Only if the phase matching condition is satisfied as $\Gamma = 0$, or $\Delta\beta = \beta_1 - \beta_2 = K$, can there be a full exchange of power between the two modes. In this case, the oscillation frequency is determined by the coupling coefficient κ.

A constant additional wavevector is typically provided by a grating with periodically varying perturbation along the z-axis, which corresponds to a strong Fourier component in momentum space. In many cases, the perturbation results in a spectrum of additional wavevectors of which the dominant Fourier component (if any) is typically considered.

A most common perturbation is fiber bends. As a general rule, a bent fiber comprises a wavevector $e^{\frac{i2\pi}{L_c}}$, where L_c is a correlation length representing characteristic beat lengths for the perturbations. Hence, to achieve $\Delta\beta \gg K$ to mitigate the mode coupling, one should have $\Delta n_{eff} \gg \frac{\lambda}{L_c}$, at least by an order of magnitude. Typically, L_c ~ 1mm to 1cm, and hence it is easy to see that Δn_{eff} between modes of ~10^{-4} to 10^{-3} typically minimizes the mode coupling.

4.1.1 Degenerate Mode Coupling

Modes degenerate in β are mostly likely to couple with each other as they are in phase all along the fiber (therefore no need for additional wavevector for phase matching). As previously described for coupling between two degenerate modes with orthogonal polarization, this explains why $LP_{0,m}$ modes seldom maintain polarization in a bent fiber.

Given that the two orthogonally polarized $LP_{0,m}$ modes have identical amplitude patterns, only birefringence is required of the perturbation. Since the cylindrical symmetry of an optical fiber implies that *all* modes have, at least, two-fold (polarization) degeneracy, one would expect this mixing to be commonly encountered, as in SMF or $LP_{0,m}$ modes.

However, there is also accidental degeneracy between modes with different L and m as mentioned in the preceding chapter. This degeneracy exists regardless of the polarization, so there is no need for birefringence. Figure 4.1 is an exemplary n_{eff} distribution illustrating the accidental degeneracy between L=6, m=1 and L=2, m=2 modes in a ring-core fiber with a ring diameter of ~16um (Gregg et al., 2016). The L=6 SOaa, m=1 mode is excited at various wavelengths using a CW laser and the corresponding output images are recorded at the output of the ~1m fiber (setup in the Fig. 3.1). The strongest mode coupling occurs at the wavelength where two n_{eff}'s intersect. The four-fold symmetry of the interference pattern reveals the ΔL between the two modes and the double rings indicate m=2 for the accidentally degenerate mode (Sec. 3.1.3). Such mode coupling goes away at least ~40nm from the crossing wavelength for sufficiently large n_{eff} separation. This mode coupling disappears at a wavelength where the n_{eff} separation is sufficiently large, at least 40 nm away from the crossing wavelength. Thus, the mode coupling range extends to ~80nm. This mode coupling range in a ~1km fiber increases to ~210nm (1430-1690nm) because of the core-diameter variation along the length of the fiber. Due to the difference in dispersion between these two modes, the change in fiber size (equivalent to a change in the wavelength) alters the n_{eff} of the two modes differently, causing a shift in the degenerate wavelength. In fact, the different wavelengths of

accidental degeneracy are observed in various fiber sections. This accidental degeneracy completely disables the desired m=1 mode in the mode coupling range, resulting in a decrease in the number of spatial channels for multiplexing.

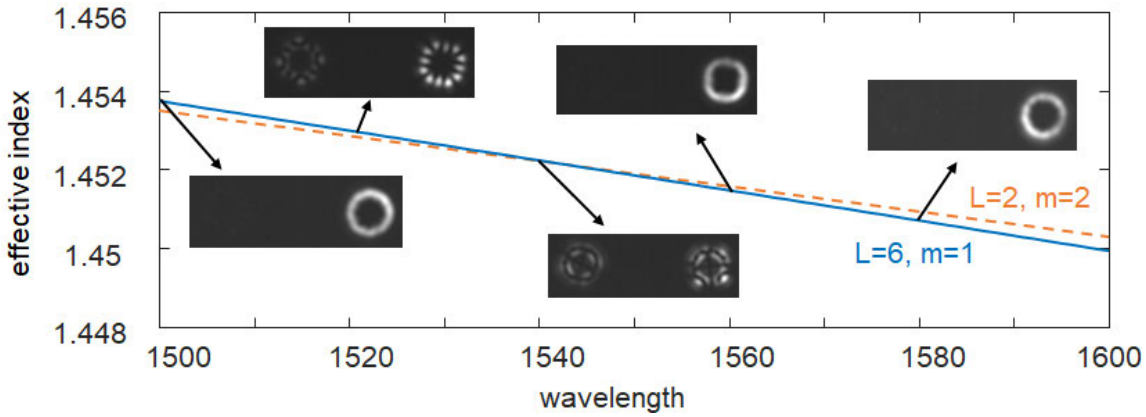

Figure 4.1: Accidental degeneracy between L=6, m=1 and L=2, m=2 in a 16-um ring-core fiber. The inset images are the outputs of the 1-m fiber when a L=6 SOaa, m=1 mode is launched at various wavelengths using a CW laser. Using polarization binning method (Sec. 3.4), the two opposing circular polarizations are separated in each output image.

The L=6 SOaa mode is degenerate with the L=-6 SOaa mode, which has the opposite circular polarization, as detailed in Chapter 2. Yet, Fig. 4.1 demonstrates that there is no coupling between the two polarizations at the wavelength where accidental degeneracy is absent. This polarization-maintaining property remains even in a ~km scale fiber due a general OAM conservation principle (Gregg et al., 2015). It is distinct from degenerate mode coupling for the aforementioned L=0 and also low-|L| modes. It differs from the aforementioned L=0 and low-|L| modes, which suffer from degenerate mode coupling.

If the radial and azimuthal components of the perturbation can be decoupled, the coupling coefficient in the OAM bases may be rewritten as

$$\kappa = \frac{\omega \epsilon_0}{4i} \iint \boldsymbol{E_1}(r) \overline{\overline{\boldsymbol{P_{pert}}(r)}} \boldsymbol{E_2^*}(r) e^{i(L_1 - L_2 - \delta l)\varphi} dA \tag{4.7}$$

where δl is the extrinsic OAM that can be provided by various kinds of perturbations. Intuitively, fiber twist is capable of yielding such extrinsic OAM (Zhao et al., 2019; Wong et al., 2012). Yet, a twist that is excessively strong can lift the degeneracy between the two degenerate modes (Alexeyev et al., 2004; Alexeyev et al., 2012). Besides, simple bend perturbation has a matrix element of the form $e^{i\delta l\varphi}$ that spans all δl, but $|\delta l| = 1$ is often the strongest component (Gregg et al., 2015). However, coupling between the degenerate counterparts involves changing OAM order from $+L$ to $-L$, i.e., by $|\Delta L| = |2L|$. Hence, this degenerate coupling of higher-$|L|$ OAM modes require larger extrinsic OAM provided by the perturbation. In addition, such a perturbation must provide sufficient birefringence to concurrently couple two orthogonal polarizations. Thus, degenerate states with high $|L|$ OAM modes do not mix in fibers with the proper design. In other words, even in strictly circular fibers, select modes can be polarization maintaining.

4.1.2 Degeneracy Lifting

Due to its complex and stochastic nature, leveraging transverse deformation as a means of controlling mode coupling is not a practical solution. Instead, a commonly employed strategy for mitigating mode coupling is to lift the n_{eff} degeneracy of the modes, which can be accomplished through appropriate fiber design or by selecting a suitable subset of modes.

In general, the coupling efficient κ between modes with $|\Delta L| = 1$ (and the same polarization) appears to be the highest, as common fiber bends can readily provide extrinsic

OAM $|\delta l| = 1$. Thus, they need a sufficiently high n_{eff} to mitigate mode coupling. Figure 4.2 schematically shows the n_{eff} for select modes with indices L and m in select index-guided fiber designs. Early HOM-based dispersion compensation (Ramachandran et al., 2001, Gnauck et al., 2000) efforts involved "W" fiber designs that separated the n_{eff} of the desired $LP_{0,2}$ mode from the $LP_{2,1}$ and $LP_{1,2}$ modes (Δn_{eff} denoted as red arrows in Fig. 4.2) by $\Delta n_{eff} > 10^{-3}$. This enables the stable propagation of the desired $LP_{0,2}$ mode for dispersion control designs. Simple step index fibers have a naturally mode-separating feature, where Δn_{eff} between a desired $LP_{0,m}$ and the undesired $LP_{1,m}$ or $LP_{1,m-1}$ modes monotonically increase with radial order m (green arrows in Fig. 4.2) (Ramachandran et al., 2006). This feature has been used for scaling the A_{eff} of fiber modes (Ramachandran et al., 2008), and stable modes with $A_{eff} \sim 6000\mu m^2$ and yet $\Delta n_{eff} > 5 \times 10^{-4}$ have now been demonstrated (Nicholson et al., 2012) for fiber laser applications.

As mentioned in Sec. 2.3, SOI lifts the degeneracy between SOa and SOaa modes (or, equivalently, HE and EH modes) and the Δn_{eff} can reach the order of $> 5 \times 10^{-5}$ for high-$|L|$ modes in a fiber with high index contrast (blue arrow in Fig. 4.2) (Brunet et al., 2014, Ramachandran et al., 2015). The large Δn_{eff} inhibit the coupling between SOa and SOaa modes with the same $|L|$ (thus the name intra-$|L|$ modes coupling). Hence, both SOa and SOaa modes can propagate stably, yielding OAM mode stability in fibers. The ring-core design helps minimize the number of other radial order modes that might be accidentally degenerate (and hence inadvertently mix) with the desired OAM modes (details in Chapter 5).

Intra-$|L|$ mode coupling requires extrinsic OAM $|\delta l| = 2|L|$ or sufficient perturbation-induced birefringence. Hence, its coupling coefficient κ is lower than that of $|\Delta L| = 1$ inter-$|L|$ mode coupling under common bend perturbation. On the other hand, the Intra-$|L|$ Δn_{eff}'s ($\sim 10^{-4}$) of available modes are typically an order of magnitude lower than the $|\Delta L| = 1$ inter-$|L|$ Δn_{eff}'s ($\sim 10^{-3}$). Given the scholastic and phenomenological nature of the transverse deformation in practical fibers, particularly over longer length (e.g. ~1km), it is expected that the Δn_{eff} plays a predominating role in the mode coupling. Hence, mode mixing between modes separated by $|\Delta L|$=1 between them is always less than intra-$|L|$ mode coupling. Furthermore, at long fiber lengths of up to ~1km, the mode coupling may not be solely dependent on Δn_{eff} due to the presence of numerous fiber imperfections. For instance, the intra-$|L|$ mode coupling for a mode with Δn_{eff} ~5×10^{-5} (L=5) is around -10dB/km in the prior benchmark Gen4 fiber (Gregg et al., 2016), while it is around -15dB/km for a mode with similar Δn_{eff} in the Gen5B fiber (L=14) described in Chapter 4. Admittedly, this mode coupling is not insignificant, but it is much lower than that of conventional MMFs, and it is just adequate for achieving sufficiently low Bit Error Rates (BER) in telecommunications.

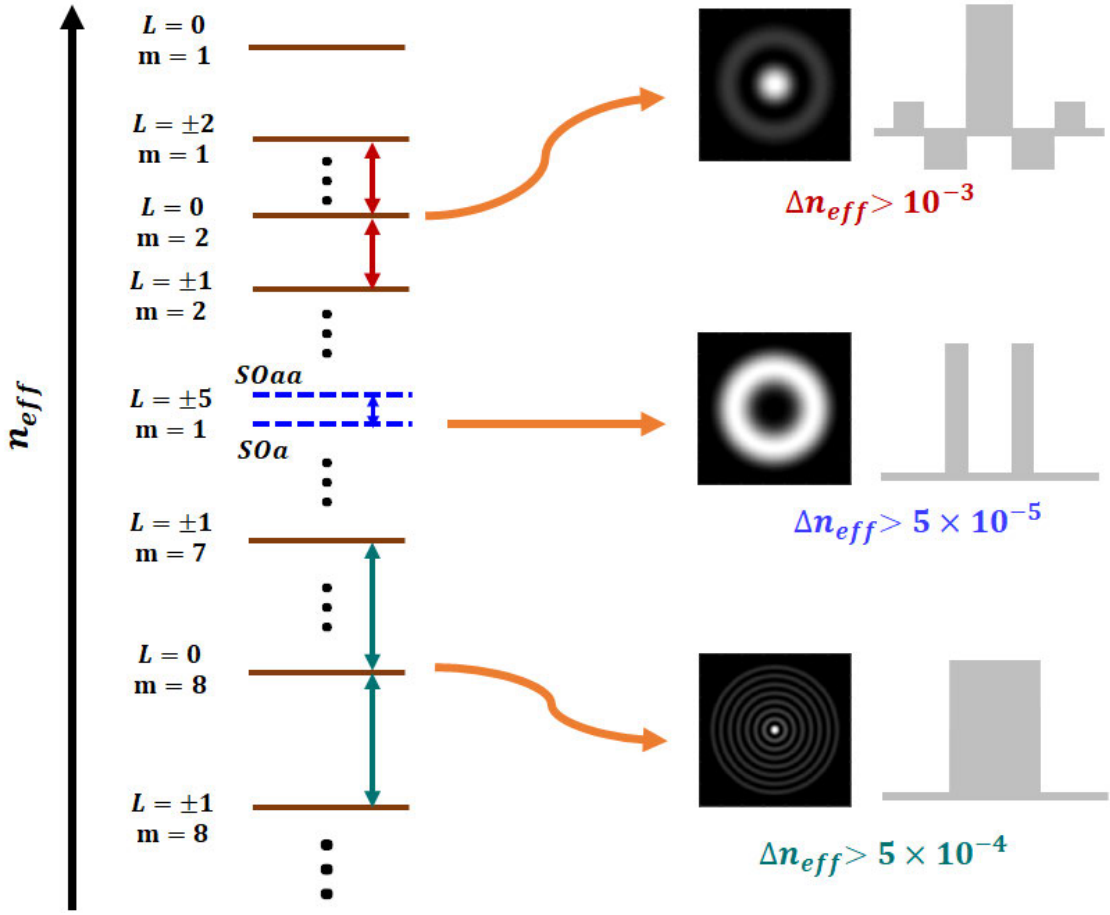

Figure 4.2: n_{eff} distributions for select modes with indices L and m. For visual clarity, not illustrated are polarization degeneracies of any of the modes or the n_{eff} degeneracies of any except for the $|L| = 5$ mode. Orange arrows leading to representative mode images for corresponding fiber designs (grey shaded features) describe mode separations (quantified by Δn_{eff}) for a select class of modes in their respective fibers. The n_{eff} of the $LP_{0,2}$ mode can be separated from $LP_{2,1}$ and $LP_{1,2}$ modes (red arrows) by using the class of "W" shape fiber designs. The n_{eff} splitting of $|L| = 5$ OAM modes (blue arrow) can be at least 5×10^{-5} in ring-core fiber designs. The n_{eff} splitting between $LP_{0,8}$ and its nearest neighboring $LP_{1,m}$ modes can be larger than 5×10^{-4} in simple step-index fibers (green arrows).

4.2. Out-of-Plane Redirection and Geometric Phase

4.2.1 Circular and Linear Polarizations

The eigenmodes obtained in Chapter 2 are only applicable to a perfectly straight, perturbation-free fiber. As shown in Sec 4.1, they can be corrected in the presence of common fiber perturbations. However, the light path was assumed to be in a plane under these perturbations. In contrast, a slow, adiabatic redirection of light in 3D space (out of plane) would have non-trivial effects. After all, this is a rather common perturbation encountered with a flexible fiber. This geometrical transformation adds up an extra phase, which is distinct from the more common propagating phase associated with βz of a beam of light.

The sign of this phase depends on the handedness of the circular polarization of a photon. Each degenerate mode in the $\mathrm{CP}_{0,1}$ basis acquires a geometric phase $\emptyset_g$ of sign opposite to that of its polarization ($\hat{\sigma}^{\pm}$). Thus, an $\mathrm{LP}_{0,1}$ mode, which is the linear combination of two orthogonal $\mathrm{CP}_{0,1}$ modes, rotates under such geometric perturbations. The fact the power oscillates between two linear orthogonal polarization suggest that LP modes doesn't satisfy the definition eigenmodes under such 3D redirection, in contrast to CP modes that remain unchanged in the transverse electrical field while pickup an additional phase. Hence, the linear and circular polarizations no longer form a pair of MUBs any more in the presence of geometric phase. Actually, such geometric phase associates with 3D redirection manifest even for free-space light.

Fundamentally distinct from the conventional dynamic phase (which includes, birefringence, angular momentum exchange, etc., discussed earlier) with dependence on propagation length, the geometric phase stores “memory” of the evolution (like geometry of the pathway) of a lightwave (Berry, 1990, Anandan, 1992).

A carefully constructed experiment with SMF showed that a fiber, configured to traverse a 3D route in space, acquired phase that was dependent only on the solid angle subtended by the fiber-path in momentum (wavevector) space. The ray trajectory can be continuously deformed into any shape without changing the geometric phase as long as the solid angle remains unchanged, pointing to the topological nature of the effect.

The discovery and exposition of this geometric phase, radically different from the propagating dynamic phase, dates back to the seminal report by S. Pancharatnam in 1956 (Pancharatnam, 1956). It took ~30 years for its significance to be appreciated, awaiting the generalization of this concept in quantum mechanics by M. Berry (Berry, 1984). This concept is intimately related to the idea that light carrying circular polarization denotes photons carrying spin angular momentum (SAM), and that a 3D path of light imparts *extrinsic* angular momentum to it. The aforementioned spin-redirection phase (Tomita et al., 1986) is one important manifestation of this concept.

The composite effect of (bend-induced) birefringence as well as geometric perturbations on SMFs is illustrated in Fig. 4.3. The first section of the fiber illustrates only a 3D path (geometric transformation — the fact that the fiber is lifted out of plane is schematically illustrated by a shadow it subtends, in-plane). This adds phase in the $CP_{0,1}$ basis, hence a single $CP_{0,1}$ mode merely acquires a phase. In contrast, the $LP_{0,1}$ mode

rotates in polarization orientation. Following that, the second section of the fiber illustrates a conventional bend that induces birefringence, which serves to convert both the $CP_{0,1}$ as well as $LP_{0,1}$ modes into modes with arbitrary elliptical polarization states.

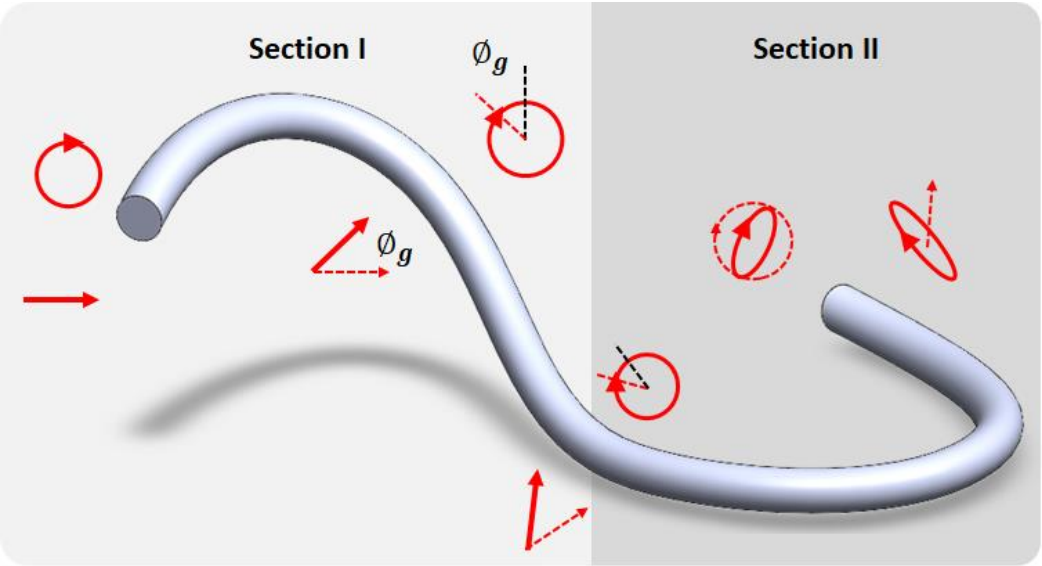

Figure 4.3: The effect of nonplanar and birefringent perturbations on the polarization of light launched into SMF, illustrated as a flexed grey cylinder. Solid red arrows represent linear polarization states of light in the fiber at different positions along the propagation direction, with the dashed arrows denoting the state it possessed just prior to propagating to that position. Similarly, arrows on red circles represent circular polarization states and ellipses denote arbitrary elliptically polarized states. Mode transformations described below assume that light enters the fiber at the upper left end. The first section (I) represents an out-of-plane path (schematically illustrated by a shadow it subtends in plane) that is of large bending radii and hence free from fiber birefringence. The second section (II) represents an in-plane path that has strong birefringence. For a fundamental $CP_{0,1}$ mode with right-hand circular polarization, the nonplanar path imparts an extra phase $\emptyset_g$ due to geometric effects arising from Pancharatnam-Berry phases, but otherwise does not perturb the polarization state. This extra phase is illustrated by an azimuthal shift of the arrowhead. A mode with left circular polarization would behave similarly but accumulate an opposite phase $\emptyset_g$. In contrast, a fundamental $LP_{0,1}$ mode with horizontal polarization, being a linear combination the two orthogonal circular polarizations, is rotated by an angle $\emptyset_g$ along the nonplanar path. The subsequent bend of section II induces birefringence, and hence transforms any $LP_{0,1}$ or $CP_{0,1}$ mode into arbitrary elliptically polarized states, with ellipticity and handedness controlled by the strength of the bend-induced birefringence.

4.2.2 OAM and Vector modes

The preceding analysis was restricted to the fundamental mode of SMF, i.e. the L = 0, m = 1 mode (though similar behavior is expected for higher-m $\mathrm{LP}_{0,m}/\mathrm{CP}_{0,m}$ modes). In these modes, the only contribution to angular momentum arises from the polarization ($\hat{\sigma}^{\pm}$). This concept is extendable to beams carrying OAM in addition to SAM, and the resultant geometric phase is given by (Bliokh, 2006):

$$\emptyset_g(\mathrm{C}) = -(\sigma + L)\Omega(\mathrm{C}) \tag{4.8}$$

where C represents the path-contour, $\Omega(\mathrm{C})$ represents the solid angle subtended by this path in momentum space, and σ represents the handedness of circular polarization or amount of SAM, taking values of ±1 for light with $\hat{\sigma}^{\pm}$, and all other quantities have been previously defined. As is evident, geometric phase is enhanced for OAM modes, and depends on the *total* angular momentum (TAM) of a photon.

Observing this effect has historically been obscured by the fact that fiber modes experience all aforementioned dynamic and geometric perturbations simultaneously. One report (Abdulkareem et al., 2016), describing the strength of a so-called optical Magnus effect, showed that the speckle pattern out of a multimode fiber rotates when changing the sign of circular polarization, with the effect being proportional to the solid angle subtended by the fiber coil in the momentum space. A fiber in which low $|L|$ OAM or vector modes were excited showed the rotation of polarizations pattern to be explicitly dependent on mode order L (Huang et al., 2018). Unfortunately, concurrent birefringent and angular momentum coupling implied that the experimentally observed rotation did not match the theory well, since the SOa and SOaa modes also coupled due to bends and birefringence.

In fact, the first experiment with SMF (Tomita et al., 1986), described earlier, emphasized the need for short fibers and large bending radii to observe the effect with reasonable fidelity.

The advent of ring-core fibers greatly aids the study of geometric phase because of the ability to isolate the effects of the disparate perturbations described in Sec. 4.2.1. As described earlier, the ring core fiber minimizes coupling within the mode group – i.e., coupling between the SOa and SOaa pairs of modes (Fig. 4.2), and the angular momentum conservation effect forbids coupling between degenerate states for high enough $|L|$.

Figure 4.4 shows the experimental setup (Ma et al., 2018) used for studying the mixing of two degenerate OAM or vector modes, in a 4-m long ring-core fiber (Gregg et al., 2015) supporting stable propagation (i.e. without SOa-SOaa mixing) of high-$|L|$ modes ($|L| = 5, 6, 7$). The incoming Gaussian beam at 1550nm from an external cavity laser (ECL) is converted into the desired OAM or vector mode using a Pancharatnam–Berry optical element called a q-plate (Marrucci et al., 2011, Gregg et al., 2015). A q-plate with topological charge q can project circular polarization onto OAM modes of order $|L| = |2q|$, with the spin-orbit alignment dependent on the sign of q (Eq. 4.9).

$$\mathrm{A}\hat{\sigma}^{+} + \mathrm{B}\hat{\sigma}^{-} \xrightarrow{q} \mathrm{A}\hat{\sigma}^{-}e^{i2q\varphi} + \mathrm{B}\hat{\sigma}^{+}e^{-i2q\varphi} \tag{4.9}$$

where the arrow denotes the transformation induced by the q-plate and A and B are mode amplitudes.

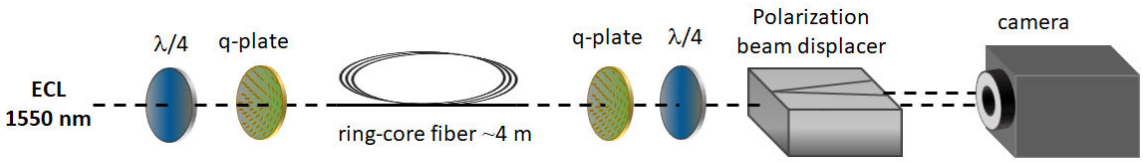

Figure 4.4: Experimental setup used for studying the mixing ratio of two degenerate OAM or vector modes. For the OAM basis, the quarter-wave plate (λ/4) is rotated to an angle such that the fast axis is 45º with respect to the axis of polarizer to generate circularly polarized light, which is converted to OAM modes by the q-plate. In contrast, for the vector basis, the fast axis of the quarter-wave plate is aligned with the axis of the polarizer, such that linearly polarized light can be projected on to corresponding vector modes; A reciprocal setup at the fiber output converts the modes back to Gaussian beams, with the power in each polarization bin being proportional to the power of the individual degenerate (OAM or vector) modes at the fiber output. For the vector mode measurement, the output quarter-wave plate is removed. When measuring OAM mode stability, the input was a ~15-dB pure $L = -7\ \hat{\sigma}^+$ mode, whereas, during the vector mode stability measurements, the input was a ~10-dB pure $EH_{6,1}^{even}$mode.

In the following representative experiments we used $q = \frac{7}{2}$, which causes Gaussian beams of two circular polarizations $\hat{\sigma}^+$ and $\hat{\sigma}^-$ to be converted into two degenerate SOaa OAM modes of $L = +7\ \hat{\sigma}^-$, and $L = -7\ \hat{\sigma}^+$, respectively. The purity of OAM modes excited in the fiber is confirmed to be greater than 15dB via spatial interferometry (Sec. 3.2). The output of the ring-core fiber is then converted back to a fundamental Gaussian-shaped free-space mode using an identical q-plate. Thereafter, with appropriate polarization optics, the two orthogonal polarization components of the output beam can be spatially separated and projected onto a camera. Therefore, the power ratio between polarization bins on the camera represents the mixing ratio of two degenerate OAM modes in the fiber. By launching a pure mode into the fiber, its stability within the fiber can be deduced by measuring the relative power scattered into its degenerate counterpart. The combination of q-plate and wave plates can not only generate two degenerate OAM modes, but also any of their linear combinations. Since linear polarizations are linear combinations

of circular polarizations and vector modes are linear combinations of OAM modes, Gaussian beams with two orthogonal linear polarizations can be mapped onto two degenerate vector modes ($A = \pm B$ in Eq. 4.9). Reciprocally, measuring the power ratio in the two linearly polarized bins yields the mode-mixing ratio between the two degenerate vector modes. By switching the polarization between circular and linear using quarter-wave plates (or their lack, thereof), we are able to switch between the OAM and vector modal bases with ease while maintaining all other experimental (perturbative) conditions. Representative experimental results on propagation stability in the presence of in-plane and out-of-plane bends are shown for the $|L| = 7$ SOaa OAM modes and the corresponding mathematically rotated basis of $EH_{6,1}$ odd and even modes.

The plots in Fig. 4.5(b) and (c) show the measured power fluctuations between two degenerate OAM and vector modes, respectively, as the fiber is bent, in plane, as illustrated in Fig. 4.5(a). When the input is an OAM mode ($L = -7\ \hat{\sigma}^+$), a negligible amount of power (around −12dB) is scattered to its degenerate counterpart. This is consistent with earlier observations that high $|L|$ OAM modes are stable, even between degenerate modes, in ring-core fibers (Gregg et al., 2015). For a vector mode input ($EH_{6,1}^{even}$), the power of parasitic degenerate mode ($EH_{6,1}^{odd}$) remains mostly low, at the −10dB level. Some power jumps to around −7 dB are evident. This is due the experimental inability of maintaining a strictly in-plane perturbation. Later, we will describe the origin of this discrepancy, but a higher-level summary of these two experiments is that OAM and vector modes remain robust to degenerate mode coupling in the presence of in-plane bend perturbations. Given that OAM mode stability was already known, this was to be reasonably expected, given that its

mathematically equivalent counterpart, the vector modes, would also possess similar stability. The plots in Fig. 4.5(e) and (f) show the mode mixing between two degenerate OAM modes and vector modes as the fiber is moved out of plane, as illustrated in Fig. 4.5(d). Again, for the OAM mode input ($L = -7\ \hat{\sigma}^{+}$), the power of parasitic degenerate mode remains at a very low level (~14dB). In contrast, when the input is the EH_{61}^{even} mode, the two degenerate modes completely mix with each other with 3D fiber perturbations.

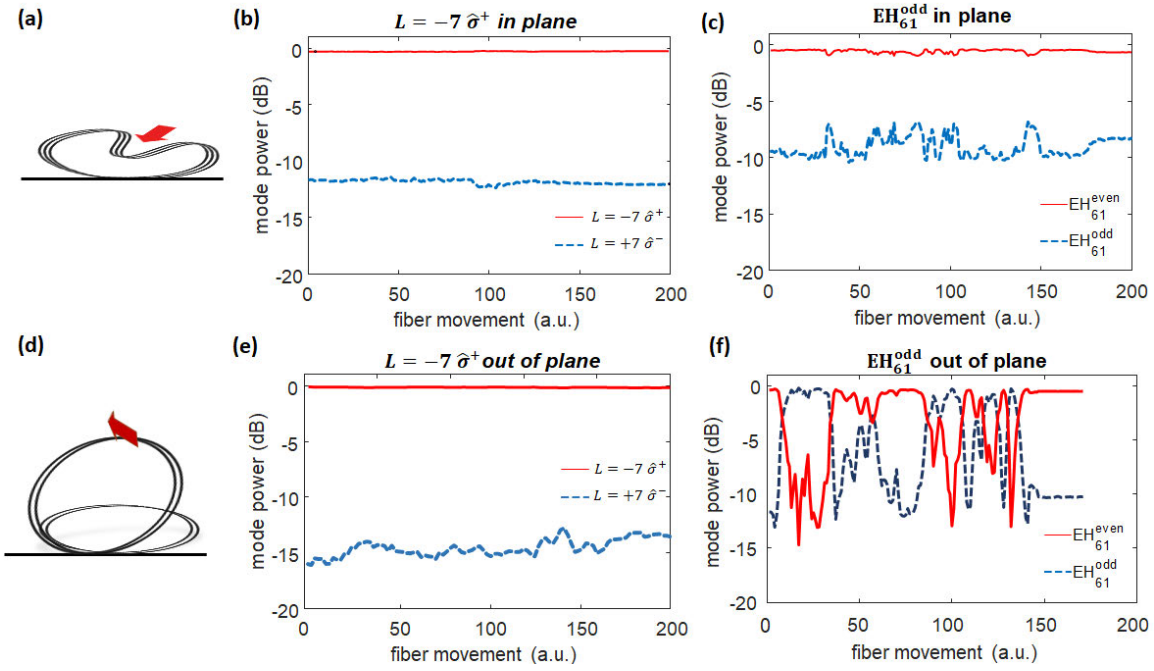

Figure 4.5: (a) Schematic of fiber loops being bent in-plane to varying degrees, during the measurement. Part of the fiber loops (radius ~12cm) are gradually bent into radius ~4cm, and then return back to the original; (b) Plot of relative power in the two degenerate OAM modes ($L = \mp 7\ \hat{\sigma}^{\pm}$) under the application of perturbations as shown in (a); (c) Corresponding plot of relative power in the two degenerate $EH_{6,1}$ modes for in-plane perturbations; (d) Schematic of fiber partly (2 out of 4 fiber loops) being lifted out of plane to different heights during measurements. The plane of lifted fiber is moved to the plane perpendicular to the original and then moved back; (e) Plot of relative power in the two degenerate OAM modes ($L = \mp 7\ \hat{\sigma}^{\pm}$) as the fiber is moved out of plane, as shown in (d); (f) Corresponding plot of relative power in the two degenerate EH_{61} modes for out-of-plane perturbations. OAM modes remain stable to bend as well as 3D perturbations, while the vector modes are completely mixed by 3D path redirections of the fiber.

This curious result, of two mathematically identical sets of modes behaving differently under 3D perturbations, is a manifestation of the geometric phase discussed in section 4.2.1. An OAM mode traversing a nonplanar path (modified mode represented as $\widetilde{OAM}$) obtains an extra phase factor compared with the input (Eq. 4.10). As two degenerate OAM modes have opposite sign of L and σ, the geometric phases they accumulate, as per Eq. 4.8, have opposite signs. The vector modes under such a perturbation ($\widetilde{EH}_{6,1}^{even}$) remain a linear combination of perturbed OAM modes, but they are now projected onto two degenerate vector modes $\mathrm{EH}_{6,1}^{even}$ and $\mathrm{EH}_{6,1}^{odd}$, as shown in Eq. 4.11. Hence, out-of-plane geometric perturbations fundamentally lead to mode mixing in the vector basis but not in the OAM basis. Note that this result follows previous experiments on geometric phases (Huang et al., 2018), but here, realistic lengths of fibers could be used, in contrast, because the ring-core fiber design and use of high $|L|$ modes helped avoid the competing effects of mode coupling due to bends and birefringence. While the length of fiber used in this experiment was only 4 m, OAM stability in ring core fibers has been observed up to 13.4 km propagation lengths (Gregg et al., 2016).

$$\begin{cases} \widetilde{OAM}_{+L}^{-} = \mathrm{OAM}_{+L}^{-} e^{i\emptyset_g} \\ \widetilde{OAM}_{-L}^{+} = \mathrm{OAM}_{-L}^{+} e^{-i\emptyset_g} \end{cases} \tag{4.10}$$

$$\begin{cases} \widetilde{EH}_{L-1,1}^{even} = \dfrac{1}{2}\left(\widetilde{OAM}_{+L}^{-} + \widetilde{OAM}_{-L}^{+}\right) = \cos\emptyset_g \cdot EH_{L-1,1}^{even} - \sin\emptyset_g \cdot EH_{L-1,1}^{odd} \\ \widetilde{EH}_{L-1,1}^{odd} = \dfrac{1}{2i}\left(\widetilde{OAM}_{+L}^{-} - \widetilde{OAM}_{-L}^{+}\right) = \sin\emptyset_g \cdot EH_{L-1,1}^{even} + \cos\emptyset_g \cdot EH_{L-1,1}^{odd} \end{cases} \tag{4.11}$$

4.3. Geometric Phase Control

To quantitatively study the effect of geometric phase on high $|L|$ modes, we configure the fiber into a uniform helix shown in Fig. 4.6 (a). Input and output OAM and vector modes are shown schematically, for visual clarity. Although both feature a donut-shaped intensity profile, the illustrations here show spiral patterns for OAM modes, obtained when an OAM mode is interfered with an expanded Gaussian (with the number and orientation of parastiches denoting L and its sign, respectively). Likewise, vector modes are schematically illustrated by their projection patterns, obtained when they are imaged through a polarizer (with the number of "beads" being $|2L|$). Figure 4.6 (b) shows that the k-vector of light in a helical path encloses a solid angle, Ω . As the fiber helix is compressed, the solid angle increases accordingly, resulting in an extra geometric phase of the beam traveling in the fiber, without changing the path length of the light (and hence its dynamic phase). This solid angle is related to the period of the helix Λ, by $\Omega = 2\pi\left(1 - \frac{\Lambda}{l}\right)$, where l represents the length of fiber in one loop. This helical arrangement is realized by loosely inserting the fiber into a Teflon tube with 1-mm inner diameter to minimize any torsion, stress or stretching during winding. This Teflon tube is then adhered to a metal spring, with which solid angle Ω can be controllably varied. This level of care is not needed for the OAM mode, which is stable, but is required for the vector mode, which, as shown in Fig. 4.5(f), is sensitive to 3D fiber movement. Part of a 3.4-m-long segment of a ring-core fiber of length is wound into a uniform helix of 6.5 loops (light propagating in and out of fibers are in opposite directions). The length of each loop l is 16.3 cm. Note that the k-vector of

the mode in the fiber, with magnitude β (its propagation constant), is well approximated to be parallel to the axis of the fiber under the weakly guiding approximation. Therefore, the solid angle subtended by the k-vector is approximately equal to the solid angle spanned by the fiber's physical path, which follows that of the metal spring. As the spring is compressed, the pitch period Λ decreases from 2.3cm to 0.2cm, and the solid angle correspondingly increases from 1.72π to 1.96π. The total geometric phase acquired for a mode in this setup is equal to the geometric phase acquired in one loop multiplied by the number of loops *N*, as shown in Eq. 4.12:

$$\emptyset_g(\mathrm{C}) = -N(\sigma + L)\Omega(\mathrm{C}) \tag{4.12}$$

For an OAM mode with $L = -7\ \hat{\sigma}^+$ the extra geometric phase results in a counterclockwise rotation of the beam. This rotation angle is equal to the additional phase divided by OAM order L, or $\Theta = \frac{\emptyset_g(\mathrm{C})}{L}$. Similarly, an OAM mode with $L = +7\ \hat{\sigma}^-$ would obtain an extra geometric phase of the same amount but with opposite sign. As the signs of both OAM order and geometric phase are flipped, the beam rotation would have the same magnitude and direction. Therefore, the vector modes (EH_{61} odd/even), which are the combinations of the two degenerate OAM modes, rotate counterclockwise with the same angle (shown schematically on the output patterns of Fig. 4.6(a)). However, this rotation would lead to power oscillation between the odd and even degenerate vector modes, since they are not rotationally invariant.

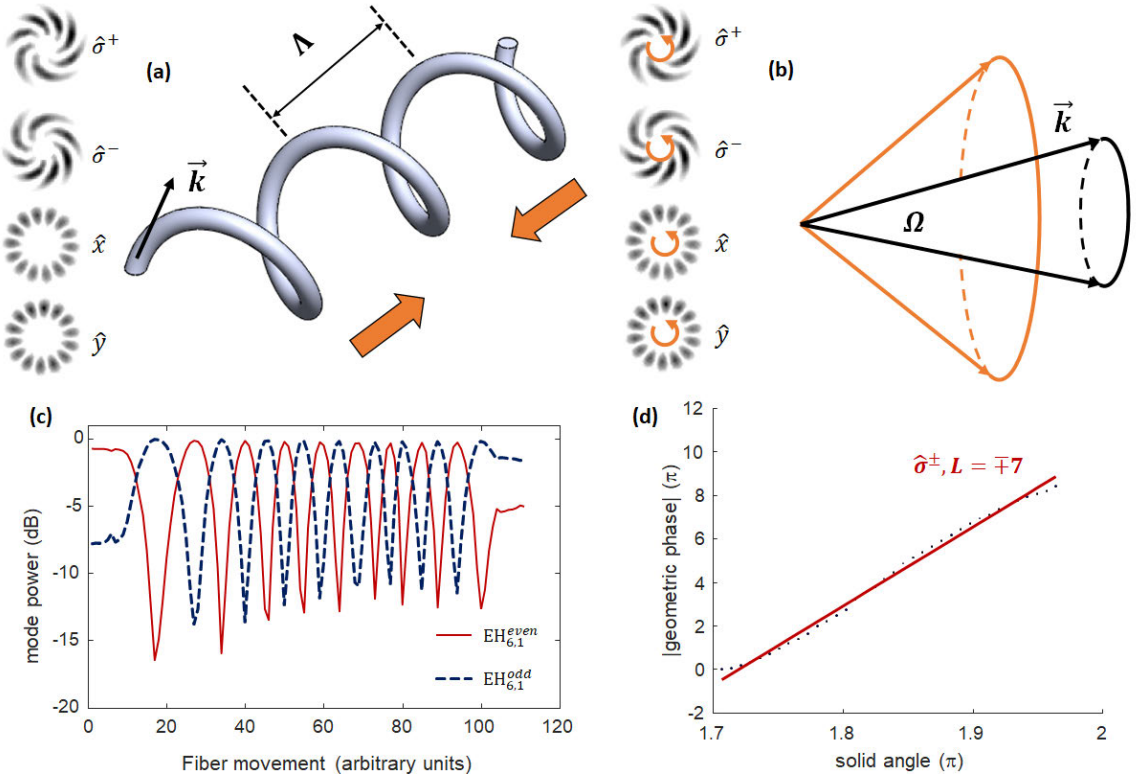

Figure 4.6: Systematic control of Pancharatnam-Berry phases in optical fibers. (a) An OAM mode supporting ring-core fiber, inserted in a loose Teflon tube, is attached to a flexible spring to configure a helical with variable period. A combination of two degenerate OAM modes ($L = -7\,\hat{\sigma}^+$ and $L = +7\,\hat{\sigma}^-$) is launched into the fiber. For visual clarity, the OAM modes are illustrated with spiral patterns that arise from their interference with an expanded Gaussian beam. The corresponding projection of this superposition state into $\hat{x}$ and $\hat{y}$ polarization-bins yields petal patterns, illustrated at the bottom left hand side of (a). The mode illustrations on the right side of the helical arrangement show the corresponding modes at the output of the fiber, all of which are rotated counterclockwise due to the geometrical transformation; (b) Geometric illustration of the solid angle Ω enclosed by the k-vector of the light path in this helical arrangement. The illustration in orange depicts the higher Ω obtained from compressing a spring from its original state, depicted in the black illustration; (c) Measured power fluctuations between even and odd modes for EH_{61}, using the reciprocal mode transmission setup of Fig 5(a), when the spring was compressed (pitch period Λ decreases from 2.3cm to 0.2cm). The uneven periodicity results from the uneven speed with which the spring was compressed; (d) Geometric phase, measured from vector mode power ratios, versus solid angle, for two degenerate OAM modes $L = -7\,\hat{\sigma}^+$ and $L = +7\,\hat{\sigma}^-$ as the helical spring is compressed. The red line is a linear fit of the experimental data (solid circles). Near-linear relationship shows exclusive influence of fiber path on geometric phase, and hence relative mode amplitudes.

Figure 4.6 (c) shows the measured power fluctuations between even and odd modes as the spring is gradually compressed, for an input comprising a pure $EH_{6,1}^{even}$ mode. As with the previous experiment of Fig. 4.5 (f), the two degenerate vector modes mix completely. The main difference is that the oscillation is now periodic and systematic, since the geometric phase is accumulated monotonically, in a controlled fashion, with the helical arrangement. Based on the rotation angle of the vector modes, the accumulated geometric phase of the OAM modes can be calculated. As shown in Fig 4.6 (d), the geometric phase shows a linear relationship with the solid angle, which matches the theoretical prediction (Eq. 4.12) of a linear relationship between these parameters. It clearly shows that image rotation, and hence mixing, of vector modes is linearly proportional to the solid angle enclosed by the k-vector of light.

We repeat this experiment on five other pairs of modes that are stable in this ring-core fiber. As shown in Fig 4.7 (a), the geometric phase shows a linear relationship with the solid angle in all cases. As evident, image rotation, and hence vector mode instability, increases as the TAM (equal to $L + \sigma$) of participating modes increases. Figure 4.7 (b) shows that the slopes for each pair of OAM modes is linearly proportional to the TAM of the corresponding OAM modes. The magnitude of this slope (i.e. slope of the slopes vs. TAM), which is, effectively the number of loops N (per Eq. 4.12), is 6.2, which is close to the expected value of $N = 6.5$. The lack of a better match may be due to the fact that input mode purity was only 10 dB, but even so, this confirms that the perturbations experienced by these modes predominantly arise from the experimentally induced geometric, and not inadvertent bend or birefringence, perturbations

While the controlled experiments helped rigorously verify the influence of different kinds of perturbations on an optical fiber and, especially, their influence on different modes, the results of Fig. 4.7(a) also point to applications towards a novel type of shape sensor, with sensitivity controlled by the OAM content of light in a fiber. One key distinction from other types of interferometric sensors that depend on the conventional dynamic phase of light is that this depends only on geometry. As mentioned earlier, dynamic phase arises from $e^{i\beta z}$, which is strongly wavelength dependent. In contrast, there is no wavelength dependence in geometric phase, meaning that its sensitivity does not depend on the bandwidth of the source, facilitating the use of low-cost sources even in high-sensitivity applications. Likewise, the lack of dynamic phase dependence also makes such sensors robust to ambient perturbations, such as temperature or pressure induced changes of the refractive index of the fiber.

To demonstrate its independence to wavelength, we conduct the same helix experiment with $|L|$=7 SOa modes ($L = \pm 7\ \hat{\sigma}^{\pm}$) using light sources of different bandwidths. Figure 4.7(c) shows the measured geometric phase as a function of solid angle, just as in Figs. 4.6(d) and 4.6(a), when employing sources of varying bandwidths. ECL denotes a narrow-linewidth (100 kHz) source at 1550 nm; “ps laser” is a picosecond laser at 1550 nm with ~0.5nm bandwidth; the LED has a bandwidth ~35 nm around 1525 nm; and “superK” represents a supercontinuum source with 3-dB bandwidth of ~250 nm centered at ~1475 nm. The spatial interferometry method used to previously guarantee mode purity does not work with broadband sources (because it utilizes *dynamic* phase). Hence, the purity of OAM modes is adjusted to be higher than 15 dB using the ECL, as before, and

then the light source is carefully switch to other broadband sources without disturbing alignment, expecting minimal changes in mode purity. The geometric phase shows a linear dependence on solid angle regardless of the bandwidth of light source, as shown in Fig. 4.7(c). However, the slopes obtained with the broadband sources differ from that obtained with the ECL by up to 12%. The mismatch probably arises from the lack of our ability to maintain high-purity excitation with the broadband sources, a problem easily solved in the future with the plethora of emerging mode-conversion technologies for OAM fiber modes Nevertheless, the results point to a novel means of developing low-cost shape sensors that are insensitive to environmental perturbations such as temperature, pressure, mechanical vibrations and bends, while maintaining high sensitivity.

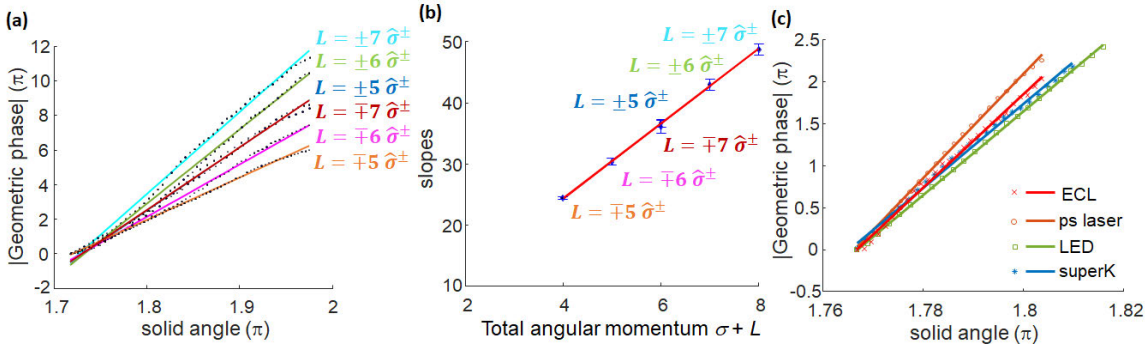

Figure 4.7: (a) Geometric phase versus fiber path solid angle for 6 distinct pairs of OAM modes. The colored lines are linear fits of the experimental data (black solid circles). All modes show a clear linear relationship; (b) The slope of each trace (for each mode) shown in (a) versus the $TAM = L + \sigma$ of the respective modes. The high degree of linearity as well as the slope of this line match well with theory that accounts only for geometric effects; (c) Geometric phase versus solid angle for two degenerate OAM modes $L = \pm 7\ \hat{\sigma}^{\pm}$ (as shown earlier in (a)), using multiple light sources. ECL is a narrow linewidth (100kHz) source at 1550nm; ps laser is a picosecond laser at 1550nm with ~0.5nm bandwidth; the LED has a bandwidth ~35nm around 1525nm; superK represents a supercontinuum source with 3dB bandwidth up to ~250nm at around 1475nm. Similar slopes for all these sources demonstrates weak dependence of wavelength on geometric phase.

4.4. Summary and Discussion

We have studied how ideal HOMs interact with each other under in-plan or out-of-plane perturbations and found the linear stability is intimately connected to properties of the modes themselves (their angular momentum content, and even the mathematical basis used to describe them) as well as the form of perturbations a fiber encounters.

Considering the two most common fiber perturbations – bends, which induce birefringence as well as OAM transfer, and light's path-memory, manifested in the 3D trace that light follows – we arrive at the following conclusions related to modal stability for HOMs (illustrated in Fig. 4.8). The commonly used LP modes are actually linear combinations of eigenmodes of dissimilar phase velocities, and thus they are not translationally invariant even in a perfect, straight fiber. On the other hand, the vector and OAM modes, as two mathematically equivalent bases for mode representations, remain stable in an unperturbed fiber. However, when their modal index $|L|$ is low, they mix completely with their degenerate counterpart in a fiber that is bent (in-plane), because of birefringent coupling that couples polarizations in SMFs too. High-$|L|$ vector and OAM modes are, in contrast, stable even across (in-plane) bent fibers, because of inherent OAM conservation rules. Finally, when a fiber is not only bent, but also lifted out-of-plane, even high-$|L|$ vector modes become unstable, in that their polarization distributions rotate, because of the Pancharatnam-Berry phase that light accumulates in 3D paths.

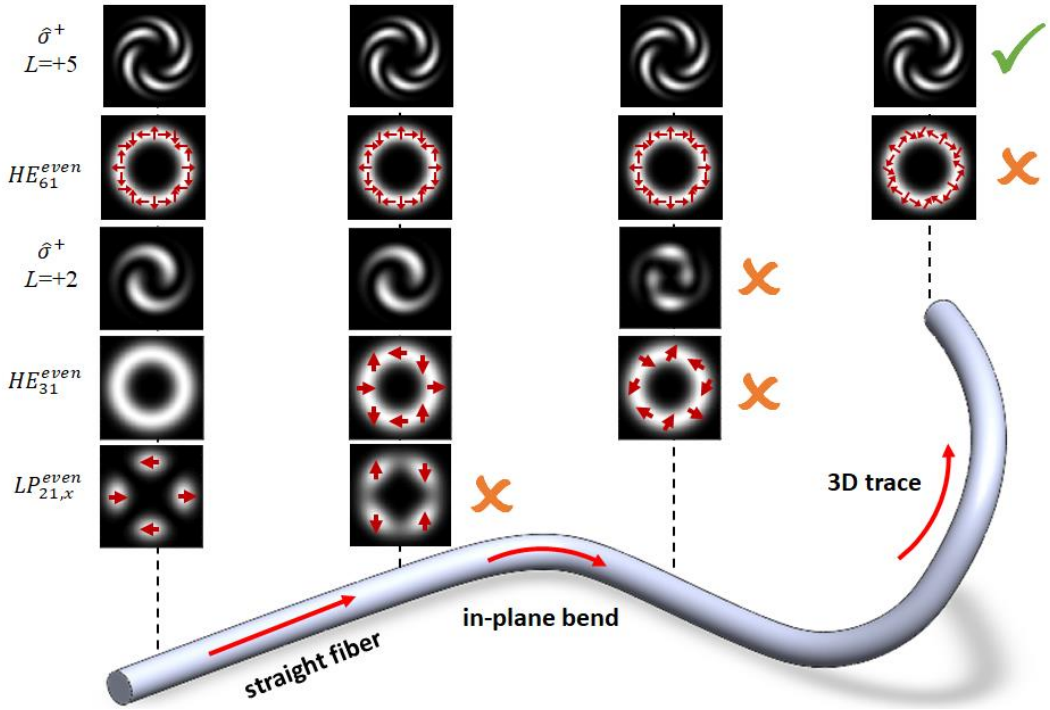

Figure 4.8: Summary of the propagation stability of optical fiber modes of different classes when the fiber is deployed with commonly encountered perturbations. The illustration depicts modes launched at the left end of a perfectly circular fiber, and all modes are schematically illustrated at four positions (black dashed lines) along the fiber propagation axis. From left to right: The input comprises pure modes in all the classes; the second position represents propagation through a straight fiber without any perturbations; this is followed by a position after propagation through a fiber that is bent only in plane; and, the final position represents propagation through a fiber that experiences an out-of-plane (3D) redirection as well. The modes from bottom to top represent LP modes ($LP_{2,1}$), low order vector modes ($EH_{3,1}^{even}$), low order OAM modes ($L = 2\ \hat{\sigma}^+$), high order vector modes ($EH_{6,1}^{even}$), and high order OAM modes ($L = 5\ \hat{\sigma}^+$). After propagating through the straight fiber section, LP modes mix between orthogonal modes of the same class, while all the other modes remain stable. As such, LP modes, designated at this point with an orange cross, are not illustrated across subsequent perturbations, having failed to propagate through the most elementary arrangement. In-plane fiber bends easily couple a low order vector ($EH_{3,1}^{even}$) or OAM ($L = 2\ \hat{\sigma}^+$) mode with its degenerate counterpart, while it doesn't impart enough angular momentum to couple a higher order OAM mode $L = 5\ \hat{\sigma}^+$ or the corresponding vector mode EH_{61}^{even} to their respective degenerate counterparts. Again, therefore, no further depiction of low $|L|$ vector or OAM modes is illustrated (as indicated by the orange cross). After propagating through the 3D trace, a higher order vector mode $EH_{6.1}^{even}$ mixes completely with its degenerate counterpart, while the corresponding OAM mode $L = 5\ \hat{\sigma}^+$ merely acquire a common geometric phase and remains remarkably stable. Hence, across all perturbations, only the high $|L|$ OAM mode survives without coupling, to its degenerate or non-degenerate counterparts.

In contrast, a high-$|L|$ OAM mode remains remarkably stable, except for accumulating a common phase. Hence, as mode propagation is studied across a range of perturbations, starting from none (straight fiber) to bends, to, finally, 3D paths, modes of the same L and m indices, but represented in different mathematical bases are not, somewhat counterintuitively, identical.

Considering all these perturbations, OAM modes of sufficiently high $|L|$ are the most stable eigenmodes of a circularly symmetric optical fiber. A few important clarifications are in order: this stability is observable only once a fiber is designed such that n_{eff} splittings between pertinent non-degenerate modes is maximized, and this analysis ignores very long (>> km) length propagation, where higher order effects of bends and twists may play a role. In such cases, one would expect modes of any class to mix, although the fundamental nature of the effects described here suggest that even in conditions where all modes mix, the circularly polarized OAM modes will likely be more robust compared to others. In addition, the OAM eigenbasis yields a stable platform in which to exploit path-memory effects arising from geometric transformations (Pancharatnam-Berry phases), which while studied extensively in free space, may now lead to new opportunities for wavelength-agnostic or wavelength-insensitive phase control with fibers. We expect that these findings will help inform the optimal modal basis to use in the variety of applications that envisage using higher order modes of optical fibers.

Chapter 5

5. Scaling OAM Mode Count in Fibers

As demonstrated in the preceding chapter, the OAM bases is fundamentally the most stable eigenbasis in fibers. In addition, by enhancing the SOI, one can lift the four-fold degeneracy of a certain $|L|$, which results in a large amount of spatially efficient stable modes for unmixed SDM. This provides great advantages in using OAM mode for SDM.

Since the first generation of OAM fiber in 2011 (Bozinovic et al., 2013), there has been significant progress in scaling the OAM mode count, which goes up to 12 over a km fiber (Gregg et al., 2016). This benchmark is the Generation-4 OAM fiber, the one used for illustrating the properties of OAM mode in Chapters 2 & 3. Even though it achieves the maximum number of unmixed modes in multimode fiber, its channel count and crosstalk are not comparable with the MCF technology (Sasaki et al., 2017). The lowest crosstalk (determined by intra-$|L|$ coupling) is fundamentally limited by the index contrast achieved in fiber manufacture. However, channel count has a more significant effect. As the capacity scales linearly with the channel count while logarithmically with overall SNR (Eq. 1.2), we may still benefit from scaling the OAM mode count, especially for device-length applications. Therefore, in this chapter, we aim to investigate the scalability of OAM modes conventionally bound in a fiber.

As we have discussed in Chapter 1 & 4, mode coupling is the primary concern in a multimode fiber. There are two main causes of mode coupling for desired m=1 OAM modes: intra-$|L|$ mode coupling among desired m=1 mode and accidental degeneracy with

high-m modes. In the following sections, we will describe our efforts to address these concerns by sculpting the refractive index profile of the fiber. We will also show the characteristic of the resultant ring-core fiber and discuss the challenges of utilizing this approach for mode count scaling.

5.1. Fiber Design

5.1.1 Mitigation of Intra-|L| Coupling

As described in the Chapter 4, the intra-L coupling can be mitigated by increasing the Δn_{eff} between SOa and SOaa modes. We have also concluded that the Δn_{eff} criterion is around 5×10^{-5} regarding bend resistance. Such Δn_{eff} is associated with -10dB/km crosstalk in the previous benchmark Gen4 fiber over ~1km, thus accounting for various perturbations. Hence, we tentatively set it as the criteria.

Now the question is how many modes satisfy this criterion. As demonstrated in Chapter 2, the intra-|L| Δn_{eff} scales with L but the maximum Δn_{eff} becomes smaller for larger fiber with the same index contrast. Figure 5.1 is a re-plot of Fig. 2.6 with respect to the relative topological charge L-L_c, where L_c is the topological charge last bound mode, guided conventionally by TIR, before cutoff. Note that the index contrast is set as 0.035, which is the same as the benchmark Gen4 fiber. The high refractive index is realized by doping Germanium (Ge) into silica and thus is fundamentally limited by the amount of Ge that can be doped.

As shown in Fig. 5.1, while the maximum value of Δn_{eff} (for L=L_c) decreases with the core diameter, the Δn_{eff} at the lower-(L-L_c) end rises for larger fibers, resulting in a

larger number of modes exceeding the 5×10^{-5} threshold. The mode counts saturated at $5\times4=20$ modes. Among all the fiber reaching such mode count, the fiber with a diameter of 30-μm is optimal for it also has large Δn_{eff} at $L=L_c$.

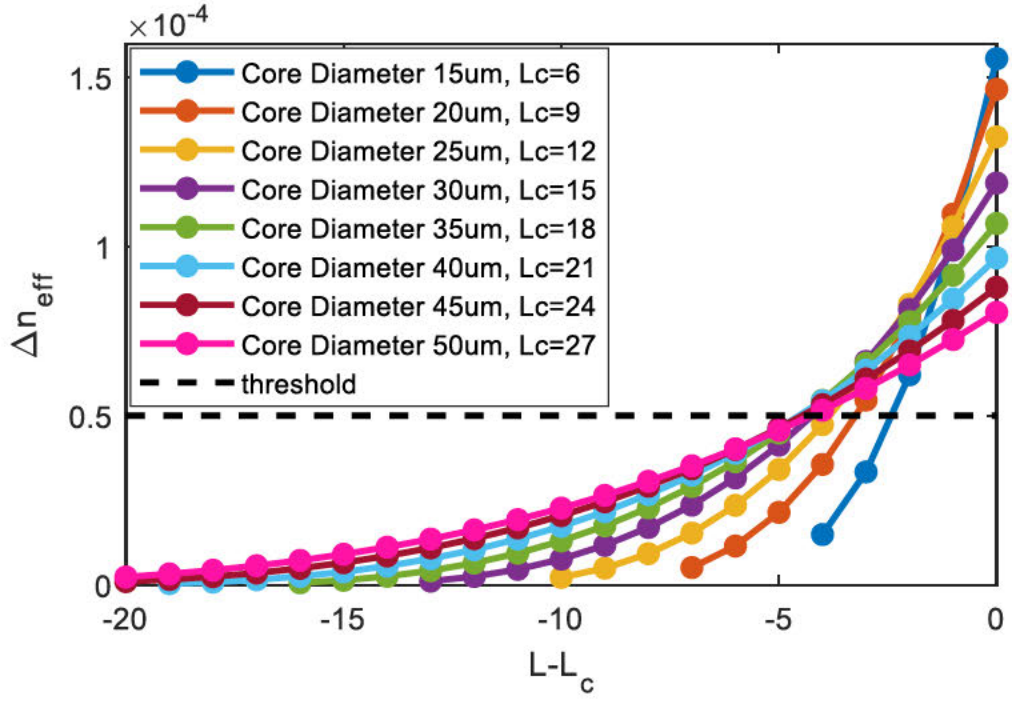

Figure 5.1: Intra-$|L|$ Δn_{eff} versus $(L\text{-}L_c)$ for step-index fibers with various core diameters.

Figure 5.2 shows the index profile and intensity distribution of all the modes. As all the high-$|L|$ modes with $\Delta n_{eff}>5\times10^{-5}$ are situated close to the core-cladding interface, such high mode count can also be achieved in a ring-core fiber shown in the following section.

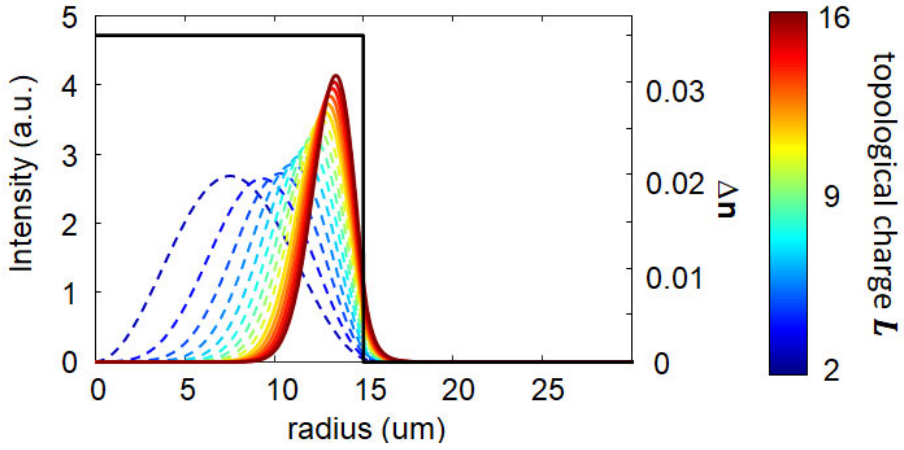

Figure 5.2: Index profile and modal intensity distribution of the design fiber with optimal core diameter.

5.1.2 Avoidance of Accidental Degeneracy

Another problem is the accidental degeneracy of the high-m modes. Such modal degeneracies are the primary reason behind speckle patterns resulting from multimode fibers, and hence loss of signal fidelity, no matter how well the input mode launch is optimized. This is also one of the main reasons behind the current lack of progress in scaling optical fiber mode counts using conventional TIR-based bound modes. Strictly speaking, such accidental degeneracy only occurs at a specific wavelength where the n_{eff} of the m=1 mode and high-m mode cross. However, as shown in Chapter 4, the wavelengths at which such mode coupling can be significant can be up to $\pm$40nm away from the wavelength of modal degeneracy, even in a 1m fiber, as the n_{eff} difference between the modes needs to be large enough to reduce the coupling. Given the much smaller bandwidth (35nm) of the conventional C-band (1530nm–1565nm), it is critical to move the n_{eff} crossing point much further away otherwise we lose the 4 channels (of the same $|L|$) provided by the desired m=1 modes. Based on that 80-nm coupling bandwidth,

the n_{eff} crossing wavelength needs to be at least 40nm away from the C-band. Considering diameter fluctuations and manufacture inaccuracies in longer fibers, it is advisable to design the crossing wavelength to be much larger than 40nm than this 40-nm span (e.g., >110nm in Gen4 fiber).

This accidental degeneracy with undesired high-m modes is much more detrimental for SDM applications than intra-$|L|$ mode coupling. The aforementioned engineering of the intra-$|L|$ Δn_{eff} was driven by the intention of avoiding high-order MIMO. Also, the Δn_{eff} criterion can be loosened to have more available modes in certain circumstances where fibers experience weaker perturbations or lower mode purity is allowed. As the last resort, the intra-$|L|$ mode coupling can be disentangled by 4x4 MIMO (Amin et al., 2011) as they are all the desired channels. However, the coupling to the undesired high-m mode results in irrevocable loss of information. Also, such mode coupling is wavelength dependent which makes the WDM even more incompatible.

This high-m coupling is the main culprit for the mode mixing inside conventional step index fiber. Thus, it is critical to restrict the number of high-m modes that can couple with the desired m=1 modes. This can be achieved by making the guiding core into ring shape. In other words, it can reduce the number of modes in the radial direction. One radical solution to the high-m coupling issue is making the ring core super thin such that it only supports m=1 modes. However, in such strong guidance regimes, the eigenmodes become the peculiar spin-orbit-coupled modes (Gregg et al., 2019) that are very complicated to excite and characterize. Also, such strong confinement may also induce high loss due to strong interface scattering. Finally, as discovered, this regime of fiber design may make

the modes susceptible to coupling between modes separated by ΔL=2. This increases the problem of managing mode spacings while increasing mode count. Therefore, we tune the ring thickness such that *m*=3 modes are cutoff in the C-band while *m*=2 modes are still guided so the weakly guided approximation with SOI corrections is still valid. Furthermore, we design the fibers such that only the *m*=2 modes, besides the desired m=1 modes, reside in the fiber in the spectral range occupied by the C-band. The ring radius and thickness are carefully tuned to move wavelength of accidental degeneracy away from the C-band.

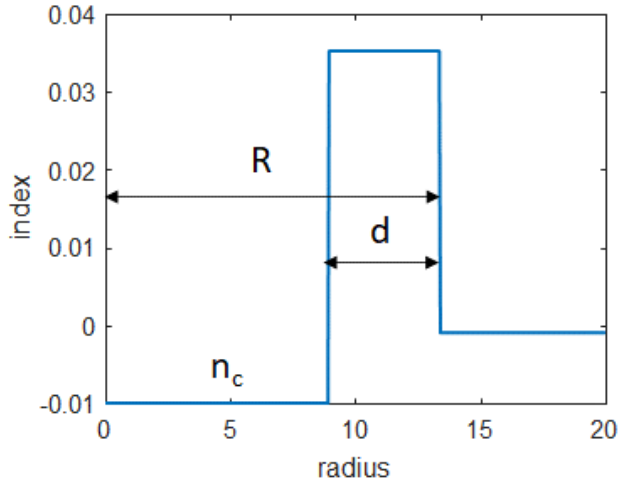

Figure 5.3: Schematic of the refractive index profile of the designed ring-core fiber.

Figure 5.3 shows the schematic index profile of the designed ring-core fiber. The high-index ring region is doped with Ge and the low-index center region is doped with Fluorine. Apart from sweeping the ring radius and thickness, the Fluorine-doped index can also be tuned from 0 to -0.005, which also moves the wavelength of the accidental degeneracy a bit. The critical metric is $\Delta\lambda_x$ defined as the wavelength separation between the crossing point of the *m*=1 and *m*=2 modes on either spectral range outside the C-band. Note that there can be multiple $\Delta\lambda_x$'s for all the desired *m*=1 modes, and so the overall

avoidance of the accidental degeneracy is evaluated by the minimum of them – $\Delta\lambda_{x,min}$.

The $\Delta\lambda_{x,min}$ of all the fibers are shown in the Fig 4.4. Note that the sweep was initially on the inner radius of the ring-core, which results in the blank region at both sides when plotted in terms of the outer radius. The $\Delta\lambda_{x,min}$ is assigned zero for the cases where (a) there is n_{eff} crossing between m=1 and m=2 mode or (b) m=3 modes is not cutoff in the C-band. The max $\Delta\lambda_{x,min}$ is only ~80nm (good for 1m fiber but not enough for 1km according to the phenomenological metrics for accidental degeneracy developed for Gen4 fiber; see Sec. 4.11). Moreover, this value was found to be very sensitive to parameter (core index, waveguide dimensional) changes.

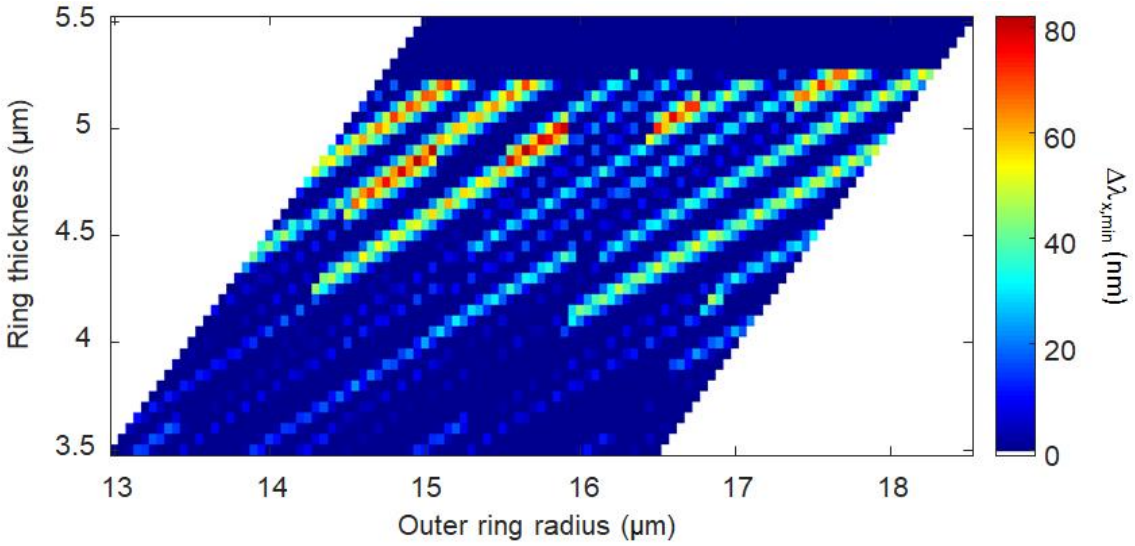

Figure 5.4: $\Delta\lambda_{x,min}$ of ring-core fibers with various combinations of outer ring radius and ring thickness. $\Delta\lambda_{x,min}$ is assigned to zero for the following cases (i) there is n_{eff} degeneracy between *m*=1 and *m*=2 modes in the C-band; or (ii) *m*=3 modes are not cutoff in the C-band.

Note that the inner interface of the ring core can also make a difference to the Δn_{eff}. According Eq. 2.28, the Δn_{eff} is dependent on the integral of the whole modal field profile

and index gradient profile. In the step index fiber, only the outer interface makes a contribution. However, given the inverse gradient of the inner interface of the ring core, its contribution to the Δn_{eff} actually has an opposite sign as the that from the outer interface. Hence, the overall Δn_{eff} in the ring-core fiber is smaller than that in a step-index with identical outer diameter. Actually, given the lack of the opposite slope of the ring core at the inner ring interface, step index fiber determines the highest Δn_{eff}. As a results, the maximum number $|L|$'s free from intra-L coupling ($\Delta n_{eff} > 5 \times 10^{-5}$) decreases to 4 for all the aforementioned ring-core fibers, rather than 5 in the initial step-index design.

5.1.3 Other Criteria

The aforementioned consideration of the $\Delta\lambda_{x,min}$ doesn't take the intra-L Δn_{eff} into account. Actually, some combination of the outer ring diameter and ring thickness can result in relatively small Δn_{eff}, resulting in the maximum number $|L|$'s free from intra-L coupling ($\Delta n_{eff} > 5 \times 10^{-5}$) even smaller than 4. Figure 5.5 shows the $\Delta\lambda_{x,min}$ of all the swept fiber with 4 $|L|$'s (or 16 unmixed modes) thus the range of choices is much narrower.

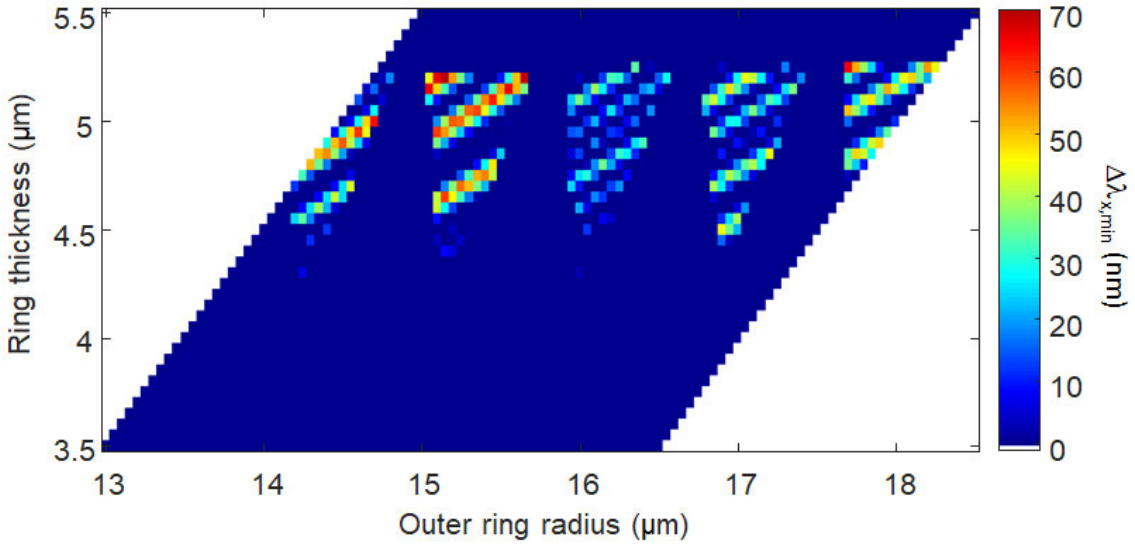

Figure 5.5: $\Delta\lambda_{x,min}$ of various ring-core fibers with various combinations of outer ring radius and ring thickness. $\Delta\lambda_{x,min}$ is assigned to zero for following cases (i) there is n_{eff} degeneracy between m=1 and m=2 modes in the C-band; (ii) m=3 modes are not cutoff in the C-band; (iii) the number of good $|L|$'s ($\Delta n_{eff} > 5 \times 10^{-5}$) is less than 4.

Another criterion is how far the n_{eff} of the highest-L bound mode is away from the cladding index (silica), which theoretically has effect on its loss especially in the presence of bend perturbations. Figure 5.6 shows the $\Delta n_{L,si}$ defined as the difference between the n_{eff} of the highest-L modes and the refractive index of silica at the longer end of C-band (1565nm) when such n_{eff} difference is the smallest.

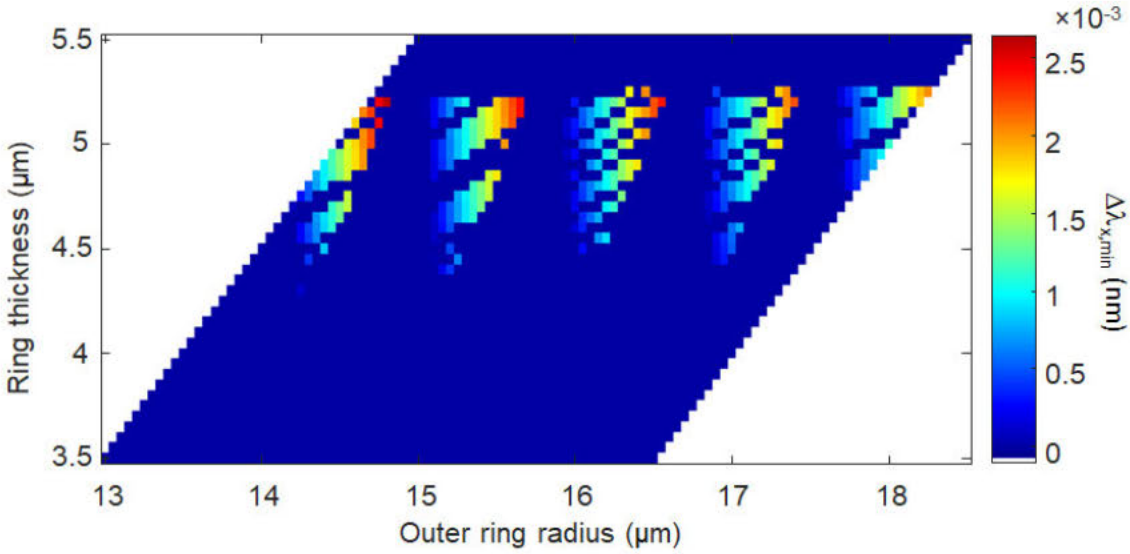

Figure 5.6: $\Delta n_{L,\mathrm{si}}$ of various ring-core fibers with various combinations of outer ring radius and ring thickness. $\Delta n_{L,\mathrm{si}}$ is assigned to zero for following cases (i) there is n_{eff} degeneracy between m=1 and m=2 modes in the C-band; (ii) m=3 modes are not cutoff in the C-band; (iii) the number of good $|L|$'s ($\Delta n_{eff} > 5 \times 10^{-5}$) is less than 4.

5.1.4 Final Design

In search for an ideal fiber with max $\Delta\lambda_{\mathrm{x,min}}$ and $\Delta n_{L,\mathrm{Si}}$, we end up getting the final design with the parameters summarized in Table 5.1

Table 5.1: Summary of the fiber parameter of the final design of ring-core fiber

R (um)	d (um)	n_c	n_{max}	L	L_c	$\Delta n_{\mathrm{L,Si}}$	$\Delta\lambda_{\mathrm{x,min}}$	high-m coupling
15.65	**5.20**	**-0.005**	**0.035**	**12-15**	**15**	**0.0024**	**-69nm**	**$SOa_{15,1}$× $SOaa_{10,2}$**

Figure 5.7 shows the index profile of the designed fiber and the intensity distribution of the modes. For L=12-15 modes with sufficient large Δn_{eff}, the intensity profiles locate at the outer core/clad interface, such as those in the step-index fiber (Fig.

5.2). According to Eq. 28, for large n_{eff} splitting to occur, the field's intensity at the outer interface ought to be sufficiently high.

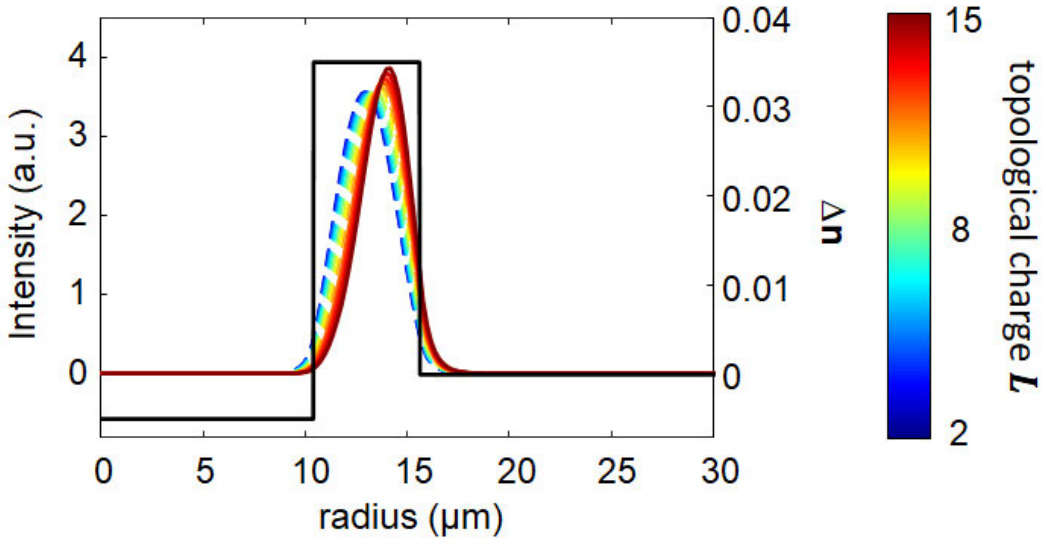

Figure 5.7: Index profile of the designed fiber and the intensity distribution of all the modes. The available modes with *L*=12-15 are represented with solid curves while the others are shown with dashed curves.

5.2. Generation-5 Ring-Core Fiber

The preform from which the fiber is drawn is fabricated using modified chemical vapor deposition (MCVD) by our collaborators at OFS Fitel ApS. When scaled appropriately (by choice of fiber draw conditions), it matched the design as closely as possible, as shown in Fig. 5.8. The draw down ratio was tuned (as a final adjustment) to optimize the crossing wavelength as $\Delta\lambda_{x,min}$ = 63nm, which is close to that of the design. However, the drawn fiber turned out to be very different. Overall, the refractive index is higher due to drawing tension (Yablon et al., 2004), such that the Δn become 0.04 rather than 0.035. The index profile was measured using an interferometry-based fiber profiler (IFA-100 Interfiber Analysis) at 633 nm. This fiber is referred to as Gen5A3.

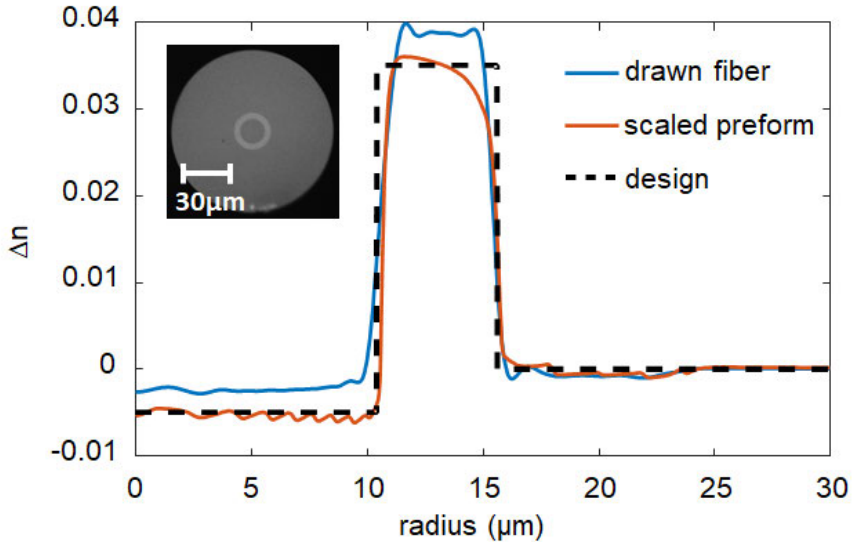

Figure 5.8: Refractive index profile of the design fiber, the final preform scaled to optimal size and the final drawn fiber. Inset: the cross-section image of the drawn fiber.

The fact that the drawn profile is distinct from that designed, changes the n_{eff} distribution dramatically. As shown in the n_{eff} distribution in Fig. 5.9, the L_c becomes L=16 (as opposed to L_c=15, as was the case for the designed fiber). The two panels are the output images of the corresponding modes over a 1.1km and 100m using a ECL source (setup in Fig. 3.1). As is evident, the accidental degeneracy become very different from the design. As shown in the output images over both the 1.1km fiber and 100m, L=16 and L=12 have high-m couplings. The aforementioned fine tuning of index profile turns out to be pointless given such a big mismatch between the designed and drawn fiber. Even the modal output images of the L=14-15 modes out of the 1.1km fiber show a slight defect on the ring image, although they are much clearer of a 100m-long fiber. This is likely due to OD fluctuations. Interestingly, L=17 and L=18 also show non-negligible transmission out of the 100-m-long fiber, though they are too lossy for propagating over a 1.1km-long fiber. We will discuss this unexpected behavior, of the observation of modes that should have been cutoff, based

on waveguide calculations, in the next chapter. Also, another problem is the mismatching of the wavelength of accidental degeneracy between simulation and experiment. It's likely due to measurement error of the index profiler (resolution ~0.5um) or the lack of accurate knowledge of the Sellmeier coefficients of silica, which causes errors in determining the index profile at the wavelength of operation (~1550 nm) from a measurement conducted at the wavelength of operation of the index profiles (633 nm).

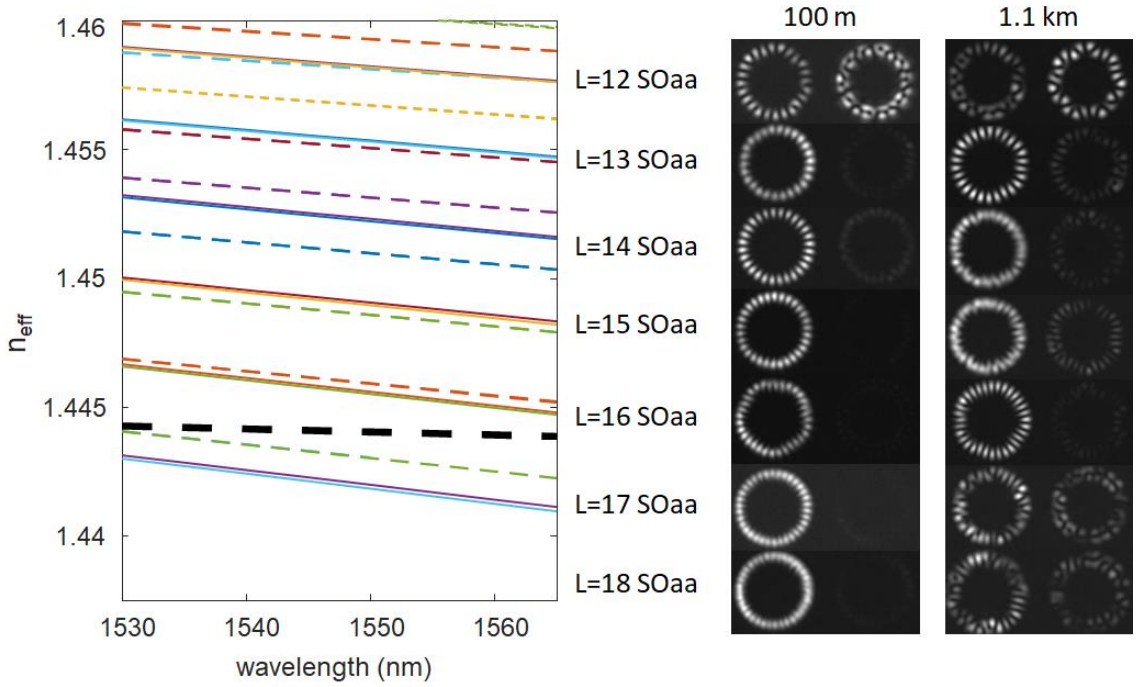

Figure 5.9: Left panel: n_{eff} distribution of select modes in Gen5A3 ring-core fiber. Right panel: modal images over a 100-m and 1.1-km Gen5A3 fiber using a 1550-nm ECL source.

The range of high-m coupling for L=16, m=1 is found out by recording output images while sweeping the wavelength using a ~1m Gen5A3 fiber. As shown in Fig. 5.10, such wavelength range is ~10nm out of a 1m fiber. The ΔL=5 content from Ring Method can be used to evaluate the relative content of the L=11, m=2 mode. Note that the center degenerate wavelength varies from sections to section due to the variation of the core

diameter all along the fiber, resulting in a much wider high-m coupling range of 120 nm (1440-1560 nm) over the 1.1km fiber. The core-diameter variation inevitably comes from the insufficient control of the fiber size when drawing the fiber with relatively low speed. Nevertheless, such solid ring-core fiber greatly ease the fiber manufacture compared with the one with air hole which also introduce strong perturbation, thus the such high-m coupling wavelength range in Gen5A3 is much narrower that that encountered in air core fibers (Sec. 4.1.1).

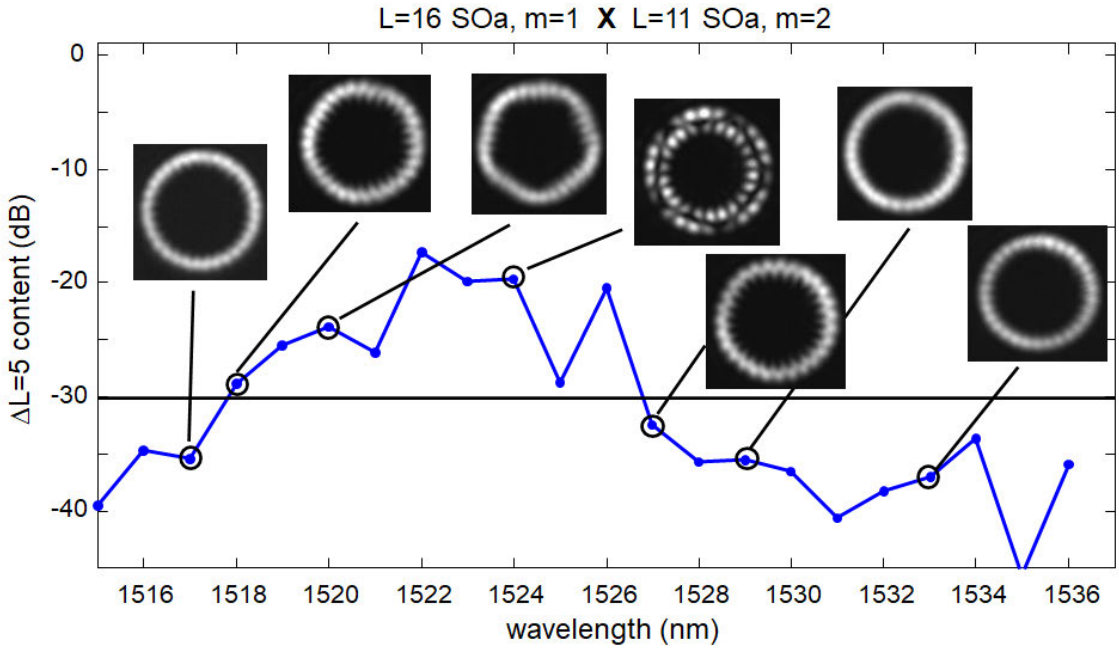

Figure 5.10: Accidental degeneracy between L=16, m=1 and L=11, m=2 in the Gen5A3 ring-core fiber. The inset images are the outputs of the 1-m fiber when a L=16, m=1 mode is launched at the input using a 1550-nm ECL.

Figure. 5.11 shows the intra-|L| mode coupling over the 100-m and 1.1km measured by time of flight (ToF) (Sec. 3.3) using a New Focus 1444-50 InGaAs fast detector with ~20ps rise time. The Δn_{eff} for each mode is shown on the right axis. Excluding the outlier of L=13, the intra-|L| couplings over 1.1km is around ~-10dB. Such intra-|L| coupling is ~-

20 dB over the 100-m. The intra-|L| coupling is slightly higher than that of Gen4 fiber (-8.5 dB to −17dB) where the modes have similar Δn_{eff}.

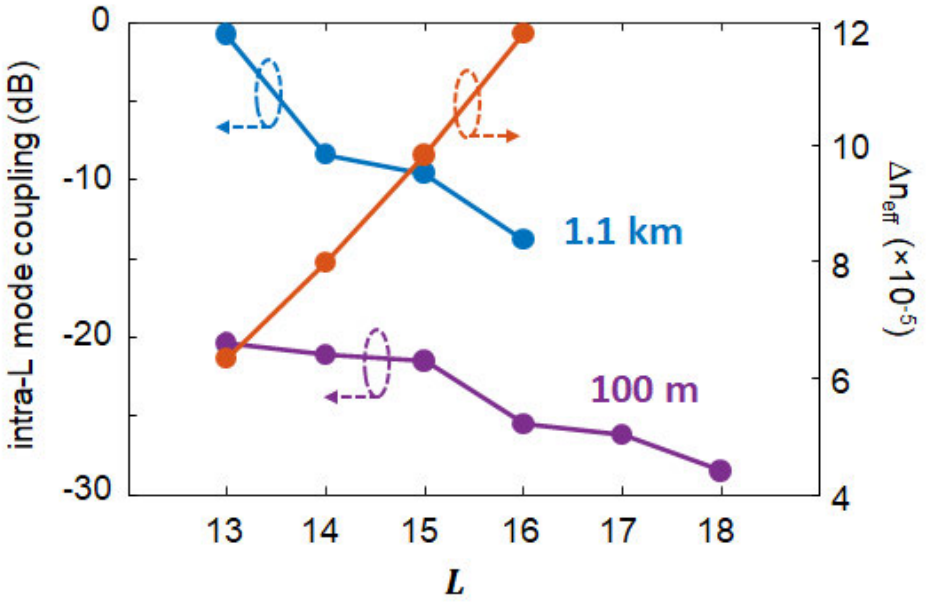

Figure 5.11: Intra-|L| mode coupling and Δn_{eff} in the Gen5A3 ring-core fiber

Another benefit we gain from the silica center is the absence of water absorption. The Figure 5.12 is the transmission loss in a spectrum of 1300-1600nm using a supercontinuum source. The high transmission loss of the air-hole ring-core Gen4 fiber suggests that there is likely water inside the air hole given the resonance wavelength of -OH bond around 1400 nm.

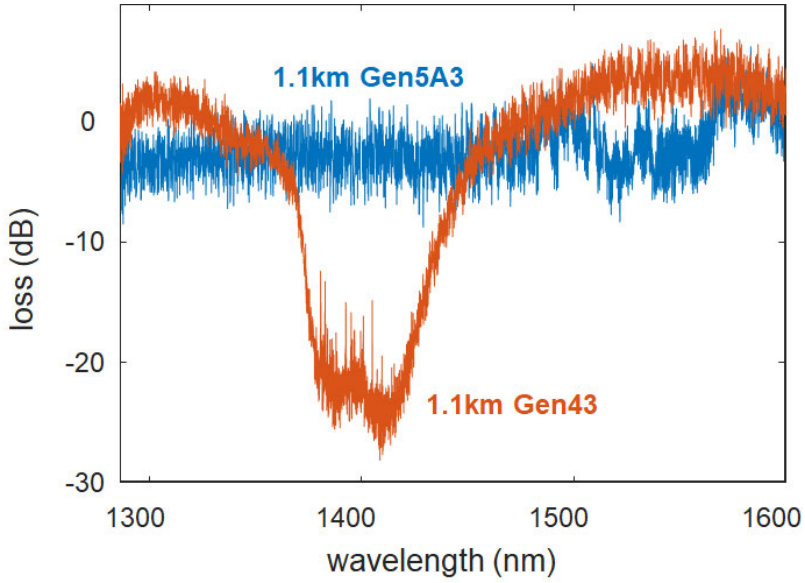

Figure 5.12: Transmission spectrum of the Gen5 and Gen4 fibers with ~1.1km long.

Figure 5.13a shows the cutback loss of L=13-16 SOa (SOaa modes have similar loss) measured using the 1.1km Gen5A3 fiber. L=16 SOa has sightly higher loss than the others due to coupling with high-m modes. Overall, the loss is slightly higher that of Gen4 fiber (~1.0 dB/km) despite the fact that this fiber doesn't suffer from excess loss due to water absorption, mentioned above. The aforementioned cutoff modes (L>=17) are too lossy to survive over a 1.1km, thus they are measured using a 100-m-long fiber, as shown in Fig. 5.13b. Even though their losses are indeed much higher compared with that of L=14-16, they are still much lower than what we expect of cutoff modes. As mentioned earlier, this effect will be discussed in the next chapter.

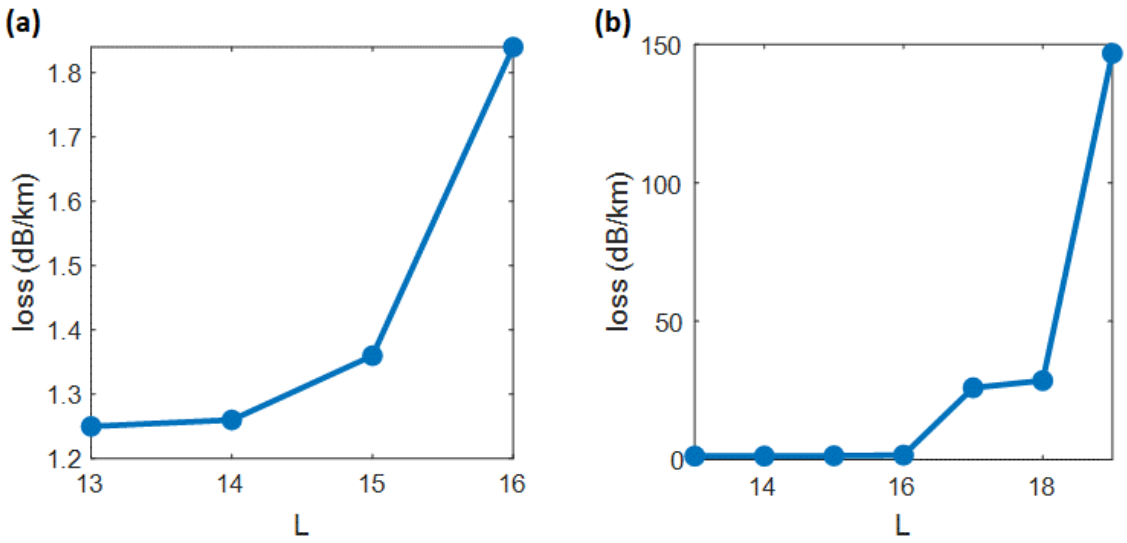

Figure 5.13: Cutback loss versus L in measured in (a) 1.1-km and (b) 100-m Gen5A3 fiber.

In summary, the number of good modes free from accidental degeneracy is around 3×4=12 over a 1-km Gen5A3 fiber. Its mode count is similar to that of the Gen4 fiber while the intra-$|L|$ coupling and loss in Gen5A3 are slightly worse. The improvement includes narrower high-m coupling bandwidth and absence of excess loss due to water absorption, which are likely inherent benefits of a solid ring-core, as opposed to ring-core, design.

The loss in a high-index fiber primarily comes from the core-clad interfacial scattering which can be alleviated by increasing the draw tension (Line, 1984, Wandel, 2005). Therefore, we redrew the preform using higher tension (300g) in contrast to the standard draw tension (100g) used for Gen5A3 fiber. Equivalently the draw stresses are 20.7 kg/mm^2 and 6.9 kg/mm^2 for the two fibers, respectively. The high-tension/stress fiber is referred to Gen5B3. The comparison of their refractive index profile is shown in Fig. 4.13a. As is evident, the higher drawing tension raises up the refractive index further more. Such a change of the index profile barely changes the Δn_{eff} of the modes.

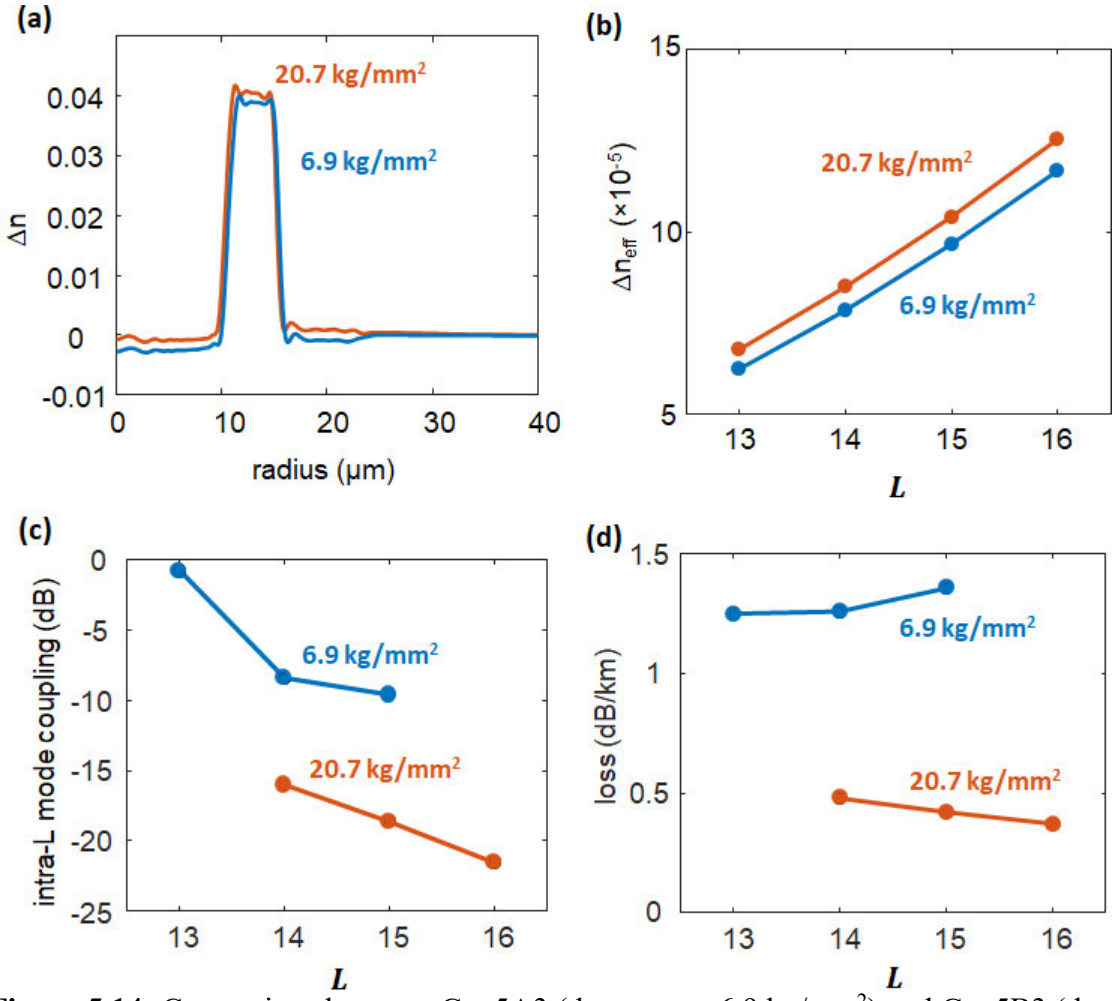

Figure 5.14: Comparison between Gen5A3 (draw stress 6.9 kg/mm^2) and Gen5B3 (draw stress 20.7 kg/mm^2) in terms of (a) refractive index profile and (b) intra-$|L|$ Δn_{eff}; (c) measured intra-$|L|$ mode coupling and (d) measured cutback loss at 1550nm.

As shown in Fig. 4.13(c)&(d), both the intra-$|L|$ coupling and loss in the high-tension Gen5B3 are much better than those of Gen5A. Increasing the stress from 6.9 kg/mm^2 to 20.7 kg/mm^2 decreases the loss from ~1.3 dB/km to ~0.4 dB/km (Fig. 5.14d). This is similar to the loss achieved in commercial dispersion compensating fiber (DCF) with a similar index contrast (Akasaka et al., 1996). Note that modes with accidental degeneracy are not plotted in these figures. The accidental degeneracy of L=16 in Gen5B3 is away from 1550nm while L=13 becomes accidental degenerate with a high-m mode at

1550nm. In contrast with the intra-|L| n_{eff} splitting, the accidental degeneracy is very sensitive to slight changes of refractive index profile, as we also found during the fiber design process.

5.3. Summary and Discussion

We have attempted to further increase the OAM mode count by sculpting the refractive index profile (primarily the ring core radius and thickness) to mitigate the two main issues one encounters while attempting to scale unmixed mode counts in optical fibers – intra-|L| couplings and high-m couplings. However, both of the two induce fundamental constraints in scaling the mode count even in an ideal fiber. Using the index contrast of the previous benchmark Gen4 fiber with 12 unmixed modes, we ended up designing an optimized ring-core fiber with 16 unmixed modes which are barely free from accidental degeneracy with undesired high-m modes.

However, the drawn fiber still experiences high-m mode coupling for one |L| given that its index profile is inevitably very different from the design and also the accidental degeneracy is very sensitive the fiber structure as we learned from the design process. As a result, the mode count remains the same despite of so many efforts. By careful calibration and more trials, we may be able to fabricate a ring-core fiber without accidental degeneracy for all the desired 16 modes in ~1km fiber, but admittedly it is not a great improvement compared with Gen4 benchmark. Simply put, there is fundamental bottleneck for scaling the number unmixed OAM bound modes.

Nonetheless, we found that high drawing stress and reductions in intra-L mode coupling from these designs helped decrease transmission loss to record value of ~0.4

dB/km. Also, the solid fiber provides us a few benefits over the previous air-hole designs for (a) eliminating excess loss problems arising from water absorption; (b) easing the fiber manufacturing process, potentially decreasing the cost of a future fiber deployment using these designs; and (c) obtaining smaller spectral ranges over which accidental degeneracies exist, likely due less fiber diameter fluctuations. Interestingly, in our experiments, we found that there are some cutoff modes that survive over a ~100m-long fiber even though their losses are too high over a ~1km-long fiber. We will unveil the fundamental mechanism behind the observation of modes that should have, otherwise, been completely attenuated, and point out a new direction for scaling mode counts in the next chapter.

Chapter 6

6. Topologically Confined Modes

6.1. Light Guidance Beyond Cutoff

In the previous chapter, it was concluded that there exists a limitation to scaling the OAM mode count. However, the analysis only considered the modes that were not cut off (i.e., bound modes). The assumption that modes do not survive beyond cutoff per TIR was considered common sense (Sec. 2.1). The possibility of using these cutoff modes for spatial channels was not previously considered until we experimentally observed them in the laboratory. Referring to the previously mentioned Gen5 ring-core fiber, a few additional modes existed beyond the cutoff. Despite the fact that these modes had comparatively higher loss and could not survive km-scale transmission, their losses were significantly lower than expected compared to other conventionally known cutoff modes (e.g., LP_{11} in SMF28). The guidance of these cutoff modes is a fundamental effect enabled by their high OAM.

The concept of OAM-induced confinement is schematically depicted in Fig. 6.1. An exemplary fiber comprises a high-index core n_{co}, surrounded by a low-index cladding n_{cl}. Three representative OAM modes have different topological charges but identical effective index below the cladding index ($n_{eff}<n_{cl}$). Due to violation of TIR, the low-$|L|$ mode radiates away from the fiber (Sec. 2.1), resulting in a high confinement loss. This confinement loss is exactly zero for conventional bound modes and it is distinct from losses caused by material absorption and scattering effects (detailed in Sec. 6.3 and 6.6). The

confinement loss of unbound, radiative modes decreases as the mode's topological charge increases. The confinement loss of the high-$|L|$ modes become negligible, and therefore they behave as bound modes. In other words, light's topological charge enables confinement for itself. Thus, we refer to this phenomenon as topological confinement, and the corresponding modes as topologically confined modes (TCMs).

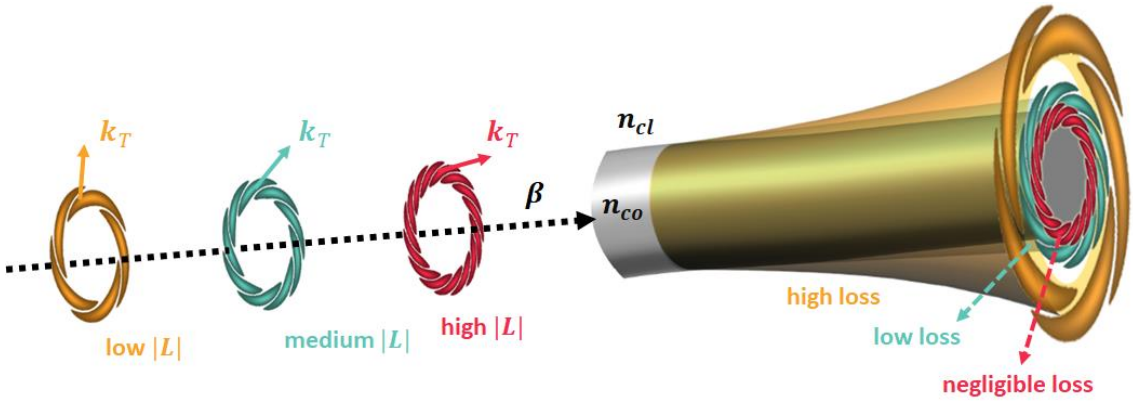

Figure 6.1: Light guidance beyond cutoff enabled by high OAM. The propagation of three cutoff OAM modes with different L's but identical n_{eff} in an exemplary step index fiber. Select OAM modes in this fiber are illustrated as spiral patterns for visual clarity, with number of spiral arms equal to $|L|$. Confinement loss of these modes decreases as $|L|$ increases, as their transverse wave vectors k_T become progressively more azimuthally oriented.

The OAM-enabled topological confinement can be intuitively understood by analyzing the transverse wavevector k_T. As shown in Fig. 6.1, the transverse wavevector k_T becomes increasingly oriented in the azimuthal rather than the radial direction as $|L|$ increases. Heuristically, these higher-$|L|$ modes tend to resonate azimuthally (thus being confined) as opposed to "escaping" radially. More specifically, high-$|L|$ modes correspond to skewed rays as opposed to meridian rays (detailed in Sec. 6.6). These tunneling leaky rays (Snyder & Love, 1984) satisfy TIR partially and the loss decreases as the ray align more closely with the tangent of the curved surface. In the wave picture, even though the

$|L|$-dependent loss of the leaky modes can be solved using Maxwell equations (Snyder & Love, 1984), the physics intuition for the OAM-dependent loss is unclear. Notably, this effect also manifests in a larger proportion of modal power in the core at the cutoff for high-$|L|$ modes (Gloge, 1971).

6.2. Centrifugal Barrier

The concept of centrifugal barrier can be used to explain TCMs validly, while also offering intuitive physics insight for the OAM-dependent confinement loss. The scalar eigenmode equation (Eq. 2.13) can be rewritten as

$$\frac{d^2F(r)}{dr^2}+\frac{1}{r}\frac{dF(r)}{dr}+\left[k_0^2\left(n^2(r)-\frac{L^2}{k_0^2r^2}\right)-\beta^2\right]F(r)=0 \tag{6.1}$$

By absorbing the OAM term, one can rewrite the refractive index term as

$$n_{OAM}^2(r)=n^2(r)-\frac{L^2}{k_0^2r^2} \tag{6.2}$$

where the second term with r^{-2} dependence induces an index trench at the core-cladding interface which deepens as $|L|$ increases. This treatment of the refractive index is analogous to how the effective refractive index is obtained (Sec. 2.1). The effective index n_{eff} absorbs the linear momentum (corresponding to β) while the topologically modified index n_{OAM} absorbs the orbital angular momentum. Under this representation, a mode with non-zero OAM order L in a fiber with index profile $n\,(r)$ is equivalently considered as a mode with zero OAM order L in a fiber with index profile $n_{\mathrm{OAM}}(r)$.

Figure 6.2 schematically shows the topologically modified profile $n_{\mathrm{OAM}}(r)$ experienced by the three modes with non-zero L's depicted in Fig. 6.1. Their n_{eff} is below

n_{cl}, so they are cut off according to TIR. The OAM-induced index trench for low-$|L|$ modes is relatively shallow and has little effect on the radiation of cutoff modes. L=0 represents the most extreme case for low $|L|$, in which the topologically modified profile $n_{\mathrm{OAM}}(r)$ is identical to the real index profile $n(r)$. A mode with a sufficiently high $|L|$ induces a deep index trench below the n_{eff}, thereby satisfying TIR at the core-cladding interface. Given that the topologically modified index returns to n_{cl} at large radii, there can be a certain amount of the loss due to the tunneling effect. But this confinement loss becomes progressively smaller as the trench depth increases with higher $|L|$. The OAM-induced index trenches acts as centrifugal barriers that prevent light from leaking out, therefore topologically confining the light. Although the mode is no longer strictly bound by TIR (so it no longer experiences zero theoretical loss), its loss strongly depends on $|L|$. For a high-$|L|$ mode with sufficiently deep index trench, the confinement loss become negligible and this cutoff mode behaves like bound modes because of the centrifugal barrier light's OAM creates for itself. This topological confinement is thus distinct from conventional light guidance mechanism enabled by solely sculpting the refractive index profile of the fiber via TIR or photonic bandgap. A simple step-index fiber is used to illustrate the TCM principle but it can apply to any fiber with similar outer core boundary (for similar index contrasts) given that the intensity profiles of high-$|L|$ modes reside at the outer core boundary (Sec. 4.1; Sec. 6.5.1).

The fact that light is guided by the centrifugal barrier that light's OAM creates for itself justify the nomenclature "topological confinement". It only enables guidance beyond the conventional TIR cutoff, but also differs from other guidance mechanisms such as

photonic bandgap or anti-resonance. All these guiding mechanisms are based on the fiber's refractive index (that is, "physical confinement") rather than the topological property of light itself.

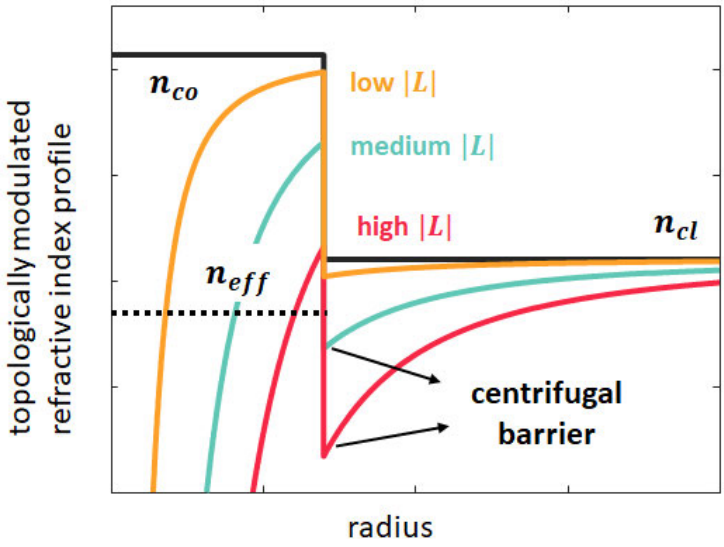

Figure 6.2: Topologically modulated refractive index profile for the three cutoff OAM modes shown in Fig. 6.1. Higher $|L|$ induces a deeper index trench, creating a "centrifugal barrier" that prevents the cutoff modes from leaking out.

This centrifugal barrier effect has been well-known for decades in nuclear physics (Blatt and Weisskopf, 1952). The OAM-induced centrifugal barrier prevents the particle from leaving the nucleus (Fig. 6.3). Therefore, high OAM increases the lifetime of a nucleus, manifested by the extended half-lives of proton radioactivity. This inspired our understanding of TCMs in regard to the centrifugal barrier (credit to Dr. Poul Kristensen).. By drawing an analogy between energy potential and the refractive index of fibers, we gain valuable insights into the behavior of TCMs.

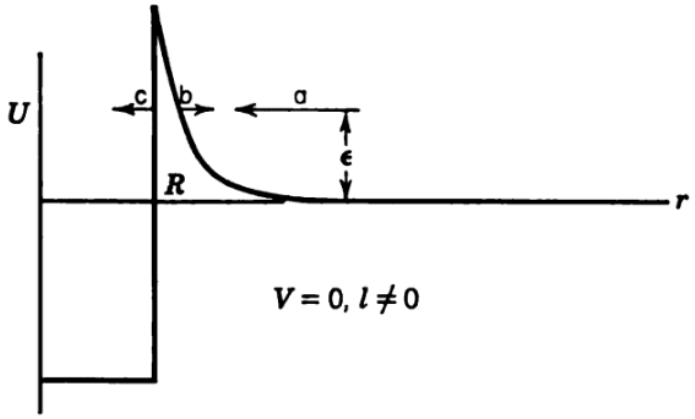

Figure 6.3: Potential barriers inside and outside the nucleus (Blatt and Weisskopf, 1952). R is the nucleus radius. The Coulomb potential is negligible (V=0). The potential inside the nucleus (governed by strong force) is approximately a constant.

Note that a system with short-range quantized potential is required for the angular momentum term to become dominant, leading to the counter-intuitive manifestation of the centrifugal barrier effect. In contrast, a continuous r^{-2}-dependent potential (e.g., gravitational or Coulomb potential) always dominates at the equilibrium point when interacting with angular momentum. In these systems (e.g., binary-star systems), the centrifugal barrier effectively keeps the two bodies apart. Actually, the short-range strong interaction dominates the central potential in a nucleus, while the Coulomb potential is negligible. Even though the Coulomb potential is known as continuous, the potential between the nucleus and electron becomes short-range in a short pulse regime, leading to the manifestation of the centrifugal barrier such that electrons with higher OAM needs higher ionization energy (Freeman et al., 1991). Similar short-range potential occurs in Feshbach molecules where the OAM-induced centrifugal barrier increases the metastability of high rotational states (Knoop et al., 2008), as shown in the schematic of Fig. 5.3.

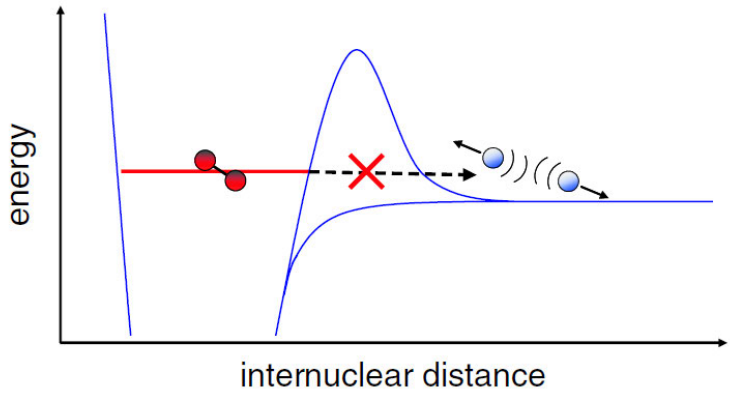

Figure 6.4: Illustration of a long-lived metastable Feshbach molecule in a high rotational state. A large centrifugal barrier prevents direct dissociation of the molecules (Knoop et al., 2008).

For light, centrifugal barriers provide intuitive insights into the long lifetimes of photons (i.e., high quality factor) of high-OAM states in large whispering gallery cavities (Chiasera et al., 2009). Note that this effect can also be attributed to lower bend loss (Bogaerts et al., 2011). Distinct from a cavity where the spectral and spatial modes are coupled, a fiber permits the presence of multiple states for a specific wavelength or OAM. Moreover, the propagation constant allows for the propagation of TCMs over long distances with low loss, thus significantly enlarging its range of applications.

6.3. Demonstration of TCMs

Due to OAM-induced centrifugal barrier, it was anticipated in the preceding section that the confinement loss of TCMs with identical n_{eff} decreases with increasing $|L|$. This is due to the deeper index trenches induced by higher $|L|$'s. However, at a particular wavelength, the n_{eff} also decreases with $|L|$ (Fig. 2.3) – that is, the n_{eff} of high-$|L|$ TCMs becomes farther away from the cutoff (n_{cl}). In this regard, the mode violates the TIR condition even more and is more likely to leak out. Whether the overall loss increases or decreases depends

on which index reduction is greater – the $n_{OAM}(r_{co})$ or the n_{eff} of high-$|L|$ TCMs. The latter case typically prevails, as evidenced by the higher losses for high-$|L|$ modes in Gen5A3 fiber at 1550nm (Fig. 5.12).

In order to demonstrate the OAM-dependent TCM effect, n_{eff} of each TCM (which is below n_{cl}) must be maintained at a similar level. This can only be achieved by measuring the loss each mode at a distinct wavelength. Regarding the material dispersion of silica, it is the relative n_{eff} *(*i.e., n_{eff}/n_{cl}*)* that should be held constant. Measuring the n_{eff} of a mode can be difficult and laborious. Alternatively, controlling relative n_{eff} in measurements can be achieved by comparing the measured wavelength λ_m with the cutoff wavelength λ_c of each mode. The cutoff wavelength λ_c (defined in Sec. 2.2) for a mode is calculated as the wavelength at which its effective index equals the refractive index of the cladding. By ignoring the dispersion difference between distinct modes within the range of λ_c and λ_m (validity shown below), it is reasonable to assume that n_{eff}/n_{cl} equals *to* λ_m/λ_c. In other words, n_{eff} is held at a similar level below n_{cl} by holding λ_m/λ_c constant for each mode.

We use the Gen5A3 ring-core fiber to demonstrate the OAM-dependent confinement loss of TCMs (detailed setup in Fig. 3.1). The modal loss was always measured at a wavelength λ_m such that $(\lambda_m-\lambda_c)/\lambda_c$=15.27% for each mode. For the modes tested, ranging from OAM L=19 to 42, λ_c ranges from 1363 nm to 675 nm, as show in Fig. 6.4. Measurement with the *L*=42 mode is conducted with ~100 m lengths of fiber using a ~780-nm ECL, those for the *L*=30, 31, 32 modes use ~25-m lengths with a ~1064-nm ECL,

and the L=19, 20, 21 modes are measured with ~10-m lengths of the same fiber using a ~1550-nm ECL. Different lengths are used to ensure measurement accuracy given that attenuation varies significantly with mode order. The mode purities analyzed via spatial interferometry (Sec. 3.2) is around 15 dB, no less than 13 dB. The high purity ensures that measuring power of one mode is not affected by the parasitic light in another. The attenuation of each mode is measured by cutback normalized for material loss (deduced by measuring cutback loss for the LP_{01} mode in this fiber).

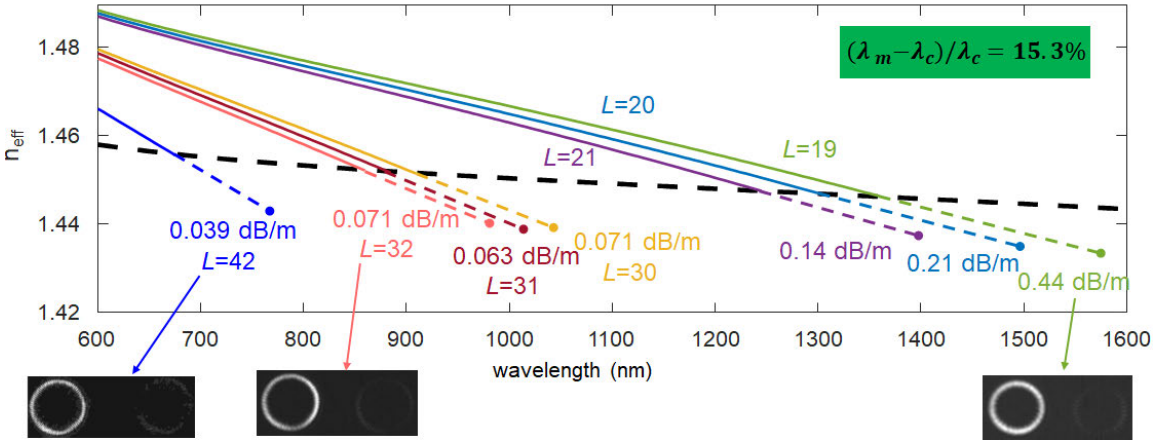

Figure 6.5: The n_{eff} distribution for the measured modes. The black dashed line is the refractive index of the silica cladding. Color solid lines indicate the mode are TIR-bound while the n_{eff} in the TCM regime is represented by color dashed lines. Each dashed n_{eff} line is ended by a color dot indicating the measured wavelength, which is 15.3% away from the cutoff wavelength of each mode. The measured loss of each mode at this wavelength is written below the corresponding n_{eff} and a few representative output mode images show clear ring shape indicating pure mode excitation.

The L-dependent loss is summarized as plotted in Fig. 6.5(a), showing that the measured loss decreases substantially with L, reaching 0.039 dB/m for L=42, even though it is 100 nm beyond the cutoff wavelength for this mode (Fig. 6.4). The overlaid dashed line is the simulated confinement loss from a scalar mode solver incorporating a standard

phase-matched layer (PML) model (Appendix A). Similar decreasing trend of L-dependent loss was ascertained by the simulated confinement loss, which matches well with the experimental ones for L~20 but becomes even lower for high-L modes. Same measurement was attempted on the more familiar LP_{11} mode in SMF-28, but the loss was too high to measure at 15% relative wavelength past its cutoff. In fact, the simulated confinement loss for the LP_{11} mode in SMF-28 at 15% relative wavelength past its cutoff is higher than 1000 dB/m. As is evident, losses of measured TCMs shown in Fig. 6.5(a) are orders of magnitude lower than what conventional wisdom posits for "cutoff" modes, validating the idea that centrifugal barriers greatly aid light transmission for modes that are supposed to be radiated away. The measured losses of TCMs shown in Fig. 6.5(a) are significantly lower than the conventional LP_{11} mode, indicating that centrifugal barriers effectively aid light transmission for radiated modes. The lower losses for higher $|L|$ modes promise the utilization of high order modes for low loss guidance.

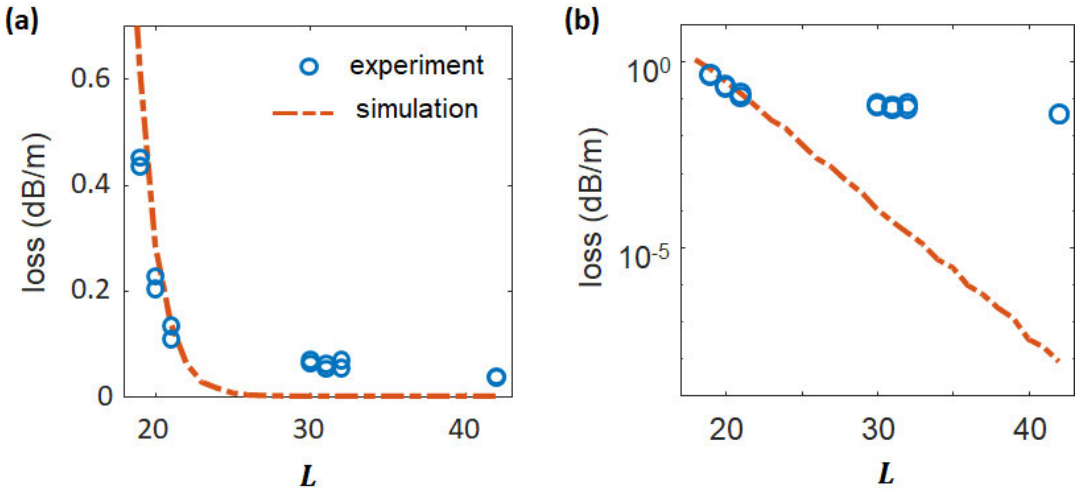

Figure 6.6: Experimental (open circles) and simulated (dashed curve) loss versus L in Gen6A3 ring-core fiber with ~30 μm ring diameter, at a wavelength 15% beyond the cutoff wavelength of each mode in (a) linear and (b) log scale.

Figure. 6.5(b) is the log-scale version of Fig. 6.5(a). While the simulated confinement loss and the measured loss match well for L~20 modes, their difference increases by orders of magnitude for high-L modes. In contrast to the slow decrease of measured loss, which is flattened at ~10^{-2} dB/m, the simulations predict exponentially decaying confinement loss down to ~10^{-10} dB/m for L = 42. This discrepancy suggests the presence of a noise floor in the measured loss, arising from absorption and scattering losses that become dominant when confinement loss is negligible. In telecom-grade single-mode fibers (SMF) where confinement loss is zero, the measured loss is minimized at ~10^{-4} dB/m around 1550nm. The noise floor (~10^{-2} dB/m) of this measure loss is much higher than that of the standard SMF due to unoptimized fiber manufacturing and shorter wavelength (detailed in Sec 6.6). Only L~20 modes were measured at the telecom wavelength ~1550nm, while higher-L modes were measured at shorter wavelengths (L~30 at ~1000nm and L=42 at 780nm, as shown in Fig. 6.4) where both absorption and scattering losses are much higher. Hence, any confinement loss below ~10^{-2} dB/m becomes impossible to measure. On the other hand, the simulation promises further decreasing the confinement loss to negligible by increase topological charge L.

6.4. Mode-Count Scalability

As discussed in Sec. 2.3, the intra-$|L|$ Δn_{eff} increases monotonically with $|L|$. Given the guidance beyond cutoff, the Δn_{eff} of all TCMs exceeds that of the highest bound mode at $L=L_c$, and surpasses the mode-stability threshold criterion of 5×10^{-5}. As a result, TCMs can provide additional modes that exhibit large Δn_{eff} to inhibit intra-$|L|$ coupling.

It is true that the TCM effect in Gen5A3 fiber at 1550 nm is not very significant because none of the TCMs have propagation losses low enough to cover a km distance, and there is limited number of TCMs that can survive for over a 100-m fiber. On the other hand, the exponential dependence of the confinement loss (depicted in Fig. 6.5b) leads to negligible confinement loss of L~42 (at ~780nm), even at the wavelength 100nm away from the cutoff wavelength. Even though the confinement loss still rises with L at a particular wavelength, it is still possible for there to be a large number of modes with reasonable loss. In fact, increasing the fiber size is mathematically equivalent to decreasing the wavelength. Therefore, obtaining modes of higher $|L|$ at a fixed, desired wavelength of operation, could be practically achieved by increasing waveguide core diameter.

Figure 6.6 shows the simulated loss versus relative topological charge ($L-L_c$,) at 1550 nm for six different step-index fibers with core diameters ranging from 15 μm to 75 μm. Also shown with a dashed line is the overall loss (~0.2 dB/km) for conventional transmission fibers (e.g., SMF-28). The number of modes that have theoretical confinement loss lower than the overall loss of SMF-28 increases with L_c. This yields a crucial design criterion for realizing fibers that scale mode count with TCMs. Any fiber with a discrete index step at its outer core boundary that guides, via conventional TIR, sufficiently high-$|L|$ modes, has a large ensemble of even higher-$|L|$ cutoff modes that also experience negligible loss, and the number of available TCMs simply increases with TIR bound mode count. It also clarifies why cutoff modes have not previously been considered as viable candidates for photon transport – the 15-μm core fiber (with L_c=7) has no cutoff modes

that are low loss, and the theoretically simulated confinement loss for the first mode past cutoff (|L|=1) in SMF-28 is as high as 10^3 dB/km.

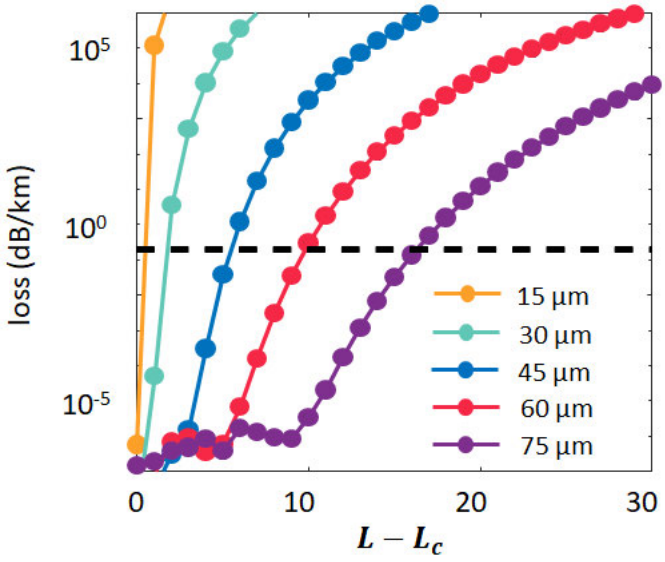

Figure 6.7: Simulated loss at 1550 nm versus relative OAM order $L - L_c$, in five step index fibers with the same index contrast but different core sizes. L_c is the OAM order of the last TIR bound mode (L_c = 7, 16, 25, 35 and 45 for fiber core sizes of 15, 30, 45, 60 and 75 µm, respectively). Dashed line represents the loss (0.2 dB/km) of SMF-28.

6.5. Generation-6 Ring-Core Fiber

6.5.1 Enhanced Topological Confinement

To enhance the TCM effect, the preform used to draw the Gen5A3 fiber was redrawn into a larger ring-core fiber, referred to as Gen6A. Its ring core has double the diameter of the Gen5A3 fiber. The preform was drawn into three fibers with identical sizes – Gen6A1, Gen6A3 and Gen6A5, under stresses of 20 kg/mm^2, 10.2 kg/mm^2 and 5.5 kg/mm^2, respectively. Each fiber is around 500-m long. In this section, the benchmark Gen6A3 fiber will be described first, followed by the discussions of the problems associated with the other two Gen6A fibers.

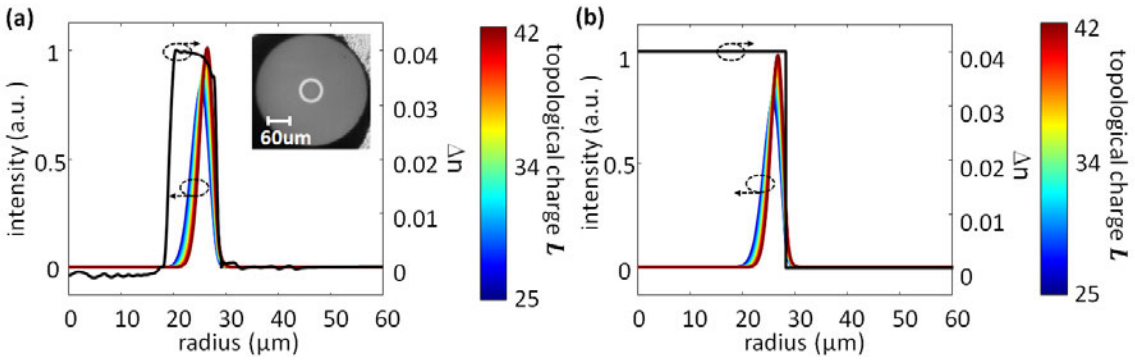

Figure 6.8: Modal intensity profiles and refractive index profiles of the Gen6A3 ring-core fiber (Inset: cross-sectional fiber facet image).

Figure 6.7a right axis shows the refractive index profile of the Gen6A3 fiber and the inset is a microscope image of the cross-section of the fiber facet. Note that the fiber size of the 57-μm ring-core fiber is expanded by 2% in the simulation for better correspondence with the accidental degeneracy and loss measured in the experiment. This adjustment is consistent with commonly employed modifications of simulated parameters necessitated by the lack of accurate knowledge of the Sellmeier coefficients of silica. Figure 6.7a left axis shows the intensity profiles of all modes of interest in the ring-core fiber (L_c=33). The similarity of their intensity profile promises gain-equalized optical amplification of all modes with a common, shared pump. In addition, all these intensity profiles reside at the outer core boundary, even in a conventional step-index fiber (Fig. 6.7b). Hence, the concept and scalability of TCMs described with the aid of step-index fiber in Fig. 6.6 can apply to any fiber with similar outer core boundary (for similar index contrasts). Despite its functional similarity to a step-index fiber, a ring-core fiber is used in the experiments mainly due to its advantage of ease of manufacturing and lower cost (less

dopant materials need to be deposited in regions where negligible optical power of the modes reside).

The modal loss at 1550nm in Gen6A3 fiber are measured by cutback using a 480-m long fiber (setup in Fig. 3.1). Figure 6.8(a) shows the cutback loss of all SOa and SOaa modes with m=1, $|L| \in [25,43]$. The bound modes and low-loss TCMs are shaded by grey boxes. The average loss of conventional bound modes is around 1.4 dB/km. The red crosses represent modes accidentally coupled to undesired high-m mode (Sec. 4.1.1), leading to strong mode mixing which makes it impossible to measure their losses. The TCMs with L=34-41 have an average loss around 5.1 dB/km, after ignoring high-loss outliers outside the grey shaded box (detailed in Sec. 7.1). Starting from L=42, the confinement loss of TCMs surpasses all other losses and becomes the dominant one. This abrupt increase of the TCM confinement loss is also reflected in the simulation, which are depicted by the black dashed curve. As is evident, the TCM effect is significant enhanced by merely doubling the fiber size. There are around 26 TCMs in Gen6A3 with sufficiently low loss to propagate over a ~1km fiber, while none of the TCMs in Gen5A3 can survive a km-scale fiber.

At the high-$|L|$ where the confinement loss is dominant (L=42 & 43), the losses of the SOa mode are higher than those of the SOaa mode. This is expected since the SOa mode has lower n_{eff}'s and is farther away from cutoff than the SOaa mode. This difference in confinement loss likely occurs for lower-$|L|$ modes as well. For lower-$|L|$ modes, the confinement losses are much lower than the absorption and scattering loss (which has nothing to do with the modal n_{eff}) to manifest, so most of them have the same measured

loss for SOa and SOaa modes. However, the difference in confinement loss between SOa and SOaa mode likely occurs for these lower-$|L|$ modes as well.

Figure. 6.8(b) is the log-scale version of Fig. 6.8(a). The confinement loss is supposed to be zero for bound modes ($|L|$<=33) but it fluctuates around 10^{-7} dB/km due to the noise floor of the PML mode solver. For mode with $|L|$<42, the confinement losses are orders of magnitude lower that the measured loss. It suggests that the measured loss is again due to abortion and scattering. The scattering loss is expected to be substantially reduced by manufacturing optimizations (detailed in Sec. 6.5.2).

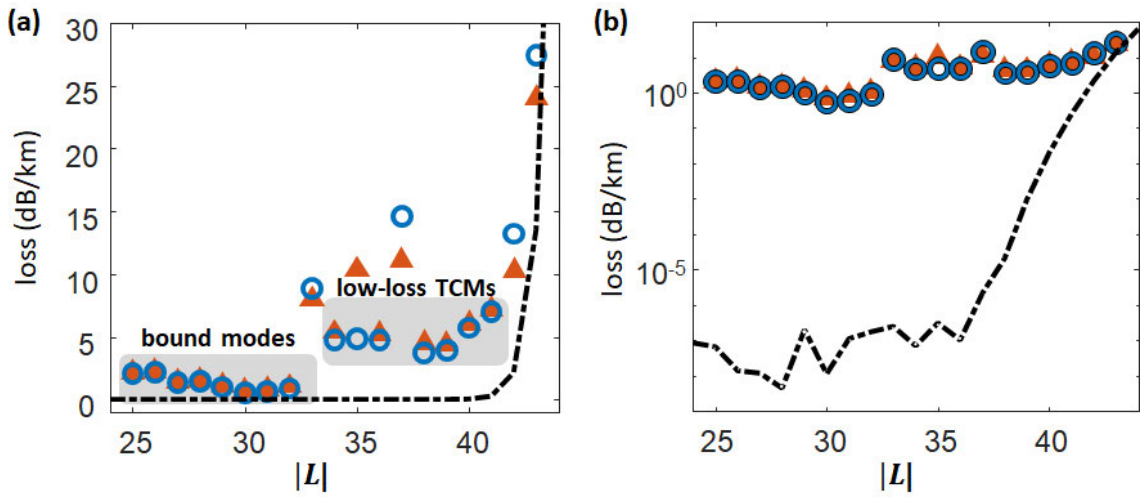

Figure 6.9: Experimental and simulated loss of Gen6A3 ring-core fiber at 1550 nm in (a) linear scale and (b) log scale.

6.5.2 Loss Analysis

The mechanism of the topological confinement is only associated with confinement loss but has nothing to do with loss due to material absorption and scattering effects. By going to larger topological charge, the confinement loss of TCMs ($|L|$<42) is substantially reduced such that they have little contribution to the measured loss. However, even though

we demonstrate record low loss for TCMs in the Gen6A3 ring-core fiber, we do observe TCM losses are higher than that of the bound modes for $|L|$=34-41 where the absorption and scattering losses are dominant. So, the questions arise as whether the absorption and scattering loss are also affected by TCM (assuming the prediction of the confinement loss is correct). In addition, the loss of both TCMs and bound modes needs to be significantly reduced for any long-haul transmission achieved by SMFs or MCFs (with ~0.2dB/km loss). Hence, it is critical to understand the loss mechanism better.

Loss in a high-index fiber is highly phenomenological and has resisted accurate theoretical predictions over decades. Nevertheless, trends can be ascertained by delineating different causes of losses. In this section, we use the model described in (Wandel, 2005) as their model gives good prediction to the experimental loss and the thesis also provides a complete review to the literature. The field profiles of all the modes look similar except for slight changes in the radius (Fig. 6.7; we'll discuss how the different field radius can result in different loss in the following), without any abrupt change between bound modes and TCMs. This is why we believe that the aforementioned model based on bound modes (in SMF) can also apply to TCMs. Note that the confinement loss is not considered in this section, given that TCMs have confinement losses as low as ~10^{-6} dB/km, making high OAM cutoff modes as viable as bound mode with zero confinement losses. Other losses are due to the material absorption and scattering effects, which can be broadly classified as Urbach absorption loss, Rayleigh scattering loss, and anomalous (or abnormal, excess; nomenclature varies in papers) scattering loss.

The Urbach absorption loss is given by (Wandel, 2005)

$$\alpha_{UV} \propto \Delta n \ \exp[g(E - E_0)] \tag{6.3}$$

where Δn is the index difference between the core and the cladding, g is a constant that depends on temperature and E_0 is a constant independent of the Ge-concentration. The Rayleigh scattering loss is given by

$$\alpha_{Rayleigh} \propto \frac{\left(1 + C_{Rayleigh} \Delta n\right)}{\lambda} \tag{6.4}$$

where $C_{Rayleigh}$ is a constant that will be determined during the calibration of the model.

These two kinds of losses are well studied in fibers, and depend primarily on Germanium mole fractions, glass fictive temperatures and viscosities. So, these loss contributions depend primarily on the index a mode experiences – since Fig. 6.7 shows that all the modes (regardless of bound or TCMs) – reside in regions of substantially similar indices, this contribution to loss should be identical for all modes. Furthermore, this contribution to TCM loss should be identical, after manufacturing optimizations (e.g., draw temperatures), to that of commercial dispersion-compensating fibers (DCF) since they feature similar index contrasts.

In contrast to the ubiquity of the other two losses mentioned above, the abnormal loss is prominent only in high-index-contrast fiber (e.g., Δn~0.04).

$$\alpha_{anomalous} \propto \Delta n^{\,2} \frac{\gamma^2}{d_{core} \lambda^3 (\gamma + 2)^2} \frac{T_{draw}}{F_{draw}} f(\Delta n) \tag{6.5}$$

where γ is the exponent of the core profile, d_{core} the core diameter, F_{draw} the draw tension, T_{draw} the temperature, and $f(\Delta n)$ is a confidential function of the core index. As is evident, depends on both the fiber profile's index and its gradient. The intensity of the scattering is proportional to modal power at the core-clad interface of the fiber. Thus, we

refer to it as interfacial scattering loss in this thesis. Wandel modifies the model for anomalous loss to have a much better prediction for the experimental loss.

$$\alpha_{anomalous} \propto \frac{\Delta n^{\,2}}{d_{core}\lambda^3}\frac{T_{draw}}{F_{draw}} f(\Delta n) \int_{-r}^{r} f[\eta(r), n(r), E(r)] r dr \qquad (6.6)$$

where f is a confidential function, $\eta(r)$ the viscosity profile, $n(r)$ the index profile and $E(r)$] the mode field distribution. The abnormal loss is proportional to the integral of a function of the viscosity profile, index profile and the mode field distribution. The viscosity is usually the highest the core-cladding interface especially in a step-index fiber, as shown in Fig. 34 in (Wandel, 2005). Therefore, such loss is the highest at the interface where the modal intensity plays a critical role, as shown in Fig. 33 in (Wandel, 2005).

Because this loss depends on mode intensity at a core-cladding interface (where index gradients are high), one surmises, from Fig. 6.7, that this loss would simply increase with OAM mode order (because higher order modes are pushed closer to the ring-core boundary); hence this loss contribution has no bearing on whether the mode is conventional TIR-bound or a TCM. While TCMs in a given fiber feature higher OAM orders than TIR modes, note that interfacial scattering depends on a mode's interaction with an index boundary/step, and not on the waveguiding mechanism.

We see evidence for the primacy of this interfacial scattering loss in Gen6A3 fibers mentioned above in– Fig. 6.9 is a replot of Fig. 6.7, but with a trend line showing a smooth, adiabatic loss increase with OAM order. This replot circles out two regions of outlier data that do not fit this narrative. The second outlier comprises the modes |*L*|=42 & 43, which have high loss because they are no longer topologically confined in the first place – so it

makes sense to remove their consideration from an analysis on interfacial scattering loss. The justification for not considering the other set of "transition" outliers is related to the dynamics of mode mixing — we will discuss that further in Chapter 7, and proceed, here, with the observation that the trend line shows an adiabatic increase in loss with OAM order, suggestive that the primary loss we encountered in these fibers was interfacial scattering loss.

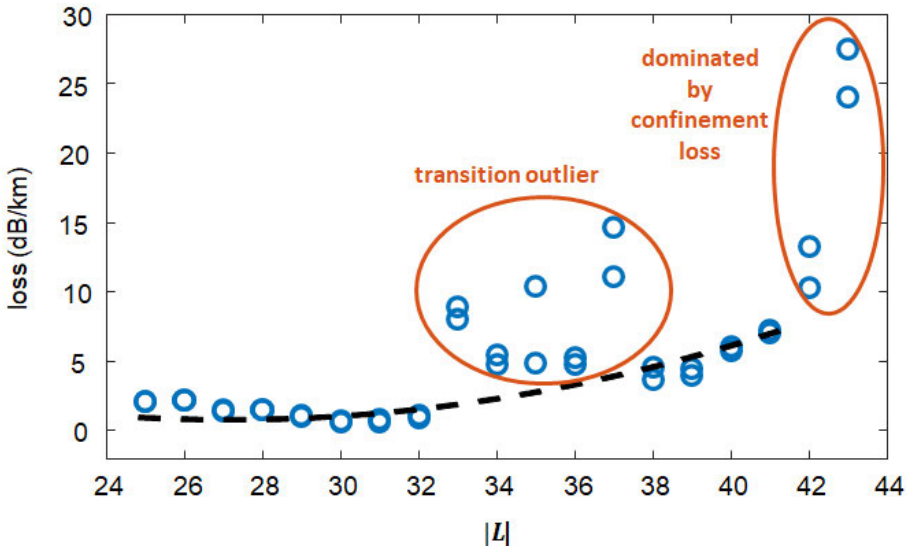

Figure 6.10: Loss versus $|L|$ in Gen6A3 ring-core fiber. The dashed line is a fitting excluding the outliers.

This anomalous loss is a strong function of fiber draw stress (Eq. 6.5 & 6.6). Figure 6.10 shows measured loss versus for the Gen6A3 drawn with 10.2 kg/mm2 and the Gen6A5 drawn with lower stress (5.5 kg/mm^2), with annotations of loss reductions due to increasing draw stress. Doubling the fiber draw tension for the same preform gave us two distinct fibers in which bound modes' loss reduced by ~2 dB/km, whereas TCM losses went down by ~4-5 dB/km. This is expected, since the influence of draw stress in reducing losses primarily pertains to this scattering mechanism of loss, and this increasingly affects

modes with progressively higher intensities at core-cladding interfaces (Fig. 6.7). Therefore, we expect even higher draw stress can further reduce the TCM loss even more.

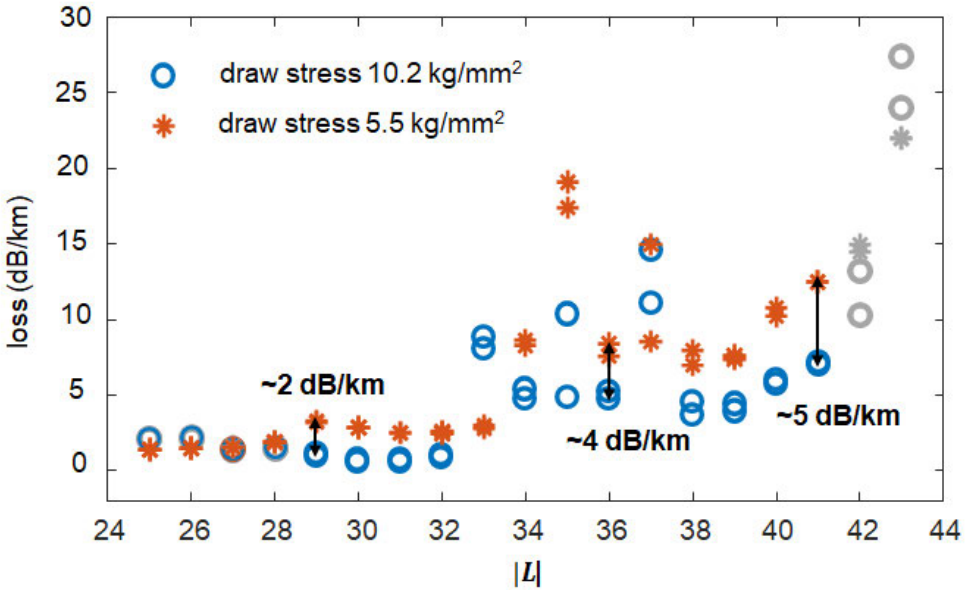

Figure 6.11: Loss versus $|L|$ for fiber drawn with stress 5.5 kg/mm^2 (Gen6A5) and 10.2 kg/mm^2 (Gen6A3). The loss reduction ranges from ~2 dB/km for low-L modes to ~5 dB/km for high-$|L|$ modes.

As shown in Fig. 5.14d, increasing the stress from 6.9 kg/mm^2 (Gen5A3) to 20.7 kg/mm^2 (Gen5B3) decreases the loss from ~1.3 dB/km to ~0.4 dB/km. Similar attempt of increasing the drawing stress was applied to Gen6A1 drawn with stress 20 kg/mm^2. However, the fiber is cracked on the ring core, shown as a few lines in the radial direction (Fig. 6.12). It may be due to the dramatically high drawing tension (1000 g) needed to achieve such high drawing stress in such a large fiber. Any uneven distribution of the tension on the cross-section can result in over stress at a local region. Actually, the core/cladding interface already has very high tension due to discrepancy of the material. Hence, further attempts would include reducing the cladding thickness and releasing the core/cladding stress (e.g., by curing) to make the fiber able to sustain higher stress. Actually,

fibers with standard 125-um cladding diameter can be drawn with up to 40-kg/mm^2 stresses (500-g tension), that are 4× higher than that of the benchmark Gen6A3 fiber. Therefore, there is a great room for loss reduction using higher draw stress. In terms of how low the measured loss can be reduced to, it is likely to come down to ~0.4 dB/km, which is (a) demonstrated in the aforementioned Gen5B3 ring-core fiber with the same index contrast and index gradients (b) the loss in commercial dispersion compensating fibers with similar index contrasts and index gradients (which have, over decades, been optimized to have such low loss levels).

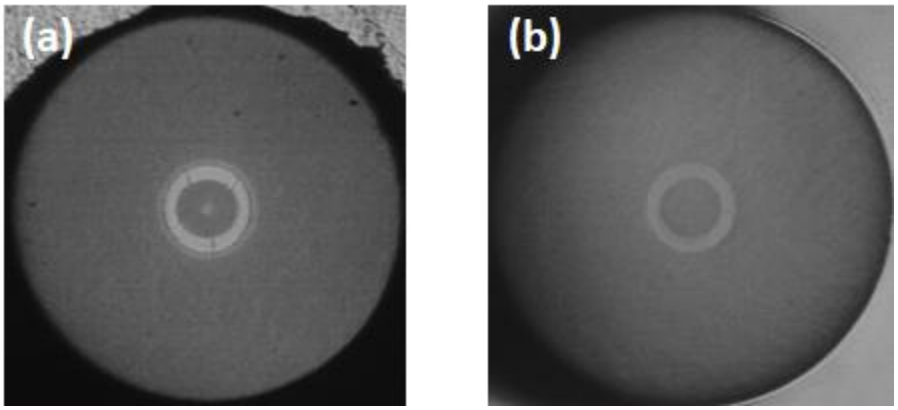

Figure 6.12: (a) Cracks on the fiber (Gen6A1), in comparison with (b) good fiber facet without cracks (Gen6A3).

Apart from draw tension/stress, there are also various ways of reducing the abnormal loss, such as matching the viscosity, increasing the draw temperature. In addition, we may also want to use lower-index fiber to reduce the loss from all three loss contributions. Actually, the TCM guidance is not primarily depended on the high index contrast, but rather on the topological charge of light. In other words, even in a fiber with lower index contrast, as long as the L_c is high enough (e.g., in a large fiber), the centrifugal barrier effect can manifest (Fig. 6.2).

We note that several other demonstrations of new fiber guidance mechanisms have had the same progression. Total-internal-reflection-based optical fibers had 20 dB/km loss in the 1970s, and are at 0.145 dB/km today. The first demonstration of hollow-core photonic bandgap fibers (Knight et al., 1998) was so lossy that it wasn't even measured over the 5cm of experimentally demonstrated fiber, but has losses of ~1 dB/km today. The first demonstration of anti-resonant fibers (Benabid et al., 2002) had losses of 1000 dB/km, and is now ~0.22 dB/km. TCMs are a new light transport mechanism guiding light below the light line, as in the case of bandgap and anti-resonant fibers, but the physics involves not structuring the waveguide, but rather the (topological) structure of the mode itself. Actually, the main loss contribution in hollow-core fibers that was brought down from the 100s to 1000s dB/km at their first demonstration to ~1 dB/km today was due to manufacturing optimizations to reduce the same interfacial scattering phenomenon.

In summary, the loss experienced by the ring-core fibers is dominated by interfacial scattering, and that the loss is not fundamentally higher for TCMs as opposed to bound TIR modes. It is promising to dramatically reduce the loss by various techniques, such as increasing the draw stress, matching the viscosity, increasing the draw temperature, or even using fibers with lower core index or gradient. There is no fundamental reason to prevent the measured loss from reducing to that of the commercial fibers with similar index contrast (~0.4 dB/km) by manufacture optimization. Nevertheless, the scattering loss is very complicated and not very predictable, and the loss reduction is involved with a lot of engineering problems which need further investigations to figure out.

6.6. Leaky Rays and Leaky Modes

The phenomenon of light guidance beyond the cutoff has been noticed and observed for decades. It was initially described in a conference paper by Snitzer in 1961 and referred to as leaky or quasi-bound modes. Selective excitation of high-order modes was achieved by illuminating different portions of the fiber. Figure 6.13 illustrates the L=73, m=1 mode in a 25-μm diameter fiber at 633nm. The highest bound mode is L=35 at 633nm. Alternatively, the L=73 mode "can propagate as true bound modes only in fibers with twice the measured core diameter for the wavelength used". In other words, it is evident that the L=73 mode operates beyond the cutoff and is still transmitted with low loss.

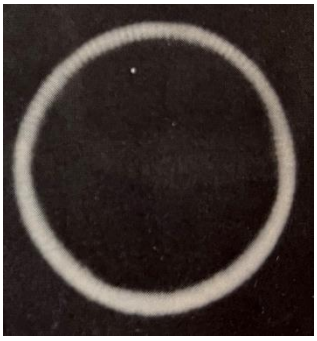

Figure 6.13: Either $HE_{74,1}$ or $EH_{72,1}$ in a 25-μm diameter fiber (Snitzer, 1961)

It is mentioned that for fibers with a diameter larger than approximately 25 μm, "the attenuation for the quasi-bound mode was not noticeably greater than that for the true bound modes in lengths of a few inches." However, the order of quasi-bound modes was not specified. Moreover, all the modes exhibit high losses, around 1 dB/m, without specifying the loss for each individual mode. Hence, there is no discussion regarding how the confinement loss of leaky mode decreases with increasing L.

From the perspective of geometric optics, a mode comprises rays that impinge on

the waveguide boundaries at the same angle relative to the normal. These quasi-bound rays "strike the surface at an angle greater than the critical angle for total internal refraction". As a result, "from a geometrical optics point of view, these modes would not be leaky at all." However, since their effective indices are lower than the cladding index, they are inherently unbound. This apparent contradiction is attributed to the "finite curvature of the core-cladding interface". Therefore, "some light is 'sprayed' around by diffraction so that it strikes at less than the critical angle."

Although Snitzer made the pioneering discovery and observation of leaky modes, the experiment was preliminary, and the theoretical explanation remained unclear. This discussion of leaky modes was omitted in his subsequent journal paper and the concept was buried in the literature. It was then rediscovered in the 1970s by Snyder et al. at Australian National University and Marcuse at Bell laboratory, respectively.

Snyder et al. categorize the rays in a step-index fiber as bound rays, tunnelling (leaky) rays, and refracting (leaky) rays (Fig. 6.13). A ray is only bound (i.e., has zero confinement loss) if its angle with the longitudinal axis is smaller than the critical angle's complement. Even though tunnelling leaky rays satisfy the TIR requirement locally, tunneling loss is always present. The refracting leaky rays fail to satisfy the TIR criterion locally or longitudinally. This range of tunnelling leaky rays between conventionally bound rays and refracting leaky rays (equivalent to cutoff modes in planar waveguide) is exclusive to $|L|>0$ modes in optical fiber. Specifically, the tunnelling leaky rays correspond to the TCMs whose n_{eff}'s are lower than the cladding index but higher than the index trench provided by the centrifugal barrier.

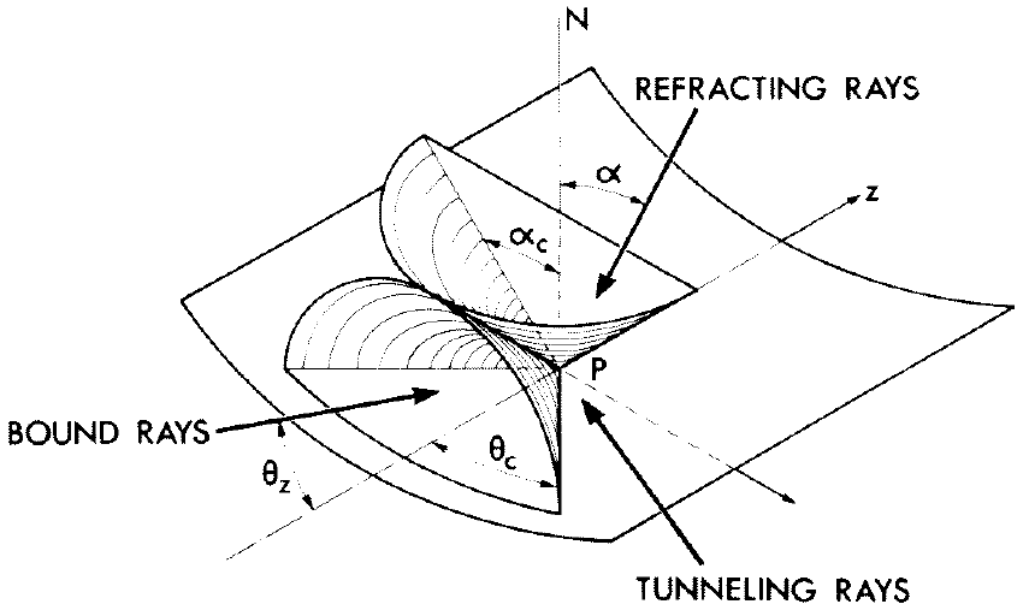

Figure 6.14: Classification of rays on a step-profile fiber according to the angle of incidence at the interface (Love & Snyder, 1975)

The loss of tunneling leaky ray was attributed to the failure of geometric optics in circular optical fibers, specifically the failure of ray tracing using Snell's law and Fresnel's coefficient on curved interfaces (Snyder et al, 1973). This loss can thus be obtained by solving the wave equation for its complex roots. Figure 6.14 shows the relationship between relative interval of V values and the azimuthal order L in a step-index fiber. This relative V value (inversely proportional to wavelength) is obtained by comparing the V value associated with a certain confinement loss to that at cutoff, analogous to how the relative wavelength is determined in Sec. 6.3. Therefore, it is evident that a mode tends to attenuate more slowly as the azimuthal order L increases. In the perspective of rays, under the same θ_z (corresponding to β in the wave picture), the attenuation of tunnelling rays decreases exponentially as azimuthal angle increases, i.e., as it becomes more highly skew.

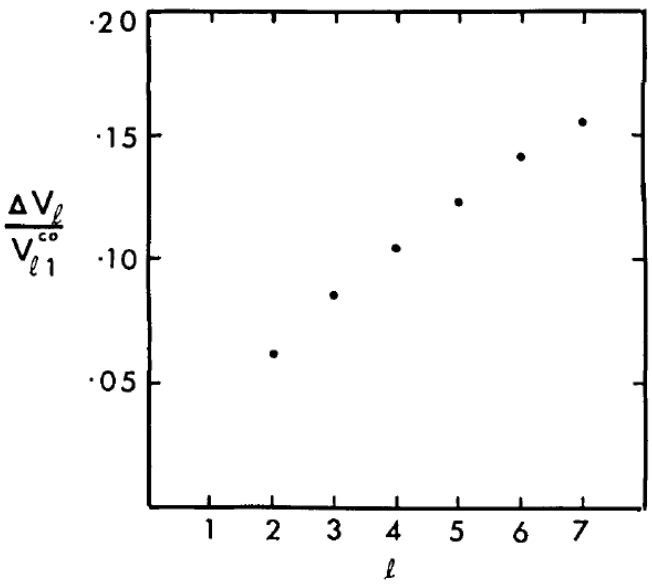

Figure 6.15: The growth of the relative interval of V values over which a HE_{l1} mode is weakly leaky as l increases. The V value is defined as $V = \frac{2\pi a}{\lambda}(n_{co}^2 - n_{cl}^2)^{\frac{1}{2}}$. $\Delta V = V_{\alpha 1}^{co} - V_{l1}^{co}$, where V_{l1}^{co} is the cutoff value for mode HE_{l1}, and is the value of V at which the product of the mode's attenuation coefficient and the fiber's radius equals to 0.01 (Sammut et al., 1976). This attenuation is equivalent to 10 dB/m in a 100-μm-radius fiber. The relative V in a certain fiber is equivalent to relative frequency.

To analyze the partial TIR of tunneling leaky modes, Snyder et al. introduced a generalized Fresnel's transmission coefficient for curved interfaces (Love et al., 1975). However, this model cannot explain why skew bound rays exhibit complete TIR (with zero confinement loss) on curved interfaces. In contrast, Marcuse proposed an alternative explanation, that the loss of tunneling leaky modes occurs when the phase velocity of the mode's evanescent wave in the cladding exceeds the velocity of a plane wave (Marcuse et al., 1973). However, this model did not reveal any dependence of the confinement loss on the mode's azimuthal order L.

6.7. High-|*L*| and High-*m* Modes

Although the term "high order modes" is often used generally, it's essential to distinguish between the azimuthal order L or the radial order m. The confinement loss decreases as the azimuthal order $|L|$ becomes larger (thus, the mode becomes more confined) but increases with high radial order m (causing them to leak out). Figure 6.14 shows the $|L|$-dependent simulated confinement loss for different m's with the same n_{eff} beyond cutoff (1% below) in the same ring-core fiber Gen6A3. The loss of each m mode decreases exponentially with $|L|$ due to the topological confinement effect, but for fixed L, it increases dramatically with m. Hence the transmission characteristics of modes with m>1, follows conventional wisdom that higher order cutoff modes are too lossy for use in transporting signals.

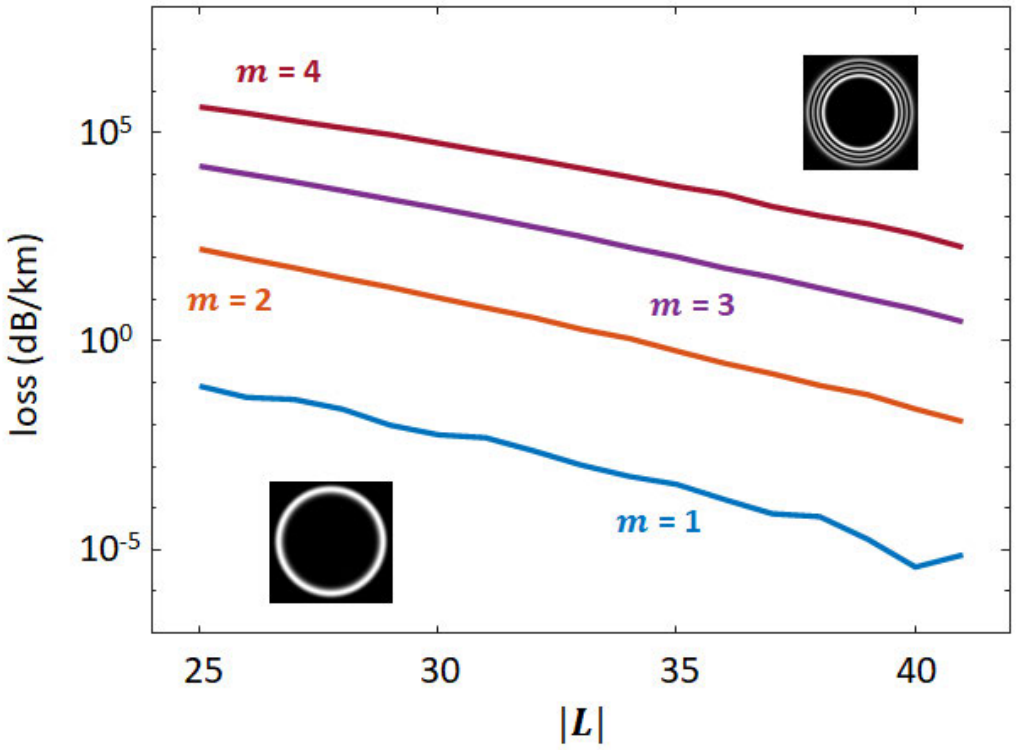

Figure 6.16: Simulated confinement loss depended on $|\boldsymbol{L}|$ and $\boldsymbol{m}$ in the Gen6A3 ring-core fiber. The n_{eff}'s of all the modes are held 1% below cladding index n_{cl}. Insets are simulated modal images of m = 1 and m = 4 modes.

The difference between high-$|L|$ and high-m modes is associated with the fundamental difference between circular fibers and planar waveguides. It is clear that high order modes readily leak out beyond the cutoff in a planar waveguide due to violation of TIR. This understanding is applicable to fibers in the case of L=0 modes with varying m's, or meridian modes (Snyder & Love, 1984). However, many conventional concepts on high-m modes may not apply to high-$|L|$ modes and can even be reversed when considering confinement loss and cutoff. As mentioned in the previous section, for $|L|$>0, there is a range of tunnelling leaky modes (corresponding to the TCMs we are discussing) between conventional bound modes and refracting leaky modes (similar to cutoff modes in planar waveguide). With high OAM, these tunnelling leaky modes are no longer "leaky" and have

negligible loss, similar to conventional bound modes. Given increasing focus on the research of OAM modes, such distinctions have become increasingly critical.

6.8. Summary and Discussion

In summary, we have demonstrated light guidance beyond cutoff and its dependence on OAM. Light is guided by the centrifugal barrier created by the OAM of itself. The centrifugal barrier is a universal effect for a highly rotational object in a system with short-range quantized potential. The effect has been well-known in nuclear physics for more than 70 years, and later has been observed in experiments in the fields of atomic and molecular physics too. The centrifugal barrier also manifests in increasing quality factor in whispering gallery cavities. Even though this light propagation beyond cutoff was investigated theoretically as "tunneling leaky rays/modes" by Snyder & Love, the interpretation of centrifugal barriers is much more elegant and provides much more physical insight into the role of OAM (enabled by the elucidation of OAM in the 1990s). In this thesis, we discuss the discovery that TCMs also enable light propagation over long distances with low loss.

The topological confinement is fundamentally a new regime of light guidance, distinct from conventional TIR-based waveguiding and other guidance mechanisms such as photonic bandgap or anti-resonance. At its current maturity, the measured loss of TCM is still relatively high compared with other guidance mechanism. This is primarily due to interfacial scattering while the fundamental confinement loss is orders of magnitude lower. Hence, the measured loss of the TCM-supporting fiber is expected to be substantially

reduced those of commercial high-index-contrast SMFs manufacturing optimizations (e.g., higher drawing stress).

Note that the distinctive properties of TCMs hold for any fiber mode with $L \neq 0$, whether or not they carry OAM. This includes modes commonly described in fiber textbooks as linearly polarized (the approximate solutions shown in Sec. 2.2) or vector modes (the exact solutions shown in Sec. 2.4). The TCM effect holds for these modes even though they do not carry OAM, because each of them can still be expressed as linear combinations of modes carrying OAM of equal and opposite signs (see Fig. 2.9), and the TCM effect is agnostic to the sign of L.

The topological confinement directly applies to scaling the mode count as spatial channels. We experimentally demonstrated the enhanced TCM effect by using a shorter wavelength or enlarging the fiber to reach a much higher $|L|$. We also demonstrate the first observation of cutoff modes propagating over fiber-lengths as long as ~0.5km.

In the following chapters, we will show more unique properties of TCMs, which provides new capabilities for scaling mode counts in optical fibers. As a result, we dramatically increase the mode count and improve their performance, potentially leading to substantial enhancements in the information capacity of optical fibers of the future.

Chapter 7

7. Suppression of Degenerate Mode Coupling

7.1. Frustrated Coupling

In the previous chapter, we demonstrate a novel light guidance mechanism and by enhancing this effect we obtain a large number of additional low-loss modes beyond cutoff. Actually, the significance and benefit of TCMs are not just limited to additional low-loss modes beyond cutoff. In the previous chapter, we aimed at reducing the confinement loss of TCMs to a negligible level comparable to those of bound modes. However, it is worth noting that mode-dependent loss plays a crucial role in mode coupling. For example, previous studies on long-period fiber gratings (LPFG) have shown that the coupling between core and cladding modes can be completely suppressed by increasing the loss of the cladding modes (Stegall et al., 1999). In this case, the degree of loss was determined by the refractive index of an outer layer outside the cladding, and therefore cannot be utilized as a modal property to suppress the coupling between guided core modes. In contrast, confinement loss of TCMs is an inherent property distinct for each guided mode and can significantly affect the intermodal interactions. Particularly, the desired m=1 TCMs and accidentally degenerate high-m TCMs have different confinement losses, which can lead distinct mode-coupling mechanism compared with that of conventional bound modes.

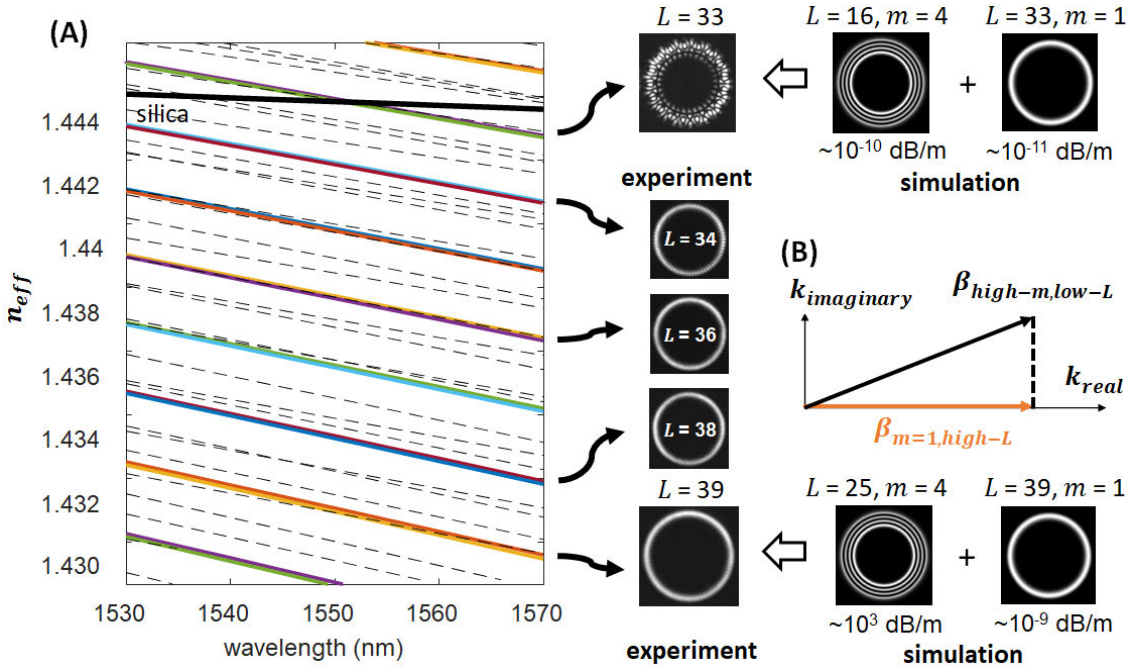

Figure 7.1: natural distortion immunity of TCMs. The left panel shows n_{eff} *vs.* λ for select modes. Solid colored lines are desired $m = 1$ modes of different $|L|$; dashed black lines represent undesired high-m modes. The solid black line shows the index of the silica cladding (conventional boundary between TIR bound and cutoff modes). Right panel: experimentally measured output images of LCP modes at 1550 nm out of a 480-m-long ring-core fiber.

Figure 7.1a shows the n_{eff} distribution of select modes in the Gen6A3 ring-core fiber. The solid-colored lines represent m=1 modes of various $|L|$'s and the dashed black lines represent high-m modes. The corresponding modal images right next to the n_{eff} of select modes are obtained out of a 478-m long fiber using a 1550nm ECL source (setup in Fig. 3.12). The bound mode L=33, m=1 is accidentally degenerate with L=16, m=4 around 1550nm. Therefore, no matter how pure the mode excitation is, L=33, m=1 is easily coupled to L=16, m=4 along the fiber with ever-present perturbation to provide the coupling coefficient (Sec. 4.1). As a result, the interference of the two shows strong, distorted pattern. In contrast, dramatically distinct behavior is evident for TCMs (whose

n_{eff} lie below the silica cladding index, depicted as a solid black curve in Fig. 7.1a). Although the n_{eff} of the L=39, m=1 is close to that of a high-m mode with L=25, the output image still shows a clear single ring image, with spatial interferometry measurements revealing mode purity as high as 25 dB.

This avoidance of mode coupling is because of the orders of magnitude different confinement losses of two modes that are nearly degenerate, the desired L=39, m=1 mode and the parasitic L=25, m=4 mode, leading to frustration of phase-matched coupling in a manner similar to the effect described for LPFGs (Stegall et al., 1999). As mentioned in Sec. 6.7, the confinement loss is higher for lower L and higher m. Particularly, the L=25, m=4 mode has confinement loss up to 10^3 dB/km while the confinement loss of L=39, m=1 is negligible. Such distinct loss equivalently suggests a distinct imaginary part of the propagation constant β, as shown in Fig. 7.1(b). Actually, the phase matching condition for mode coupling necessitates matching the complex β, not just the real one. The mode coupling process described in Sec. 4.1 assumes a lossless system that considers only the real part of β (corresponding to n_{eff}). For mode with distinct confinement losses, compensation of an imaginary k vector is needed for the phase-matched coupling but it is not provided by common fiber perturbation. In other words, degeneracy is lifted in the complex space, leading to suppression of mode coupling between degenerate TCMs.

7.2. Loss-Dependent Mode Coupling

The frustrated coupling of degenerate TCMs mentioned above relies on the high confinement loss of high-m modes. However, the loss of high-m TCMs is not always as high as 10^3 dB/m. These high-m TCMs can also have negligible loss when their n_{eff}'s are

not far beyond cutoff. The fact that they have higher *m* and lower *L* compared with desired *m*=1 modes just means that their loss grows faster with *L* at 1550nm. In other words, their centrifugal barrier effect is not sufficient. Similar to the Gen5A3 modes. What we just described above about frustrated coupling is a typical case where the confinement loss of high-m modes is very high. So, a question naturally arises as what the mode coupling will be when the loss difference is not that significant.

Such loss-dependent mode coupling is well studied in LPFG (Stegall et al., 1999). When the loss difference between the two modes is not that significant, the mode coupling still happens, but the power of lossy mode is stripped off. Hence, there is some extra loss manifested for such mode coupling.

Similar transition occurs for mode coupling between TCMs. Figure 7.2 shows the relative loss versus wavelength for five representative *m*=1 modes. Depended on the interaction with accidentally degenerate high-m modes, they can be classified into following three categories:

1) The conventional bound modes such as |*L*|=30 SOaa, which couple readily with the undesired high-m modes, resulting in distorted output mode images at the degenerate wavelength.

2) The intermediate TCMs such as |*L*|=33 & 35 SOaa, which partially couple with the undesired high-m mode, but this power is stripped off, since the high-m mode has high loss. Specifically, |*L*|=33 is a bound mode at 1550nm but it becomes TCMs at 1565nm (Fig. 7.1), where its n_{eff} crosses with that of the accidentally degenerate high-*m* mode. The experimental degenerate wavelength is ~30nm longer than the degenerate wavelength

predicted by simulation. As the wavelength becomes closer to the degenerate wavelength, the extra loss become higher while the distortion also becomes weaker. In contrast, |L|=35 SOaa is free from high-m distortion but with extra loss.

3) The frustrated coupling TCMs such as L=39 & 41 SOaa, whose coupling with high-m modes is completely frustrated. They don't show any extra loss at the wavelength ~30nm longer than the simulated degenerate wavelength, except for a smooth rise at the long wavelength due to smaller n_{eff} (thus more way from the TIR-cutoff). Thus, in this frustrated-coupling regime, the coupling between m=1 and high-m modes are completely suppressed and the output m=1 mode shows neither distortion nor extra loss.

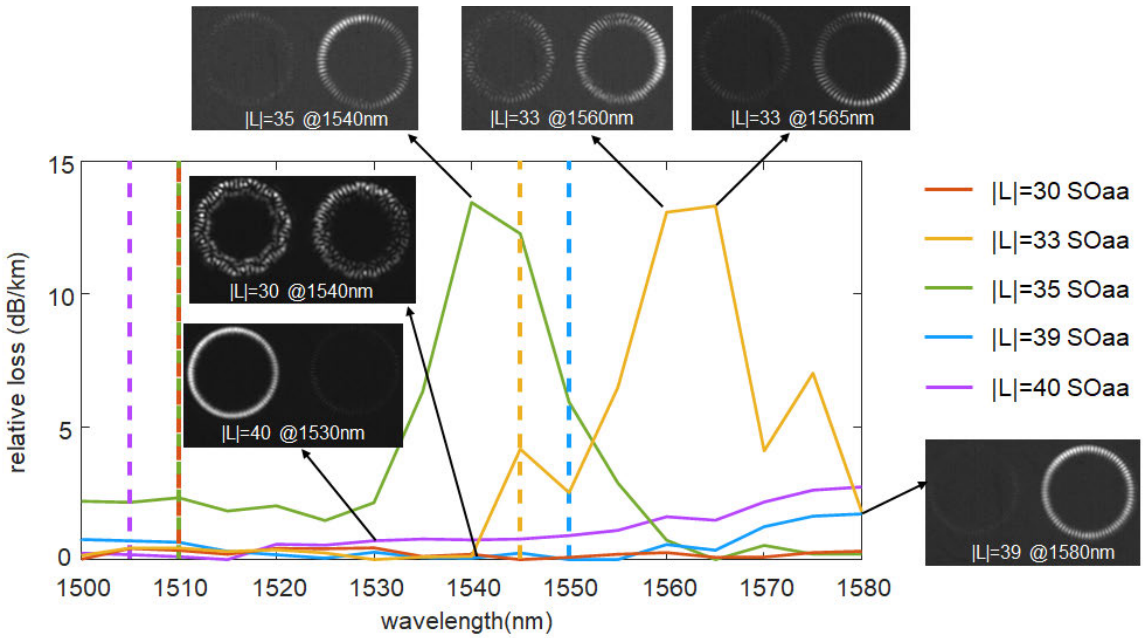

Figure 7.2: Relative losses for three representative modes in the wavelength range 1500-1580nm. The relative loss of each mode at each wavelength is obtained by comparing with the lowest loss of this mode in such wavelength range. The solid curves are measured relative loss for each mode while the vertical dashed line with the same color represent the simulated wavelength where the desired m=1 mode is degenerate with a high-m mode. Mode coupling of L=35 SOaa with high-m modes manifests as extra loss in terms while it is completely suppressed for L≥39.

These different mode-coupling behaviors are determined by the confinement loss of degenerate high-m modes, since the desired m=1 TCMs have negligible loss. To find out the loss threshold for frustrated coupling, we swept the wavelength between 1500-1580nm to measure the extra loss of different desired m=1 TCMs interacting high-m modes. The confinement loss of the degenerate high-m mode is obtained from simulation. Figure 7.3 shows the measured extra loss of m=1 modes versus the simulated confinement loss of high-m modes at the simulated degenerate wavelength. Our findings indicate that high-m modes must have a loss of over ~10^5 dB/km (L=39-41) for the frustrated coupling phenomenon to manifest.

The loss threshold required for completely frustrated coupling is exceptionally high. However, for device length applications, the relatively higher loss can be tolerated, and we are more concerned about minimizing distortion. In particular, although L=35 SOa over a fiber length of 0.5 km exhibits a single ring image at the degenerate wavelength, the same mode over a fiber length of 25 m shows image distortion due to high-m coupling. In contrast, L=37 SOa yields clean ring images regardless of fiber length. Therefore, the loss threshold required for distortion-free transmission may be much lower.

Further investigation is necessary to validate these loss threshold values. Since the measured degenerate wavelength is 0-50 nm longer than the simulated degenerate wavelength, it is possible that the exact high-m loss may be greater, leading to a higher loss threshold for frustrated coupling. Additionally, it would be more accurate to experimentally measure the high-m loss to consider the aforementioned numerical errors as well as bend loss.

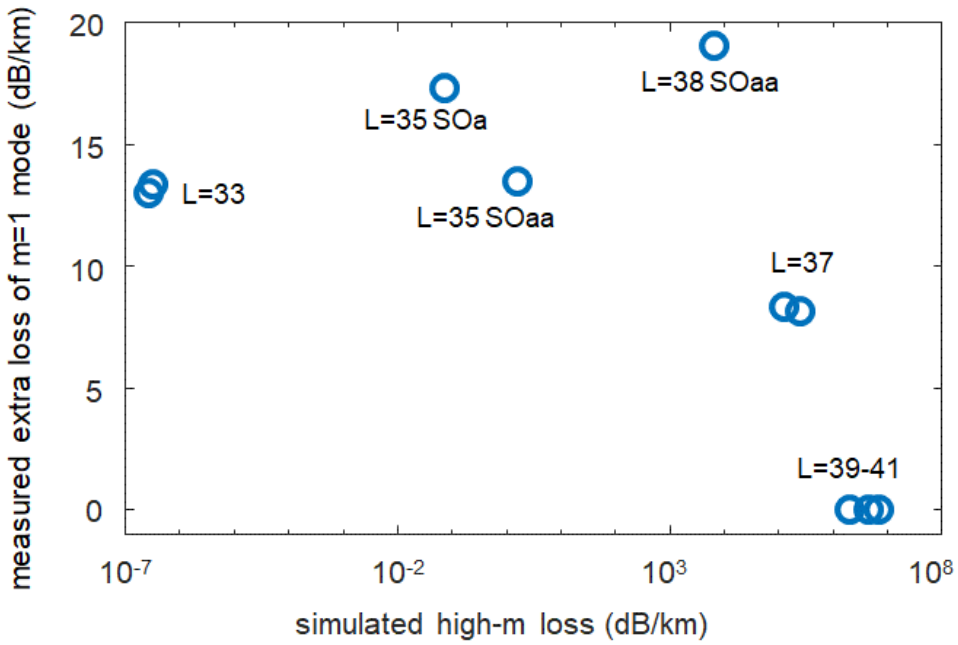

Figure 7.3: Measured extra loss of m=1 mode versus the simulated high-m loss at the simulated degenerate wavelength

7.3. Mode-Count Scalability

As discussed earlier in Chapter 5, high-m coupling is a primary obstacle to scaling the mode count. With the inherent property of mode-coupling suppression, TCMs offer a promising approach to overcome this bottleneck. Figure 7.4 is a replot of Fig. 6.8 (a) with a few representative modal images out of the 0.5-km Gen6A3 fiber. When interacting with high-m modes, bound modes are strongly distorted. Apart from L=33, there are also L=30 & 28 experiencing high-m coupling and distortion at 1550nm (indicating by the red crosses) in the conventional bound-mode regime. In contrast, all desired m=1 TCMs ($L|\geqslant 34$) show clean measured modal outputs, despite of extra loss for intermediate modes (L=35 SOaa, L=37 SOa &SOaa). Hence, operation in the TCM regime allows scaling mode count while decreasing the modal density of states that cause unwanted perturbative mixing.

As mentioned in Sec. 6.5, we gain 26 TCMs in Gen6A3 by merely doubling the size to enhance the TCM effect. These modes inherently possess large intra-$|L|$ Δn_{eff}, which helps to mitigate near-degenerate mode coupling, one of the limitations to scaling the unmixed-mode count (Sec. 5.1). What's more, these additional 26 TCMs are also free from high-m distortion. It is more advantageous to go to high L so that the accidentally degenerate high-m modes have higher loss for frustrated coupling to occur. The only limitation is the confinement loss which scales with L. Depending on the application, we can assign a loss cap to come up with a mode count. For fiber spanning ~km distances and suitable for data center applications, we select the good modes up to L=41 with a measured loss of ~7 dB/km, just before L=42 where the confinement loss starts to take off. The simulated confinement loss of L=41 is approximately 0.1 dB/km, indicating the potential to achieve low loss similar to commercial SMF (Sec. 6.5). Using the loss cap as ~7 dB/km, we have also eliminated the aforementioned intermediate TCMs with extra loss. In other words, the "good" low-loss TCMs are the mode in the orange shaded box in Fig. 7.4.

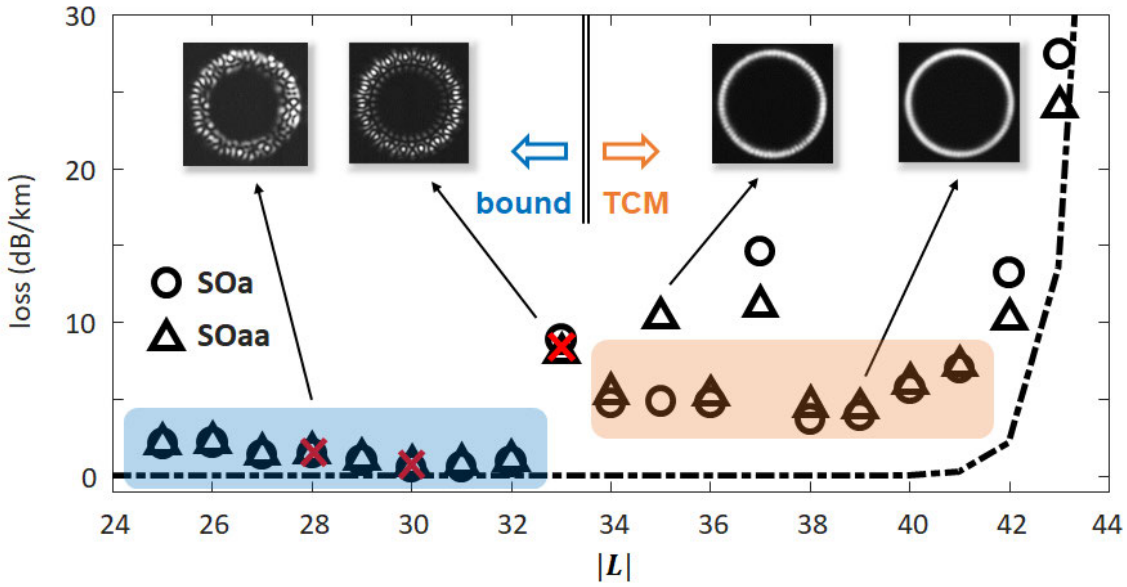

Figure 7.4: Experimental and simulated loss of Gen6A3 ring-core fiber at 1550 nm. The inserts are the output images of representative modes of the ~0.5-km ring-core fiber at 1550 nm where the corresponding m=1 mode is accidentally degenerate with another high-m mode. Such output mode images strongly distorted for bound modes while free from distortions in the TCM regime. The double vertical line represents the cutoff at 1550 nm

To demonstrate the validity of each mode as an independent channel, we measure the transfer matrices for all the modes $|L|$=25-41 with LCP and RCP in the ~500m Gen6A3 fiber, as shown in Figure 7.5. Pure mode propagation (red) occurs for all modes except for $|L|$=28, 30, 33 (deep blue). Less than −18dB power is scattered into modes of neighboring order, primarily due to misalignments in mode excitation. The average mode purity of all 48 low-loss modes is 18dB, with average polarization extinction ratios (PER) of −13dB (Fig. 7.5b). The main mode coupling occurs between near-degenerate modes with same $|L|$ but of opposite sign (diagonal), which we'll revisit in the next chapter.

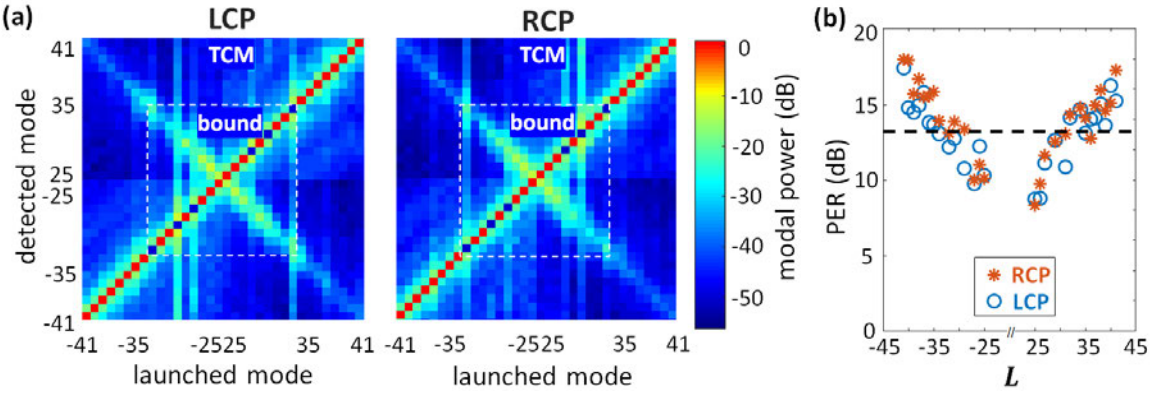

Figure 7.5: (a) Transfer matrices of all the modes |*L*|=25-41 with LCP and RCP and (b) polarization extinction ratios of all available modes in the 0.5-km Gen6A3 ring-core fiber.

In device-length applications ranging from 10 to 100 m, slightly higher loss would be more tolerable. This length scale is of relevance to applications ranging from lasers/amplifiers and data-center connections to nonlinear optics and machine learning. The loss cap can be relaxed, for instance, up to 0.1 dB/m. As a result, the highest available mode can go up to *L*=44 (Fig. 7.6). Also, we can include the aforementioned distortion-free TCMs (*L*=35 & 37) that exhibit clean output modal images but with extra loss.

Similarly, the transfer matrices for all the modes |*L*|=25-44 with LCP and RCP are measured at 1550nm in the ~25m Gen6A3 fiber. Again, each desired mode is illustrated as a red data point on the inverted diagonals with purity exceeding 19 dB. The interspersed black data points are OAM modes which show the aforementioned inadvertent mode mixing with high-m modes. Figure 7.6b shows that the PER of all the modes remains below ~16dB. As results, the total mode count is up to 68 in a 25-m fiber favorable for device-length applications. Due to accidental degeneracy primarily for the bound modes, the total mode count is reduced to 52 in the entire C-band (ascertained by sweeping the ECL in this spectral range).

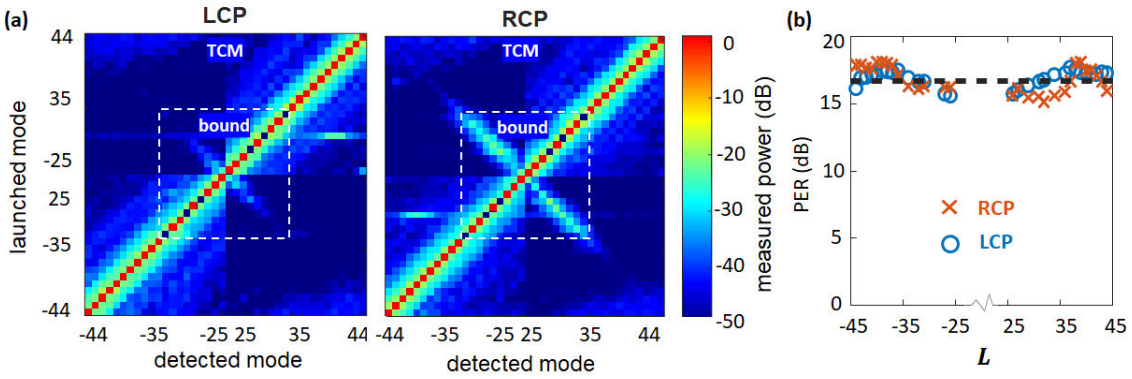

Figure 7.6: (a) Transfer matrices of all the modes |*L*|=25-44 with LCP and RCP and (b) polarization extinction ratios of all available modes in the 25-m Gen6A3 ring-core fiber.

Further mode-coupling scalability is enabled by the inherent suppression of degenerate mode coupling for TCMs thus enable further mode-coupling scalability and such TCM effect can be scaled with higher OAM in larger fibers. Following this strategy from Gen5 to Gen6 fiber, we continued increasing the fiber size, resulting in an enlarged ring-core fiber with a 77-um ring diameter, as shown in Fig. 7.7.

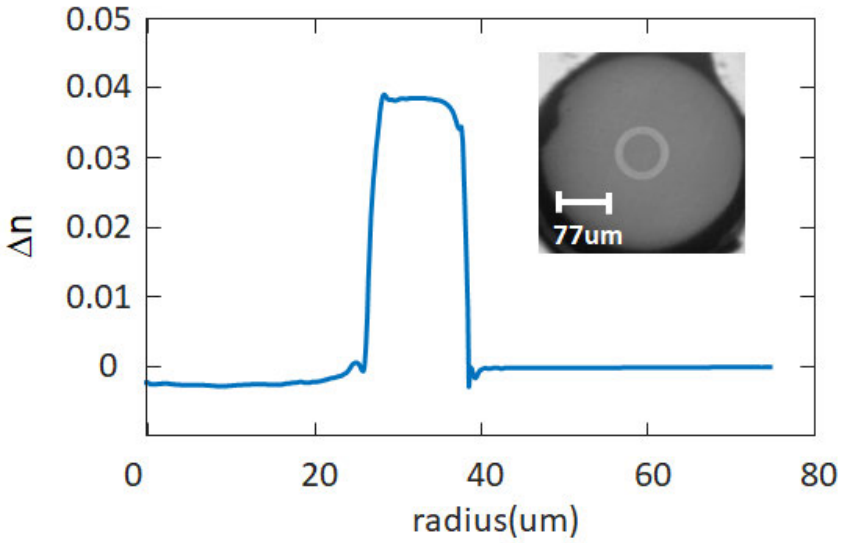

Figure 7.7: Refractive index profile of a ring-core fiber with 77-μm ring diameter. The inset is the cross-section image of the fiber facet.

Figure 7.8 shows preliminary results of measuring L=30-70 SOaa modes in the 25-m long fiber with an enlarged ring diameter of 77 μm at 1550nm. Again, we observed that most bound modes exhibited high-m coupling, while most TCMs are free from modal distortion, with only two transitioning outliers. The large number of low-loss TCMs are due to high OAM. It suggests that 20 $|L|$'s are free from high-m distortion and have low loss (<0.1 dB/m), indicating that we may achieve a record mode count of up to 80. As this trend continues, the total mode count is likely to increase further in a larger fiber.

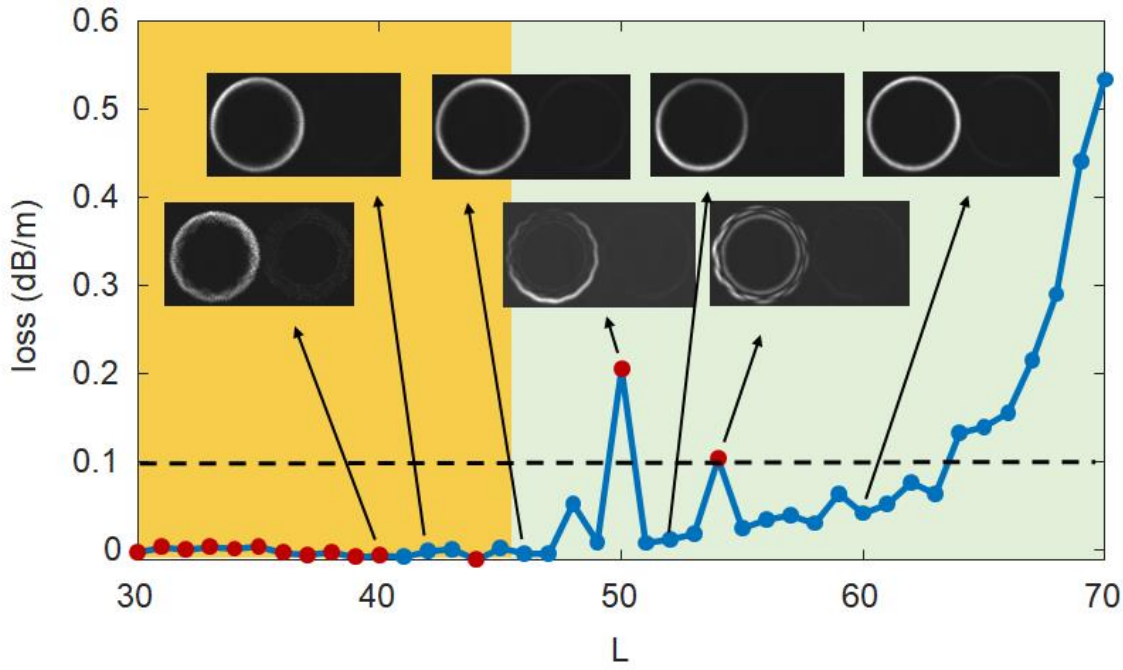

Figure 7.8: Cutback loss of representative SOaa modes in a 25-m ring-core fiber with 77-μm ring diameter at 1550nm. Red dots indicate modes distorted by high-m coupling while blue dots are modes with clean modal output. Modes in the orange band are TIR-bound while the green band indicates the TCM regime.

7.4. Simple Step-Index Fiber

As discussed in Chapter 5, the intention of sculpting the fiber core into a ring shape was to reduce the number of undesired high-m modes that can couple with desired m=1 modes.

The high-$|L|$ m=1 modes have similar intensity profile in both ring-core and step-index fiber (Sec. 5.1, 6.5). Since high-m coupling can be suppressed in the TCM regime, we don't necessarily need the ring core to restrict the high-m mode. Larger ring thickness introduces higher-m modes, which actually have much higher losses. In other words, even such simple conventional step-index fiber can transmit a more significant amount of uncoupled OAM modes without the need to manufacture other complicated fibers like the ring-core ones.

Figure 7.9 shows the cross-section image and refractive index profile of a step-index fiber that was initially designed for high-power nonlinear experiments (Rishoj et al., 2019). It has similarly large index contrast ($\Delta n \sim 0.04$) as Gen6A3 but larger core size (core diameter ~70um). The fiber used in the experiment is 90-m long (setup in Fig. 3.1)

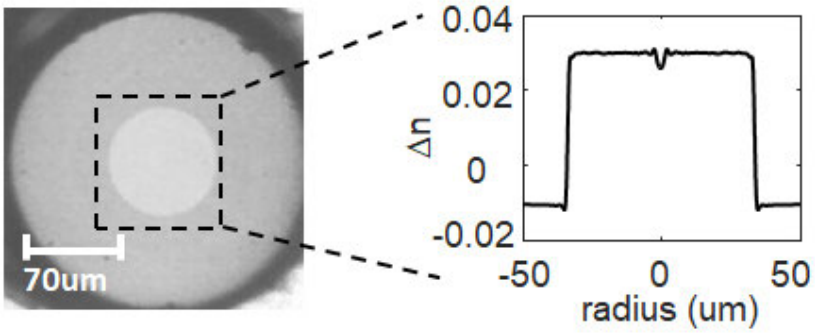

Figure 7.9: Cross-section image and index profile of a 70-μm step index fiber.

The measured cutback losses of $|L|$=40-64 with both SOa and SOaa are shown in Fig 7.10. The measured loss remains relatively low up to L = 63, way past the cutoff L=42. The black markers indicate clear modal output (representative modal images pointed by the black arrows) with average 18-dB purity using an ECL source while red marks indicate strong image distortion. Similarly, in the bound mode regime, only L=42 shows a clear ring-shape at 1550nm, while all the others dramatically mix with high-m modes, showing

speckle patterns. At the beginning of the TCM regime, the mode coupling is still present, because the losses of high-m modes in this region are not yet sufficiently high. Note that this transition regime is wider than that in the ring-core fiber, likely due to the existence of much more high-m modes in a step-index fiber. However, for modes with $L \geqslant 51$, a clean modal output is obtained regardless of whether or not it is degenerate with high-m modes, clearly illustrating the power of TCMs to naturally avoid mode mixing.

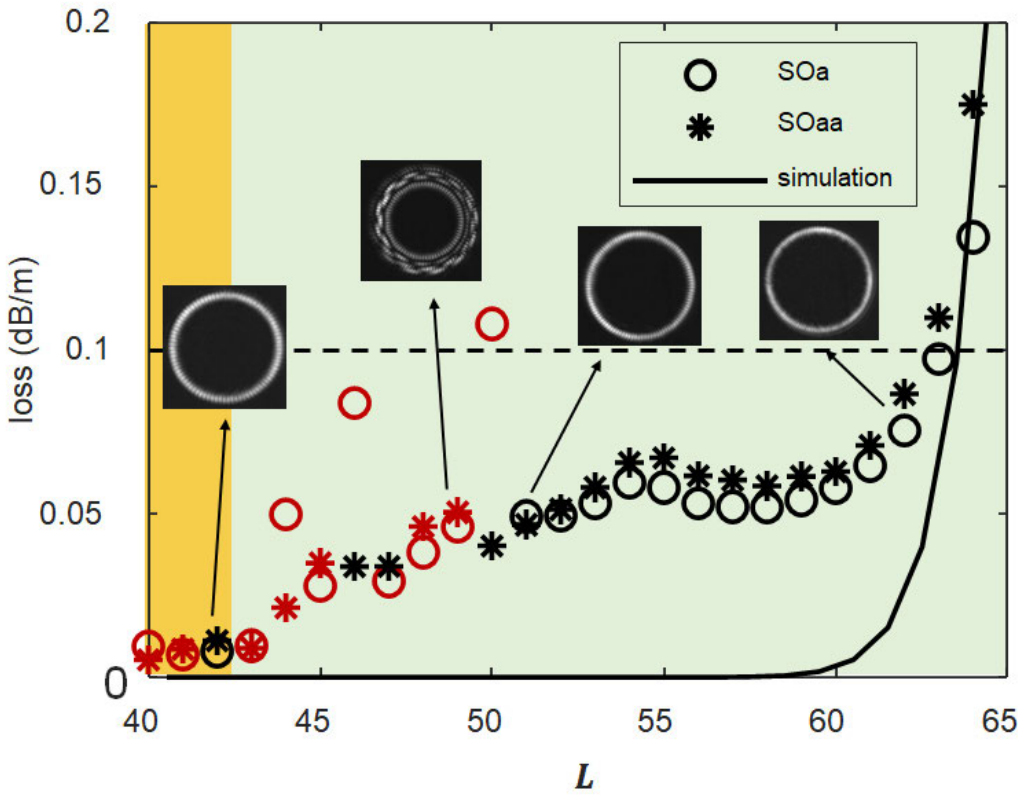

Figure 7.10: Cutback loss of $|L|$=40-64 with both SOa and SOaa measured in the 70-μm step-index fiber at 1550nm. Red markers indicate modes distorted by high-*m* coupling while black marker are modes with clean modal output. Modes in the orange band are TIR-bound while the green band indicates the TCM regime.

Overlaid in the plot is the simulated confinement loss which matches well with the experiment after L=63 where the confinement loss becomes large enough to dominate the

total loss. Before L=60 where the confinement loss starts to take off, the confinement loss is orders of magnitude lower than the measured loss, indicating that the measured loss is mostly due to interfacial scattering. Note that such scattering loss is much larger than that of the aforementioned Gen6A3 and it was not initially intended for long-haul telecom transmission. It was drawn with standard 100-g tension so the stress is as low as 4.5 kg/mm^2. However, further investigation is needed to figure out what its scattering loss is still higher than Gen6A5 fiber drawn with similar stress. Nevertheless, the scattering loss has the has a great room of improvement by better fiber manufacturing, such as higher drawing tension (Sec. 6.5). If we pick 0.1 dB/m loss as a loss cap, the available mode can go up from L=42 to L=63, most of which are mode-mixing free TCMs.

Figure 7.11 shows a quantitative summary of this fiber's modal performance. The purity of all modes with propagation loss < 0.1 dB/m (criterion set earlier) is deduced by using a narrowband tunable ECL in the 1550-nm range for mode excitation, and then employing spatial interferometry to quantify modal content. The transfer matrices shown in Fig. 6.10a illustrate that, for modes denoted with red squares, mode purity exceeds 15 dB, with an average > 18 dB. The PER (Fig. 7.11b) average ~10 dB for all modes, but were substantially better (>16 dB) for more than ½ of the modes. Overall, we conclude that this fiber supports a record value of 60 OAM modes with high purity, PER and low loss.

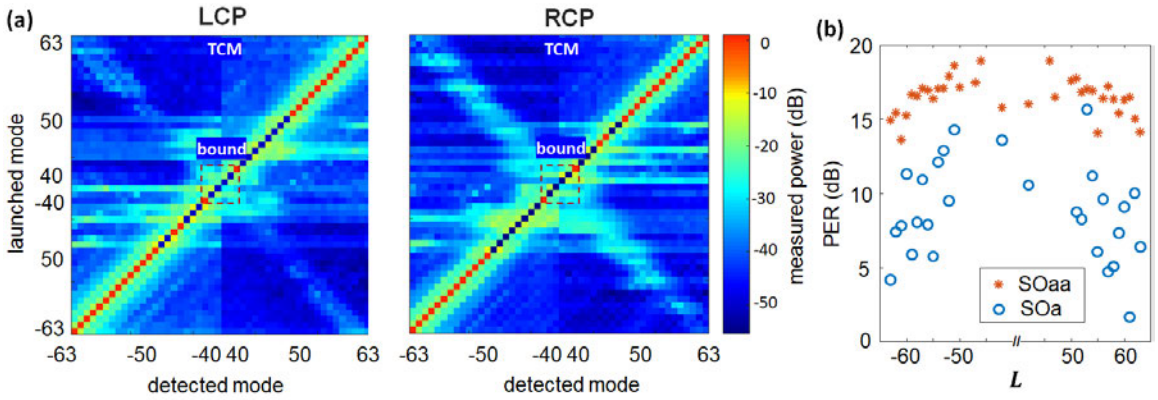

Figure 7.11: (a) Transfer matrices of all the modes |*L*|=40-64 with LCP and RCP and (b) polarization extinction ratios of all available modes in the 70-μm step-index fiber with 90-m long.

This is the first instance of utilizing a standard, simple step-index multimode fiber for transmitting a large ensemble of uncoupled modes, hence pointing to the possibility of using legacy fiber for mode multiplexing. These interesting attributes were made possible by exploiting the TCM concept described earlier.

7.5. Summary and Discussion

In this chapter, we demonstrated the fundamental mode-coupling suppression between degenerate TCMs with distinct confinement loss. As such, we mitigate the issue of the high-*m* mode coupling that has been haunting for scaling the OAM mode count. This effectively decreases the density of states of low-loss propagating modes. As a result, we reach record unmixed mode count at 1550nm – 52 over a ~0.5km fiber and 60 over a 25-m fiber. We also show preliminary results in a 77μm ring-core fiber with potentially 80m unmixed modes. These point to a promising approach for scaling the mode count by enhancing the TCM effect by using a large fiber with higher-|*L*| mode. How far this simple scalability methodology can be extended remains to be further investigated, theoretically

and experimentally. Given the simplicity of the design, TCMs in step-index fibers can potentially increase the capacity using the current fiber infrastructure without drastic alterations.

Chapter 8

8. Record Low Crosstalk of TCMs

8.1. Crosstalk and Mode Coupling

In the previous chapter, we achieved record mode count in an MMF enabled by TCMs. The benchmark is Gen6A3 with 50 low-loss pure modes. In addition to channel count, crosstalk is another critical parameter in SDM. As indicated by Eq. 1.2, crosstalk directly impacts the total SNR, thereby playing a significant role in determining the information capacity. More precisely, both channel count and crosstalk jointly determine the SDM capacity when assuming the same bandwidth. Furthermore, channel count and crosstalk are closely related, as elucidated in the subsequent discussion.

To calculate the information capacity for a specific channel, it would be necessary to add the crosstalk from all other channels. Inter-channel crosstalk in MMFs refers to the inter-mode coupling discussed in Sec. 4.1, but in uncoupled single-mode MCFs, it corresponds to the inter-core coupling. Before discussing the MMF crosstalk, it would be beneficial to examine the MCF crosstalk briefly. In this chapter, "MCF" shall refer to uncoupled single-mode MCF for the sake of brevity. The MCF established the benchmark for crosstalk of unmixed SDM fibers, and MMF may use its analysis approach. In this chapter, we'll compare them closely.

Inter-core coupling may be analyzed using the coupled mode theory outlined in Section 4.1. The inter-core spacing determines the transverse coupling coefficient. Inter-core coupling in homogeneous MCFs, where the propagation constants of all cores are

identical, is primarily determined by the inter-core spacing. Typically, the MCF crosstalk is characterized by the crosstalk between the two nearest cores, since the coupling weakens exponentially with increasing inter-core spacing. For long-haul transmission, this inter-core crosstalk is typically optimized to between -50 and -40 dB/km. Particularly, 40 dB/km crosstalk permits 100 km transmission using QPSK modulation (Tanaka, et al., 2017, Mizuno et al., 2017). There is a tradeoff between core count and inter-core crosstalk. In homogeneous MCF, the maximum number of cores in a fiber with a cladding diameter of 260μm is 22.

Heterogeneous MCF has various propagation constants for nearby cores, which further reduces inter-core coupling. The core count in a 250-μm MCF is maximized at 37 (Sasaki et al., 2017). In contrast to homogeneous MCF, inter-core crosstalk must account for all possible combinations of heterogeneous cores. In other words, the closest pair is not always the one with the least amount of crosstalk, and the β difference also plays a significant role. On the other hand, even if the heterogeneous structure suppresses inter-core coupling, it inevitably makes the crosstalk sensitive to macro-bends due to bend-induced effective index variation (S. Matsuo et al., 2016, Saitoh et al., 2013).

Similar to MCF, which encloses multiple channels in real space, MMF contains multiple channels in momentum space (k-space), i.e., in multiple modes with different propagation constants, or n_{eff}. Due to this analogy, it is likely that we can only consider the mode coupling with the closest modes (in n_{eff}) to represent crosstalk. Note, however, that the transverse coupling coefficient and n_{eff} are distinct for each mode. In other words, the closest pair in n_{eff} is not always the pair with the lowest mode coupling. This is

analogous to the heterogeneous MCF. Therefore, we may need to examine the mode coupling of each pair individually, or we may just need to consider the total mode coupling. However, a closer examination at the mode coupling can ease this analysis as shown in the following.

As mentioned in Sec. 4.1, there are two kinds of distinct inter-mode coupling for an OAM mode: intra-$|L|$ mode coupling with its nearly degenerate mode with the same $|L|$ (between SOa and SOaa modes), and inter-$|L|$ mode coupling with modes separated by ΔL=1,2,3, etc. Note that the coupling between two orthogonal polarization states (e.g., between SOa and SOaa modes with same $|L|$ but opposite polarization) is neglected since it can be disentangled by standard 2×2 MIMO technology. In terms of transverse coupling coefficient (Eq. 4.7), an extrinsic OAM needs to be provided by fiber perturbation, such as twisting or bending. The extrinsic OAM needed for intra-$|L|$ coupling is $\Delta L=2|L|$, which scales with $|L|$. In contrast, the extrinsic OAM needed for inter-$|L|$ coupling is ΔL=1,2,3, etc, which has no dependence on $|L|$ of the mode in consideration itself. Given the highest extrinsic OAM needed ($\Delta L=2|L|$), The intra-$|L|$ coupling is the least probable to occur, followed by ΔL=1 inter-$|L|$ coupling, and then other high-ΔL inter-$|L|$ coupling. In terms of n_{eff} separation, the closest pair is the intra-$|L|$ one (~10^{-4}), followed by ΔL=1 inter-$|L|$ one (~10^{-3}). The n_{eff} separation of high-ΔL inter-$|L|$ pairs are roughly $\Delta|L|$ times of the of the ΔL=1 Δn_{eff}. Under perturbations with a certain range of wavevectors, the mode coupling with smaller Δn_{eff} are more likely to occur.

Whether intra-|L| or ΔL=1 inter-|L| coupling are stronger depends on whether ΔL or Δn_{eff} plays a more dominant role. However, we can first be certain that ΔL=1 inter-|L| coupling is orders of magnitude stronger than that of the high-ΔL inter-|L| ones with larger Δn_{eff}. Therefore, crosstalk in the Gen6A3 fiber can be characterized by the intra-|L| and ΔL=1 inter-|L| mode coupling.

This chapter will focus on these two kinds of mode coupling to evaluate the crosstalk. We also compare the intra-|L| coupling with the inter-|L| mode coupling that occurs due to stochastic perturbations distributed throughout the fiber, which is differentiated from discrete inter-|L| coupling that might arise from mode excitation or fiber connections. Finally, we study the bend performance of these fibers, especially in the context of crosstalk.

8.2. Intra-|L| and Inter-|L| Mode Coupling

In this section, we will investigate whether intra-|L| or ΔL=1 inter-|L| coupling in Gen6A3 fiber is stronger. As stated above, it depends on whether ΔL or Δn_{eff} plays a more dominant role. Intra-|L| couplings are much stronger than inter-|L| couplings in both Gen4 (Gregg et al., 2015) and Gen5 (Sec. 5.2) fibers. This may not be necessarily the case for Gen6 fiber, where the |L|'s of available modes are much higher than that of Gen4 and Gen5 fibers, although the Δn_{eff}'s are similar.

The intra-|L| and the ΔL=1 content can be quantified by the ΔL=2L and the ΔL=1 content obtained from the analysis of the modal image using Ring Method (Sec. 3.1). Their contents were covered in the transfer matrix of a 0.5km Gen6A3 fiber measured in Sec.

7.2. Here we consider their parasitic power for a L=40 SOaa input as an illustrative example. As shown in Fig. 8.1 (a), the ΔL=1 content is two orders of magnitude higher than that of the ΔL=2L contents. However, it seems improbable that the ΔL-dependent transverse coupling coefficient can make such a significant difference. Actually, the ΔL=2L content varies substantially across modes. As shown in Fig. 8.1b, the ΔL=2L contents decrease rapidly from −20dB to −40dB for the bound modes but remain at a significantly lower level (~−40dB) for the TCMs. In contrast to the L-dependence of the ΔL=2L contents, the ΔL=1 content fluctuates around −20dB for all the L's. Either the L-dependent Δn_{eff} makes no difference to the inter-$|L|$ coupling, or such ΔL=1 content comes from external source (with no dependency on the modal property) as opposed to in-fiber mode coupling.

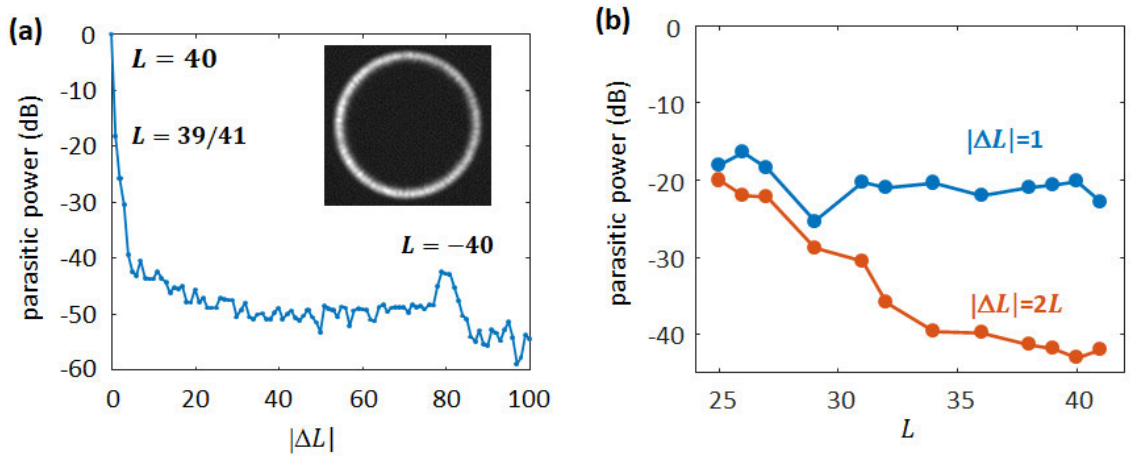

Figure 8.1: (a) Parasitic mode power spectrum for L = 40, RCP launched mode measured by spatial interferometry at 1550nm. Inset: launched mode image at fiber output; (b) The $|\Delta L|$=1 and $|\Delta L|$=2L content from Ring Method for all available modes.

The external impurity primarily comes from mode excitation. As mentioned in Sec. 3.2, the spatial interferometry based on output mode images is incapable of distinguishing between parasitic power from in-fiber mode coupling and input mode excitation. The

parasitic power from mode excitation is not associated with modes or fiber length, but the in-fiber mode coupling is typically mode-dependent (e.g., fields profile, Δn_{eff}) and also accumulate while propagating in the fiber. The length-dependent parasitic power is thus one means for distinguishing impurities from the two sources. Figure 8.2 shows the output ΔL=2L and the ΔL=1 content for modes with +|L| and LCP across three different lengths of Gen6A3 fiber. We use LCP here as the ΔL=2L contents for RCP are analogous (Fig. 7.5). Note that the 1-km length is achieved by doubling the 0.5-km Gen6A3 fiber using a Sagnac reflector (setup in Fig. 3.17). The ΔL=2L content becomes higher for longer length and lower |L| (Fig. 8.2a), while the ΔL=1 content shows no clear relationship with either length or |L| (Fig. 8.2b). Actually, using the SLM-based setup, the inter-|L| parasitic power is around −20dB after purity optimization, independent of the fiber type (Gen4 or Gen5 or Gen6). Therefore, such ΔL=1 content −20 dB is likely due to mode excitation at the input rather than the in-fiber mode coupling.

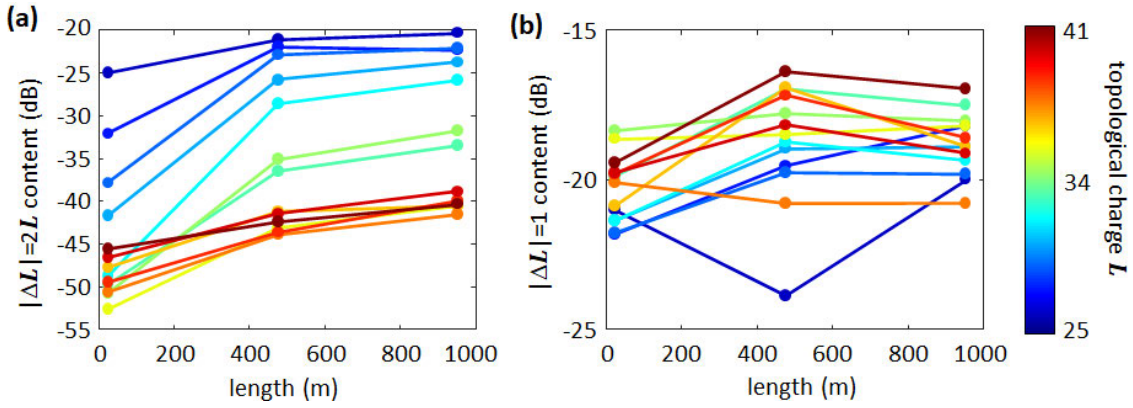

Figure 8.2: Parasitic power versus length of Gen6A3 fiber for (a) ΔL=2L and (b) ΔL=1 content.

Even though the −20 dB of ΔL=1 content in Fig. 8.1 is dominated by mode excitation, the in-fiber ΔL=1 coupling is unknown. More importantly, whether it is higher or lower than the intra-|L| coupling may have a direct impact on the overall crosstalk. It can be measured by time of flight as described in the next section. On the other hand, the content of the ΔL=1 inter-|L| coupling is also related to the understanding the low intra-|L| coupling – particularly, whether it is due to high-ΔL or TCMs. As previously mentioned, the intra-|L| coupling seems a distinctive feature of TCMs. However, it is less persuasive if it solely applies to intra-|L| coupling and the inter-|L| coupling level stays higher than the intra-|L| coupling level.

There is another concern other than the low-|ΔL| content. The noise floor ~-50dB is not very much below the ΔL=2L content, therefore their integration of can be substantial. As shown in the Sec. 3.1, the ~−50dB noise floor, together with the broadening of the ΔL=2L spectrum, actually comes from the Ring Method defect (cartesian-to-polar coordinate conversion) rather than the real modal content. Therefore, it is reasonable to consider the intra-|L| mode coupling as the total crosstalk if we can demonstrate the in-fiber inter-|L| couplings are much lower.

Figure 8.2(a) is an exemplary ToF signal from the ~0.5-km Gen6A3 fiber with an L=40 SOaa input (setup in Fig. 3.1). The majority of power is coupled to the dominant L=40 SOaa mode on the input side. Meanwhile, some parasitic modes are accidentally excited and appear as discrete spikes in the temporal trace. By integrating the power between the two corresponding spikes, the distributed coupling between the parasitic L=39 mode and the main L=40 mode can be determined. At such a low level of parasitic power,

this integration may capture the noise from the detector. The relative noise floor is minimized by increasing the oscilloscope's integration time (to 4096) and the input power to the maximum level the detector can sustain without encountering saturation. In this case, the integration of the distributed L=39 is calculated to be negative (possibly due to the ringing of the signal), therefore we assign it a value of −46dB, which is the minimum parasitic power that our present ToF can detect. It indicates that the parasitic power is less than what our current equipment can measure.

We use SOaa mode because, for a given $|L|$, SOaa mode has less time delay than SOa mode (due to lower group index of SOaa modes). Otherwise, while integrating the power between L=39 and L=40 using SOa mode, we will invariably pick up contribution form the SOaa mode. We did not measure the other SOaa mode (L=−40) since its ToF signal is similar to that of L=40.

The ΔL=1 distributed coupling of L=25-42 SOaa modes are shown in Fig. 7.2b. Modes strongly mixed with high-m modes are ignored (L=28, 30, 33). The ΔL=1 distributed coupling of all TCMs (>=34) is found to be below the measurement's noise floor (−46 dB). The outlier L=29 is a result of noise from the L=28 coupling strongly with high-m modes. The ΔL=1 distributed couplings of bound modes show a general trend of rapid decrease with higher $|L|$, as indicated by the dashed fitting line. The ΔL=1 discrete couplings are around the same level (~−20dB) as the ΔL=1 content from the Ring Method (Fig. 8.1b). It clearly shows that ~−20dB ΔL=1 content comes primarily from mode excitation but not in-fiber coupling.

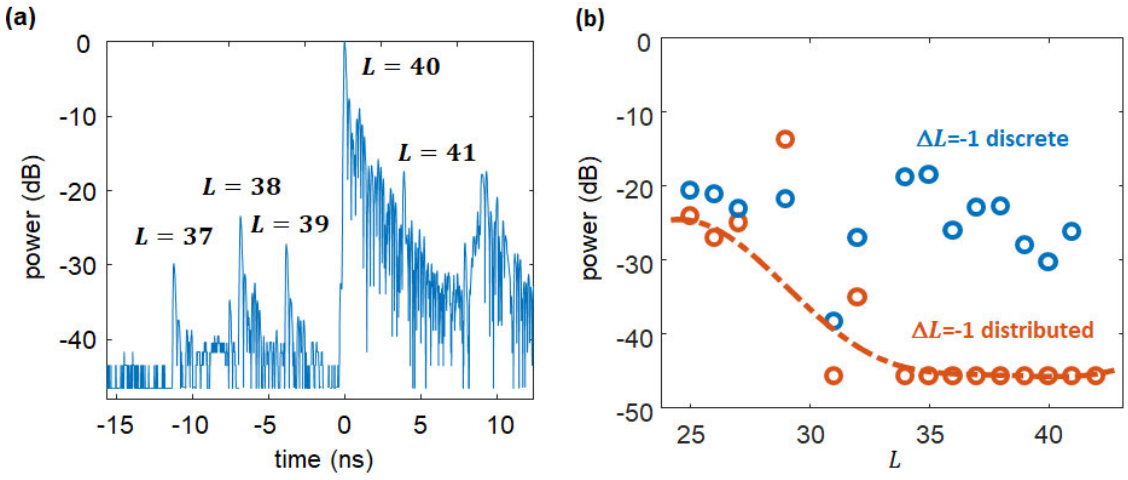

Figure 8.3: (a) Time of flight trace of L=40 RCP launched mode at 1550nm; (b) The discrete and distributed $|\Delta L|$=1 content from ToF for all available modes.

As mentioned before, the mode coupling between modes separated by $|\Delta L|$=2,3,4 should be much lower than that of $|\Delta L|$=1. Therefore, the high parasitic power of $|\Delta L|$=2,3,4 in Fig. 8.1 for L=40 input also comes from mode excitation, as that of $|\Delta L|$=1, while their in-fiber mode coupling should be much lower than -46 dB. This assertion is hard to be experimentally verified because measuring integrated power shoulders for the $|\Delta L|$=2,3,4 modes necessarily involves making assumptions on ignoring the intervening discrete peaks, which would yield large error bars in measuring a quantity that is already quite low. However, Fig. 8.3 provides a degree of confidence in this claim, since the distributed power between each discrete peak appears to be of the same order of magnitude as that between the L=39 and L=40 peaks, suggesting that this distributed crosstalk is also immeasurably low.

8.3. Record Low Crosstalk

After successfully measuring the in-fiber ΔL=1 inter-|L| mode coupling with the ToF, we can compare it to the intra-|L| mode coupling measured with the Ring Method. By comparing the two, we can determine which is stronger and calculate the overall crosstalk. As shown in Fig. 8.4, the intra-|L| mode coupling consists of all four modes for a certain |L|, while the inter-|L| mode coupling of the same |L| is represented by the mode with +|L| and RCP.

The parasitic powers of almost all intra-|L| mode couplings are higher than those of the inter-|L| mode couplings. This finding aligns with what we have found in Gen4 and Gen5 fiber that intra-|L| coupling is more likely to occur than inter-|L| coupling under common fiber perturbations. This is due to the fact that Δn_{eff} associated with inter-|L| coupling is an order of magnitude larger than associated with intra-|L| couplings. Thus, we can conclude that intra-|L| mode coupling is the primary contributor to crosstalk.

Ideally, intra-|L| and inter-|L| couplings should be combined to get the total crosstalk. Even though intra-|L| coupling is higher than inter-|L| coupling, they are roughly within the same order of magnitude. However, the measurement inter-|L| mode coupling of the TCMs is constrained by the noise floor −46dB of the ToF method. In the future, this inter-|L| mode coupling can be measured with more sensitive detector with a lower noise floor, or with long fiber where the accumulated crosstalk can be sufficiently higher than the noise floor. Therefore, we use the intra-|L| coupling to represent the crosstalk for the time being.

Since this measurement was conducted on a fiber with a length of ~0.5 km, crosstalk over 1-km fiber can be estimated by extrapolating this result, assuming similar length scaling laws for the growth of power in parasitic modes. Hence, a reasonable assumption is that the crosstalk of km-length fibers would be approximately 3-dB higher than the intra-|*L*| coupling measured from the 0.5-km fiber. Most TCMs exhibit crosstalk of <−40 dB/km, with some even achieving <−45 dB/km. There are a few outliers at the beginning of the TCM regime, where they transition from bound modes to TCMs. In comparison, the crosstalk for conventional TIR bound modes remains at ~−20 dB/km, which is the same as in previous investigations of MMFs. This indicates the inherent resistance of TCMs to mode mixing.

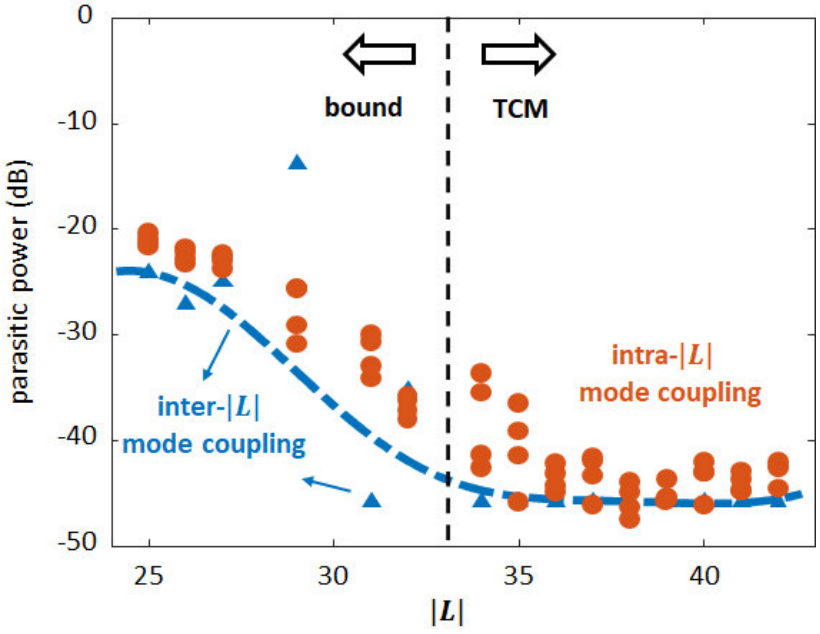

Figure 8.4: Parasitic power for inter-|*L*| and intra-|*L*| coupling in Gen6A3 ring-core fiber at 1550nm.

While high OAM may assist suppress intra-|*L*| coupling owing to larger Δ*L (=2L)*, the significant reduction in intra-|*L*| coupling in the TCM regime implies that it is

fundamentally related to the phenomenon of topological confinement itself. As elucidated in the preceding chapter, the loss difference plays a crucial role in suppressing mode coupling from the desired m=1 mode to accidentally degenerate high-m modes. This mechanism may be applicable to desired m=1 modes as well. In Fig.6.8, the cutback loss of Gen6A3 shows that the confinement losses of the SOa mode are higher than those of the SOaa mode. This loss difference, and thus the β separation in complex space, is likely to suppress the intra-L mode coupling. In addition, the loss difference also occurs between inter-$|L|$ mode pair, which can explain the rapid decrease of inter-$|L|$ mode coupling from bound to TCMs as well. In other words, distinct losses lead to suppression of mode couplings between all desired m=1 modes in the TCM regime, resulting in record-low TCM crosstalk.

TCMs make crosstalk of highly multimoded fibers on par with that of MCF for the first time. This low crosstalk allows long-haul transmission if the scattering loss can be reduced to that of commercial SMFs (Sec. 6.5.2). For example, –40 dB/km crosstalk results in –20dB crosstalk over a 100-km transmission. This crosstalk level permits QPSK modulation with 0.5 dB power penalty (Tanaka, et al., 2017, Mizuno et al., 2017). How crosstalk impacts capacity will be discussed in the next chapter. In addition, this low crosstalk is achieved via separation in k-space as opposed to real space, making it far more space-efficient than MCF.

8.4. Bend Resistance

As mentioned in Sec. 4.1, fiber bending is the most common perturbation in daily life. This perturbation introduces a wavevector for phase-matching coupling. Actually, it has a

significant impact on the heterogeneous MCF, which has n_{eff} variation across cores. The crosstalk deteriorates significantly (e.g., up to –20dB/km) around and below the threshold bending radius (~30 mm, depending on the inter-core index difference). Figure 8.5 shows the setup for examining the influence of bending. The bend is applied at the end of the 0.5-km Gen6A3 fiber. The input mode excitation is maintained by observing the discrete peaks in the ToF measurement (Fig. 8.2a).

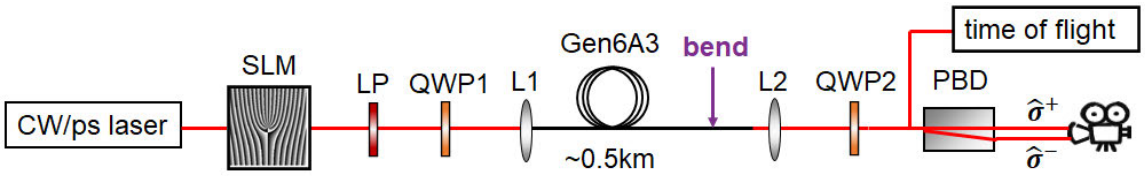

Figure 8.5: Experimental setup for examining the influence of bending on Gen6A3 fiber.

Figure 8.6 shows the intra-$|L|$ mode coupling when the fiber is bent with 10 loops to radii of 3 mm, 6 mm, and 15 mm. With 3-mm-radius bend, the crosstalk of all the modes decays. In comparison, with 6-mm-radius bend, the TCM crosstalk remains about –40dB/km while some of the bound modes degrades, demonstrating the unique robustness of TCMs. Under the 15-mm-radius bend, only two representative modes (one bound mode and the other TCM) are measured, and the crosstalk remain roughly the same as in the absence of sharp bends. Hence, the extraordinarily low crosstalk for TCMs is maintained even under tight bends with 6-mm radius.

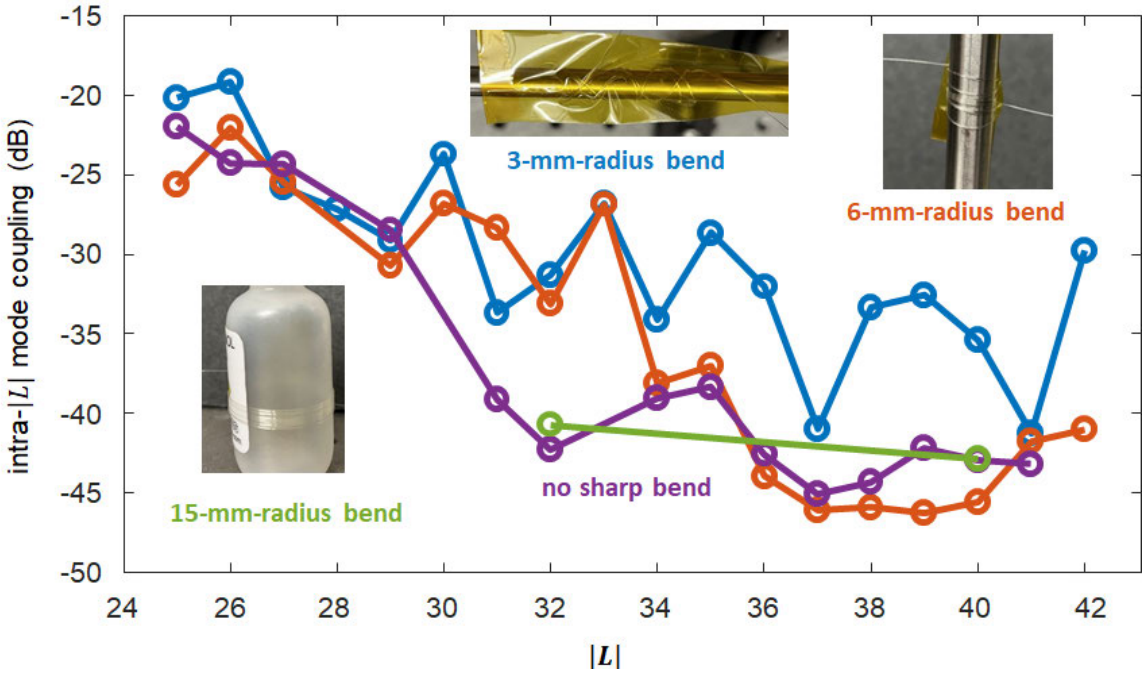

Figure 8.6: Intra-|L| mode coupling with and without sharp bends. The insets show 10 loops of fiber bent with various bend radius.

The different bend tolerance between bound modes and TCMs further affirms the inherent resistance to mode coupling for TCMs. As mentioned in the previous section, it is most likely owing to the separation of the complex propagation constants, which is unlikely to be compensated by an extra, real-valued wavevector provided by common fiber-bend perturbations. Thus, the TCM bend resistance significantly outperforms the robustness of heterogeneous MCFs (threshold bending radius ~30 mm) with similar or larger n_{eff} separations (S. Matsuo et al., 2016, Saitoh et al., 2013).

8.5. Summary and Discussion

In this chapter, we investigated the crosstalk by considering the mode coupling in the TCM-supporting fiber. With the aid of coupled mode theory, intra-|L| and ΔL=1 inter-|L| mode

couplings are chosen for close examination since all other mode couplings are orders of magnitude lower. For the ΔL=1 inter-$|L|$ mode coupling, we use time of flight to differentiate the input mode excitation and in-fiber mode coupling. We demonstrate that the mode excitation is the dominant source of ΔL=1 impurity, but the in-fiber mode coupling for TCMs is below the noise floor (-46dB) of the measurements. By comparing the ΔL=1 inter-$|L|$ and intra-$|L|$ mode coupling, we concluded the intra-$|L|$ mode coupling plays a dominant role and is used to represent the crosstalk.

As such, we found that the crosstalk reach record low values (<-40dB/km) in the TCM regime, whereas the crosstalk of the bound modes remains around –20dB/km. The TCM crosstalk maintains even in the presence of sharp 6-mm-radius bends while some of the bound modes degrade. We suspect such suppression of intra-$|L|$ coupling is fundamentally due the confinement-loss difference between SOa and SOaa modes, hence further lifting their degeneracy in the complex space. Further investigation is needed to confirm this hypothesis. We not only achieve the lowest crosstalk in MMFs but also make the crosstalk in a MMFs on par with that of MCFs for the first time. The low crosstalk potentially enables long-haul transmission using TCMs.

Chapter 9

9. Scaling the Information Capacity by TCMs

9.1. Capacity and Spectral Efficiency

Topological confinement has proven to be an effective approach not only for achieving a high mode count (Chapter 7) but also for minimizing crosstalk (Chapter 8), which are two key parameters in space-division multiplexing (SDM) for scaling the information capacity. It is essential to determine the actual capacity increase enabled by TCMs and compare it with the benchmark MCFs to fully evaluate its potential. A system test with data transmission is required to measure the information capacity of the TCM-supporting fiber. However, conducting system tests is not possible at its current maturity due to time and technical constraints (detailed in Sec. 9.5). Therefore, we need to find an alternative way to estimate the capacity enhancement enabled by TCM. To do so, we will use the Shannon formula (Eq. 1.2) to make a reliable estimation of the potential capacity increase.

The spectral efficiency (SE) is typically used in SDM to evaluate the information content transmitted over a given bandwidth in a communications system. It is given by the Shannon capacity (Eq. 1.2) divided by the bandwidth as

$$\mathrm{SE} = \frac{C}{B} = \sum_{i=1}^{M} \log_2\left(1 + \left(\mathrm{SNR}_i^{-1} + \mathrm{XT}_i\right)^{-1}\right) \tag{9.1}$$

In the previous chapters, the channel count M (Sec. 7.3) and crosstalk XT (Sec. 8.4) of TCM-supporting fiber Gen6A3 at 1550nm have been presented. While one can assume that the maximum SNR is the same as that of a standard SMFs it is worth examining it

carefully given that nonlinear properties of distinct modes may differ (detailed in Sec. 9.4).

Bandwidth is another important factor that needs to be considered. Although the bandwidth factor in Shannon capacity is eliminated by considering SE, it is crucial to verify that the SE remains stable across different wavelengths or determine the bandwidth within which the SE remains reasonably high. This is because the overall capacity of the system is a product of both the SE and the bandwidth. In other words, determining the bandwidth of SE is closely related to the compatibility with the well-established wavelength-division multiplexing (WDM) technique. It is imperative that the adoption of SDM should not come at the cost of sacrificing the benefits of mature techniques such as WDM, which is critical for realizing the full potential of spatial channels and gaining a capacity advantage over conventional non-SDM telecom systems.

The choice of the spectral window to examine depends on the spectral window of the optical amplifier for WDM. The conventional telecom spectral window is the C-band, ranging from 1530nm to 1565nm, which is determined by the amplification window of the erbium-doped fiber amplifier (EDFA). However, recent developments in fiber amplifiers have enabled extension of the amplification window to the S-band (1460–1530nm) and to the L-band (1565–1620nm). This wideband amplification was achieved using a combination of discrete Raman amplifiers, a thulium-doped fiber amplifier (TDFA), and a conventional EDFA (Galdino et al., 2020). The implementation of all these three bands has been demonstrated in MCFs (Puttnam et al., 2021). To obtain the SE across this wideband, it is necessary to determine the mode count, crosstalk, and loss across the S, C, and L bands (Sec. 9.3).

In this chapter, we re-measured the transfer matrix of Gen6A3 but with length effectively around 1-km. Then, we measure the relevant properties of all the available modes in the telecom S, C and L band. We end this section by using the measured attributes to estimate the spectral efficiency of fibers featuring TCMs, and hence make predictions for the kind of data transmission systems in which it may find uses.

9.2. Kilometer-Scale Transmission

At its current maturity, the benchmark TCM-supporting fiber Gen6A3 only features around 0.5-km long. However, it would be ideal to investigate our fibers properties over 1-km length scale. Even though such length is more than enough for device length (~10 m) applications, data center lengths are modulo km. In addition, it is a common practice to measure the 1-km fiber properties and estimation the long-haul (~100 km) transmission (37-core MCF). Although the mode count may not change significantly and crosstalk can be estimated by adding 3dB (Sec. 8.4), it would be beneficial to evaluate transmission over 1km to validate the attractive attributes of the fiber over length scales that may be of interest in applications. Given the current 0.5km length, the fiber length is effectively doubled by using a Sagnac reflector to guide the output light back to the fiber (Sec. 3.5). Figure 9.1(a) shows the full transfer matrix for all the modes $|L|$=25−42 with both LCP and RCP over 1-km Gen6A3 fiber. Similar to the 0.5-km transfer matrix (Fig. xx), the deep blue square markers along the diagonal are bound modes ($|L|$=28,30,33) that experience mode mixing, and the majority of the power in the two off-diagonals adjacent to the launched mode are from mode-launch imperfections (~–20 dB), whereas fundamental, in-fiber crosstalk in these modes is immeasurably low (Sec. 8.3). The good modes (red square markers) exhibit

crosstalk ~ −40 dB/km for TCMs and ~ −20 dB/km for conventional bound modes (based on measured power in the anti-diagonals), which confirms the crosstalk measured in the 0.5-km fiber (Sec. 8.4). The total mode count is again 50 by excluding the distorted bound modes and outliers in the TCM regime that exhibit high loss > 10 dB/km (criteria detailed in Sec. 7.3). Also measured are the polarization extinction ratios (PER) (Fig. 9.1(b)), which increase with $|L|$ from ~10 dB to ~15 dB, overall, 3-dB less than that of the 0.5-km Gen6A3 (Fig. 7.5).

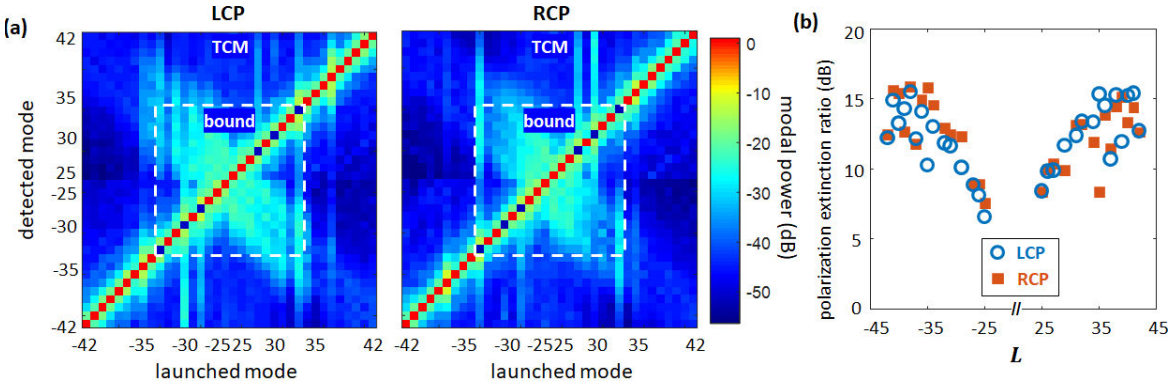

Figure 9.1: (a) Transfer matrices of all the modes $|L|$=25-41 with LCP and RCP and (b) polarization extinction ratios of all available modes in the Gen6A3 ring-core fiber with equivalent 1-km length.

Figure 9.2 displays the time-of-flight measurements obtained by transmitting 100-GHz-bandwidth telecom-compatible pulses at 1550 nm over a distance of 1 km of fiber, indicating the potential for practical signal transmission. It suggests that future work can include incorporating the data into the pulse trains for system test to measure the information capacity.

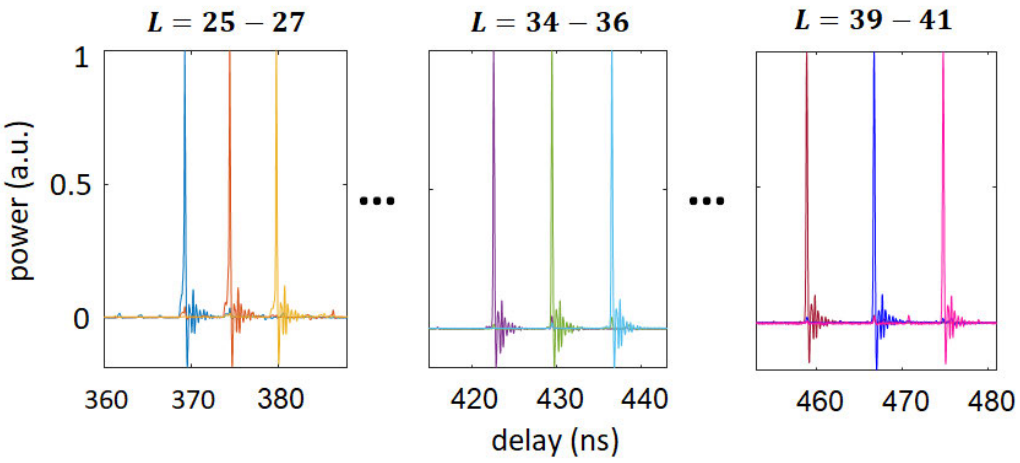

Figure 9.2: Pulse propagation of select modes with LCP in 1-km Gen6A3 fiber.

9.3. Wideband Demonstration

To measure the bandwidth the system, we repeat the same measurement using an ECL at 6 representative wavelengths (1460nm, 1505 nm, 1530nm, 1550nm, 1565nm, 1590nm) to cover the telecom S, C and L band, as shown in Fig. 9.3(a). The last part of the L band (1590-1620nm) is not covered due to the limited range of our ECL, but measured trends, described below, do not suggest any abnormal behavior in the spectral range we could not measure.

We use the crosstalk as the metric for each mode at a certain wavelength as it directly determines the capacity that can be achieved. As mentioned in Chapter 7, we use the intra-$|L|$ mode coupling to represent the crosstalk as it is the dominant in-fiber mode coupling and thus would represent the wavelength-dependent trend. The measurement of ΔL=1 inter-$|L|$ mode coupling was limited by the noise floor of the time of flight and other inter-$|L|$ couplings are expected to be orders of magnitude lower. These inter-$|L|$ mode coupling can be measured in the future with better measurement technique or longer fiber,

but they are likely to follow the spectral trend of the intra-|L| mode coupling shown here. Also, we only measure a quarter of all four modes for a given |L| as they have similar crosstalks and the total mode count is estimated by multiplying the measure mode count by four.

As before, outlier modes with excessive mode mixing or loss were excluded in the plot. Red and blue curves of various shades denote TCM and TIR bound mode crosstalks, respectively. The crosstalk of modes depicted by other colors are typically for TIR bound modes that are close to cutoff, and hence modes that resemble TCMs as wavelength increases. Again, the average crosstalk of all TCMs lies between −40 dB/km and −45 dB/km, whereas most bound modes appear pinned at a crosstalk of −20 dB/km, regardless of wavelength. Most interesting is the crosstalk of TIR bound modes close to cutoff, demonstrating that, as the guidance mechanism for light evolves from TIR to topological confinement, the crosstalk also improves by two orders of magnitude. Figure 9.3 (b),(c) depict the average crosstalk and mode count, respectively, demonstrating a 1-km-long MMF with record high mode counts of ~50 comprising ~20 conventional TIR bound modes with < −20 dB/km crosstalk and ~30 TCMs with crosstalks < −40 dB/km across three telecom spectral bands of interest.

As shown in Fig. 9.3(d) the average losses for TCMs (~5.0 dB/km), bound modes (~1.4 dB/km) and all modes (~3 dB/km) remain at similar levels across the three telecom spectral bands. The average simulated confinement loss of TCMs (~0.1 dB/km) is an order of magnitude lower than the measured TCM loss. As discussed in greater detail in Sec. 6.5, the measured loss of TCMs and also the bound primarily come from interfacial scattering

loss, which is expected to decrease to ~0.4 dB/km by manufacturing optimizations. This would make these fibers suitable for substantially longer telecom links.

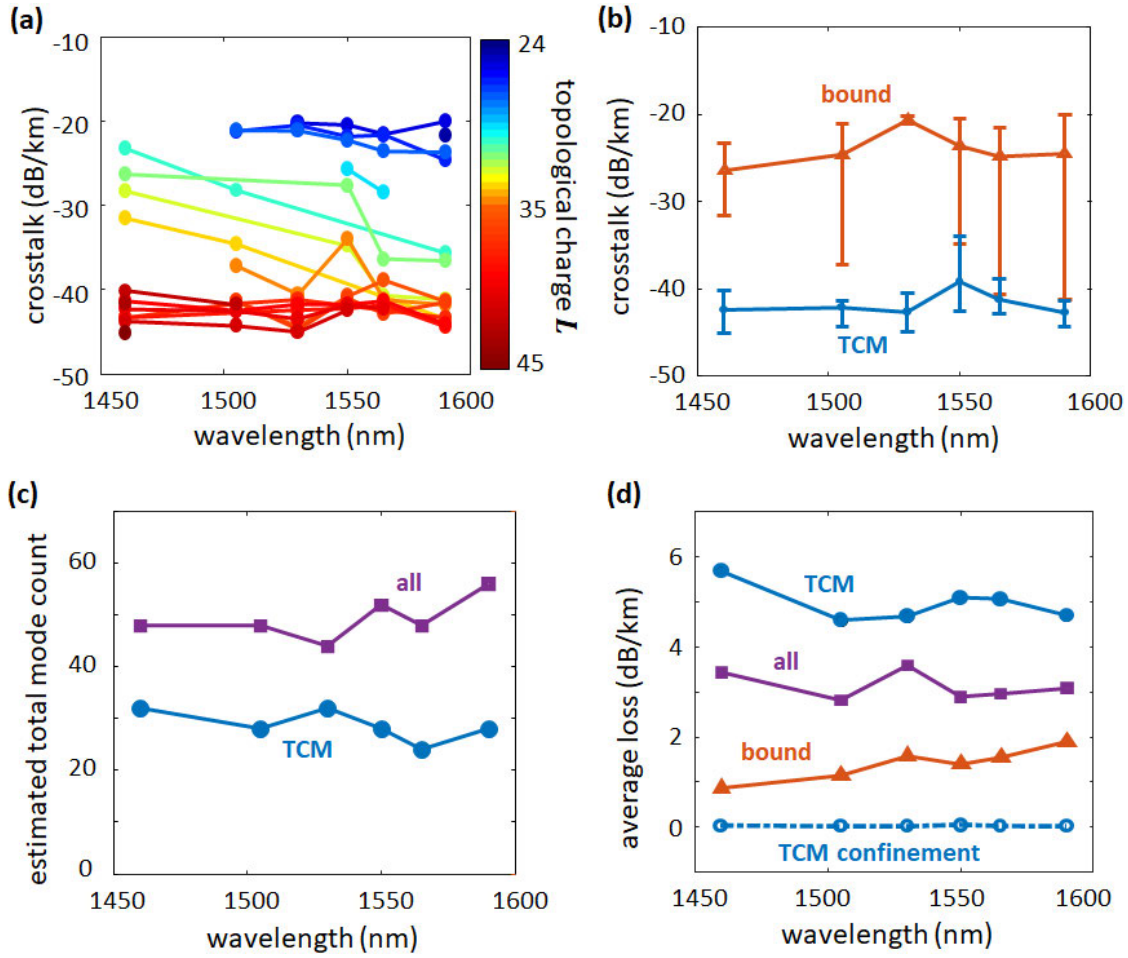

Figure 9.3: (a) Crosstalk vs. λ of modes with $+|L|$, RCP in S, C and L telecom bands; (b) Average crosstalk (left) and mode count (right) vs. λ for TIR bound modes, TCMs, or their sum. (c) Average total loss vs. λ of good bound modes, TCMs and their sum. Dashed curve represents the average simulated confinement loss of TCMs.

9.4. Maximum SNR and Fiber Nonlinearity

As discussed in Sec. 1.1, the maximum SNR allowed in conventional SMF-based communication system is fundamentally constrained by the Kerr nonlinearity in fibers. Its manifestation can be described as the modification of the refractive index:

$$\Delta n = n_2 I \tag{9.2}$$

where n_2 is the nonlinear refractive index determined by the material, and I is the optical intensity which the optical power per unit area. The fiber nonlinearity is proportional to the signal power, and can cause signal distortion when it exceeds a certain level. This limits the signal power and subsequently the SNR. Fibers with lower nonlinear indices are achieved based on new material (Dragic et al., 2012) or air-core guidance realized by photonic-bandgaps (Russel, 2003). However, none of these fibers has, to date, achieved telecom material losses and so we should stick with silica, at least for telecom related discussions.

The limitation of SNR is the primary motivation to SDM. While the SE of a particular spatial channel is limited by SNR, increasing the number of channels allows for scaling the SE and therefore the capacity. In standard SMF, the maximum SNR for long-haul transmission is approximately 30 dB (Essiambre et al., 2012), although this number may vary depending on the calculation model or application scenario. Although the same maximum SNR can be applied to TCM-supporting fiber, it would ignore the different nonlinearity properties. Typically, MMF has a larger effective area than SMF and therefore greater nonlinear resistance. We have increased the fiber size from Gen4 to Gen5 to Gen6 primarily to enhance the TCM effect, but it may also provide a larger effective area that can potentially improve the SNR.

The effective areas (A_{eff}) of available modes in Gen6A3 fiber is calculated based on recorded intensity profiles (setup in Fig. 3.1) using Eq. 2.21. The imaging stitching technique (Demas et al., 2015) is used to effectively increase the dynamic range of the

InGaAs camera. It helps to capture the long tail of the radial intensity profile for accurately measuring the effective area. We use a 0.5-nm bandwidth ps laser in this measurement rather than the ECL to avoid interference that can result in small fluctuations of the measured intensity profile, which would result in large fluctuations in A_{eff} calculated. Figure 9.4a shows that the effective areas (A_{eff}) of these modes, measured at 1550nm, are an order of magnitude larger than those for SMFs or MCFs (80 μm^2). The overlaid dashed line is the simulated A_{eff} (calculated based on the simulated field profiles) which matches the measured A_{eff} well. Given that our ps laser source has limited bandwidth, but we would need A_{eff} values across the S, C and L bands for SE estimations, we use simulated values at the other 5 wavelengths (Fig. 9.4 (b)), which remains at similar levels, 10× larger than that of SMFs and MCFs. Therefore, the TCM-supporting fiber offers a significantly larger effective area while also providing additional benefits such as a large mode count and low crosstalk.

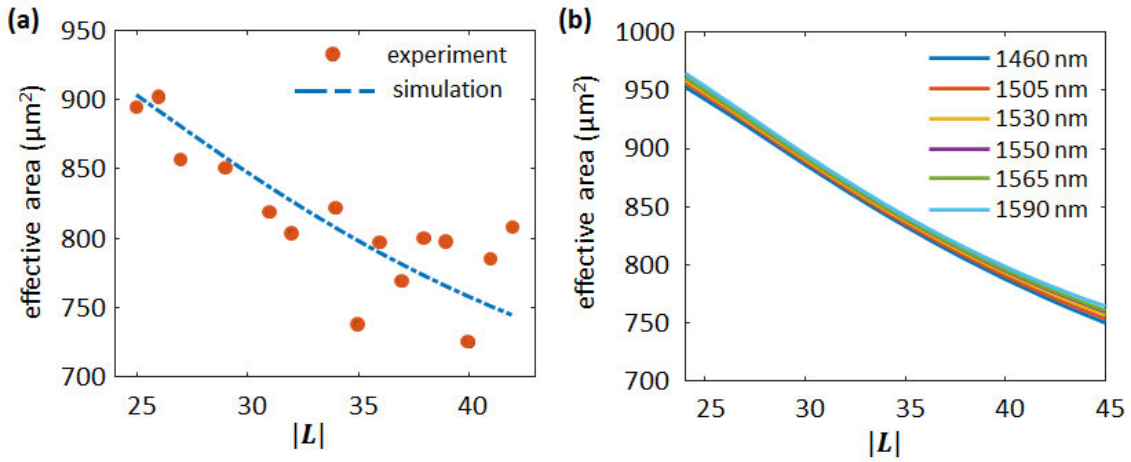

Figure 9.4: (a) Measured and simulated A_{eff} at 1550nm vs. $|L|$; (b) simulated A_{eff} vs. $|L|$, at 1460nm, 1530nm, 1550nm, 1565nm and 1590nm, respectively.

Chromatic dispersion is also known to play an important role in the nonlinear behavior of propagating pulses in a fiber (Agrawal, 2019). Figure 9.5 illustrates the simulated dispersions at all the 6 wavelengths, which are also ~10 times greater than the SMF dispersion (16.8 ps/ns-km).

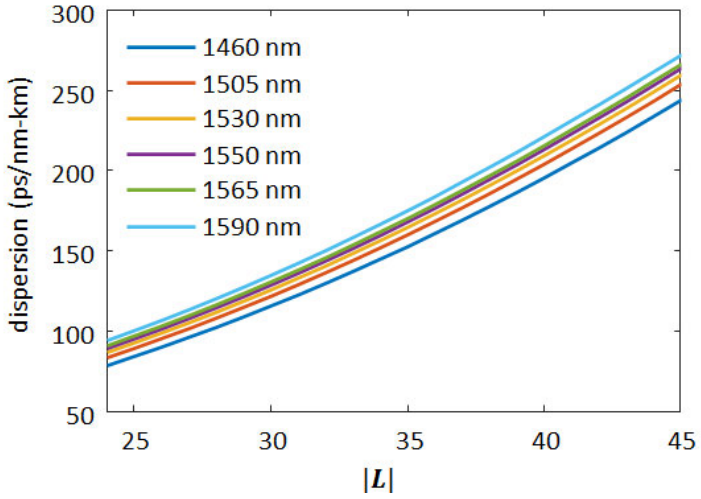

Figure 9.5: Simulated chromatic dispersion at 1460nm, 1530nm, 1550nm, 1565nm and 1590nm, respectively. Plots at these multiple wavelengths show that the high chromatic dispersion characteristics of these modes is retained across the S, C, and L bands, respectively.

While the study of the influence of dispersion and A_{eff} on the nonlinear propagation of pulses in optical fibers is well established for short fiber lengths, the presence of multiple coherent and well as incoherent, spectrally diverse pulses in a telecom system, along with strong coupling long fiber lengths, significantly complicates nonlinear pulse propagation analysis. The effect of nonlinearity to SNR can be described by the noise added by the generation of nonlinear interference (NLI). For coherent transmission systems, a Gaussian model for the NLI power can be approximated as (Poggiolini et al., 2011)

$$P_{\mathrm{NLI}} \simeq \left(\frac{2}{3}\right)^2 N_{\mathrm{s}} N_{\mathrm{s}} \gamma^2 L_{\mathrm{eff}} P_{\mathrm{Tx},ch}^3 \frac{\ln(\pi^2 |\beta_2| L_{\mathrm{eff}} B_{\mathrm{WDM}}^2)}{\pi |\beta_2| R_{\mathrm{s}}^3} B_n \tag{9.3}$$

where $P_{\mathrm{Tx},ch}$ is per-channel power, $\beta_2=-\lambda^2 D/(2\pi c)$ is related to chromatic dispersion D, $L_{eff}=[1-\exp(-\alpha L_s)]/\alpha$ is the effective length, $\gamma=2\pi n_2/(\lambda A_{eff})$ is the nonlinear coefficient, α is the power loss per unit length, L_s is the span length, N_s is the number of spans, B_n is the noise bandwidth, $B_{\mathrm{WDM}} = N_{\mathrm{ch}} R_{\mathrm{s}}$ is the WDM bandwidth, N_{ch} is number of WDM channels, R_{s} the symbol rate.

Therefore, we can calculate how much reduction of the NLI noise we may be able to obtain with the 10× higher A_{eff} and dispersion that are features of TCM fibers. Henceforth, the SNR enhancement can also be calculated. However, before proceeding with SE estimations, we need to consider ASE, which is another limiting factor for SNR. It comes from EDFAs that are essential in a practical long-haul communication system. The ASE is a fundamental quantum noise thus it is much simpler and more accurately predicted, in comparison to NLI. Assuming ideal filtering (noise bandwidth is equivalent to signal bandwidth) and the Nyquist limit of WDM (i.e., most efficient use of the available spectrum), ASE can be approximated as white Gaussian noise given by

$$P_{\mathrm{ASE}} = N_{\mathrm{s}} F (e^{\alpha L_{\mathrm{s}}} - 1) h \nu B_{\mathrm{n}} \tag{9.4}$$

where F the EDFA noise figure, h the Planck's constant, and ν the center frequency of WDM comb.

Thus, without considering the crosstalk, the overall SNR is given by

$$\mathrm{SNR} = \frac{P_{\mathrm{Tx},ch}}{P_{\mathrm{ASE}} + P_{\mathrm{NLI}}} \tag{9.5}$$

Substituting Eq 9.4 & 9.5 into the Eq 9.3, we obtain the maximum signal-to-noise (SNR) ratio (in dBs) in a fiber without crosstalk (Hayashi et al., 2012)

$$\mathrm{SNR}_{SC,max,dB}$$

$$\approx \frac{1}{3}\left[10\log_{10}\left(|\beta_2|L_{eff}\right) - 20\log_{10}\left(\gamma L_{eff}\right) - 2\alpha_{\mathrm{dB}}L_s\right] + 10\log_{10}\left(\frac{C_{\mathrm{system}}}{N_{\mathrm{s}}}\right) \qquad (9.6)$$

where the system term is given by

$$\frac{C_{\mathrm{system}}}{N_{\mathrm{s}}} = \left[\ln(\pi^2|\beta_2|L_{\mathrm{eff}}B_{\mathrm{WDM}}^2)\right]^{-\frac{1}{3}}\left(\frac{2}{\pi}\right)^{-\frac{1}{3}} {N_{\mathrm{s}}}^{-1}(Fh\nu)^{-\frac{2}{3}} \qquad (9.7)$$

When assuming moderately high $|\beta_2|$ and adequately broad B_{WDM}, the system term $\frac{C_{\mathrm{system}}}{N_{\mathrm{s}}}$ remains constant. For a standard SMF, the maximum SNR is ~27 dB after 100-km transmission in this model. The maximum SNR of any fiber mode can thus be obtained by comparing its term in the square bracket in Eq. 9.6 with that of standard SMF. The three main factors that affect the performance of the system are A_{eff}, D, and loss, which are 80 um^2, 16.8 ps/nm-km and 0.19 dB/km for standard SMF. Fig. 9.6 shows the maximum SNR at 1550nm versus transmission distance for fundamental mode in standard SMF, as well as the *L*=25 & 40 SOaa in Gen6A3 fiber with measured loss and also loss of 0.43 dB/km that we predict may be feasible for TCMs. The two modes are representative of a bound mode and TCM and the justification for anticipating that the loss of these fibers would be as low as 0.43 dB/km was provided in Chapter 6, section 6.5.2.

At short distances, the maximum SNRs for both L=25 & 40 are indeed 10 times higher than that of SMF due to 10x larger A_{eff} and D mentioned above. However, the high loss constrains the application to ~km scale. With an anticipated loss of 0.43 dB/km, the SNR advantage of these fibers, in comparison to SMF, is maintained up to ~50km. As expected, loss plays a more significant role for longer-distance transmission. On the other

hand, even though the anticipated loss in high-index-contrast fiber is higher than that in standard SMF, the 10x larger A_{eff} and D greatly enhance the SNR and enable potential long-haul transmission.

It should be noted that the model presented here is for systems with distances typically exceeding 50 km, where EDFAs are necessary and introduces additional noise. Therefore, the results may not be directly applicable to short-range applications such as data centers or devices, where distances are typically around or below 1 km and EDFA is not required. Nevertheless, it can still be useful to see the trend and make comparisons between the TCM-supporting fibers and SMFs (and thus MCFs).

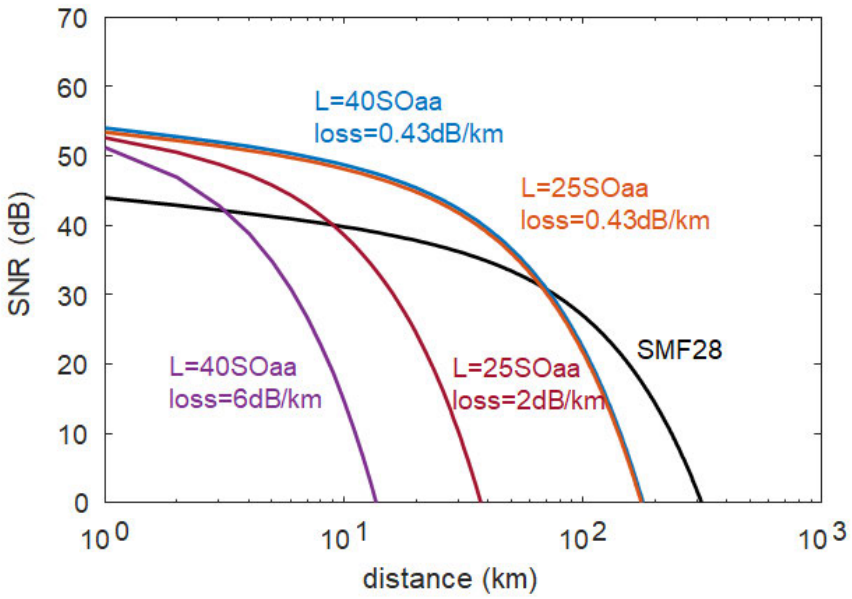

Figure 9.6: Maximum SNR at 1550nm versus fiber distance for fundamental mode in standard SMF, *L*=25 & 40 SOaa in Gen6A3 with actual loss and also assumed loss 0.43 dB/km.

9.5. Spectral Efficiency Estimation

Using the estimated SNR (Fig. 9.6), along with the measured crosstalks and mode counts (Fig. 9.3a), we can calculate the SE for all modes at 1550nm, as illustrated in Fig. 9.7. Note that this SE estimation is based on several assumptions: (a) (de)multiplexers are readily available to fully utilize each spatial channel; (b) the associated device technologies have advanced sufficiently to minimize contributions to crosstalk; (c) there is no nonlinear interaction between modes; (d) 2×2 MIMO is implemented to fully exploit degenerate modes with opposite polarization; and (e) perfect modulation is achieved.

With the current measured loss, the SEs of both TCM and all the modes decrease dramatically after ~10km (Fig. 9.7). Hence, under its current maturity, the TCM-supporting fiber would be suitable for fiber-device or data-center applications.

Assuming a loss of 0.43 dB/km (Sec. 6.5.2), the aggregate SE reaches 211 bit/s/Hz over a 100-km long fiber link. In addition, TCMs account for the majority of the SEs, particularly over long distances. Even though the maximum SNR of the bound mode and TCMs are almost the same (Fig. 9.7), their different crosstalk may have a substantial impact on the SE. For example, a bound mode with –20dB/km crosstalk results in 0-dB total SNR after 100 km of transmission (thus zero SE), but a TCM with -40 dB/km crosstalk is possible to reach 20-dB total SNR (without considering the effect of maximum SNR and loss).

Also plotted is the SE of the benchmark 22-core MCF which holds the record in SE, as of this writing, for uncoupled MCFs. Note that here we use the theoretical SE which is ~270 bit/s/Hz over a 50km fiber (Luis et al., 2017) while the experimental value is a bit

lower, at 211 bit/s/Hz after 30km (Puttnam et al., 2015). As is evident, TCMs enable the SE of MMFs to be on par with that of MCF. A key distinction between the two fibers is the required fiber size. In contrast to the MCF, which requires a 250µm cladding diameter, the TCM-supporting fiber supports all modes within a 56µm diameter core. While the fibers we used in this thesis had 250µm diameter (based not on any performance requirement, but on the diameter this particular fabricated fiber had), given that the entire signal occupies a spatial extent substantially defined by the 56µm core diameter, these fibers could have been drawn with standard 125µm claddings. Hence, the spatio-spectral efficiency of the TCM-supporting fiber for which we conducted these calculations is four times that of the best performing MCF, as of this writing. More generally, TCM fibers share the attribute of MMFs that they are significantly more spatially efficient than MCFs.

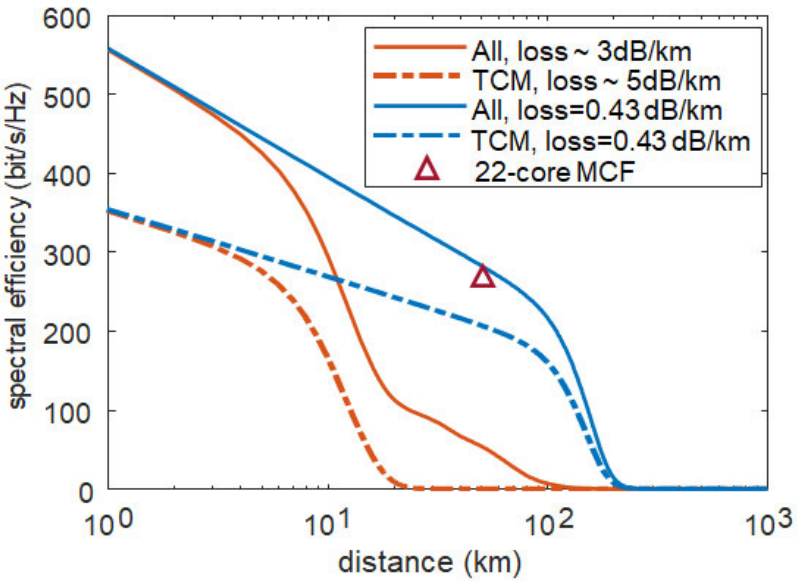

Figure 9.7: Spectral efficiency versus fiber distance with all available modes and only TCMs at 1550nm. It is calculated using the actual loss value and also the assumed loss 0.43 dB/km.

Similarly, the SE of the remaining wavelengths shown in Fig. 9.3 can be calculated based on Eq. 9.1. The maximum SNR can be estimated using the simulated A_{eff} (Fig. 9.4b) and dispersion (Fig. 9.5). Again, 0.43 dB/km is anticipated as the loss to estimate the long-haul SE. As shown in Fig. 9.9, the aggregate SE of all available modes across a 50-km fiber remains at ~300 bit/s/Hz in the S, C and L bands. This can enable WDM compatibility and hence result in high information capacity.

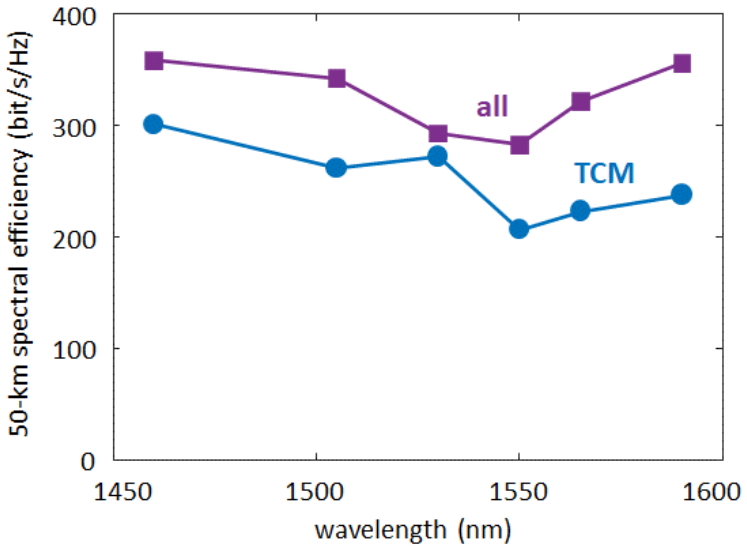

Figure 9.8: Spectral efficiency of all modes and just TCMs over 50-km Gen6A3 fiber across S, C and L band.

It is important to highlight that the crosstalk values used for the SE estimation are specifically for the intra-|L| coupling, which shows the best performance at approximately -45 dB/km for TCMs (Fig. 9.3a). As discussed in Chapter 8, the inter-|L| mode coupling is expected to be much lower than the intra-|L| coupling. Hence, a 4x4 MIMO configuration can be employed to disentangle the intra-|L| coupling and thereby further reduce the crosstalk by focusing solely on the inter-|L| mode coupling. As depicted in Fig. 9.6, the maximum SNR of the TCMs can reach approximately ~53 dB for ~1km fibers. Therefore,

by utilizing a 4×4 MIMO, it becomes possible to fully leverage the high maximum SNR and achieve an even higher capacity for the system.

9.6. Summary and Discussion

This chapter investigates the information capacity of an optical fiber enabled by TCMs. We achieved a 1-km transmission by doubling the 0.5-km Gen6A3 fiber using a Sagnac reflector. By repeating the measurement at 6 representative wavelengths across telecom S, C and L bands, we demonstrate that all the metrics remain stable in a 130-nm wideband. These metrics include the average crosstalk of both TCM and bound modes, the mode count and the average loss. Hence, we demonstrate a 1-km-long transmission with record high mode counts of ~50, comprising ~20 conventional TIR bound modes with < −20 dB/km crosstalk and ~30 TCMs with crosstalks < −40 dB/km across telecom S, C and L bands. Using a model for coherent transmission systems, we estimated a 10-fold increase in SNR at a ~km distance as a result of 10× larger effective area and dispersion. This can enable long-haul transmission based on the anticipation that the measured loss can be optimized to ~0.43 dB/km as other high-index-contrast fiber. The overall spectral efficiency is estimated to be ~300 bit/s/Hz over a 50-km fiber across the S, C and L band. This would be comparable to the uncoupled MCF record. In addition, the spatial spectral efficiency would potentially be four times that of MCF.

While the capacity estimation shows promising results, it is important to acknowledge that it relies on several assumptions. Some of these assumptions are reasonable and well-established, such as the utilization of 2×2 MIMO, which is a mature technique, and perfect modulation, which is commonly employed for capacity estimation.

Some assumptions pose technical challenges but are likely achievable, such as the development of a low-crosstalk MUX capable of simultaneous multiplexing of all ~50 modes. However, certain assumptions remain uncertain or unknown. For example, the absence of inter-modal nonlinear interaction has not been well investigated and it is uncertain whether it can be achieved, although the large group velocity differences between the modes makes this a possibility. In addition, the anticipated loss of 0.43 dB/km may require further investigation and validation. In this regard, the most probable application in the near future may include fiber devices or data centers within 1-km range, rather than long-distance transmission. Furthermore, the suitability of the coherent transmission model for our specific case may require further examination. Ultimately, to obtain a definitive capacity value, it is necessary to conduct data-transmission system tests that validate the assumptions made throughout the estimation process.

Chapter 10

10. Conclusion and Outlook

10.1. Conclusion

We have demonstrated topological confinement as unique regime of light guidance beyond conventional cutoff in optical fibers. We demonstrated that the confinement loss decreases with OAM order, leading to low-loss transmission in fibers of km length scales for these cutoff modes. The frustrated coupling of TCMs helps address the inevitable mode coupling that has posed a fundamental limit in scaling the number of unmixed bound modes in any type of multimode fiber. As such, we are able to scale the mode count past the numbers at which scaling with conventional OAM bound modes has stagnated. The frustrated coupling of TCMs also enables record amount of unmixed OAM modes in a conventional step-index fiber in which all conventionally bound modes mix completely. Finally, we achieve up to 50 low-loss modes with record low crosstalk over a ~1km ring-core fiber. Moreover, the 130-nm bandwidth of these modes make this mode guidance regime compatible with WDM. Calculations of the spectral efficiency of these modes reveals that up to ~210 bit/Hz/s may be achieved over 100km of propagation. This calculation was based on the SNR estimated from an ideal uncompensated system and by assuming that future manufacturing optimizations would bring the losses of these modes down to ~0.43 dB/km. The inherent scalability of TCMs also promises further scalability in mode counts and thus record information capacity, potentially making it the preferred choice for transmission links in future SDM systems. Apart from significantly increasing the information content

per photon for quantum or classical networks, TCMs have the potential to find applications in nonlinear signal processing and light-matter interactions, where having a large ensemble of independent orthogonal states of light may be beneficial.

10.2. Outlook

10.2.1 Classical Telecommunications

Even though we have estimated the spectral efficiency for long-haul transmission, a central caveat to those calculations was that we assumed that mode losses would reduce considerably, compared to currently measured losses. In the shorter term, while the loss optimization goal is pursued, we expect that the TCM-supporting fiber may be especially useful in data-center and device length applications. We would need to confirm the estimated spectral efficiency and information capacity by system experiments in which we hope to use a ~1km Gen6A3 fiber replica rather than double-passing through a fiber, as was done in the experiments described in this thesis. To simultaneously demonstrate all the spatial channels, we would need to develop a 50-mode MUX to generate all available modes. Such high-mode-count MUX'es have been achieved, and among the variety of technologies that may be candidates for such devices, we expect devices made with MPLCs (Bade et al., 2018) to be especially promising.

Among device-length applications, we expect a 50-mode amplifier would be most impactful given that shared-pump amplification can potentially save a lot of energy (Jung et al., 2020). In addition, the similarity in the intensity profiles of OAM mode also promises low differential modal gain. Furthermore, a core-pump scheme (Kang et al., 2015, Jung et al., 2017) could potentially increase the power efficiency even further. Preliminary

simulations conducted using the properties of the fiber described in this thesis show promise in this regard (Greenberg et al., 2023).

We demonstrated wideband transmission with these fibers, which makes the scheme compatible with WDM. However, we need further account for inter-modal nonlinear effects that are likely to be strongly phase matched for channels with sufficient wavelength detuning (Ellis, et al., 2013, Rademacher et al., 2016). This can potentially lead to an increase in nonlinear crosstalk scaled with mode count and adversely affect the capacity. Hence, the SE estimation in Chapter 8 needs to further elaborated by taking all the impairments into account. Ultimately, a system test is needed to validate the capacity estimation.

The OAM-enhanced TCM effect also points out a direction for further scaling the mode count by going to larger fibers that support bound modes with higher OAM values. Even though we already demonstrated record mode count, we expect it can be scaled even further. In addition, we expect such large number of unmixed modes can be primarily comprised by TCMs so we also benefit from the inherent low crosstalk provided by TCMs. Preliminary, unpublished results in this regard (see Sec. 7.3) provide confidence for this assertion. In contrast to the Gen6A3 fiber with ring core size of 57 μm, with which we described all the detailed investigations in this thesis, we have found that a replica of this design drawn to a core size of 77 μm already yields as many as 80 stable modes, with over 80 % of them being TCMs. As such, as core size increases, we not only expect the overall mode count to increase, we also expect that the modes of utility will primarily comprise TCMs rather than conventional bound modes that have been used for every other SDM

application to date.

For long-haul transmission, great effort needs to be made reduce the scattering loss. We point to a direction of increasing the drawing stress to reduce the loss down to ~0.4 dB/km. However, we need to understand the mechanism of fiber cracks under high drawing stress/tension and seek ways to achieve the high drawing stress needed for low loss. The scattering loss may also be related to other drawing parameters including drawing speed, temperature, etc. (Wandel, 2005).

Another interesting schematic in which TCMs could be deployed involves data transmission in mixed ensembles of the four modes of a given $|L|$. Since inter-$|L|$ crosstalk was below the noise floor of our measurement, a series of low-complexity 4×4 MIMO receivers would suffice to substantially enhance achievable SEs. For achieving this, we could potentially use conventional scalar LP modes as four modes of a given $|L|$ that mix completely (Chapter 2).

10.2.2 High-Dimensional Quantum communication

Increasing the dimension of photonic entanglement has advantages over increasing the number of entangled photons which are very hard to manage and remain coherent for all of them. Apart from other convention dimensions as time, frequency, polarization, OAM promises another degree of freedom for high-dimensional entanglement (Mair et al., 2001). However, it has been a great challenge to stably transmit such high-dimensional entangled OAM states over fairly long fibers, which is especially desired for quantum key distribution (Sit et al., 2017). As discussed in Chapter 3, even two orthogonal polarizations (a common dimension for entanglement) completely mix in fiber under common perturbations. We

expect such large number of unmixed OAM modes would find favorable applications in high-dimensional entanglement of photons. A plethora of low-crosstalk modes potentially enables low crosstalk per superpositions of modes as well (Greenberg et al., 2020), even though a superposition over all 50 modes would a great challenge. Such supposition is required for quantum transport, thus effectively allowing high-dimensional encoding. In addition, generating high-dimensional entangled photons in a fiber (Cruz-Delgado et al., 2016) is attractive as an integrated schematic compatible with optical fiber networks, and this should be eminently feasible by exploiting nonlinear wave mixing in TCM fibers. (Shahar et al., 2023; Liu et al., 2022). The next section further expands on the promise of using the TCM platform for enhanced nonlinear applications.

10.2.3 Nonlinear Interactions

OAM provides an alternative degree of freedom to control the nonlinear interactions of light in fibers. Particularly, the SOI-induced optical activity introduces exceptional phase matching in Raman (Liu et al., 2022) and Brillouin (Greenberg et al., 2022) scattering. The TCM supporting fiber demonstrated in this these not only provide modes with high OAM, but also a large ensemble of unmixed modes. This provides a great number of phase-matching possibilities among available modes, which enables high selectivity for parametric four-wave mixing, thus leading to a promising platform for light sources at on-demand power levels and wavelengths (Liu et al., 2021). The plethora of phase-matching possibilities also allows the generation of photon pairs with user-defined joint spectral densities at a variety of wavelengths (Liu et al., 2022). Note that the plethora of phase-matching possibilities provided by the high mode count also poses a great challenge in

eliminating the undesired inter-modal interactions.

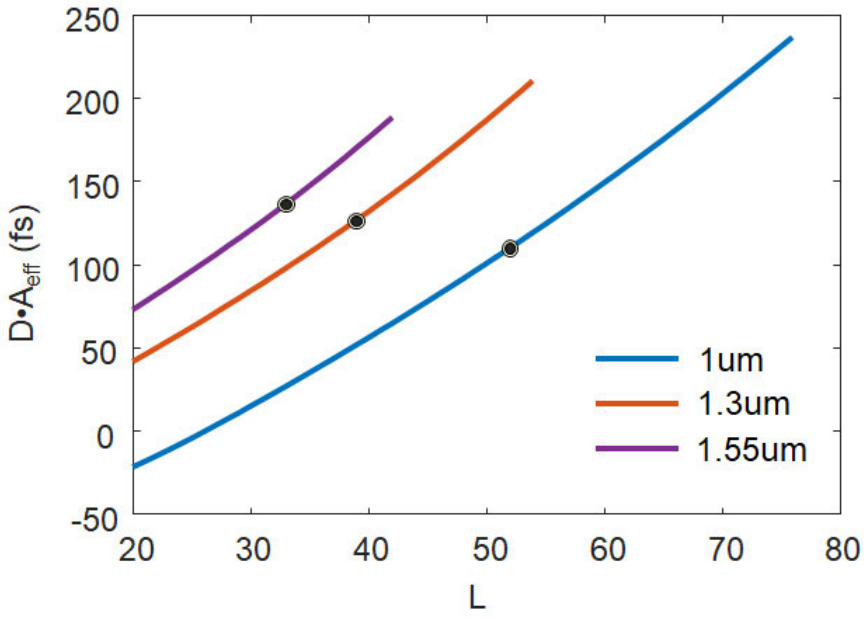

Figure 10.1: $D \bullet A_{eff}$ versus L in Gen6A3 fiber at various wavelengths. Dots on the curves marks the highest bound mode L_c for each wavelength. The highest-$|L|$ TCMs have confinement loss <0.01 dB/m.

Moreover, the large dispersion and effective areas of TCMs are also of great interest in scaling the energy of ultrafast soliton pulse propagation (Kabagoz et al., 2021). The energy of a soliton can be written as (Agrawal, 2019)

$$E = \frac{\lambda^3 N^2 D A_{eff}}{2\pi^2 c n_2 T_0} \tag{10.1}$$

N is the soliton number (usually set as one), and T_0 is duration of the pulse. It is clear from the above equation that the soliton energy scales as $D \bullet A_{eff}$. Figure 10.1 shows such $D \bullet A_{eff}$ versus L in Gen6A3 fiber at various wavelengths. The $D \bullet A_{eff}$ values of TCM exceed 200 fs^2, which is ~100 times that of conventional SMF mode. This is due to the fact that the dispersion and effective area of TCMs in this ring-core fiber are ~10 times of those

of standard SMFs (Sec. 9.4). Such energetic soliton with short pulse duration can be useful for various applications, e.g., machining, fusion, electron acceleration, particle acceleration and deep-tissue multi-photon microscopy.

Appendix A

A. PML Scalar Mode Solver

To solve the TCMs with certain loss, one needs to put an absorbing layer at the end of cladding (Fig. A.1). Its impedance needs to be matched with the preceding index layers to avoid reflection s and hence properly emulate an infinite cladding in which light radiates away, thus the name perfectly-match layer (PML) (Berenger, 1994).

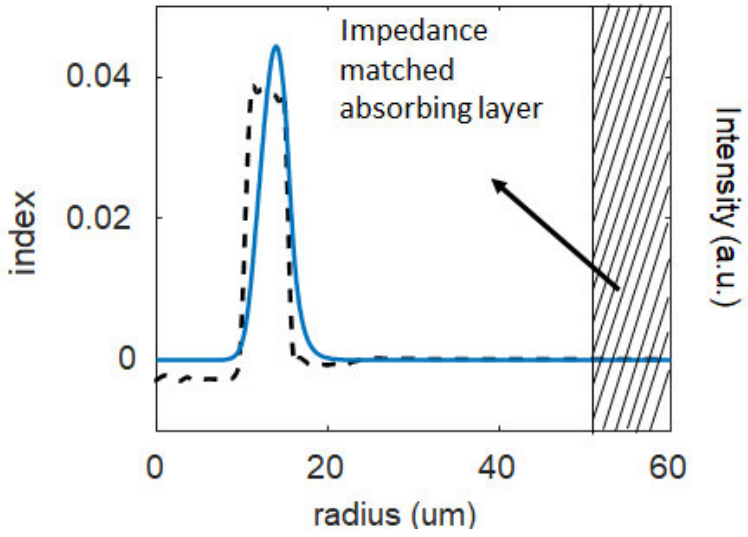

Figure A.1: Schematic of the impedance matched absorbing layer. Dashed black curve is fiber's refractive index profile and solid blue curve is the intensity profile of representative mode.

The scalar modes in a fiber can be readily solved by a standard finite different method. Furthermore, the effective index of OAM/vector modes can be corrected by the polarization correction integral.

The scalar wave equation for the radial field $F(r)$

$$\frac{d^2F(r)}{dr^2}+\frac{1}{r}\frac{dF(r)}{dr}+k_0^2\left(n^2-\frac{L^2}{k_0^2r^2}\right)F(r)=\beta^2F(r) \qquad (A.1)$$

Using a one-dimensional mesh [$r_0, r_1, r_2 \ldots r_{N-1}, r_N$]

$F_i=F(r_i)$, $n_i=n(r_i)$, $r_i=i\Delta r$, $\Delta r=r_{cl}/N$, $i=0, 1, 2 \ldots N$

$$\frac{dF(r)}{dr} = \frac{F_{i+1} - F_{i-1}}{2\Delta r} \tag{A.2}$$

$$\frac{d^2F(r)}{dr^2} = \frac{F_{i+1} - 2F_i + F_{i-1}}{\Delta r^2} \tag{A.3}$$

Therefore, the scalar mode equation becomes

$$F_{i-1}\left(\frac{1}{\Delta r^2} + \frac{1}{2r_i\Delta r}\right) + F_i\left(n_i^2k_0^2 - \frac{2}{\Delta r^2} + \frac{L^2}{r_i^2}\right) + F_{i+1}\left(\frac{1}{\Delta r^2} - \frac{1}{2r_i\Delta r}\right) = \beta^2 F_i \tag{A.4}$$

The boundary conditions are $F_0=0$, $F_{N+1}=0$; $r_{N+1}= r_N$ for symmetric modes and $r_{N+1}= -r_N$ for anti-symmetric modes. Based on Eq. A.4, the β and corresponding modal fields can be solved.

For an 1D lossy layer in frequency domain

$$\frac{\partial H}{\partial r} = j\omega\tilde{\varepsilon}E \tag{A.5}$$

$$\frac{\partial E}{\partial r} = -j\omega\tilde{\mu}H \tag{A.6}$$

where

$$\tilde{\varepsilon} = \varepsilon - j\frac{\sigma_e}{\omega} \tag{A.7}$$

$$\tilde{\mu} = \mu - j\frac{\sigma_m}{\omega} \tag{A.8}$$

Impedance

$$\tilde{\eta} = \sqrt{\frac{\tilde{\mu}}{\tilde{\varepsilon}}} = \sqrt{\frac{\mu\left(1 - j\frac{\sigma_m}{\omega\mu}\right)}{\varepsilon\left(1 - j\frac{\sigma_e}{\omega\varepsilon}\right)}} \tag{A.9}$$

Impedance matching requires

$$1 - j\frac{\sigma_e}{\omega\varepsilon} = 1 - j\frac{\sigma_m}{\omega\mu} \tag{A.10}$$

Leading to

$$\frac{\sigma_e}{\varepsilon} = \frac{\sigma_m}{\mu} \tag{A.11}$$

For 2D cases, an anisotropic absorbing material (the complex permittivity and permeability become tensor) is required to match the impedance for all oblique incidence (and all frequency), which is the so-call "perfectly matched layer". A more easy and general way is complex coordinate stretching:

$$\frac{1}{s}\frac{\partial H}{\partial r} = j\omega\varepsilon E \tag{A.12}$$

$$\frac{1}{s}\frac{\partial E}{\partial r} = -j\omega\mu H \tag{A.13}$$

Or

$$\frac{\partial}{\partial r} \to \frac{1}{s}\frac{\partial}{\partial r} \tag{A.14}$$

where

$$s = 1 - j\frac{\sigma_e}{\omega\varepsilon} \tag{A.15}$$

To avoid the numerical reflections from discretization, the conductivity should be slowly varying, usually chosen as quadratic

$$\sigma_e(\rho) = \sigma_{\max}\left(\frac{\rho}{d}\right)^2 \tag{A.16}$$

$$s = 1 - j\frac{3\lambda}{4\pi n d}\left(\frac{\rho}{d}\right)^2 \ln\left(\frac{1}{R}\right) \tag{A.17}$$

where $\rho = r - r_{PML}$, d is the thickness of PML, R is reflection coefficient, set as 10^{-16}.

The second derivative

$$\frac{\partial^2}{\partial r'^2} = \frac{1}{s^2}\frac{\partial^2}{\partial r^2} - \frac{1}{s^3}\frac{\partial s}{\partial r}\frac{\partial}{\partial r} \tag{A.18}$$

where

$$\frac{\partial s}{\partial r} = -j\frac{3\lambda}{2\pi n d^3}\ln\left(\frac{1}{R}\right)\rho(D.1) \tag{A.19}$$

From $\frac{\partial}{\partial r'} = \frac{1}{s}\frac{\partial}{\partial r}$, we have

$$r' = \int s\partial r = r - j\frac{\lambda}{4\pi n}\ln\left(\frac{1}{R}\right)\left(\frac{\rho}{d}\right)^3 \tag{A.20}$$

$$\frac{d^2F(r')}{dr'^2} + \frac{1}{r'}\frac{dF(r')}{dr'} + k_0^2\left(n^2 - \frac{L^2}{k_0^2 r'^2}\right)F(r') = \beta^2 F(r') \tag{A.21}$$

Thus, the Eq. A.4 in FDM can be re-written as

$$F_{i-1}\left(\frac{1}{(s\Delta r)^2} + \frac{1}{2r'_i s\Delta r} + \frac{1}{s^2}\frac{ds}{dr}\frac{1}{s\Delta r}\right) + F_i\left(n_i^2 k_0^2 - \frac{2}{(s\Delta r)^2} + \frac{L^2}{r_i'^2}\right)$$

$$+ F_{i+1}\left(\frac{1}{(s\Delta r)^2} - \frac{1}{2r'_i s\Delta r} - \frac{1}{s^2}\frac{ds}{dr}\frac{1}{s\Delta r}\right) = \beta^2 F_i \tag{A.22}$$

Based on Eq. A.22, the complex β and corresponding modal fields can be solved.

Appendix B

B. Endcap for Ring-Core fiber

An endcap is a piece of coreless fiber at the end of a fiber tip. It is widely used in high power fiber lasers and amplifiers to avoid Fresnel reflections at the fiber facet. In the ~km transmission experiment, the output beam is reflected back into the fiber and measured at the input (Chapter 9). To avoid reflections at the input and output side mixing with the desired modes, each side is spliced with a 340-μm-diameter endcap.

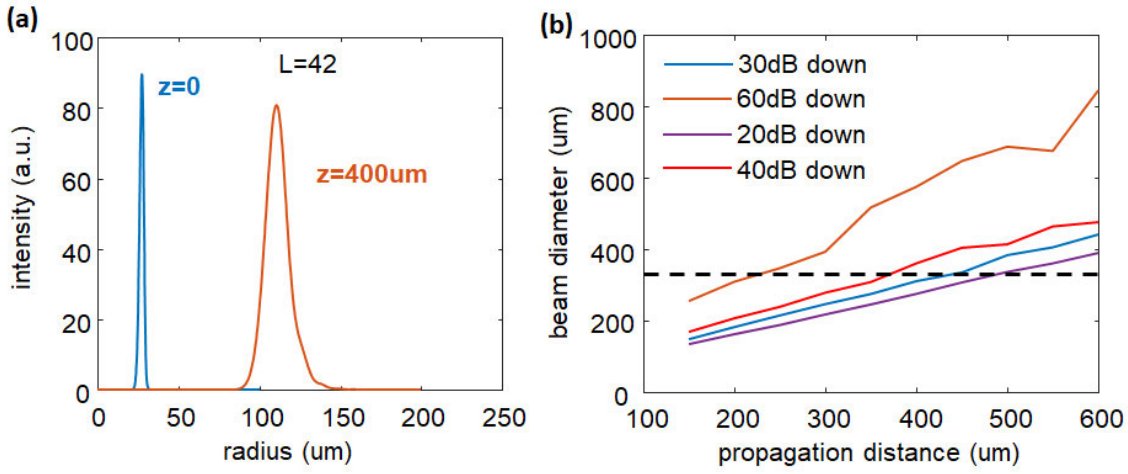

Figure B.1: (a) The intensity distribution of *L*=42 mode at the fiber facet (z=0) and after propagating for 400um; (b) The beam diameter versus propagation distance. The beam diameter is obtained based on evaluating how much the intensity goes down (20dB, 30dB, 40dB, 60dB) compared with the peak. The black dashed is the diameter of the endcap (340μm).

The endcap should be long enough to avoid the reflection from mixing with the signal but it shouldn't be too long to clip the beam. Thus, it is important to know the beam-size dependence on the propagation distance before making the endcap. The field distribution after propagation is calculated using the Fresnel diffraction integral (Vasara et

al., 1989). Fig. B.1 shows an exemplary comparison between the L=42 mode at the fiber facet (z=0) and after propagating for z=400um in the glass. The beam diameter critically depends on definition of the ring radius, which is given as the distance between the center and point where its intensity has decayed by 20dB, 30dB, 40dB and 60dB, respectively. Figure B.1b shows the beam diameter versus propagation distance based on these four definitions of the ring radius. Therefore, to avoid clipping of the beam on the endcap (whose diameter is show as a dashed line in Fig. C.1b), the length of the endcap should be around 200–500um.

Table B.1: Splice recipe for splicing the endcap and ring-core fiber

Gap (um)	Overlap (um)	Prefuse power (bit)	Prefuse time (ms)	Arc power (bit)	Arc time (ms)
30	10	250	50	250	6000

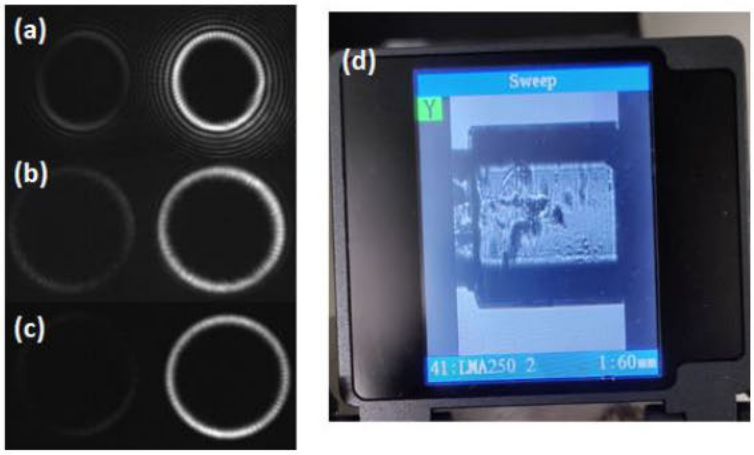

Figure B.2: L=40 SOa out of an endcap with length (a) 1 mm; (b) 450 μm; (c) 350 μm. (d) the image of the endcap shown on the splicer.

The 340-μm-diameter coreless fiber is spliced to the end of the Gen6A3 fiber by a Fujikura splicer FSM-100 using the recipe shown in Table B.1. Then it is cut and polished

to various lengths. An L=40 SOa mode is excited at the other side and the fiber facet with the endcap is imaged on a camera (setup same as Fig. 3.1). If the endcap is too long, the mode is clipped as illustrated by the apprearence of outer rings due to diffraction (Fig. B.2a). The length of endcap is esimmated by comparing it with the endcap diameter using the splicer iamge (Fig. B.2d). These diffraction ripples are eliminated when the endcap is poslished down to around 350um (Fig. B.2c).

BIBLIOGRAPHY

Abdulkareem, S., & Kundikova, N. (2016). Joint effect of polarization and the propagation path of a light beam on its intrinsic structure. *Optics Express*, *24*(17), 19157. https://doi.org/10.1364/oe.24.019157

Abedin, K. S., Ahmad, R., DeSantolo, A. M., & DiGiovanni, D. J. (2019). Reconversion of higher-order-mode (HOM) output from cladding-pumped hybrid Yb:HOM fiber amplifier. *Optics Express*, *27*(6), 8585. https://doi.org/10.1364/oe.27.008585

Akasaka, Y., Sugizaki, R., Umeda, A., & Kamiya, T. (1996). High-dispersion-compensation ability and low nonlinearity of W-shaped DCF. *Optical Fiber Communications, OFC.*, *paper ThA3*. https://doi.org/10.1109/ofc.1996.908225

Al Amin, A., Li, A., Chen, S., Chen, X., Gao, G., & Shieh, W. (2011). Dual-LP_11 mode 4x4 MIMO-OFDM transmission over a two-mode fiber. *Optics Express*, *19*(17), 16672. https://doi.org/10.1364/oe.19.016672

Alexeyev, C. N., Volyar, A. V., & Yavorsky, M. A. (2004). Vortex-preserving weakly guiding anisotropic twisted fibres. *Journal of Optics A: Pure and Applied Optics*, *6*(5), S162–S165. https://doi.org/10.1088/1464-4258/6/5/002

Alexeyev, C., Barshak, E., Fridman, Y., & Yavorsky, M. (2012). Optical vortices in twisted elliptical optical fibers with torsional stress. *Applied Optics*, *51*(10), C163. https://doi.org/10.1364/ao.51.00c163

Allen, L., Beijersbergen, M. W., Spreeuw, R. J. C., & Woerdman, J. P. (1992). Orbital angular momentum of light and the transformation of Laguerre-Gaussian laser

modes. *Physical Review A*, *45*(11), 8185–8189. https://doi.org/10.1103/physreva.45.8185

Anandan, J. (1992). The geometric phase. *Nature*, *360*(6402), 307–313. https://doi.org/10.1038/360307a0

Bade, S., Denolle, B., Trunet, G., Riguet, N., Jian, P., Pinel, O., & Labroille, G. (2018). Fabrication and Characterization of a Mode-selective 45-Mode Spatial Multiplexer based on Multi-Plane Light Conversion. *Optical Fiber Communication Conference Postdeadline Papers*, *paper Th4B.3*. https://doi.org/10.1364/ofc.2018.th4b.3

Benabid, F., Knight, J. C., Antonopoulos, G., & Russell, P. St. J. (2002). Stimulated Raman Scattering in Hydrogen-Filled Hollow-Core Photonic Crystal Fiber. *Science*, *298*(5592), 399–402. https://doi.org/10.1126/science.1076408

Berenger, J.-P. (1994). A perfectly matched layer for the absorption of electromagnetic waves. *Journal of Computational Physics*, *114*(2), 185–200. https://doi.org/10.1006/jcph.1994.1159

Berry, M. (1990). Anticipations of the Geometric Phase. *Physics Today*, *43*(12), 34–40. https://doi.org/10.1063/1.881219

Berry, M. V. (1984). Quantal phase factors accompanying adiabatic changes. *Proceedings of the Royal Society of London. A. Mathematical and Physical Sciences*, *392*(1802), 45–57. https://doi.org/10.1098/rspa.1984.0023

Bliokh, K. Yu. (2006). Geometrical Optics of Beams with Vortices: Berry Phase and Orbital Angular Momentum Hall Effect. *Physical Review Letters*, *97*(4). https://doi.org/10.1103/physrevlett.97.043901

Bogaerts, W., De Heyn, P., Van Vaerenbergh, T., De Vos, K., Kumar Selvaraja, S., Claes, T., Dumon, P., Bienstman, P., Van Thourhout, D., & Baets, R. (2011). Silicon microring resonators. *Laser & Photonics Reviews*, *6*(1), 47–73. https://doi.org/10.1002/lpor.201100017

Bozinovic, N., Golowich, S., Kristensen, P., & Ramachandran, S. (2012). Control of orbital angular momentum of light with optical fibers. *Optics Letters*, *37*(13), 2451. https://doi.org/10.1364/ol.37.002451

Bozinovic, N., Yue, Y., Ren, Y., Tur, M., Kristensen, P., Huang, H., Willner, A. E., & Ramachandran, S. (2013). Terabit-Scale Orbital Angular Momentum Mode Division Multiplexing in Fibers. *Science*, *340*(6140), 1545–1548. https://doi.org/10.1126/science.1237861

Brunet, C., Ung, B., Belanger, P.-A., Messaddeq, Y., LaRochelle, S., & Rusch, L. A. (2014). Vector Mode Analysis of Ring-Core Fibers: Design Tools for Spatial Division Multiplexing. *Journal of Lightwave Technology*, *32*(23), 4648–4659. https://doi.org/10.1109/jlt.2014.2361432

Chiasera, A., Dumeige, Y., Féron, P., Ferrari, M., Jestin, Y., Nunzi Conti, G., Pelli, S., Soria, S., & Righini, G. C. (2009). Spherical whispering-gallery-mode microresonators. *Laser & Photonics Reviews*, *4*(3), 457–482. https://doi.org/10.1002/lpor.200910016

Chin, C., Grimm, R., Julienne, P., & Tiesinga, E. (2010). Feshbach Resonances in Ultracold Gases. *Reviews of Modern Physics*, *82*(2), 1225–1286. https://doi.org/10.1103/RevModPhys.82.1225

Čižmár, T., & Dholakia, K. (2012). Exploiting multimode waveguides for pure fibre-based imaging. *Nature Communications*, *3*(1), 1027. https://doi.org/10.1038/ncomms2024

Cregan, R. F., Mangan, B. J., Knight, J. C., Birks, T. A., Russell, P. St. J., Roberts, P. J., & Allan, D. C. (1999). Single-Mode Photonic Band Gap Guidance of Light in Air. *Science*, *285*(5433), 1537–1539. https://doi.org/10.1126/science.285.5433.1537

Cruz-Delgado, D., Ramirez-Alarcon, R., Ortiz-Ricardo, E., Monroy-Ruz, J., Dominguez-Serna, F., Cruz-Ramirez, H., Garay-Palmett, K., & U'Ren, A. B. (2016). Fiber-based photon-pair source capable of hybrid entanglement in frequency and transverse mode, controllably scalable to higher dimensions. *Scientific Reports*, *6*(1), 27377. https://doi.org/10.1038/srep27377

Demas, J., Prabhakar, G., He, T., & Ramachandran, S. (2017). Wavelength-agile high-power sources via four-wave mixing in higher-order fiber modes. *Optics Express*, *25*(7), 7455. https://doi.org/10.1364/oe.25.007455

Demas, J., Rishøj, L., & Ramachandran, S. (2015). Free-space beam shaping for precise control and conversion of modes in optical fiber. *Optics Express*, *23*(22), 28531. https://doi.org/10.1364/oe.23.028531

Dietrich Marcuse, & American Telephone and Telegraph Company. (1991). *Theory of dielectric optical waveguides*. Academic Press.

Dong, L., Peng, X., & Li, J. (2007). Leakage channel optical fibers with large effective area. *Journal of the Optical Society of America B*, *24*(8), 1689. https://doi.org/10.1364/josab.24.001689

Dragic, P. D., Hawkins, T., Foy, P., Morris, S., & Ballato, J. (2012). Sapphire-derived all-glass optical fibres. *Nature Photonics*, *6*(9), 627–633. https://doi.org/10.1038/nphoton.2012.182

Durt, T., Englert, B.-G., Bengtsson, I., & Życzkowski, K. (2010). On mutually unbiased bases. *International Journal of Quantum Information*, *8*(4), 535–640. https://doi.org/10.1142/s0219749910006502

Efimov, A., Taylor, A., Omenetto, F., Knight, J., Wadsworth, W., & Russell, P. (2003). Nonlinear generation of very high-order UV modes in microstructured fibers. *Optics Express*, *11*(8), 910. https://doi.org/10.1364/oe.11.000910

Ellis, A. D., Mac Suibhne, N., Gunning, F. C. G., & Sygletos, S. (2013). Expressions for the nonlinear transmission performance of multi-mode optical fiber. *Optics Express*, *21*(19), 22834. https://doi.org/10.1364/oe.21.022834

Erhard, M., Krenn, M., & Zeilinger, A. (2020). Advances in high-dimensional quantum entanglement. *Nature Reviews. Physics*, *2*(7), 365–381. https://doi.org/10.1038/s42254-020-0193-5

Essiambre, R.-J., Kramer, G., Winzer, P. J., Foschini, G. J., & Goebel, B. (2010). Capacity Limits of Optical Fiber Networks. *Journal of Lightwave Technology*, *28*(4), 662–701. https://doi.org/10.1109/jlt.2009.2039464

Essiambre, R.-J., & Tkach, R. W. (2012). Capacity Trends and Limits of Optical Communication Networks. *Proceedings of the IEEE*, *100*(5), 1035–1055. https://doi.org/10.1109/jproc.2012.2182970

Eznaveh, Z. S., Zacarias, J. C. A., Lopez, J. E. A., Shi, K., Milione, G., Jung, Y., Thomsen, B. C., Richardson, D. J., Fontaine, N., Leon-Saval, S. G., & Correa, R. A. (2018). Photonic lantern broadband orbital angular momentum mode multiplexer. *Optics Express*, *26*(23), 30042. https://doi.org/10.1364/oe.26.030042

Fontaine, N. K., Ryf, R., Chen, H., Benitez, A. V., Antonio Lopez, J. E., Correa, R. A., Guan, B., Ercan, B., Scott, R. P., Ben Yoo, S. J., Grüner-Nielsen, L., Sun, Y., & Lingle, R. J. (2015). 30×30 MIMO Transmission over 15 Spatial Modes. *Optical Fiber Communication Conference Post Deadline Papers*, *paper Th5C.1*. https://doi.org/10.1364/ofc.2015.th5c.1

Freeman, R. R., & Bucksbaum, P. H. (1991). Investigations of above-threshold ionization using subpicosecond laser pulses. *Journal of Physics B: Atomic, Molecular and Optical Physics*, *24*(2), 325–347. https://doi.org/10.1088/0953-4075/24/2/004

Galdino, L., Edwards, A., Yi, W., Sillekens, E., Wakayama, Y., Gerard, T., Pelouch, W. S., Barnes, S., Tsuritani, T., Killey, R. I., Lavery, D., & Bayvel, P. (2020). Optical Fibre Capacity Optimisation via Continuous Bandwidth Amplification and

Geometric Shaping. *IEEE Photonics Technology Letters*, *32*(17), 1021–1024. https://doi.org/10.1109/lpt.2020.3007591

Ghatak, & Thyagarajan. (1998). *An introduction to fiber optics*. Cambridge University Press.

Gloge, D. (1971). Weakly Guiding Fibers. *Applied Optics*, *10*(10), 2252. https://doi.org/10.1364/ao.10.002252

Gnauck, A. H., Garrett, L. D., Danziger, Y., Levy, U., & Tur, M. (2000). Dispersion and dispersion-slope compensation of NZDSF over the entire C band using higher-order-mode fibre. *Electronics Letters*, *36*(23), 1946. https://doi.org/10.1049/el:20001312

Google. (2019). *Google Cloud Blog*. Google Cloud Blog. https://cloud.google.com/blog/products/infrastructure/a-quick-hop-across-thepond-supercharging-the-dunant-subsea-cable-with-sdmtechnology

Govind Agrawal. (2019). *Nonlinear Fiber Optics.* Elsevier Academic Press.

Greenberg, A. P., Ma, Z., Kabagöz, H. B., Shahar, D. I., & Ramachandran, S. (2023). 60-Mode Erbium Doped Fiber Amplifier with Low Differential Modal Gain. *Conference on Lasers and Electro-Optics (CLEO)*.

Greenberg, A. P., Ma, Z., & Ramachandran, S. (2022). Angular momentum driven dynamics of stimulated Brillouin scattering in multimode fibers. *Optics Express*, *30*(16), 29708. https://doi.org/10.1364/oe.462677

Greenberg, A. P., Prabhakar, G., & Ramachandran, S. (2020). High resolution spectral metrology leveraging topologically enhanced optical activity in fibers. *Nature Communications*, *11*(1). https://doi.org/10.1038/s41467-020-18931-6

Gregg, P., Kristensen, P., & Ramachandran, S. (2015). Conservation of orbital angular momentum in air-core optical fibers. *Optica*, *2*(3), 267. https://doi.org/10.1364/optica.2.000267

Gregg, P., Kristensen, P., & Ramachandran, S. (2016). 134km OAM state propagation by recirculating fiber loop. *Optics Express*, *24*(17), 18938. https://doi.org/10.1364/oe.24.018938

Gregg, P., Kristensen, P., Rubano, A., Golowich, S., Marrucci, L., & Ramachandran, S. (2019). Enhanced spin orbit interaction of light in highly confining optical fibers for mode division multiplexing. *Nature Communications*, *10*(1). https://doi.org/10.1038/s41467-019-12401-4

Gregg, P., Mirhosseini, M., Rubano, A., Marrucci, L., Karimi, E., Boyd, R. W., & Ramachandran, S. (2015). Q-plates as higher order polarization controllers for orbital angular momentum modes of fiber. *Optics Letters*, *40*(8), 1729. https://doi.org/10.1364/ol.40.001729

Hayashi, T., Taru, T., Shimakawa, O., Sasaki, T., & Sasaoka, E. (2012). Uncoupled multi-core fiber enhancing signal-to-noise ratio. *Optics Express*, *20*(26), B94. https://doi.org/10.1364/oe.20.000b94

Hopkins, H. H., & Kapany, N. S. (1954). A Flexible Fibrescope, using Static Scanning. *Nature*, *173*(4392), 39–41. https://doi.org/10.1038/173039b0

Huang, X., Gao, S., Huang, B., Liu, W., & Li, Z. (2018). Demonstration of spin and extrinsic orbital-angular-momentum interaction using a few-mode optical fiber. *Physical Review A*, *97*(3). https://doi.org/10.1103/physreva.97.033845

John Markus Blatt, & Victor Frederick Weisskopf. (1979). *Theoretical nuclear physics*. New York, Heidelberg, Berlin Springer.

Johnson, S. D., Ma, Z., Padgett, M. J., & Ramachandran, S. (2019). Measurement of the spin-orbit coupling interaction in ring-core optical fibers. *OSA Continuum*, *2*(10), 2975. https://doi.org/10.1364/osac.2.002975

Jung, Y., Alam, S., Richardson, D. J., Ramachandran, S., & Abedin, K. S. (2020). Multicore and multimode optical amplifiers for space division multiplexing. *Optical Fiber Telecommunications VII*, 301–333. https://doi.org/10.1016/b978-0-12-816502-7.00008-7

Jung, Y., Kang, Q., Sidharthan, R., Ho, D., Yoo, S., Gregg, P., Ramachandran, S., Alam, S.-U., & Richardson, D. J. (2017). Optical Orbital Angular Momentum Amplifier Based on an Air-Hole Erbium-Doped Fiber. *Journal of Lightwave Technology*, *35*(3), 430–436. https://doi.org/10.1109/jlt.2017.2651145

Kabagöz, H. B., Ma, Z., & Ramachandran, S. (2021). Nonlinear Generation of Energetic Ultrashort Vortex Pulses with Spectral and Topological Charge Diversity. *Conference on Lasers and Electro-Optics*, *paper SW3R.7*. https://doi.org/10.1364/cleo_si.2021.sw3r.7

Kang, Q., Gregg, P., Jung, Y., Lim, E. L., Alam, S., Ramachandran, S., & Richardson, D. J. (2015). Amplification of 12 OAM Modes in an air-core erbium doped fiber. *Optics Express*, *23*(22), 28341. https://doi.org/10.1364/oe.23.028341

Knight, J. C., Broeng, J., Birks, T. A., & Russell, P. St. J. (1998). Photonic Band Gap Guidance in Optical Fibers. *Science*, *282*(5393), 1476–1478. https://doi.org/10.1126/science.282.5393.1476

Knoop, S., Mark, M., Ferlaino, F., Danzl, J. G., Kraemer, T., Nägerl, H.-C., & Grimm, R. (2008). Metastable Feshbach Molecules in High Rotational States. *Physical Review Letters*, *100*(8). https://doi.org/10.1103/physrevlett.100.083002

Krummrich, P. M. (2011). Optical amplification and optical filter based signal processing for cost and energy efficient spatial multiplexing. *Optics Express*, *19*(17), 16636. https://doi.org/10.1364/oe.19.016636

Leary, C. C., Raymer, M. G., & van Enk, S. J. (2009). Spin and orbital rotation of electrons and photons via spin-orbit interaction. *Physical Review A*, *80*(6). https://doi.org/10.1103/physreva.80.061804

Limpert, J., Roser, F., Schreiber, T., & Tünnermann, A. (2006). High-power ultrafast fiber laser systems. *IEEE Journal of Selected Topics in Quantum Electronics*, *12*(2), 233–244. https://doi.org/10.1109/jstqe.2006.872729

Lines, M. E. (1984). Scattering losses in optic fiber materials. I. A new parametrization. *Journal of Applied Physics*, *55*(11), 4052–4057. https://doi.org/10.1063/1.332994

Lines, M. E., Reed, W. A., Di Giovanni, D. J., & Hamblin, J. R. (1999). Explanation of anomalous loss in high delta singlemode fibres. *Electronics Letters*, *35*(12), 1009. https://doi.org/10.1049/el:19990673

Liu, X., Christensen, E. N., Rottwitt, K., & Ramachandran, S. (2020). Nonlinear four-wave mixing with enhanced diversity and selectivity via spin and orbital angular momentum conservation. *APL Photonics*, *5*(1), 010802. https://doi.org/10.1063/1.5130715

Liu, X., Kim, D. B., Lorenz, V. O., & Ramachandran, S. (2022a). Engineering Joint Spectral Densities with Orbital Angular Momentum States in Optical Fibers. *Conference on Lasers and Electro-Optics*, *paper FF2J.1*. https://doi.org/10.1364/cleo_qels.2022.ff2j.1

Liu, X., Kim, D. B., Lorenz, V. O., & Ramachandran, S. (2022b). Shaping Biphoton Spectral Correlations with Orbital Angular Momentum Fiber Modes. *Quantum 2.0 Conference and Exhibition*, *paper QTh4B.1*. https://doi.org/10.1364/quantum.2022.qth4b.1

Liu, X., Ma, Z., Antikainen, A., & Ramachandran, S. (2022). Raman gain control in optical fibers with orbital-angular-momentum-induced chirality of light. *Optics Express*, *30*(15), 26967. https://doi.org/10.1364/oe.457259

Love, J. D., & Snyder, A. W. (1975). Fresnel's and Snell's laws for the multimode optical waveguide of circular cross section. *Journal of the Optical Society of America*, *65*(11), 1241. https://doi.org/10.1364/josa.65.001241

Luís, R. S., Puttnam, B. J., Rademacher, G., Klaus, W., Agrell, E., Awaji, Y., & Wada, N. (2017). On the Spectral Efficiency Limits of Crosstalk-Limited Homogeneous Single-Mode Multi-Core Fiber Systems. *Advanced Photonics 2017 (IPR, NOMA, Sensors, Networks, SPPCom, PS)*, *paper NeTu2B.2*. https://doi.org/10.1364/networks.2017.netu2b.2

Ma, Z., Khalid, M. W., & Ramachandran, S. (2022). Long-distance Pulse Propagation of 50 Uncoupled Fiber Modes due to Topological Confinement. *Conference on Lasers and Electro-Optics*, *paper STu4P.3*. https://doi.org/10.1364/cleo_si.2022.stu4p.3

Ma, Z., Kistensen, P., & Ramachandran, S. (2021). Record (60) Uncoupled Modes in A Step-Index Fiber due to A New Light Guidance Mechanism: Topological Confinement. *2021 European Conference on Optical Communication (ECOC)*, *paper TU4A.3*. https://doi.org/10.1109/ecoc52684.2021.9606128

Ma, Z., Kristensen, P., & Ramachandran, S. (2020). Light guidance beyond cutoff in optical fibers. *Conference on Lasers and Electro-Optics*, *paper SF1P.2*. https://doi.org/10.1364/cleo_si.2020.sf1p.2

Ma, Z., Kristensen, P., & Ramachandran, S. (2021). Light Guidance Based on Topological Confinement Yielding Fiber Mode Counts Exceeding 50. *Conference on Lasers and Electro-Optics*, *paper SM1F.4*. https://doi.org/10.1364/cleo_si.2021.sm1f.4

Ma, Z., Kristensen, P., & Ramachandran, S. (2023). Scaling information pathways in optical fibers by topological confinement. *Science*, *380*(6642), 278–282. https://doi.org/10.1126/science.add1874

Ma, Z., Prabhakar, G., Gregg, P., & Ramachandran, S. (2018). Robustness of OAM fiber modes to geometric perturbations. *Conference on Lasers and Electro-Optics*, *paper SW3K.1*. https://doi.org/10.1364/cleo_si.2018.sw3k.1

Ma, Z., & Ramachandran, S. (2020). Propagation stability in optical fibers: role of path memory and angular momentum. *Nanophotonics*, *10*(1), 209–224. https://doi.org/10.1515/nanoph-2020-0404

Mair, A., Vaziri, A., Weihs, G., & Zeilinger, A. (2001). Entanglement of the orbital angular momentum states of photons. *Nature*, *412*(6844), 313–316. https://doi.org/10.1038/35085529

Marcuse, D. (1973). Cutoff condition of optical fibers. *Journal of the Optical Society of America*, *63*(11), 1369–1369. https://doi.org/10.1364/josa.63.001369

Marrucci, L., Karimi, E., Slussarenko, S., Piccirillo, B., Santamato, E., Nagali, E., & Sciarrino, F. (2011). Spin-to-orbital conversion of the angular momentum of light and its classical and quantum applications. *Journal of Optics*, *13*(6), 064001. https://doi.org/10.1088/2040-8978/13/6/064001

Matsuo, S., Takenaga, K., Sasaki, Y., Amma, Y., Saito, S., Saitoh, K., Matsui, T., Nakajima, K., Mizuno, T., Takara, H., Miyamoto, Y., & Morioka, T. (2016). High-Spatial-Multiplicity Multicore Fibers for Future Dense Space-Division-

Multiplexing Systems. *Journal of Lightwave Technology*, *34*(6), 1464–1475. https://doi.org/10.1109/jlt.2015.2508928

Mears, R. J., Reekie, L., Jauncey, I. M., & Payne, D. N. (1987). Low-noise erbium-doped fibre amplifier operating at 1.54μm. *Electronics Letters*, *23*(19), 1026. https://doi.org/10.1049/el:19870719

Mitra, P. P., & Stark, J. B. (2001). Nonlinear limits to the information capacity of optical fibre communications. *Nature*, *411*(6841), 1027–1030. https://doi.org/10.1038/35082518

Mizuno, T., & Miyamoto, Y. (2017). High-capacity dense space division multiplexing transmission. *Optical Fiber Technology*, *35*, 108–117. https://doi.org/10.1016/j.yofte.2016.09.015

Mizuno, T., Shibahara, K., Ye, F., Sasaki, Y., Amma, Y., Takenaga, K., Jung, Y., Pulverer, K., Ono, H., Abe, Y., Yamada, M., Saitoh, K., Matsuo, S., Aikawa, K., Bohn, M., Richardson, D. J., Miyamoto, Y., & Morioka, T. (2017). Long-Haul Dense Space-Division Multiplexed Transmission Over Low-Crosstalk Heterogeneous 32-Core Transmission Line Using a Partial Recirculating Loop System. *Journal of Lightwave Technology*, *35*(3), 488–498. https://doi.org/10.1109/jlt.2016.2615070

Nicholson, J. W., Fini, J. M., DeSantolo, A. M., Liu, X., Feder, K., Westbrook, P. S., Supradeepa, V. R., Monberg, E., DiMarcello, F., Ortiz, R., Headley, C., & DiGiovanni, D. J. (2012). Scaling the effective area of higher-order-mode erbium-

doped fiber amplifiers. *Optics Express*, *20*(22), 24575. https://doi.org/10.1364/oe.20.024575

Omenetto, F. G., Taylor, A. J., Moores, M. D., Arriaga, J., Knight, J. C., Wadsworth, W. J., & Russell, P. St. J. (2001). Simultaneous generation of spectrally distinct third harmonics in a photonic crystal fiber. *Optics Letters*, *26*(15), 1158. https://doi.org/10.1364/ol.26.001158

Pancharatnam, S. (1956). Generalized theory of interference, and its applications. *Proceedings of the Indian Academy of Sciences - Section A*, *44*(5), 247–262. https://doi.org/10.1007/bf03046050

Poggiolini, P., Carena, A., Curri, V., Bosco, G., & Forghieri, F. (2011). Analytical Modeling of Nonlinear Propagation in Uncompensated Optical Transmission Links. *IEEE Photonics Technology Letters*, *23*(11), 742–744. https://doi.org/10.1109/lpt.2011.2131125

Post, E. J. (1967). Sagnac Effect. *Reviews of Modern Physics*, *39*(2), 475–493. https://doi.org/10.1103/revmodphys.39.475

Puttnam, B. J., Luis, R. S., Klaus, W., Sakaguchi, J., Delgado Mendinueta, J.-M. ., Awaji, Y., Wada, N., Tamura, Y., Hayashi, T., Hirano, M., & Marciante, J. (2015). 2.15 Pb/s transmission using a 22 core homogeneous single-mode multi-core fiber and wideband optical comb. *2015 European Conference on Optical Communication (ECOC)*, *paper PDP 3.1*. https://doi.org/10.1109/ecoc.2015.7341685

Puttnam, B. J., Rademacher, G., & Luís, R. S. (2021). Space-division multiplexing for optical fiber communications. *Optica*, *8*(9), 1186. https://doi.org/10.1364/optica.427631

Puttnam, B., Luis, R. S., Rademacher, G., Yoshinari Awaji, & Furukawa, H. (2021). High-Throughput and Long-Distance Transmission With >120 nm S-, C- and L-Band Signal in a 125μm 4-Core Fiber. *Journal of Lightwave Technology*, *40*(6), 1633–1639. https://doi.org/10.1109/jlt.2021.3128725

Rademacher, G., & Petermann, K. (2016). Nonlinear Gaussian Noise Model for Multimode Fibers With Space-Division Multiplexing. *Journal of Lightwave Technology*, *34*(9), 2280–2287. https://doi.org/10.1109/jlt.2016.2520562

Ramachandran, S., Fini, J. M., Mermelstein, M., Nicholson, J. W., Ghalmi, S., & Yan, M. F. (2008). Ultra-large effective-area, higher-order mode fibers: a new strategy for high-power lasers. *Laser & Photonics Review*, *2*(6), 429–448. https://doi.org/10.1002/lpor.200810016

Ramachandran, S., Golowich, S., Yan, M. F., Monberg, E., Dimarcello, F. V., Fleming, J., Ghalmi, S., & Wisk, P. (2005). Lifting polarization degeneracy of modes by fiber design: a platform for polarization-insensitive microbend fiber gratings. *Optics Letters*, *30*(21), 2864. https://doi.org/10.1364/ol.30.002864

Ramachandran, S., Gregg, P., Kristensen, P., & Golowich, S. E. (2015). On the scalability of ring fiber designs for OAM multiplexing. *Optics Express*, *23*(3), 3721. https://doi.org/10.1364/oe.23.003721

Ramachandran, S., & Kristensen, P. (2013). Optical vortices in fiber. *Nanophotonics*, *2*(5-6), 455–474. https://doi.org/10.1515/nanoph-2013-0047

Ramachandran, S., Mikkelsen, B., Cowsar, L. C., Yan, M. F., Raybon, G., Boivin, L., Fishteyn, M., Reed, W. A., Wisk, P., Brownlow, D., Huff, R. G., & Gruner-Nielsen, L. (2001). All-fiber grating-based higher order mode dispersion compensator for broad-band compensation and 1000-km transmission at 40 Gb/s. *IEEE Photonics Technology Letters*, *13*(6), 632–634. https://doi.org/10.1109/68.924050

Ramachandran, S., Nicholson, J. W., Ghalmi, S., Yan, M. F., Wisk, P., Monberg, E., & Dimarcello, F. V. (2006). Light propagation with ultralarge modal areas in optical fibers. *Optics Letters*, *31*(12), 1797. https://doi.org/10.1364/ol.31.001797

Ramachandran, S., & Yan, M. F. (2007). Static and tunable dispersion management with higher order mode fibers. In *Fiber Based Dispersion Compensation*, 187–248. https://doi.org/10.1007/978-0-387-48948-3_7

Redding, B., Popoff, S. M., & Cao, H. (2013). All-fiber spectrometer based on speckle pattern reconstruction. *Optics Express*, *21*(5), 6584. https://doi.org/10.1364/oe.21.006584

Richardson, D. J., Fini, J. M., & Nelson, L. E. (2013). Space-division multiplexing in optical fibres. *Nature Photonics*, *7*(5), 354–362. https://doi.org/10.1038/nphoton.2013.94

Rishøj, L., Tai, B., Kristensen, P., & Ramachandran, S. (2019). Soliton self-mode conversion: revisiting Raman scattering of ultrashort pulses. *Optica*, *6*(3), 304. https://doi.org/10.1364/optica.6.000304

Roberts, P. J., Couny, F., Sabert, H., Mangan, B. J., Williams, D. P., Farr, L., Mason, M. W., Tomlinson, A., Birks, T. A., Knight, J. C., & St. J. Russell, P. (2005). Ultimate low loss of hollow-core photonic crystal fibres. *Optics Express*, *13*(1), 236. https://doi.org/10.1364/opex.13.000236

Russell, P. (2003). Photonic Crystal Fibers. *Science*, *299*(5605), 358–362. https://doi.org/10.1126/science.1079280

Russell, P. ST. J., Culverhouse, D., & Farahi, F. (1990). Experimental observation of forward stimulated Brillouin scattering in dual-mode single-core fibre. *Electronics Letters*, *26*(15), 1195. https://doi.org/10.1049/el:19900773

Saitoh, K., & Matsuo, S. (2013). Multicore fibers for large capacity transmission. *Nanophotonics*, *2*(5-6), 441–454. https://doi.org/10.1515/nanoph-2013-0037

Sakamoto, T., Matsui, T., Saitoh, K., Saitoh, S., Takenaga, K., Mizuno, T., Abe, Y., Shibahara, K., Tobita, Y., Matsuo, S., Aikawa, K., Aozasa, S., Nakajima, K., & Miyamoto, Y. (2017). Low-Loss and Low-DMD 6-Mode 19-Core Fiber With Cladding Diameter of Less Than 250 μm. *Journal of Lightwave Technology*, *35*(3), 443–449. https://doi.org/10.1109/jlt.2016.2610479

Sammut, R., & Snyder, A. W. (1976). Leaky modes on circular optical waveguides. *Applied Optics*, *15*(2), 477. https://doi.org/10.1364/ao.15.000477

Sasaki, Y., Takenaga, K., Aikawa, K., Miyamoto, Y., & Morioka, T. (2017). Single-Mode 37-Core Fiber with a Cladding Diameter of 248 μm. *Optical Fiber Communication Conference*, *paper Th1H.2*. https://doi.org/10.1364/ofc.2017.th1h.2

Shahar, D. I., Liu, X., Kim, D. B., Lorenz, V. O., & Ramachandran, S. (2023). Photon Pair Generation in OAM Modes at 780 and 1550 nm via Spontaneous Intermodal Four Wave Mixing. *Conference on Lasers and Electro-Optics, paper FF1L.5*.

Shannon, C. E. (1948). A Mathematical Theory of Communication. *Bell System Technical Journal*, *27*(3), 379–423. https://doi.org/10.1002/j.1538-7305.1948.tb01338.x

Sit, A., Bouchard, F., Fickler, R., Gagnon-Bischoff, J., Larocque, H., Heshami, K., Elser, D., Peuntinger, C., Günthner, K., Heim, B., Marquardt, C., Leuchs, G., Boyd, R. W., & Karimi, E. (2017). High-dimensional intracity quantum cryptography with structured photons. *Optica*, *4*(9), 1006. https://doi.org/10.1364/optica.4.001006

Snitzer, E. (1961). Optical Dielectric Waveguides. *Advances in Quantum Electronics.* Columbia University Press: New York.

Snyder, A. W., & Love, J. (2010). *Optical waveguide theory*. Springer.

Snyder, A. W., Mitchell, D. G., & Pask, C. (1974). Failure of geometric optics for analysis of circular optical fibers. *Journal of the Optical Society of America*, *64*(5), 608–608. https://doi.org/10.1364/josa.64.000608

Soma, D., Wakayama, Y., Beppu, S., Sumita, S., Tsuritani, T., Hayashi, T., Nagashima, T., Suzuki, M., Takahashi, H., Igarashi, K., Morita, I., & Suzuki, M. (2017). 10.16

Peta-bit/s Dense SDM/WDM transmission over Low-DMD 6-Mode 19-Core Fibre Across C+L Band. *2017 European Conference on Optical Communication (ECOC)*. https://doi.org/10.1109/ecoc.2017.8346082

Stegall, D. B., & Erdogan, T. (1999). Leaky cladding mode propagation in long-period fiber grating devices. *IEEE Photonics Technology Letters*, *11*(3), 343–345. https://doi.org/10.1109/68.748229

Sumetsky, M. (2013). Delay of Light in an Optical Bottle Resonator with Nanoscale Radius Variation: Dispersionless, Broadband, and Low Loss. *Physical Review Letters*, *111*(16). https://doi.org/10.1103/physrevlett.111.163901

Tanaka, T., Pulverer, K., Habel, U., Castro, C., Bohn, M., Mizuno, T., Isoda, A., Shibahara, K., Inui, T., Miyamoto, Y., Sasaki, Y., Amma, Y., Aikawa, K., Jain, S., Jung, Y., Alam, S., Richardson, D. J., Nooruzzaman, Md., & Morioka, T. (2018). Demonstration of Single-Mode Multicore Fiber Transport Network With Crosstalk-Aware In-Service Optical Path Control. *Journal of Lightwave Technology*, *36*(7), 1451–1457. https://doi.org/10.1109/jlt.2017.2785844

Tur, M., Menashe, D., Japha, Y., & Danziger, Y. (2007). High-order mode based dispersion compensating modules using spatial mode conversion. *Journal of Optical and Fiber Communications Reports*, *4*(2), 110–172. https://doi.org/10.1007/s10297-007-0081-0

Vasara, A., Turunen, J., & Friberg, A. T. (1989). Realization of general nondiffracting beams with computer-generated holograms. *Journal of the Optical Society of America A*, *6*(11), 1748. https://doi.org/10.1364/josaa.6.001748

Vitullo, D. L. P., Leary, C. C., Gregg, P., Smith, R. A., Reddy, D. V., Ramachandran, S., & Raymer, M. G. (2017). Observation of Interaction of Spin and Intrinsic Orbital Angular Momentum of Light. *Physical Review Letters*, *118*(8). https://doi.org/10.1103/physrevlett.118.083601

Wandel, M. (2005). *Attenuation in silica-based optical fibers* [Doctoral dissertation – Technical University of Denmark]. https://orbit.dtu.dk/files/5070648/Marie_Wandel_PhD_fina051204l.pdf

Wandel, M., & Kristensen, P. (2007). Fiber designs for high figure of merit and high slope dispersion compensating fibers. *Fiber Based Dispersion Compensation*, 7–42. https://doi.org/10.1007/978-0-387-48948-3_2

White, A. D., Su, L., Shahar, D. I., Yang, K. Y., Ahn, G. H., Skarda, J. L., Ramachandran, S., & Vučković, J. (2022). Inverse Design of Optical Vortex Beam Emitters. *ACS Photonics*. https://doi.org/10.1021/acsphotonics.2c01007

Winzer, P. J. (2011). Energy-Efficient Optical Transport Capacity Scaling Through Spatial Multiplexing. *IEEE Photonics Technology Letters*, *23*(13), 851–853. https://doi.org/10.1109/lpt.2011.2140103

Winzer, P. J. (2012). High-Spectral-Efficiency Optical Modulation Formats. *Journal of Lightwave Technology*, *30*(24), 3824–3835. https://doi.org/10.1109/jlt.2012.2212180

Winzer, P. J. (2014). Making spatial multiplexing a reality. *Nature Photonics*, *8*(5), 345–348. https://doi.org/10.1038/nphoton.2014.58

Winzer, P. J., & Neilson, D. T. (2017). From Scaling Disparities to Integrated Parallelism: A Decathlon for a Decade. *Journal of Lightwave Technology*, *35*(5), 1099–1115. https://doi.org/10.1109/jlt.2017.2662082

Winzer, P. J., Neilson, D. T., & Chraplyvy, A. R. (2018). Fiber-optic transmission and networking: the previous 20 and the next 20 years [Invited]. *Optics Express*, *26*(18), 24190–24239. https://doi.org/10.1364/OE.26.024190

Wong, G. K. L., Kang, M. S., Lee, H. W., Biancalana, F., Conti, C., Weiss, T., & Russell, P. St. J. (2012). Excitation of Orbital Angular Momentum Resonances in Helically Twisted Photonic Crystal Fiber. *Science*, *337*(6093), 446–449. https://doi.org/10.1126/science.1223824

Yablon, A. D., Yan, M. F., Wisk, P., DiMarcello, F. V., Fleming, J. W., Reed, W. A., Monberg, E. M., DiGiovanni, D. J., Jasapara, J., & Lines, M. E. (2004). Refractive index perturbations in optical fibers resulting from frozen-in viscoelasticity. *Applied Physics Letters*, *84*(1), 19–21. https://doi.org/10.1063/1.1638883

Zhao, H., Wang, P., Yamakawa, T., & Li, H. (2019). All-fiber second-order orbital angular momentum generator based on a single-helix helical fiber grating. *Optics Letters*, *44*(21), 5370. https://doi.org/10.1364/ol.44.005370

Zhu, G., Hu, Z., Wu, X., Du, C., Luo, W., Chen, Y., Cai, X., Liu, J., Zhu, J., & Yu, S. (2018). Scalable mode division multiplexed transmission over a 10-km ring-core fiber using high-order orbital angular momentum modes. *Optics Express*, *26*(2), 594. https://doi.org/10.1364/oe.26.000594